Structural Studies of Electroactive Transition

Metal Oxide Films

A thesis submitted for the degree of

Doctor of Philosophy

at the University of Leicester

by

Nicola Rita St. Jude Farley

Department of Physics and Astronomy

University of Leicester

September 2001

Structural Studies of Electroactive Transition Metal Oxide Films

by

Nicola Rita St. Jude Farley

Abstract

This thesis is concerned with measuring the short-range structural changes that are induced when electrochromic transition metal oxide films are electrochemically oxidised and reduced. Three systems are studied: electrochemically-deposited nickel hydroxide, sol-gel-derived niobium oxide and oxide films anodically-grown on tungsten. Structural changes are measured using extended X-ray absorption fine structure (EXAFS), a technique that is sensitive to atomic structure up to about 5 Å, providing interatomic distances, and the number and identity of neighbouring atoms. Standard and quick transmission, energy dispersive, fluorescence and reflection modes are utilised. Additionally, the crystal impedance technique is used to study rheological changes during the sol-gel conversion of niobium oxide, and the X-ray reflectivity of the tungsten oxide films is measured at several stages of growth.

For the nickel hydroxide system, a distorted first Ni-O shell is observed in the anodically charged electrode, which reverts to a regular octahedral form as charge density decreases. An antagonistic movement is observed in the first Ni-Ni shell. For the niobium oxide system, the structures of both uncharged and cathodically charged electrodes are determined. The initially distorted first Nb-O shell of the uncharged Nb_2O_5 film is replaced by a regular octahedral Nb-O shell when charged. Again, a reversed effect is displayed by the first Nb-Nb shell. Also, the rheological development taking place during the sol-gel transformation is characterised. For the tungsten oxide films, a separation of W-O and W-W shells initially occurs during formation, reaching a maximum of 1.3 Å, then diminishes with a further increase of electrode charge density. Shell separation coincides with cation insertion during the formation of HWO_3; the subsequent shell convergence results from cation expulsion when WO_3 is being formed.

Dedicated to Mum

Acknowledgements

Firstly, I would like to express my thanks to my supervisors Steve Gurman and Rob Hillman for their help, support, patience and good humour throughout this PhD.

Special thanks to Kev for everything.

I am very grateful to all of the guys and gals in CMP/Theory for providing an excellent atmosphere conducive to work and fun in equal measure. Extra gratitude is given to Steve Baker, Merv Roy and Peter Maksym for helping me out whenever I'm stuck.

Many thanks to all of my friends, especially my old pals Caroline Cox, Marjorie Coulon and Gavin Edwards for providing emotional support and a constant torrent of abuse to keep me sane.

Thanks to Ted Davis for the use of his evaporator, sputterer, talysurf, dry box and UV/vis spectrophotometer. Thanks also to the guys in the Chemistry Workshop for constructing my cells, meeting many tight deadlines and teaching me about their work.

I reserve my deepest gratitude for my family, Mum, Andrew, Peter and Ebbo.

Contents

List of Figures

List of Tables

Chapter 1

Introduction

The reversible colouration of electrochromic transition metal oxide films is induced by the application of an anodic or cathodic voltage. This phenomenon is important to the development of optoelectronic devices. To understand this effect, it is necessary to investigate the structural responses of these oxides to the applied electrode charge. EXAFS is an ideal tool for the study of these systems as it is able to provide both structural and electronic information *in situ*, on a timescale that is relevant to optoelectronic technology.

This thesis is structured as follows. The theoretical grounding for the techniques used is established in chapter 1. The experimental procedures associated with the most commonly used techniques are described in the second chapter. In chapters 3, 4 and 5, the experimental results are presented for electrochemically-deposited nickel hydroxide, sol-gel-derived niobium oxide and oxide films anodically-grown on tungsten, respectively. The results are discussed in depth and conclusions are drawn at the end of each chapter.

1.1 X-ray Absorption Spectroscopy

Many structural X-ray techniques based on the scattering of radiation [1, 2, 3], particularly X-ray diffraction [2, 3, 4] and the standing wave method [1, 2, 3, 5, 6] demand that samples exhibit a high degree of structural order. This condition makes them unsuitable for studying the structures of disordered or amorphous materials such as electrochemically deposited films. In contrast, X-ray absorption spectroscopy (XAS) requires measuring the absorption coefficient of an element within an elemental or molecular sample in the crystalline, amorphous, solution, or even the gaseous state as a function of X-ray energy.

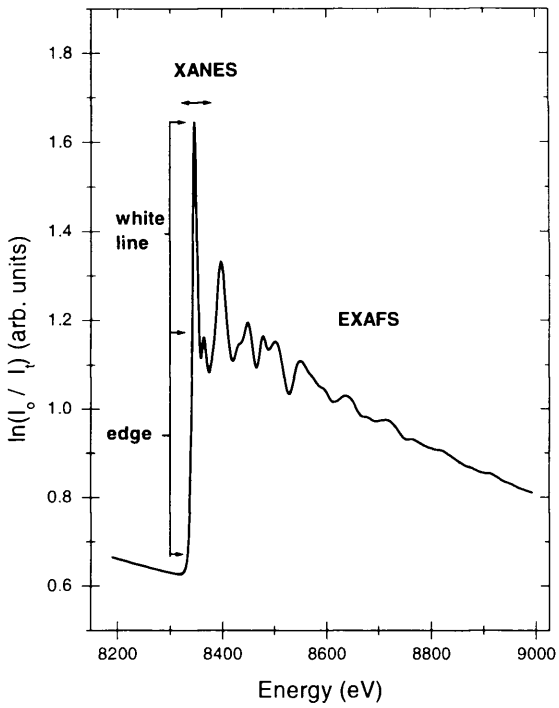

Figure 1.1: Raw XAS spectrum of NiO powder at the Ni K-edge.

When a beam of monochromatic X-rays of energy $\hbar\omega$ and intensity I_o

passes through a homogeneous sample of uniform thickness x, they interact to cause an inevitable loss of intensity. This loss of intensity is represented by Beer's law:

$$I_t = I_o\, e^{-\mu x}$$

or

$$\text{Absorbance} = \ln\left(\frac{I_o}{I_t}\right) = \mu x = \mu' \rho x \tag{1.1}$$

where I_t is the transmitted intensity, μ is the linear absorption coefficient (cm^{-1}), ρ is the density of the sample, and the mass absorption coefficient μ' (cm^2g^{-1}) $= \frac{\mu}{\rho}$ is independent of the physical state of the sample. Several attenuation processes compete to diminish I_t, making μ or μ' the sum of these contributions (eqn. 1.2), the dominating effect being strongly dependent on energy (fig. 1.1 [7]). In this section, the description is centred upon the X-ray region of 1–30 keV, particularly the area at and about the absorption edge, where it can be seen that photoelectric absorption is the major contributor to the absorption coefficient.

$$\mu' = \mu'_{ph} + \mu'_{cs} + \mu'_{is} + \mu'_{pa} \tag{1.2}$$

Contributions to the total mass absorption coefficient μ' come from photoelectric absorption μ'_{ph}, coherent (elastic, Rayleigh) scattering μ'_{cs}, incoherent (inelastic, Compton) scattering μ'_{is}, and pair production (*i.e.* electron + hole, ion or positron) μ'_{pa}.

Equation 1.1 shows that the intensity ratio I_t/I_0 decreases with increasing x or ρ. Additionally, it is evident that for any element μ decreases with increasing energy in the 1–30 keV region (fig. 1.2 [7]), so XAS spectra display a general drop in absorption, a trend which is interrupted by the occurrence of the absorption edge(s) (figs. 1.1 and 1.2). Photoabsorption of X-rays at or just exceeding the binding energy E_b of an electron in a core initial state (at E_i) of the absorbing atom results in its ejection from the core state into the continuum. This process involves the excitation of the electron from a core

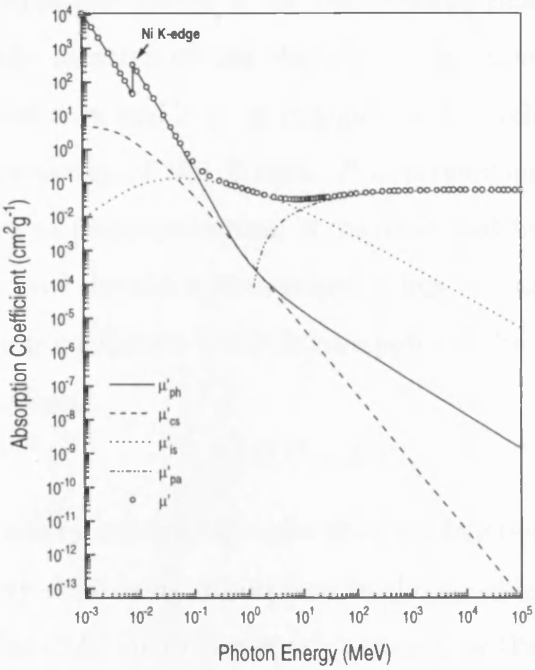

Figure 1.2: Calculated mass absorption coefficient for nickel as a function of photon energy.

level to the first fully unoccupied final state at E_f allowed by electric-dipole selection rules (K or $1s \rightarrow \epsilon p$ for a K-edge and $2p^3 \rightarrow \epsilon d$ for an L_3-edge). It therefore follows that μ is linked to the energy-dependent transition probability P for photoelectric absorption (in the dipole approximation) which is given by:

$$P = \frac{2\pi^2 e^2}{\omega c^2 m_e} \mid < \psi_f \mid \boldsymbol{\varepsilon} \cdot \mathbf{r} \mid \psi_i > \mid^2 \rho\,(E_f) \tag{1.3}$$

and

$$\mu = \frac{4\pi e^2 \omega}{c} \mid < \psi_f \mid \boldsymbol{\varepsilon} \cdot \mathbf{r} \mid \psi_i > \mid^2 \rho\,(E_f) \tag{1.4}$$

Here, $|\psi_i >$ is the initial state wavefunction for a bound electron before photoionisation, $< \psi_f|$ is the final state wavefunction for the ejected photoelectron, and $\rho\,(E_f)$ is the density of final allowed states at the final state energy E_f. $\mid \boldsymbol{\varepsilon} \cdot \mathbf{r} \mid$ is the electric-dipole matrix element, which contains the

electric field polarisation vector $\boldsymbol{\varepsilon}$ for the incident beam, and $\mathbf{r}$, the position vector for the location of the electron in the wavefunction; m_e is the rest-mass of an electron and e is its charge; c is the velocity of light, and ω is the angular frequency of the X-rays. P is proportional to μ so the edge transition, known as photoionisation, is characterised by a large and abrupt increase in μ, to give the absorption edges in figs. 1.1 and 1.2.

The absorption coefficient away from edges can be approximated using the Victoreen formula:

$$\mu = C\lambda^3 - D\lambda^4 \tag{1.5}$$

where C and D are tabulated constants that are functions of atomic number Z [8]. The slowly decreasing absorption in the pre-edge region of figs. 1.1 and 1.2 (where $\hbar\omega < E_b$ for $1s$ electrons) is caused by the excitation of higher energy outer shell electrons well beyond their absorption edges. Absorption in the post-edge region is a continuation of this, but the photoabsorption cross-section now includes the K-shell electrons whose probability for excitation has become higher.

It can be seen from equation 1.5 and figures 1.1 and 1.2 that absorption decreases as energy increases. Consequently, in the X-ray region there is relatively little interaction with materials (depending on sample thickness and the concentration of absorbing atoms), resulting in small signal changes. For this reason, the use of synchrotron-generated radiation has become common practice for XAS. The high beam intensity (large number of photons per unit area) or flux (typically $> 10^{12}$ photons/s at 10 keV) is advantageous because the signal-to-noise ratio is greatly improved; this is important because homogeneous sample areas are usually small, so the illuminated region is also small. High intensity is an especially valuable property to electrochemists whose *in situ* work is hampered by absorption by the electrolyte. The broad, continuous spectral range and the great tunability offered by synchrotron radiation is also beneficial because typical XAS spectra span just under 1 keV and the absorption edges of most elements can be covered.

X-ray absorption spectra can be measured via several different instrumental configurations, all of which relay the same information and share many common features. The choice of experimental configuration may depend upon factors such as the region of interest *e.g.* interfaces [3, 9], maximising the signal-to-noise ratio (which is related to the concentration of absorbing atoms in the sample), and the desired frequency for recording spectra. Four commonly used configurations will be described next.

i) Transmission Mode

The most straightforward way of recording X-ray absorption spectra is in the transmission mode (fig. 1.3). The intensity of the monochromatic, collimated beam incident on, and transmitted through the sample is detected by noble gas filled ion chambers, as the angle of the monochromator crystals is changed in order to scan the required energy range (eqn. 1.11). The energy scan can be carried out in two ways, by changing the angle in a gradual stepwise manner (standard transmission XAS) or in a continuous sweep (quick XAS), taking less than half the time of the former method. Simultaneous internal calibration of the edge energy is achieved by placing a calibrant of known edge energy in the beam path *i.e.* a foil of known thickness, consisting of the pure absorber atoms. The intensity of the beam transmitted through the calibrant I_c is detected by a third ionisation chamber; so the absorption spectrum of the calibrant, as well as the sample is measured, thus errors in the energy scale caused by slippage of the monochromator are correctable.

ii) Fluorescence Mode

The emission of fluorescent X-rays is a direct consequence of absorption, and arises from the relaxation of excited absorber atoms following absorption throughout the whole XAS spectrum. A core-hole remaining after ejection of a photoelectron is filled by an outer electron in an allowed higher energy state; this radiative transition is accompanied by the emission of fluorescent X-rays.

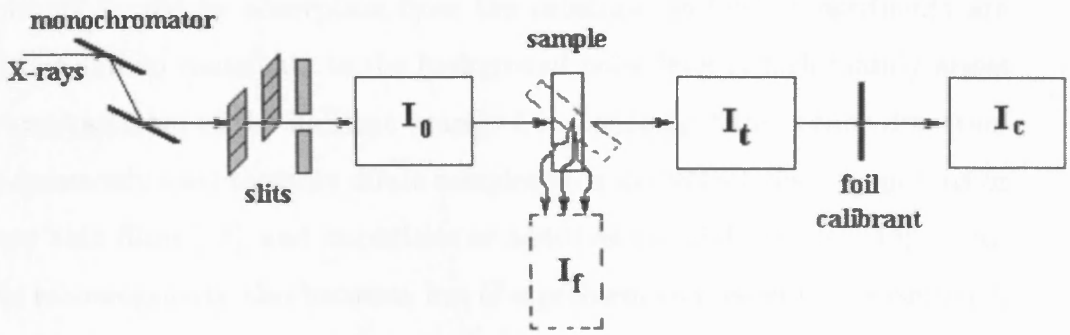

Figure 1.3: Transmission and fluorescence (dashed) geometries.

Owing to the dependence of fluorescence on absorption, I_f is proportional to, but lower than I_t for two major reasons. First, this relaxation process is rivalled by other competing non-radiative routes, primarily the production of Auger electrons. The probability of Auger transitions increases as energy or atomic number Z decreases; as a result, the fluorescence yield rises from ~0.5 at $Z = 30$ to ~0.9 at $Z = 60$ [8]. Second, the mean free path of the low kinetic energy fluorescent photons is short, resulting in some reabsorption into the sample, substrate and cell cross-section, thus decreasing the intensity even further and causing substantial problems for experimentalists, though this may be overcome by the use of thin layer cells (section 2.1.3). This detrimental effect is compensated by the consequent near-surface sensitivity of the signal (up to a few hundred Angstroms deep), a property which has been successfully exploited for XAS of thin, dilute samples [10].

$$\text{Fluorescence} = \frac{I_f}{I_o} = \mu x \tag{1.6}$$

Fluorescent radiation is typically measured in the arrangement shown in fig. 1.3 (dashed lines), so both I_t and I_f can be detected simultaneously [11]. The sample is positioned at 45° with respect to the incident beam and a solid-state detector is aligned at 90° to the first ion chamber to measure the fluorescent intensity. This configuration, and the short escape depth of the photons, improves the sensitivity of the signal, because many contri-

butions caused by absorption from the substrate and cell constituents are not as able to contribute to the background noise level (which mainly arises from scattering of the incident beam). Consequently, fluorescence detection is commonly used to study dilute samples such as electrolytes [12], porous or very thin films [13], and impurities or additives in solid samples [14]. Sample inhomogeneity also becomes less of a problem compared to transmission XAS. The fluorescence mode is especially useful for studying films that are electrochemically deposited, because the films tend to have low densities or low concentrations of absorbing atoms [15].

iii) Reflection Mode

The reflection mode is a surface-sensitive geometry for measuring X-ray absorption spectra. The previously stated configurations have used a fixed angle, varying energy arrangement. Reflection mode XAS (reflXAS) is described in this context, and an additional description of reflectivity profiles is given in terms of a fixed energy, varying sample angle arrangement. Absorption will be described at various angles, and reflectivity will be presented at various energies, thereby explaining reasons for choosing an optimum fixed value (of angle or energy, respectively) in each case.

In the reflection mode (fig. 1.4), the incident monochromatic beam of intensity I_0 and angle θ_0 impinges on the sample at grazing angles less than the critical angle for total reflection θ_c. This results in total external reflection for ideal, dense, highly reflective, planar surfaces with negligible roughness, such as the tungsten mirror exemplified in figures 1.5 – 1.6 & 1.8 – 1.9 [16]. In this ideal case, specular reflection takes place ($\theta_0 = \theta_R$), no loss of intensity occurs upon reflection *i.e.* the reflective intensity coefficient or reflectivity $R = \frac{I_R}{I_0} = 1$, with zero absorption and a short beam penetration depth ($<$ 20 Å, see fig. 1.5 dashed line). The penetration depth (*i.e.* attenuation length or extinction distance) is the depth into the material, normal to the surface, where I_0 falls to $1/e$ of its original value. All metal samples are

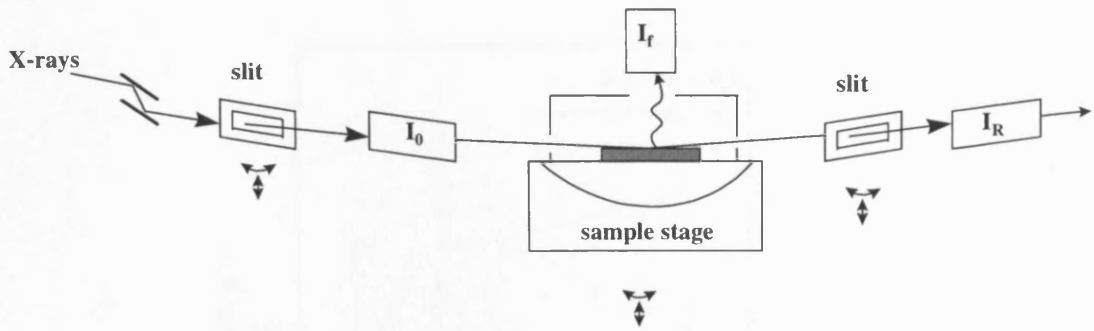

Figure 1.4: Reflection mode configuration with simultaneous fluorescence detection.

at least microrough, scattering the reflected beam and damping reflectivity by a factor of $\exp - (\sigma 4\pi \sin\theta_R/\lambda)^2$, where λ is X-ray wavelength and σ is the roughness, making actual metal reflectivities (below the critical angle) slightly less than one (fig. 1.6).

The complex energy-dependent refractive index n of solids in the X-ray region is

$$n = 1 - \delta - i\beta \tag{1.7}$$

The tabulated real δ and imaginary β terms responsible for n being slightly less than one account for refraction (transmission) and absorption of the beam, respectively ($\delta,\ \beta \sim 10^{-2} - 10^{-6}$). For a given incident energy E:

$$\delta = \frac{A\rho}{E^2} \tag{1.8}$$

and

$$\beta = \frac{\mu\hbar c}{2E} \tag{1.9}$$

Here, A is essentially constant and contains scattering factors for the atoms present. δ is dependent on the density ρ of the reflecting material, and equation 1.8 shows that δ and ρ are directly proportional. δ is always finite, so in the case of a dense ideal material, part of the incident beam is refracted

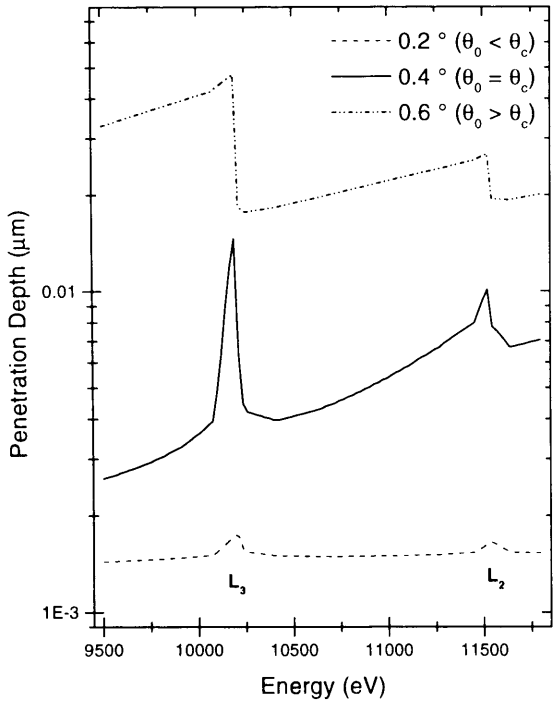

Figure 1.5: Calculated extinction distance as a function of energy for an ideal W mirror with zero roughness.

(transmitted) through the solid and part is reflected at $\theta_R = \theta_0$ (fig. 1.10). Ideal solids do not in fact exist as β is always finite, making R considerably less than 1 for all materials. It is evident from equation 1.9 that β is both energy-dependent and a function of μ, so when E is scanned, at fixed angle, in the desired range (as for the transmission mode, part i) the absorption spectrum is obtained by measuring the specularly reflected intensity I_R [17]. A standard absorption spectrum can then be extracted from β [2, 17] and analysed using conventional computational procedures (section 5.3.2). The remaining terms in equation 1.9 are standard physical constants.

Figure 1.6 shows that reflectivity is a slowly decreasing function of energy, punctuated with dips caused by the absorption edges. The abrupt increase

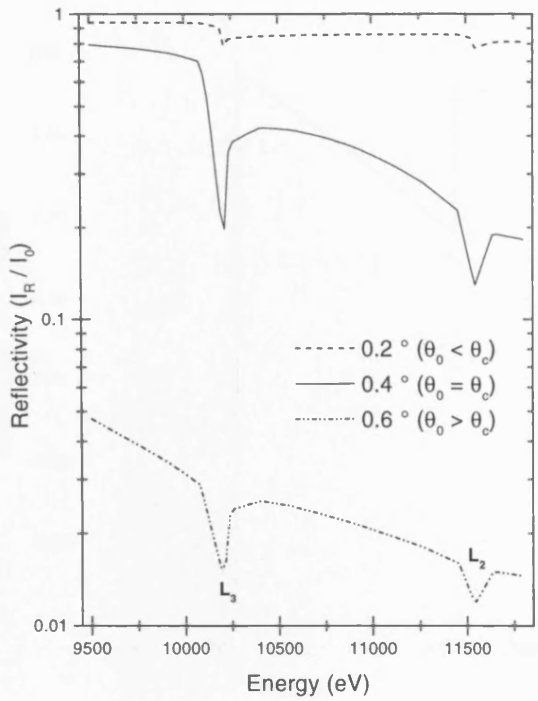

Figure 1.6: Calculated reflectivity as a function of energy for a tungsten mirror with zero roughness.

in absorption at the edge (figs. 1.1 and 1.7) is at the expense of reflection, resulting in reflectivity curves (spanning an absorption edge) having an overall appearance similar to an inverted absorption spectrum. When analysing the regions between edges in plots of energy *vs.* reflectivity, deviation from the slowly declining baseline, such as that shown figure 1.6, is caused by roughness; such an observation is therefore a useful qualitative check on the flatness of a sample.

When considering reflXAS experiments at fixed angle, the quality of spectra depends not only on the sample's roughness σ, but also on the choice of incident angle. Figure 1.6 shows that it is imperative to keep the grazing angle fixed below θ_c if reflectivity (and hence surface sensitivity) is to be

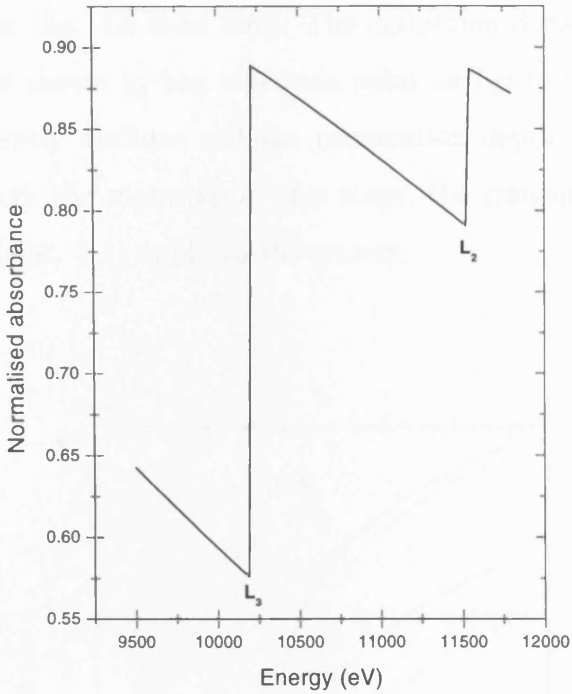

Figure 1.7: Calculated transmission mode absorption spectrum for a 5 μm thick W foil at the L_2 and L_3 edges.

maximised, and if the penetration depth is to be kept almost constant (fig. 1.5 dashed line). When the angle of incidence is very low, the critical angle is given by equation 1.10 [17].

$$\theta_c = \sqrt{2\delta} \tag{1.10}$$

Combining equations 1.10 and 1.8 show that θ_c and ρ are proportional, and that θ_c depends on photon energy, as depicted in figures 1.8 and 1.9. These plots illustrate the importance of keeping the grazing angle fixed well below θ_c when measuring reflXAS spectra.

It was stated that the penetration depth is low and almost constant when $\theta_0 < \theta_c$; in fact, maximum surface sensitivity is achieved when $\theta_0 \approx \theta_c/2$ (see

figs. 1.5 dashed line and 1.8). At incident angles close to θ_c, the penetration depth steadily increases with energy, except for the regions at the absorption edges (fig. 1.5 solid line). The extinction distance also increases sharply at θ_c, as shown by the inflection point on figure 1.8. When $\theta_0 > \theta_c$ reflectivity abruptly declines and the penetration depth rises as the beam transmits through the material; at this stage, the transmission expressions for absorption (eqn. 1.1) apply to the system.

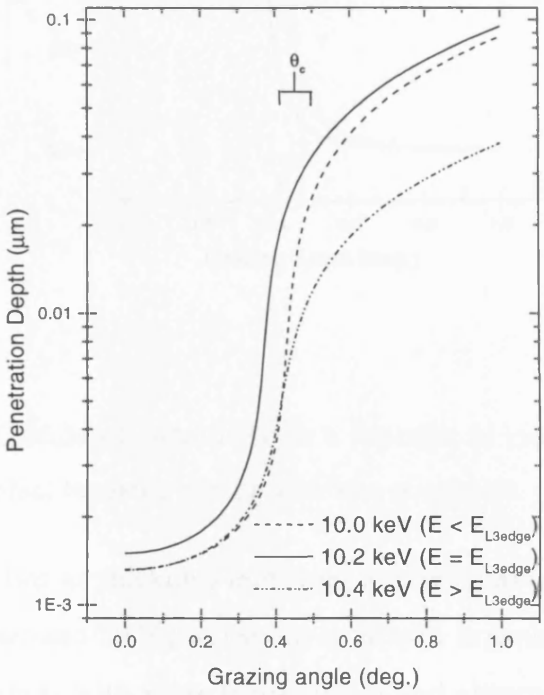

Figure 1.8: Calculated extinction distance as a function of grazing angle for an ideal W mirror with zero roughness.

A further drop in reflectivity results from the presence of a less dense, absorbing overlayer such as an oxide film, and ΔR (or alternatively $\Delta\beta$) is proportional to the linear absorption coefficient of the element of interest (eqn. 1.9). Very thin overlayers do not significantly reduce the reflectivity of

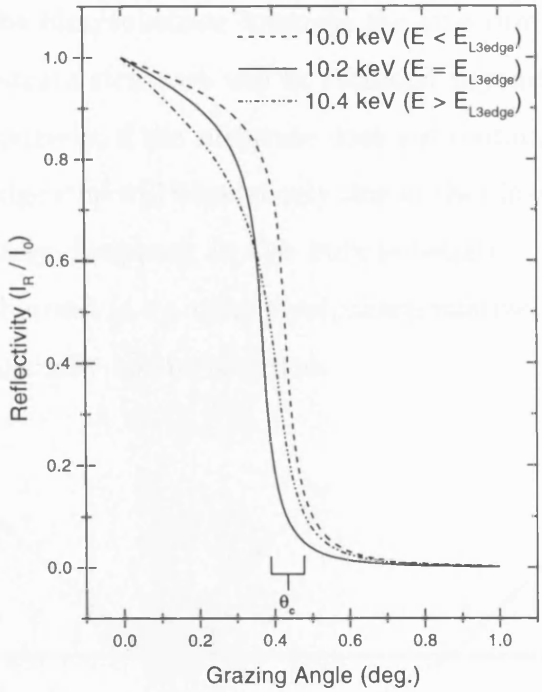

Figure 1.9: Calculated reflectivity as a function of grazing angle for an ideal tungsten mirror with zero roughness.

a metal surface, but as thickness increases, a considerable drop in reflectivity takes place (to around 50 %) as overlayer growth is usually accompanied by increasing roughness with more transmission and absorption.

For reflXAS as well as fluorescence detection, it is preferable that the substrate contains none of the absorbing element present in the film. If this condition cannot be met, it is not a serious problem because overlayer and substrate can still be distinguished if their densities differ. When $\rho_{\text{film}} < \rho_{\text{substrate}}$, $\theta_{c(\text{film})} < \theta_{c(\text{substrate})}$ so θ_0 can be tuned to probe the surface structure of the film, without contributions from the substrate. The dependence of penetration depth on incident angle (fig. 1.8) can also be used to evaluate film thickness when both overlayer and substrate contain the same element of

interest. Several XAS spectra can be recorded at progressively higher incident angles/probing depths; the structure will be characteristic of the bulk film at low depths; at the film/substrate interface the structure will be mixed, and finally, bulk substrate structure will be recorded beyond the film/substrate interface. Alternatively, if the substrate does not contain the same elements as the film, the edge step will be relatively tiny at the film/substrate interface, and will ultimately disappear in the bulk substrate. In cases where the interface is less blurred (*i.e* a more ideal, sharp interface where $\sigma \rightarrow 0$), the intermediate stage may not be recorded.

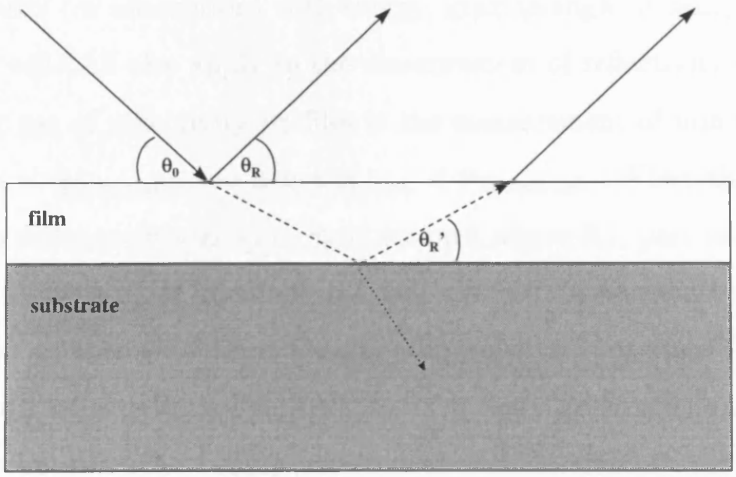

Figure 1.10: Reflection (solid lines) and refraction (dashed lines) in a two layered system. Partial reflection occurs from the film surface at θ_R; the transmitted beam then reflects from the film/substrate interface at θ'_R before leaving the film.

Critical angles at particular energies are tabulated for many elements and common materials [16]. If θ_c is not listed, a reflectivity profile (R *vs.* θ_0) is measured. Also, measuring the reflectivity profile of a sample will help to determine an optimum grazing angle for subsequent reflXAS experiments.

When measuring reflectivity profiles at fixed energy, the response of reflectivity and attenuation length to energy must be known in order to choose an appropriate static energy value. It can also be seen, in figures 1.5 and 1.6 that the incident energy should be fixed either far below or far above an absorption edge (edge energy $> \pm 50$ eV) because both the attenuation length and reflectivity vary widely with energy within 50 eV of an absorption edge, though it can be seen from absorption spectra (figs. 1.1 and 1.7) and figures 1.5 and 1.6 that both terms gradually increase with energy, making the highest surface sensitivity, highest reflectivity and lowest absorption obtainable when $E < E_{edge}$. Therefore, the stated evidence, relating penetration depth and reflectivity (or absorption) with energy, grazing angle or sample characteristics for reflXAS also apply to the measurement of reflectivity profiles.

Another use of reflectivity profiles is the measurement of film thickness, where $\rho_{(\text{film})} < \rho_{(\text{substrate})}$ and hence $\theta_{c(\text{film})} < \theta_{c(\text{substrate})}$. When the angle of incidence is sufficiently high (*i.e.* θ_0 is scanned above θ_c), part of the beam is reflected at the surface/medium interface and part is transmitted through the overlayer to then be reflected at the film/substrate interface (fig. 1.10). The resulting reflectivity profile consists of a series of fringes arising from interference between the beams reflected at each interface. The period of these oscillations *i.e.* the (regular) spacing between successive minima of the fringes indicate film thickness. The interference pattern becomes more complex when several layers are present with varying thickness. In ordered single crystals such as the polychromator described in the next section, the fringes are Bragg peaks, yielding the layer spacing in the crystal (eqn. 1.11).

iv) Energy Dispersive Mode

An alternative way to take transmission measurements is in the energy dispersive mode (fig. 1.11) which requires the use of a triangular Si crystal that is cylindrically bent in order to produce a polychromatic beam of the desired energy range. This is achieved because the incoming horizontal white

beam is reflected off the perpendicular layer planes of the curved crystal at different Bragg angles so that the reflected, dispersed beam (coming off the same face of the crystal) consists of X-rays with a spread of energies. The curvature of the crystal serves a dual purpose by also focusing the dispersed beam onto the sample at its focal point, before it diverges toward a position sensitive detector to measure I_t [2, 18]. The modified form of Bragg's law (eqn. 1.11), which defines the relationship between the angles of the reflected rays in the dispersed beam and their energy, is used to correlate the position of each pixel (or sensing element) in the linear array of the position sensitive detector with the energy of the detected X-rays.

$$n\lambda = 2d\ \sin\theta \left(1 - \left[\frac{\delta}{\sin^2\theta}\right]\right) \tag{1.11}$$

Where λ is the incident or reflected X-ray wavelength, n is the order of reflection, d is the crystal layer spacing, θ is the angle the incident or reflected X-rays make with the crystal's surface, and δ is the decrement of refractive index resulting from refraction within the crystal (see eqn. 1.7). Both the curvature of the crystal (hence the energy range produced) and the pixel-energy correlations are calibrated using standard transmission XAS spectra of an absorber atom foil with known edge energy. Operating in this mode enables the entire XAS spectrum to be recorded simultaneously, making it ideal for *in situ* structural studies of fast physical or chemical processes. A set of good quality time-resolved absorption spectra can be obtained in timescales on the order of 2 minutes, individual spectra having acquisition times as short as 3 ms.

The XAS spectra recorded in all of these configurations display their features in two distinct regions, the X-ray absorption near edge structure and the X-ray absorption fine structure. Both of these regions will be described in detail in the following sections.

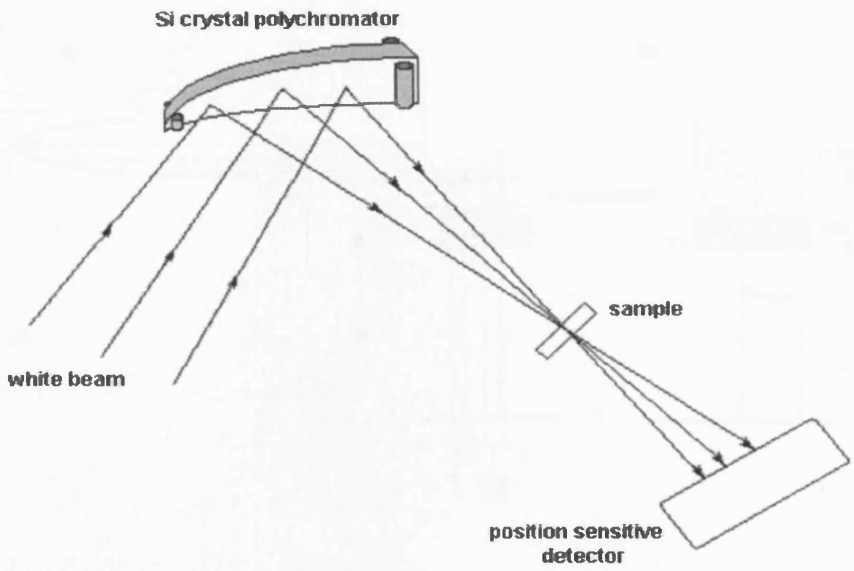

Figure 1.11: The energy dispersive configuration.

1.1.1 X-ray Absorption Near Edge Structure

The X-ray absorption near edge structure (XANES) are features present in the range 10 eV below to 50 eV above and including the absorption edge (fig. 1.1). A simple diagram (fig. 1.12) is used to relate the main electronic transitions to the observed spectral features.

Peaks in the pre-edge region are caused by the promotion of bound, ground state electrons to outer, part-occupied hybridised states (if present). Such transitions are not fully permitted because these hybrid states do not wholly posses the correct symmetry or character necessary for the excitation (according to electric-dipole selection rules). Consequently, this partially-allowed, low probability transition produces peaks with small amplitudes. The emergence (or disappearance) and magnitude of these features provides information about the existence and occupancy of discrete hybridised states (*i.e.* impurity levels) just below the conduction band.

The most important XANES feature is the absorption edge. As the point

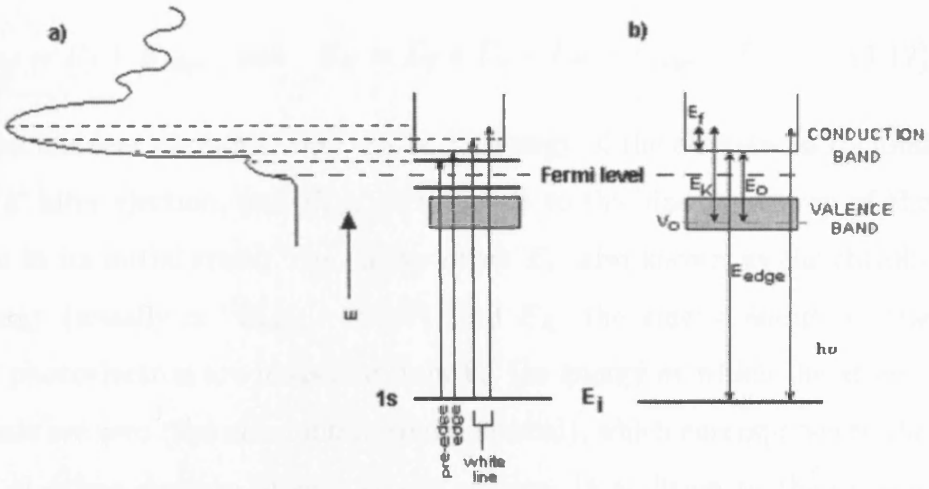

Figure 1.12: b) X-ray-induced 1s electronic transitions and a) the resulting K-edge spectral features for a simple insulator.

at which the edge appears is dependent on the binding energy (E_b) of the core electron, which is itself dependent on the composition of the substance, a shift in edge position indicates a change to the valency of the absorbing element. For some elements, as valency increases the higher nuclear charge causes the energy of all bound states to drop *i.e.* the binding energies of all bound electrons rise; consequently, a decrease in Fermi energy takes place as valence electrons in the outermost states are removed upon oxidation. At the same time, the predominant increase in core-level screening means that the energy separation between the innermost levels and accessible fully unoccupied states at the edge of the conduction band widens with increasing valency. As a result, the magnitude of E_b increases, decreasing the probability of the edge transition, and hence an increase in edge energy with valency. For some elements, screening has a weaker effect with increasing valency, so the opposite may occur (*i.e.* a decrease in edge position with increasing valency).

Figure 1.12b shows the energies which correspond to each XANES tran-

sition are

$$\hbar\omega = E_f + E_{edge} \quad \text{and} \quad E_K = E_f + E_o = \hbar\omega - E_{edge} + E_o \tag{1.12}$$

$\hbar\omega$ is the incident photon energy, E_f is the energy of the electron in its final state *i.e.* after ejection, and E_{edge} corresponds to the binding energy of the electron in its initial state. The energy offset E_o, also known as the threshold energy (usually $\simeq$ E_{edge} - 10 eV), and E_K, the kinetic energy of the ejected photoelectron are measured from V_o, the energy at which the atomic potentials are zero (the mean interstitial potential), which corresponds to the energy of a free electron of zero kinetic energy. In addition to the expressions in 1.12, the outgoing photoelectron (wave) of kinetic energy E_K can be described in terms of its momentum or wavevector k:

$$E_K = \frac{\hbar^2 k^2}{2m} \tag{1.13}$$

where

$$k = \frac{2\pi}{\lambda} \tag{1.14}$$

Additional qualitative information, regarding conduction band structure and symmetry can be extracted from the white line intensity. The white line (fig. 1.1) appears as a continuation of the edge rise and is caused by the excitation of core electrons beyond the original edge transition, and up to allowed levels in successively higher shells, if a high density of these states exists in the conduction band. The location of the white line makes it difficult to pinpoint the precise edge position, which is characterised by the E_{edge}; it is defined as the energy corresponding to half the normalised edge height (*i.e.* half the main edge excluding the white line, fig. 2.2). In practice, if the white line is small (*e.g.* in some metals), the obscuring effect is deemed negligible, so the edge position may be measured as the energy at the inflection point of the full edge or 'edge jump' [19], or alternatively as the energy at half the height of the full edge jump. Methods using the full edge are acceptable if the absolute value of the edge position is not as important as the relative

position, as with samples that have been oxidised or reduced, unless the size of the white line increases as valency changes.

In summary, values for the position and magnitude of all XANES features provide direct qualitative information about the density of unoccupied states, which in turn relates to valence band structure and symmetry; XANES also provides quantitative information about the oxidation state of absorbing atoms (section 2.2.3). So far it has been assumed that photoionisation produces a free electron, scattering effects being negligible. In order to complete this description of XAS, the fate of the ejected photoelectron will be considered with a discussion of final state effects in the following section.

1.1.2 Extended X-ray Absorption Fine Structure

Extended X-ray absorption fine structure (EXAFS) refers to oscillations in the slowly declining absorption coefficient at the high energy side of the absorption edge; these oscillations span the range from ~50 eV above to several hundred eV beyond the absorption edge, *i.e.* to the end of the XAS spectrum (fig. 1.1).

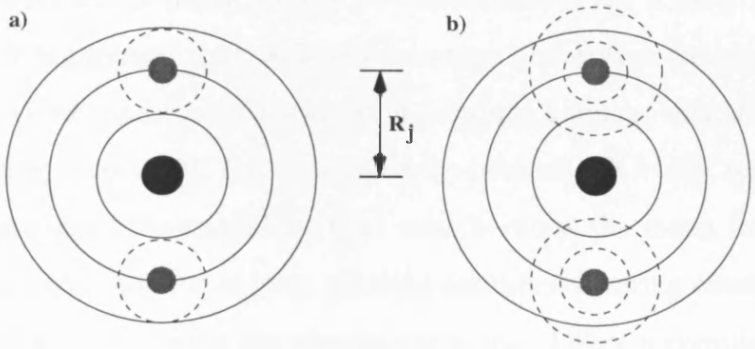

Figure 1.13: Spherical photoelectron waves, outgoing (solid circles) and backscattered (dashed circles), a) in phase and b) out of phase.

The cause of the oscillations is explained by treating the ejected photoelectron as a spherical wave of wavevector k emanating isotropically from an

absorbing atom (fig. 1.13, solid circles). A small fraction of the outgoing wave is scattered by surrounding atoms (if present), converting these parts into a backscattered wave (fig. 1.13, dashed circles) which then returns to the absorbing atom. Because this process pertains to the ejected photoelectron, backscattering affects the final state wavefunction $< \psi_f|$ in equations 1.3 and 1.4 so that it comprises the sum of outgoing and backscattered components $< \psi_f^{out}|$ and $< \psi_f^{back}|$, respectively. If the absorbers are isolated free atoms, as in a gaseous element, there are no near neighbours from which the photoelectron can scatter. As a result, the only contribution to $< \psi_f|$ is from $< \psi_f^{out}|$, producing a free electron; no oscillations are observed and μ smoothly decreases with $\hbar\omega$. This smooth decline for isolated atoms is denoted μ_o and forms the background absorption level in XAS spectra (eqn. 1.15). Conversely, $< \psi_f^{back}|$ is always nonzero in molecular gases and condensed matter, so both waves interfere constructively or destructively (depending on their wavelength) giving rise to oscillations in the absorption coefficient on either side of μ_o. When the outgoing and backscattered waves are in phase, interference is constructive and additive so μ rises (fig. 1.13a); the opposite takes place for out of phase, destructive interference (fig. 1.13b). In this description, it is assumed that each photoelectron undertakes one single elastic scattering event, and forward scattering does not happen; this is called single scattering theory [20, 21]. Alternatively, post-edge XANES may contain multiple scattering contributions that arise because the mean free path of the low E_K photoelectron is long, allowing another scattering event to occur. During multiple scattering the photoelectron may follow a complex path (if the atoms are collinear or triangular), so several scattering events may take place *before* the photoelectron returns to an absorbing atom.

The oscillatory behaviour of μ is described as a function of photoelectron wavevector k, and is given by:

$$\mu(k) = \mu_o(k)[1 + \chi(k)] \tag{1.15}$$

where $\chi(k)$ is the EXAFS function, which contains terms that account for modulations in the photoelectron-wave's phase and amplitude that give rise to EXAFS. Since the oscillations are caused by atoms in close proximity to the absorber, $\chi(k)$ also contains local structural information. The plane-wave approximation [21] provides a simple and satisfactory expression for the EXAFS function, for j shells within identical scattering atoms surrounding the absorber:

$$\chi(k) = \sum_{j=1}^{j} A_j(k) \underbrace{\sin(2kR_j + 2\delta_l + \phi_j)}_{\text{phase function}} \tag{1.16}$$

where $A_j(k)$ is the amplitude function:

$$A_j(k) = \underbrace{\frac{S_o^2(k)e^{-\frac{2R_j}{\lambda}}}{kR_j^2}}_{\text{damping}} \overbrace{N_j \cdot |f_j(k)|}^{\text{backscattering}} \underbrace{e^{-2\sigma_j^2 k^2}}_{\text{disorder}} \tag{1.17}$$

In the phase function, $2\delta_l + \phi_j$ is the total phase shift that results when the photoelectron-wave passes out from the central atom (absorber) with a phaseshift of δ_l (orbital quantum number $l = +1$ for the K-edge), encounters backscattering atoms with a phaseshift of ϕ_j, then returns to the central atom (hence $2\delta_l$), thereby modifying the sinusoidal EXAFS oscillations. During this interaction, the photoelectron of wavevector k travels twice the mean interatomic distance R_j, *i.e.* prior to and following the scattering event, hence the factor of two (fig. 1.13).

In the amplitude function, the terms which describe damping of the photoelectron-wave include the amplitude reduction factor $S_o^2(k)$ (usually ≤ 1 [22]), which accounts for energy loss due to many-body effects in the central atom, such as multielectron excitations *i.e.* excitation of outer electrons (termed shake-up and shake-off processes) in addition to photoionisation. The mean free path factor $e^{-2R_j/\lambda}$ accounts for inelastic loss as the photoelectron-wave excites the scatterers and medium, where λ is the elastic mean free path of the photoelectron; also, $1/kR_j^2$ describes the loss of ampli-

tude as distance increases; both of these damping terms show that scattering from only the nearest neighbours contribute to EXAFS (within $R_j \simeq 5$ Å from the absorber). The backscattering factor is $F_j(k) = |f_j(k)|e^{-i\psi_j}$, where ψ_j is the phase of $F_j(k)$ and $|f_j(k)|$ is the element-specific and energy-dependent electron scattering amplitude; this can be used to identify the N_j identical neighbours in the jth coordination shell. The term $e^{-2\sigma_j^2 k^2}$ is another damping factor which accounts for amplitude loss due to disorder in the system; it contains the Debye-Waller factor σ_j^2 which is the root mean square fluctuation about R_j (hence the factor of 2). The extent of fluctuation arises from the sum of structural or static disorder (high in amorphous materials) and thermal contributions *i.e.* vibrations ($\sigma^2 = \sigma^2_{\text{stat}} + \sigma^2_{\text{therm}}(T)$), assuming the fluctuation is harmonic and therefore a Gaussian pair distribution function with maximum at the mean interatomic distance R_j, a half-width of $2\sigma_j$ and a standard deviation of σ_j.

The origin of EXAFS has been described in a simple way, and it can be seen that the elemental identity of backscatterers and structural parameters such as interatomic distances, coordination numbers and disorder are contained within the EXAFS function. Accordingly, these values can be extracted using computational methods to fit the EXAFS region of XAS spectra (section 2.2.4). For these procedures, the more advanced (and complex) rapid curved wave theory [20, 23] replaces the plane wave approximation in order to interpret EXAFS data.

1.2 Spectroelectrochemistry

Combined spectroscopy and electrochemistry reveals more about the behaviour of electrochemically active materials than spectroscopic techniques and electrochemistry used separately. This is because a more complete understanding of electrochemical performance can be achieved if structural changes in the involved species are monitored spectroscopically *during* electrochemical experiments. Such *in situ* investigations therefore enable electrochemists to conclusively verify the connection between the spectroscopically-derived quantities and the potentials that affect them.

1.2.1 Electrochemical Techniques

A potentiostat is used in electrochemical experiments to deliver controlled potentials which induce reduction and oxidation (redox) reactions in a three-electrode cell filled with electrolyte. A three-electrode cell is a circuit that consists of a working electrode (WE), a counter electrode (CE) and a reference electrode (RE), all of which are immersed in a conducting electrolyte (fig. 1.14). These components are used in a way that enables controlled redox reactions to take place at the working electrode, and the current at the WE must be nonzero for it to perform its function as the site for redox reactions. Chemical species that can be manipulated by applied potentials are termed electroactive. In modified electrodes, the material of interest is an electroactive film attached to the surface of the working electrode. Modified electrodes comprising nickel hydroxide, niobium oxide and tungsten oxide films on various pure metal WEs form the subjects of this thesis.

At open circuit, the current and voltage fluctuate slightly about zero as electrons are exchanged at the electrode/electrolyte interfaces and an equilibrium is reached. To ensure that zero current and potential are constant and known, the current and potential at the reference electrode (at equilibrium) are taken to be zero. Also, when a potential E is applied by the poten-

tiostat, the reference electrode remains at equilibrium, so no current passes from it and all quantities are stated with reference to it; the RE is therefore used to calibrate the applied and measured voltage ($E = E_{\mathrm{WE}} - E_{\mathrm{RE}}$). The electrode maintains its equilibrium by its own redox reaction exemplified by the mercury/mercuric oxide, saturated mercury/mercurous chloride (saturated calomel electrode, SCE) and mercury/mercurous sulphate reference electrodes [24]:

$$\begin{aligned} \text{Cell:} \quad & Pt(m) \mid Hg(m) \mid HgO(s) \mid NaOH(aq) \\ \text{Reaction:} \quad & HgO + 2e^- \rightleftharpoons Hg + O^{2-} \end{aligned}$$

$$\begin{aligned} \text{Cell:} \quad & Pt(m) \mid Hg(m) \mid Hg_2Cl_2(s) \mid KCl(sat'd) \\ \text{Reaction:} \quad & Hg_2Cl_2 + 2e^- \rightleftharpoons 2Hg + 2Cl^- \end{aligned}$$

$$\begin{aligned} \text{Cell:} \quad & Pt(m) \mid Hg(m) \mid Hg_2SO_4(s) \mid H_2SO_4(aq) \\ \text{Reaction:} \quad & Hg_2SO_4 + 2e^- \rightleftharpoons 2Hg + SO_4^{2-} \end{aligned}$$

The parenthesised letters (aq), (s) and (m) refer to the aqueous, solid and metallic states, respectively, and *sat'd* represents a saturated aqueous solution. The contents of the electrode are separated from the bulk electrolyte and other electrodes by a fine porous frit or sinter (permeable to only the smallest ions) to avoid contaminating the rest of the cell. As no current flows from the RE, the current i passes between the WE and the counter (or auxiliary) electrode whose function is simply to pass a current of equal magnitude (in the opposite direction) to the WE via the electrolytic medium, for continuity of the circuit (see fig. 1.14). It is important that the CE is inert because as oxidation happens at the WE, reduction occurs at the CE (and *vice versa*), so the products of the CE reaction must not be electroactive or else they would interfere with those at the WE. To combat this problem, another frit or semi-permeable membrane is often used.

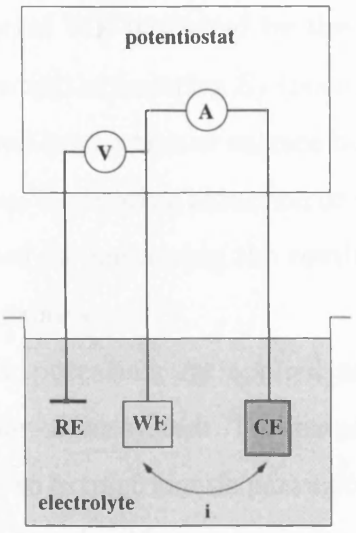

Figure 1.14: Schematic three electrode cell.

The electrolyte is a conductive solid or liquid solution consisting of an inert solvent (preferably high dielectric constant) with a dissolved excess of non-electroactive ionic species. These mobile solution species are called counter and co-ions because their charge is either the same or opposite to the charge of the electroactive species. Their function is not only conductive but also to preserve electroneutrality at the working electrode. For instance, a sufficiently negative (cathodic) potential at the WE initiates electron transfer so that reducible electroactive film species gain electrons and are reduced. The negative charge in this region is counterbalanced by a diffusive influx (or mass transport) of cations into the pores or interstices of the film from the bulk electrolyte, hence charge is conserved. In this case, there is an influx of counter ions of opposite charge to the reduced film species and/or expulsion of co-ions of similar charge. In the reverse situation, oxidation of the film, expulsion of cations and influx of anions happens at more positive (anodic) potentials [25].

In electrochemical experiments, redox reactions at the WE/film interface are induced by delivering known potentials between the working and reference electrodes (fig. 1.14). Redox reactions take place at this junction because

the Fermi level of the metal WE is altered by the applied potential, either raising E_f (negative potential) or lowering E_f (positive potential) to above or below the energy of allowed conduction or valence band states in the adjacent electroactive material, thus facilitating reduction or oxidation. The effect this has on the film is detected by measuring the resulting current between the working and counter electrodes.

The pattern by which potentials are applied provides a specific insight into the physical behaviour of the system. For instance, potentiostatic experiments may be performed to extract kinetic parameters such as rate constants and diffusion coefficients, to identify the extent to which charge transfer or diffusion influence the electrode process. Potentiodynamic investigations add to this mechanistic information by enabling the response of the system to a (perhaps rapidly) changing driving force to be determined. Cyclic voltammetry is one such potentiodynamic technique, and its use will be described next.

1.2.2 Cyclic voltammetry

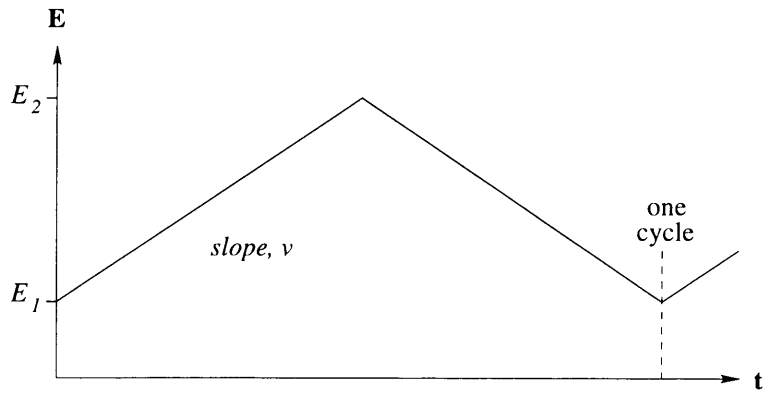

Figure 1.15: Potential *vs.* time for cyclic voltammetry.

Cyclic voltammetry is a technique by which the applied potential is driven linearly between two selected limits E_1 and E_2 (with respect to time), then returned linearly to E_1 to complete one cycle (fig. 1.15). The linearity of the

incline or decline illustrates a constant scan rate $\nu = \left|\frac{dE}{dt}\right|$ throughout a cycle, though many cycles at the same or varying scan rates may be performed. The result is sequential oxidation and reduction (or *vice versa*) of electroactive film species, during which the current is measured as a function of potential to produce a cyclic voltammogram or CV (fig. 1.16). The anodic and cathodic current is respectively proportional to the amount of electroactive species oxidised and reduced during that cycle. In the CV shown in figure 1.16, the rising current during the anodic, forward or positive scan ($E_1 \rightarrow E_2$) corresponds to oxidation of an increasing number of oxidisable film species until a maximum i_{pa} is reached, and the number of electrons generated by oxidation reaches its peak (at E_{pa}), after which the remaining available film species are oxidised and the current falls toward zero at E_2. By the time that E_2 is reached, most of the available electroactive species should be oxidised, therefore the number of reducible film species is high and consequently these are reduced during the cathodic, reverse or negative scan ($E_2 \rightarrow E_1$), during which electrons are consumed and a negative current results, peaking at i_{pc} and E_{pc}. It follows that comparing the anodic to cathodic peak area within a particular cycle indicates the reversibility of the redox reaction. Also, variations in peak separation ($\Delta E_p = E_{pa} - E_{pc}$) and the decay of one or both of the current peaks over successive cycles signifies the stability of that redox reaction. The availability of oxidisable and reducible species (and hence the number of species converted) is governed by the mobility of electrons and counter/co-ions across the film.

The immobility of electroactive species in surface-confined films of modified electrodes means that kinetic parameters such as fluxes and diffusion coefficients refer only to the movement of counter and co-ions, limiting the extractable quantities (regarding the film) to the charge Q passed during oxidation and reduction, the amount of electroactive species present N (mol) and the coverage of these sites on the electrode surface, Γ (mol cm^{-2}).

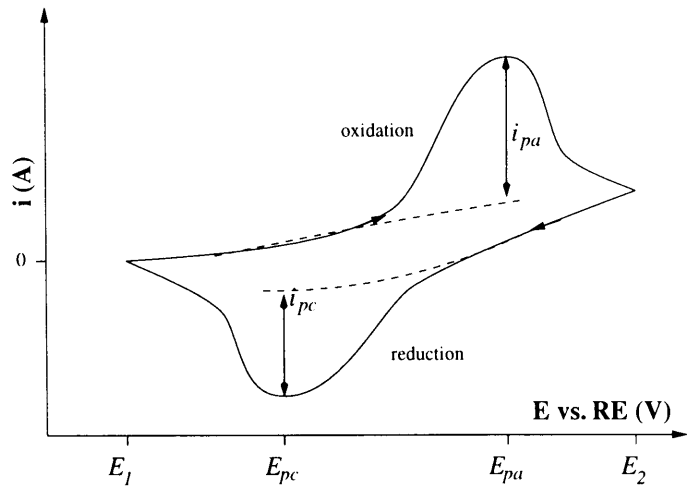

Figure 1.16: A schematic cyclic voltammogram.

$$Q = \int i\,dt = nFA\Gamma = nFN \tag{1.18}$$

i is the current, n is the number of electrons transferred to or from each site, F is Faraday's constant, A is the electrode area and t is time. If a modified electrode consists of a thin surface-bound film, all of the stationary electroactive sites are oxidised and reduced during the course of a CV. This situation applies to adsorbed monolayers, very thin films and films 'sandwiched' between working and counter electrodes (thin layer cells), where charge transport is facile and the diffusion of ions is faster than the experimental timescale. Many films do not in fact conform to these criteria, limiting the amount of sites converted, distorting CVs and requiring a more complex model to explain electrode processes which will be described in section 1.2.3.

1.2.3 Electrochromism

The above general description of dynamic electrochemical redox processes in modified electrodes will be presented in terms of the constituent steps: electron transfer at the electrode/film interface, charge transport across the film and the subsequent movement of counter and co-ions throughout the film (fig. 1.17), with emphasis on transition metal oxide systems and observed

colour changes.

As mentioned previously, application of an anodic or cathodic potential at the WE induces the oxidative or reductive conversion of electroactive film species. Electron transfer only takes place at the WE/film interface, enabling direct redox conversion of only very thin films at this junction. Charge transport is more complicated in films thicker than a monolayer because the charge has to spread throughout the full depth of the film (often $\sim$ 1 μm); this may be accomplished by movement of electrons across the film structure via polarisation of the molecules. The take-up or loss of an electron at a redox site of course changes the polarisation of sites nearby, the electron subsequently travels by 'hopping' to the nearest electron deficient site [26]. For this model, oxidation initially occurs at a film site adjacent to the working electrode; the closest electron deficient site is the WE which collects the electron, thereby creating a vacancy at the first site, toward which another electron passes from the bulk film to again be taken up by the WE. Conversely, during electro-reduction the electron is taken up from the WE by film species at the WE/film interface, it then hops to the nearest electron deficient site in the bulk film, causing a vacancy at the original site which is then replenished by another electron from the WE, and so on. As a result, the passage of electrons toward or away from the surface of the WE during oxidation or reduction, respectively depletes or supplies the film with electrons; the progression continues until all viable sites throughout the film are oxidised or reduced, and the measured current drops toward zero. This kind of conduction occurs in systems where electron mobility is low *e.g.* films with low conductivity. A solid state model applies to metal films and other conductors; here, highly mobile electrons are not associated with any particular atoms, and the electrons simply pass between the valence and conduction bands of the WE and film, altering E_f of each material accordingly. The molecular and solid state descriptions represent the 'bands *vs.* bonds' dichotomy when considering conduction across a material [26, 27].

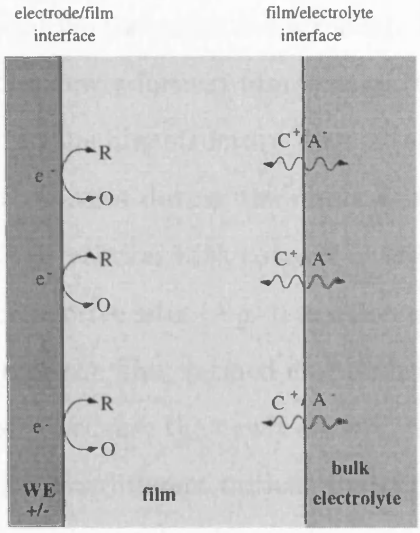

Figure 1.17: Redox reaction in a modified electrode; curved arrows show electron transfer and wavy arrows depict counter and co-ion exchange; C^+ and A^- are electrolyte cations and anions; O and R refer to oxidised and reduced species, respectively. The mechanism for charge transport within the film may be given either by a molecular and solid state description.

A specific counter/co-ion combination may not only be chosen for reasons such as the size (and hence mobility) and charge density of the ions, but also for their qualities as dopants for electrodes that behave as semiconductors, either supplying electrons or holes, thus modifying E_f and altering the oxidisability/reducability of the film. For instance, a p-type film containing substitutional Li^+ is oxidised at less positive potentials than undoped an film since electron accepting dopants create positively charged holes, thereby lowering E_f and making oxidation more favourable [25, 28, 29]. By a similar argument, reduction in n-type electrodes with electron donating dopants is also enhanced.

As already stated, during the redox process, positive and negative counter and co-ions are exchanged by diffusion between the film and bulk electrolyte so that electroneutrality prevails in all areas (except, at the electrode/film

interface where the initial perturbation takes place). In some cases, counter or co-ions react with the newly-formed film species, therefore becoming reversibly incorporated into the film structure, thus altering the chemical composition of electroactive species during the redox process (eqn. 1.19). The electrochemically-induced reaction with counter or co-ions that accompanies valency changes at electroactive sites (*e.g.* transition metal atoms) can evoke a reversible colouration of the film, termed electrochromism. This occurs as a result of charge transfer because the newly-formed compound, with altered electronic structure, displays different optical absorption behaviour *i.e.* different visible region transitions take place either within the valence band or across the optical band gap of the new species. The characteristic colour change displayed by a system may be counter or co-ion specific - which is affected by their size and charge density, or also by the morphology (*e.g.* porosity) of the film. In many transition metal oxide systems electrochromism may be exemplified simplistically by the following redox reaction, also known as 'bronze' formation.

In terms of cation loss/insertion:

$$\underbrace{MO_y}_{\text{bleached}} + nC^+ + ne^- \underset{\text{ox}}{\overset{\text{red}}{\rightleftharpoons}} \underbrace{C_nMO_y}_{\text{coloured}} \tag{1.19}$$

Here M represents a transition metal centre, O is oxygen, and C is a cationic co-ion. The above description gives a general idea of the most common type of transition metal oxide electrochromism (*i.e.* colouration upon cation insertion) [30]). Some details may vary according to the system; for example, in some cases the colouration/bleaching cycles may be opposite to that stated above (*i.e.* anodic as opposed to cathodic colouration), or anion incorporation/expulsion may be the dominant pathway for electrochromic action. Alternatively, in some instances, counter and co-ions may not be required for electrochromic action, though this is more common in non-transition metal oxide systems [30]. Ambiguities exist regarding mechanistic details

of many systems; techniques such as probe beam deflection [31, 32] or the electrochemical quartz crystal microbalance (EQCM) [33] are used to resolve uncertainties by analysing electrolyte movement.

1.2.4 Electrochromic Devices

Extensive studies have been carried out, involving transition metal and rare earth oxides [30, 34], and more recently organic conducting polymers [35, 36], in order to develop electrochromic display devices, energy efficient windows and anti-glare car door mirrors [30, 37]. The main advantage is low power consumption because once induced, colouration persists with little (if any) further voltage input, this is called the memory effect. In addition to memory effects, the colour(s) observed, the difference in the reflective intensity of bleached and coloured states (contrast ratio), the time required for full colouration or bleaching (response time), the change in optical absorbance achieved per unit of charge for colouration and reversal (colouration efficiency and write-erase efficiency, respectively), and the ability of the system to withstand repeated transformation between the two states (cycling durability) are factors that are assessed and optimised when developing a system for specific applications in optoelectronic technology.

Electrochromic devices (ECDs) have been developed on large and small scales *e.g.* windows and pixels in display devices, respectively. They are built to operate in either the transmission or reflection mode (fig. 1.18), but the reflected intensity is half the transmitted intensity as the optical path length doubles upon reflection.

A typical ECD has a multilayer arrangement consisting of a 'sandwich' of thin glass substrates coated on the inside surface with an optically transparent conductor such as indium-doped tin oxide (ITO). The outer surfaces may be strengthened with a supporting layer of glass. The conductive coatings are very thin and have low resistance, typically 0.5 $\Omega\,\mathrm{cm}^{-2}$, restricting prob-

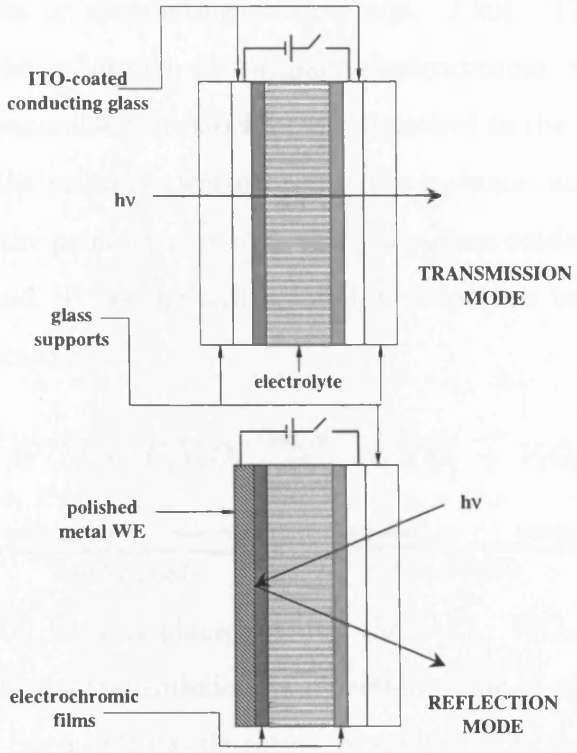

Figure 1.18: Schematic cross-sectional view of electrochromic devices with reflection and transmission configurations.

lems relating to uneven current density due to voltage drop over fairly large areas. The inside surface of one conducting glass layer acts as the working electrode and the other is the counter electrode, so oxidation at one electrode is accompanied by reduction at the other, and *vice versa.*

A thin, even electrochromic film is deposited onto the conducting side of each electrode by electrodeposition, sputtering (section 5.2.1), thermal evaporation, sol-gel deposition, spin-coating or some other method. The choice of film is primarily made so that one layer takes up cations while the other film expels them (and *vice versa* for anions); also, materials are chosen so the anodic or cathodic occurrence of their colouration and bleaching cycles

synchronise to achieve the desired effect *e.g.* combined absorptive and reflective properties or contrasting colours (eqn. 1.20). The more strongly colouring material is termed the primary electrochrome, which is attached to the WE; the secondary electrochrome is attached to the CE and is chosen to complement the primary electrochrome. For instance, an ECD with tungsten trioxide as the primary electrochrome, vanadium oxide as the secondary electrochrome and H^+ as the active counter/co-ion has been reported [30]. Shown simplistically:

$$\underbrace{WO_3 \;+\; H_xV_2O_5}_{\text{pale yellow} \quad \text{pale blue}} \;\underset{\text{ox/red}}{\overset{\text{red/ox}}{\rightleftharpoons}}\; \underbrace{H_xWO_3 \;+\; V_2O_5}_{\text{metallic blue} \quad \text{brown}} \tag{1.20}$$

BLEACHED COLOURED

Here, if the WO_3 layer is placed behind the V_2O_5, WO_3 acts as a reflective layer, enabling a transmission $\rightarrow$ reflection mode of operation and thus reducing glare. Such anti-dazzle action is applicable to devices such as car rearview mirrors, sunglasses, office windows or windscreens [30, 34]. In some cases the secondary electrochrome may be absent if a contrasting colour is not required.

The electrolyte forms the central layer in the 'sandwich'; it may be a solid, liquid or an elastomer and acts both as an ionic conductor and a source of diffusive counter/co-ions, as described in section 1.2.1. A liquid of low viscosity may be unfavourable as leakage of noxious chemicals may be difficult to prevent. A solid electrolyte may not be ideal because the mobility of dissolved ions is reduced, hindering response times, or where stresses arising from swelling/shrinkage due to counter/co-ion movement or thermal expansion/contraction is considerable. On the other hand, a viscous liquid or elastomeric electrolyte damps these stresses and may act as an adhesive, binding the two halves of the ECD.

ECDs are spectroelectrochemical devices operating in the visible region. In this work, the structural changes taking place in their electrochromic

oxide constituents were measured in the X-ray region, in experiments that are representative of one half of a working ECD.

1.2.5 *In situ* X-ray Spectroelectrochemistry

In situ spectroelectrochemistry is of vital importance because the structure and oxidation state of the material of interest may alter upon its removal from the electrolyte for *ex situ* measurements; some experiments may also require conditions such as ultra high vacuum that adversely affect film structure and prohibit electrode operation, so measured results may be unrepresentative of the working system. For this reason, *ex situ* spectroelectrochemistry is undesirable, but may be unavoidable when working in the reflection mode (sections 1.1, part iii and 5.2.3) or when quantitative information about electronic transitions from X-ray photoelectron spectroscopy (XPS) or surface topology from scanning electron, scanning tunnelling and atomic force microscopies (SEM, STM and AFM, respectively) is required, though the *in situ* scanning electrochemical microscope (SECM) overcomes these problems but is limited in its applicability [25]. *In situ* XAS is an extremely powerful tool for spectroelectrochemical investigations; the intense radiation can be directed to impinge on the sample in several ways (section 1.1 i – iv), and when coupled with an appropriate detection system provides the means to observe short range atomic structure even in composite samples, at regions of particular interest to electrochemists. XAS is especially beneficial when studying electrochemically-deposited films that have little order further than the molecular level and therefore fail to provide conclusive X-ray diffraction (XRD) patterns, this is because only the short-range structure ($\sim 1.5 - 5$ Å) is probed. Relatively little use of spectroelectrochemical techniques has been made compared to UV-vis., Raman and infrared spectroscopies because of problems with *in situ* application hence, the novelty of the spectroelectrochemical studies presented in this thesis.

As previously stated in section 1.1, X-rays interact weakly with matter resulting in weak signals; this is particularly true when probing surfaces or interfacial regions of electrochemical interest forming only a small proportion of the sample, though the high intensity offered by synchrotron-generated sources compensates for this by greatly enhancing the signal. The extinction distance ($\geq$ 1 mm) of the beam in aqueous and short-chain organic solutions is not prohibitive when mid-range to hard X-rays ($\geq$ 8 keV) are used, enabling *in situ* electrochemical XAS with all three electrodes immersed in a thin layer of electrolyte to maintain potential control.

XAS and electrochemistry link to yield complementary information which can be used to reinforce the values derived from one particular experiment. For instance, both XAS and electrochemistry can be used to provide the film thickness x which can be seen by combining equations 1.1 and 1.18.

$$x = \underbrace{\frac{\ln(I_o/I_t)}{\mu}}_{\text{spectroscopic}} = \underbrace{\frac{\Delta\mu}{\Delta\sigma C}}_{\text{spectroelectrochemical}} = \underbrace{\frac{N}{AC} = \frac{\Gamma}{C} = \frac{Q}{nFAC}}_{\text{electrochemical}} \tag{1.21}$$

where

$$xA = V = \frac{m}{\rho} = \frac{N}{C} \qquad C = \frac{\rho}{ram} \quad \text{and} \quad \Delta\mu = \Delta\sigma\Gamma \tag{1.22}$$

V, m, ram and C are respectively the volume, mass, relative atomic mass and concentration of the absorber, $\Delta\sigma$ ($\mathrm{cm^2\,mol^{-1}}$) is the difference in absorption cross-section between the bottom and top of the edge, and $\Delta\mu$ is the dimensionless absorption edge step.

Over the past decade, a diverse range of *in situ* spectroelectrochemical investigations concerning electrochemically-modified transition metal oxide films has grown to encompass fields such as optoelectronics and corrosion protection to electrocatalysis and battery technology, using structural techniques such as XAS, XRD, UV-vis. and IR absorption and reflection spectroscopies [2, 3, 4, 38] and neutron reflectivity [39]. Nickel, niobium and tungsten oxides, the materials investigated in this work exemplify such actively studied systems.

1.3 The Crystal Impedance Technique

The piezoelectric properties of quartz have made it a central component of many devices, with applications ranging from time-keeping to deposition rate measurement. In this section its use is as a microbalance, where small changes in the frequency of its electromechanical oscillations can be used to calculate minute changes in the mass of an attached film. Also, by use of equivalent circuits, the electrical components of its electromechanical oscillations will be modelled to determine rheological changes in an attached film.

1.3.1 The Quartz Crystal Microbalance

The quartz crystal microbalance (QCM) is an *in situ* piezoelectric device. It consists of a thin quartz AT-cut disc, set into motion using two gold electrodes, one on each face of the wafer (fig. 1.19). These electrodes are connected to a frequency generator which produces constant oscillating shear waves (fig. 1.20) by application of an alternating electric field across the quartz.

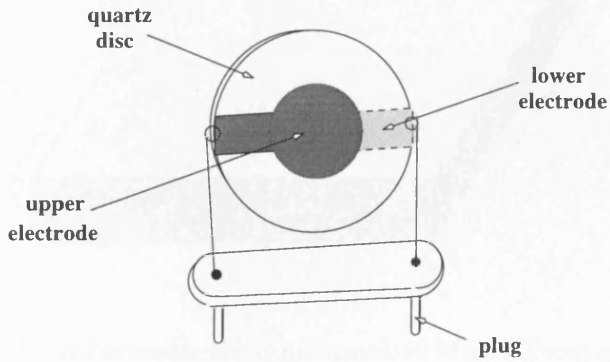

Figure 1.19: Quartz crystal

The QCM was originally used to monitor adsorption and desorption from the gas phase. Its use may be extended to the liquid phase provided that only one of the electrodes comes into contact with the solution. The face exposed to the liquid can then be used as the working electrode in an electrochemical

cell; this variation is termed the electrochemical quartz crystal microbalance or EQCM [31, 33, 39, 40].

Usage of the QCM is well established [41, 42] and is based on the principle that the shift in resonant frequency Δf of an oscillating quartz disc can be quantitatively correlated to a change in the areal density Δm (in $\mathrm{g\,cm^{-2}}$) on the surface of the crystal, caused by an attached film. This relationship is represented by the Sauerbrey equation:

$$\Delta f = f_{\Delta m} - f_0 = \left(\frac{-2f_0^2}{\rho_Q\ \nu_Q}\right)\Delta m \tag{1.23}$$

f_0 is the initial resonant frequency of the bare QCM and $f_{\Delta m}$ is the resonant frequency once matter has been deposited on its surface. ρ_Q and ν_Q are constants for quartz *i.e.* its density (2.65 $\mathrm{g\,cm^{-3}}$) and shear wave velocity (3.34×10^5 cm Hz), respectively. The negative sign indicates that an increase in mass corresponds to a decrease in frequency, and *vice versa.* The resulting frequency changes arise from the interaction of the generated shear wave with whatever is on the surface of the crystal.

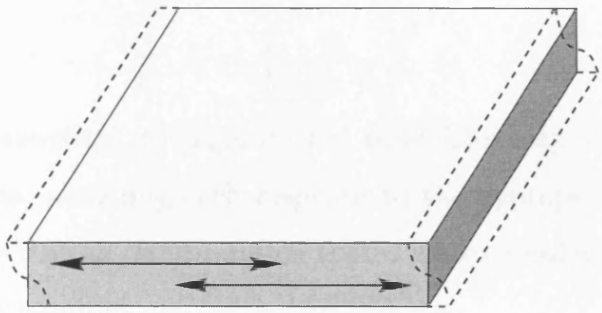

Figure 1.20: First harmonic shear deformation of an AT-cut quartz crystal.

The change in resonant frequency that occurs upon coupling one face of the resonator to a liquid, gel or solid can be related to liquid viscosity, the combination of mass with viscosity (viscoelasticity), or the mass of a solid deposit. In the Sauerbrey case, frequency changes can be described in terms of a simple physical model which treats the quartz disc as a rigid, lossless solid. If the wave penetrates the full thickness of an attached film,

without loss or lasting deformation, so that the film moves synchronously with the crystal, the film is called an ideal mass layer which is treated as a rigidly coupled extension of the quartz. This condition satisfies the Sauerbrey equation as the relationship between Δf and Δm is linear. The gold electrodes ($\ll 1$ μm) are disregarded as overlayers because the thickness of the gold electrode is assumed to be negligible compared to that of the crystal ($\sim$ 1 mm). Ideal mass conditions apply to rigid, thin overlayers (≤ 0.5 % extension of the crystal), but considerable deformation and damping of the shear wave occurs in thicker and less rigid films and fluids, so the Sauerbrey equation ceases to be a valid expression for calculating changes in mass, as the relationship between Δf and Δm becomes nonlinear. In these cases a damped shear wave propagates perpendicular to the surface of the crystal. The extent to which these shear oscillations penetrate into the material, before they are completely damped (the decay length δ) depends on the density ρ_L and viscosity η_L of the layer, a combination of which affects the rigidity of the film and the degree of coupling between the two phases:

$$\delta = \left(\frac{\eta_L}{\pi \ \rho_L \ f_0} \right)^{\frac{1}{2}} \tag{1.24}$$

It is therefore necessary to separate the total frequency response into its constituent parts, assigning each response to the appropriate contributing effect. Consequently, an interpretation that is more complex than the Sauerbrey equation is required.

1.3.2 Viscoelastic Models

Many of the problems associated with interpreting viscoelastic changes can be addressed not merely by measuring Δf, but also by measuring the acoustic admittance Y (the reciprocal of impedance Z) of the crystal as a function of the QCM frequency response. These measurements form the basis of the crystal impedance technique. Qualitatively, the shape and position of the admittance *vs.* frequency curves indicate the rigidity of an attached film

(section 1.3.3). The admittance curves can be quantitatively analysed by deriving impedance curves from them, then fitting the impedance curves to an equivalent circuit using various fitting procedures. The equivalent circuit model provides quantitative descriptions of film viscoelastic behaviour in terms of inductive elements which characterise mass changes (instead of the Sauerbrey-derived areal density, which applies to rigid films only), resistive elements which represent energy loss and complex shear moduli which quantify the elastic components of shear deformation.

Firstly, a description of the ideal elastic solid and pure viscous liquid phases will be given in terms of their physical properties and electrical representations of these characteristics. Once descriptions of the two ideal phases are established, a model of viscoelastic materials will be constructed.

It is important to state that the shear stress τ (with units of pressure) imposed on a material is the sum of elastic and viscous components [43]:

$$\tau = \underbrace{G\gamma}_{\text{elastic component}} + \underbrace{\eta \frac{d\gamma}{dt}}_{\text{viscous component}} \quad \text{where} \quad \gamma = \frac{dx}{dy} \tag{1.25}$$

Here, G is the shear modulus and η is the shear viscosity of the material. Shear deformation γ is the rate of shear displacement in the x direction per unit displacement along y; the actual thickness doesn't change, but the displacement (dx) of the standing shear wave travelling across the material (figs. 1.21–1.23) varies across its thickness (dy).

An electrical expression for the physical or mechanical factors affecting the voltage and current in a circuit such as the QCM is its complex impedance. Electrical impedance Z_E (in ohms) is the complex ratio of voltage to current in a circuit and it quantifies the extent to which the sinusoidal voltage $V(t)$ and current $i(t)$ overlap:

$$Z_E = \frac{V(t)}{i(t)} \tag{1.26}$$

and

$$Z_E = R + j\omega L + \frac{1}{j\omega C} \tag{1.27}$$

The real term R, resistance accounts for changes to the amplitude of sinusoidal voltage with respect to current (or *vice versa*) due to energy loss *i.e.* damping. In an ideal elastic solid, the shear wave propagates throughout the material without diminishment, so $R = 0$. The two imaginary parts $j\omega L$ and $\frac{1}{j\omega C}$ (both in ohms) are inductive and capacitive reactances, respectively, accounting for changes to the phase of sinusoidal voltage with respect to current (or *vice versa*) with non-dissipative origins, and may be positive or negative according to whether the voltage leads the current (due to inductance) or lags (due to capacitance), respectively. The angular frequency of the input voltage $\omega = 2\pi f$ where f is its frequency, and to avoid confusion with current $j = \sqrt{-1}$.

Owing to the electromechanical coupling within the quartz (*i.e.* the piezoelectric effect), the mechanical properties of an attached film affect the electrical properties of the resonator. For resonating devices such as the QCM, electrical impedance Z_E, is composed of the summed complex electrical load impedance arising from all contributing sources *i.e.* the bare resonating quartz Z_{E0} and the attached layer Z_{EL}:

$$Z_E = Z_{E0} + Z_{EL} \tag{1.28}$$

where

$$Z_{E0} = R_0 + j\omega L_0 + \frac{1}{j\omega C_0} \tag{1.29}$$

and

$$Z_{EL} = \underbrace{R_L + j\omega L_L + \frac{1}{j\omega C_L}}_{\text{electrical}} \equiv \underbrace{\frac{N\pi}{4\, K_0^2\, \omega_{\Delta m}\, C_0'} \left(\frac{Z_x}{Z_0}\right)}_{\text{mechanical}} \tag{1.30}$$

N is the harmonic number of the shear wave; the electromechanical coupling factor for quartz is K_0^2 (7.74×10^{-3}), the resonant frequency of the circuit $\omega_{\Delta m} = 2\,\pi f_{\Delta m}$ and static (instrumental) capacitance C_0' of the resonator (as opposed to the parameter C_0 in equation 1.29) [44, 45]. Note that the subscript $_0$ pertains to the bare crystal, $_L$ to an attached layer, and $_x$ describes

the layer, with x being 1, 2 or 3 if the film is solid, liquid or viscoelastic in nature, respectively. Electrical and mechanical impedance are analogous but dimensionally different. Equation 1.30 shows that electrical and mechanical representations of a resonating film can be given. These expressions enable physical parameters to be extracted from straightforward electrical measurements.

$$Y(\omega) = j\,\omega\,C_0' \;+\; \frac{1}{Z_E} \tag{1.31}$$

Apart from Z_1 (and hence Z_E), all of the terms stated in equations 1.28 to 1.32 are known or controlled and recorded when resonating both bare and loaded crystals. Conversely, the unknown terms within Z_E (contributing to the overall measured electrical admittance) must be extracted from the admittance *vs.* frequency curves using equivalent circuits according to the physical model most representative of the system. The overall measured admittance $Y(\omega)$ (in Siemens, S) is given in equation 1.31, where C_0' is the static capacitance of the resonator (fig. 1.25).

i) Ideal Elastic Solid

This model describes a thin rigidly-coupled solid or finite ideal mass layer, initially mentioned in section 1.3.1. The shear deformation imposed by the oscillating QCM is instantaneous and therefore independent of time, so $\frac{d\gamma}{dt} = 0$ and the viscous component of equation 1.25 can be neglected. This means that the elastic solid immediately returns to its original form once the oscillatory action of the QCM has ceased, so the overlayer can be treated as a Sauerbrey-compliant extension of the QCM, and the penetration depth of the shear wave (eqn. 1.24) is equal to the thickness of the solid layer.

Equation 1.30 contains terms for the mechanical impedance (in $\mathrm{kg\,m^{-2}\,s^{-1}}$) of the quartz Z_0 and the unattached ideal mass layer Z_1 with areal density m_1, density ρ_1 and thickness x_1 where

$$Z_0 \;=\; (\rho_0\,G_0)^{\frac{1}{2}} \;\equiv \rho_Q\,\nu_Q \tag{1.32}$$

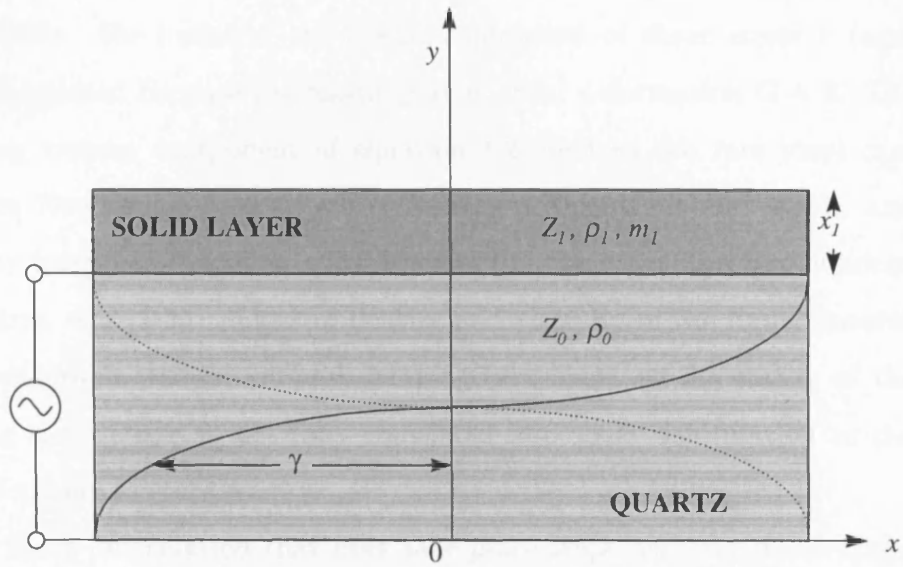

Figure 1.21: Progress of a first harmonic shear wave through a finite ideal mass layer.

and

$$Z_1 = j\omega m_1 \qquad \text{with} \quad m_1 = \rho_1 x_1 \tag{1.33}$$

Z_0 is the square rooted product of the density ρ_0 and shear modulus ($G_0 =$ 2.95 x 10^{11} dyne cm^{-2}) of quartz, or alternatively represented in terms of the quartz constants contained in the Sauerbrey equation (eqn. 1.23). As Z_1 refers to an ideal solid, non-dissipative effects dominate, so the dissipative element $R_1 = 0$ making the electrical load impedance (eqn. 1.28) of the quartz disc loaded with an ideal mass layer:

$$Z_E = R_0 + j\omega(L_0 + L_1) + \frac{1}{j\omega C_0} \tag{1.34}$$

In equation 1.33, Z_1 was generated by an ideal mass layer; a liquid or viscoelastic layer could also generate Z_x, or a composite model of the layer may consist of a combination of these elements. The remaining possibilities will be described in the following sections.

ii) Simple Liquid

Simple liquids may be considered, in part, to be the opposite of ideal elastic solids. For instance, the elastic component of shear stress τ (eqn. 1.25) is neglected because the elastic part of shear deformation $G = 0$. The remaining viscous component of equation 1.25 defines the rare ideal case of a pure Newtonian fluid where η_2 and ρ_2 are constant and small, and the decay length of the shear wave is short (on the order of a few hundred nanometres, eqn. 1.24). The low density and viscosity of the liquid ensures that considerable dissipation and damping take place, so the energy of the imposing shear stress is not fully translated into shear deformation as the liquid is unable to store energy.

The shear deformation that does take place stops once the shear stress imposed by the oscillating QCM ceases (like ideal mass behaviour), but in this case shear deformation is time dependent, and the rate of shear deformation $\frac{d\gamma}{dt}$ (the flow rate) increases linearly with shear stress. The viscosity coefficient of a fluid expresses its resistance to permanent deformation (flow); as η_2 is low the resistance to flow is low and the energy of the shear waves dissipates readily, hence shear deformation is permanent and energy loss at the decay length of the shear wave is complete.

The surface roughness of the quartz disc exaggerates measured frequency responses because material that is confined within surface cavities (valleys) moves synchronously with the crystal as it oscillates, even if the material is a Newtonian fluid. This means that material caught within surface features must be treated as an ideal mass layer with thickness equal to the depth of the corrugations, regardless of the nature of the bulk film. It was once thought that the use of polished crystals would ensure the effects of surface roughness became negligible, though this was not found to be true in many cases, despite the use of visually smooth crystals [46] *e.g.* thin films, as the relative importance of roughness decreases with increasing film thickness. Hence, a composite film with at least two layers, the first being an ideal

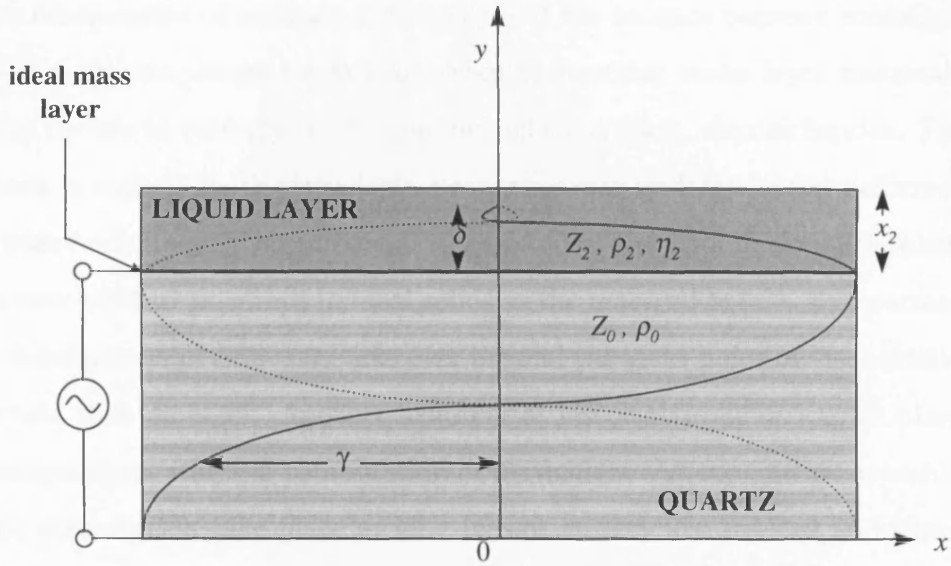

Figure 1.22: Progress of a first harmonic shear wave through an ideal mass layer plus a semi-infinite liquid.

mass layer, requires modelling; such composite films will be given further consideration in section 1.3.3 and beyond. Even though the effects of energy dissipation are great, some mass effects are contributed by the pseudo ideal mass layer, making $\omega L_2 \neq 0$, and in terms of the complex electrical load impedance (eqn. 1.28) of the QCM with a surface layer of liquid

$$Z_E = (R_0 + R_2) + j\omega(L_0 + L_2) + \frac{1}{j\omega C_0} \tag{1.35}$$

with the mechanical impedance of a simple liquid being

$$Z_2 = \left(\frac{\omega\ \rho_2\ \eta_2}{2}\right)^{\frac{1}{2}} (1 + j) \tag{1.36}$$

iii) Viscoelastic Layer

As one would expect, a viscoelastic layer has physical properties that lie somewhere between the two extremes of the previously described ideal

phases, so a viscoelastic material is simply one that has non-ideal properties, so exhibits characteristics of both energy storage and loss. Both viscous and elastic components of equation 1.25 apply, but the balance between contributions of each component toward the overall behaviour varies from materials such as metals to rubbery solids, 'sloppy' gels and thick, viscous liquids. For instance, a material with viscoelastic properties may undergo elastic deformation where γ is linearly proportional to τ up to the yield point; no mechanism takes over beyond this limit in ideal solids so the material breaks, but permanent deformation or flow may take over beyond the yield point of viscoelastic materials such as steel. Another example of viscoelastic behaviour is plastic deformation, where a combination of permanent viscous and recoverable elastic deformation take place at all τ except at very low stresses and short durations (where elastic deformation is dominant), making $\frac{d\gamma}{dt}$ nonlinear *e.g.* gels and rubber. In most cases of electrochemical use, exposure of an initially rigid film to solvents will plasticise the film, thereby increasing its loss characteristics. Viscoelastic behaviour can also be displayed by thick, normally rigid films ($> 0.5\,\%\ x_o$) [47] that sway with each shear oscillation (*i.e.* non-synchronous movement).

The intermolecular forces responsible for ideal mass behaviour are strong primary valence chemical interactions; weaker secondary electrostatic-type (polarisation) forces account for the properties of Newtonian fluids; so a mixture of primary and secondary intermolecular forces are present in viscoelastic or Maxwellian materials. Consequently, both dissipative and non-dissipative elements contribute toward the complex electrical load impedance Z_E (eqn. 1.28)

$$Z_E = (R_0 + R_3) + j\omega(L_0 + L_3) + \frac{1}{j\omega C_0} \tag{1.37}$$

The shear surface mechanical impedance of the layer is

$$Z_3 = Z_c \tanh(\lambda_3\, x_3) \tag{1.38}$$

with

$$Z_c = (\rho_3\, G_3)^{\frac{1}{2}} \tag{1.39}$$

where $Z_3 = Z_c$ when $x_3 \to \infty$ and the film is regarded a semi-infinite viscoelastic layer.

$$\lambda_3 = j\,\omega \left(\frac{\rho_3}{G_3}\right)^{\frac{1}{2}} \tag{1.40}$$

and

$$G_3 = G_3' + j\,G_3'' \tag{1.41}$$

Here, λ_3 is the propagation constant of the shear acoustic wave through the viscoelastic film of thickness x_3 and density ρ_3. Z_c, the characteristic mechanical impedance of the film, is analogous to Z_0 for quartz (eqn. 1.32), but in this case the shear modulus of the viscoelastic film G_3 (in dyne cm^{-2}) is complex, comprising storage (G') and loss (G'') moduli, respectively.

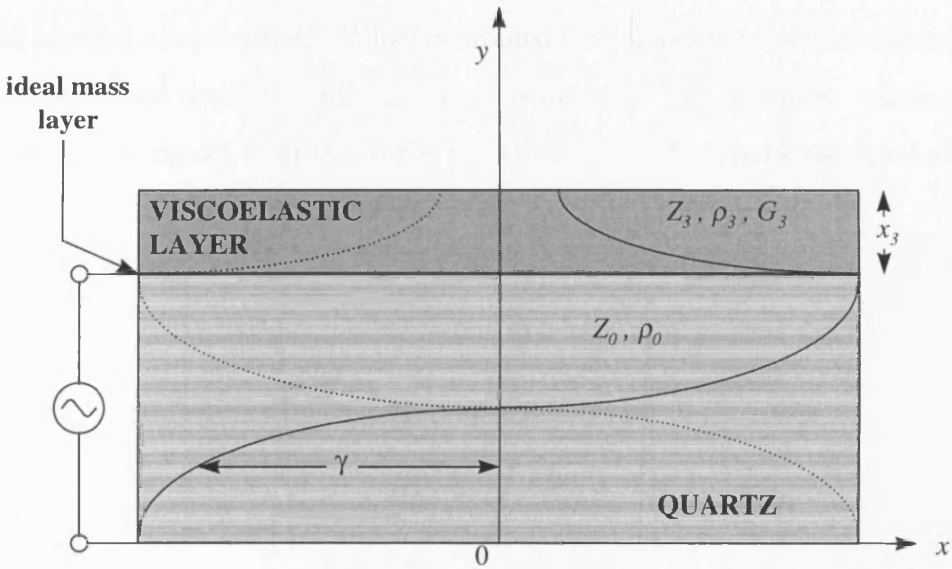

Figure 1.23: Progress of a first harmonic shear wave through an ideal mass layer plus a finite viscoelastic layer.

The movement of viscoelastic layers is not synchronous with that of the quartz resonator and the kinetic energy of the shear waves is both stored and dissipated. The storage modulus G' accounts for synchronous motion that is in phase with the acoustic shear waves of the resonator; conversely, the loss

modulus G'' accounts for out of phase, non-synchronous motion where upper regions of the film tend to lag behind the region at the QCM/film interface, resulting in a phase shift. This description of dissipative *vs.* non-dissipative contributions is analogous to the definition of electrical impedance given in equation 1.27. In summary, G_x is constant and not complex in ideal rigid, lossless solids like quartz as $G'' = 0$; in simple liquids $G' = 0$ and η is constant; in viscoelastic materials G_x is complex and G_x or η_x are variable as the ratio of G' to G'' may change, or η_x may decrease with increasing shear stress.

1.3.3 Frequency Changes

It has been shown that the magnitude of the measured admittance $|Y|$ varies according to the extent to which the acoustic shear waves launched into attached layer(s) are preserved. When combined with frequency measurements, a qualitative description of film rheology is derived. For instance, whether or not a film is rigidly coupled to the QCM can immediately be established.

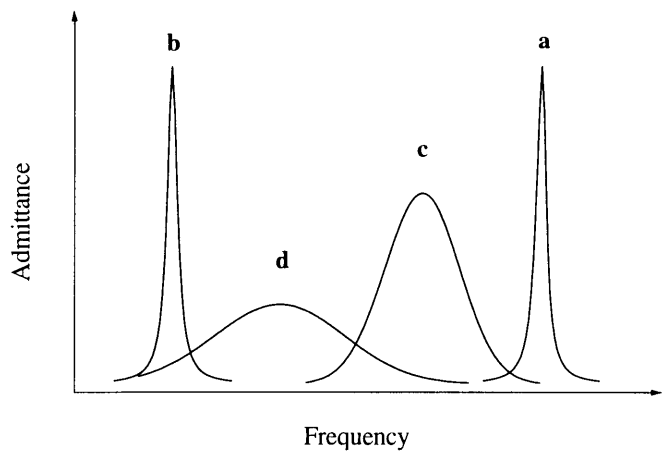

Figure 1.24: Schematic admittance *vs.* frequency curves for: a) an unloaded crystal, and a crystal with an attached b) ideal mass layer, c) Newtonian fluid, d) viscoelastic layer.

In the purely gravimetric (mass-based) case of an ideal mass layer (fig.

1.24 b), the frequency of the acoustic shear oscillations decreases in response to the mass of the film (eqn. 1.23), but the admittance remains constant as the oscillations are undiminished, so the position (but not the amplitude) of the discrete, sharp admittance *vs.* frequency curve changes and frequency responses can be interpreted in terms of the Sauerbrey equation (eqn. 1.23).

In the case of a liquid layer (fig. 1.24 c) a negative frequency shift and a decrease of admittance, with considerable broadening of the peak, are evident. The low ρ and η liquid entrapped in roughness features (of depth on the order of $\delta/2$) is responsible for the small ideal mass-like gravimetric response. Extensive dissipation of the shear wave in the bulk Newtonian fluid (as R_2 is high) take place because the resonator does not 'see' any liquid beyond the short decay length, causing both an amplitude decrease and a spread of the admittance curve. Virtually none of the liquid has any influence on the shear waves and the resonator effectively 'sees' a pseudo-ideal mass layer.

In addition to the ideal mass layer, the amount of film 'seen' (*i.e.* the amount of coupling between quartz and overlayer) increases with η and ρ *i.e.* when the attached film is a Maxwell fluid (viscoelastic liquid) or viscoelastic layer (curve d in figure 1.24). The frequency decreases toward a more realistic value (*i.e.* a truer reflection of film mass), but in this case (as opposed to a Newtonian fluid) the shear acoustic waves penetrate even further into the layer, so dissipation is more extensive, resulting in lower $|Y|$ and an even broader peak.

Dynamic crystal impedance experiments involve the measurement of $|Y|$ *vs.* f curves in quick succession, allowing film rheology to be mapped as a function of time. Such measurements are essential when studying evolving systems such as polymerisation [48], deposition rates [41] or phase changes during the sol-gel process ([49] and chapter 4). The importance of homogeneity was initially explained in the context of X-ray absorption spectroscopy (section 1.1); it is also true for the crystal impedance technique, so the influence of the film on frequency responses across the whole piezoelectrically-

active area (the region covered by a gold electrode) must be equal, requiring that films, as well as the quartz, have minimal roughness and uniform thickness.

As the frequency responses of Newtonian fluids and viscoelastic materials have contributions from two sources, the total measured frequency must be separated into its constituent parts

$$\Delta f \;=\; \Delta f_1 \;+\; \Delta f_x \tag{1.42}$$

where the subscript $_1$ refers to an ideal mass layer, $x = 2$ for a Newtonian fluid and $x = 3$ for a viscoelastic layer, with the contributions of additional layers added on. Consequently, a direct evaluation of liquid or viscoelastic film mass cannot be achieved. Nevertheless, fitted values for the inductive elements L_0 and L_x, representing energy storage and hence mass changes, can be used to predict the overall Δf. In general, for all types of layer [47]

$$\Delta f \;\cong\; -\frac{L_x\; f_{\Delta m}}{2L_0} \tag{1.43}$$

For all apart from simple liquids

$$\Delta f \;=\; -\frac{L_x\; f_{\Delta m}}{2(L_0 + L_x)} \tag{1.44}$$

and for liquids

$$\Delta f \;=\; -\frac{f_{\Delta m}^{3/2}}{N\,\rho_Q\;\nu_Q}\left(\frac{\rho_2\;\eta_2}{\pi}\right)^{\frac{1}{2}} \tag{1.45}$$

The calculated value of Δf derived from these expressions (or the Sauerbrey equation, where appropriate) can be compared with measured values as a further check on the suitability of physical model(s) chosen to represent the system. These models will be discussed in the next section.

1.3.4 Equivalent Circuits

Electrical expressions for various combinations of "quartz + loading layer" have been given when stating the complex electrical load impedance of the loaded QCM Z_E (equations 1.34, 1.35 and 1.37). It was shown in section 1.3.2(i) that all terms, apart from those within Z_x and hence Z_{EL} and Z_E (eqns. 1.28, 1.30, 1.33, 1.36 and 1.38) could be accounted for and therefore subtracted from the measured signal, leaving the terms within Z_x to be modelled in order to reconstruct the outstanding contributions to the measured admittance (eqn. 1.31).

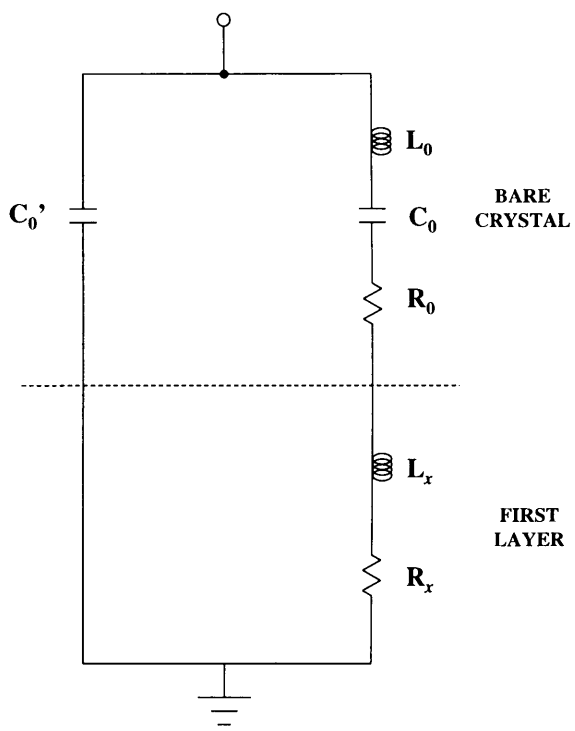

Figure 1.25: Butterworth van Dyke equivalent circuit model for a QCM with a single overlayer of type x.

The unknown elements of the remaining signal are placed in series with the known elements for quartz and fitted using various computational proce-

dures [45] (see chapter 4) to what is termed a Butterworth van Dyke (BVD) lumped element model (LEM), shown in figure 1.25. Figure 1.25 shows the equivalent circuit for the crystal with one attached layer; in the instance where a composite overlayer exists, the extra elements are added in series to the model shown. Combining equations 1.29 and 1.30 into 1.28 provides the total electrical impedance of the layered system

$$Z_E = (R_0 + R_x) + j\omega(L_0 + L_x) + \frac{1}{j\omega C_0} \tag{1.46}$$

where inductive and resistive elements can be added (in series) as required to model the system.

It could be said that the resistive and inductive elements within Z_{EL} give a qualitative yet empirical idea of the nature of attached layer(s), whereas the modelled terms constituting Z_x *e.g.* G', G'', m_x, ρ_x, η_x and x_x have direct physical significance. The evaluation of these physically-significant terms is therefore the prime motivation of crystal impedance experiments.

Chapter 2

General Experimental and Data Analysis

The techniques, equipment and procedures detailed in this chapter apply to all three of the systems studied in this thesis. The descriptions given here will therefore be general; additional information about preparative techniques and variations to standard experimental procedures or analyses will be stated in detail in the relevant sections of the next three chapters. For instance, as sample preparations differ for each system *e.g.* direct electrodeposition of nickel hydroxide, sol-gel synthesis of niobium oxide and anodisation of tungsten, such details will be described in their respective chapters. Non-standard methods for recording EXAFS such as quick EXAFS (quEXAFS), energy dispersive EXAFS (EDE) or reflection mode EXAFS (reflEXAFS) will also be detailed in the appropriate experimental section(s). Such variations in measurement will also affect the design of spectroelectrochemical cells, making each cell specific to its application. Other techniques, specific to each system, such as crystal impedance (chapter 4) and non-standard electrochemical manipulations *e.g.* anodisation (chapter 5) also will not be stated here.

2.1 Experimental

2.1.1 Reference Samples

Correct and thorough interpretation of the structures and oxidation states of initially unknown samples required the use of XAS spectra from a number of well-defined, ordered crystalline or elemental reference materials (standards), each having known absorbers and backscatterers and published structures [50]. Assuming that a qualitative idea of the predominant elements present in a sample was known (*e.g.* an amorphous tungsten oxide), reference materials with similar constituents were chosen (*e.g.* W, WO_2 and WO_3), and their structures were derived and compared with crystallographic literature [50] before the unknown samples were analysed, to ensure that the data analysis procedure was correct and consistent.

2.1.2 Preparation of Reference Compounds

Reference materials were usually bought as high purity reagent grade powders or metal foils. If standards could not be obtained commercially or borrowed (from a reliable source), they were synthesised and purified using established procedures. 5 or 15 μm thick pure metal foils, provided by Daresbury Laboratory, were always used as standards and as the calibrant when a third ion chamber was used. When using crystalline standards, each compound was mixed to about 3:1 standard:powdered high purity boron nitride (Fluka). Boron nitride has low absorption in mid to hard X-ray regions and limits excessive absorption by the reference sample, which distorts the spectra. The mixture was ground finely using an agate mortar and pestle, and the resulting homogeneous powder was sprinkled evenly onto the sticky side of a strip of adhesive tape. The powder was then firmly sealed in with a clean strip of tape. For XAS measurements, the sample absorption was optimised by folding and therefore overlapping the strip, thus altering the thickness of the

sample in order to obtain a good edge step ($\Delta\mu$ or Δabs $\simeq$ 1.0, eqns. 1.1 and 1.21).

2.1.3 *In situ* Spectroelectrochemical Cells

In situ cells that are capable of meeting the demands of both XAS and electrochemical methods have been used for many years [4, 12, 51]. Many have been successfully employed in the study of transition metal oxide films. Several innovative thin layer configurations have been used to restrict electrolyte absorption in the transmission or fluorescence mode [6]. More versatile designs allow spectral acquisition in both modes, removing ambiguities associated with sample variability and repositioning [13]. Additionally, sub-surface regions may be probed, or films with low absorber concentrations (*e.g.* porous films or foreign ions such as dopants, incorporated during deposition) may be examined from the fluorescence signal [15].

A spectroelectrochemical cell that meets spectroscopic, electrochemical and practical demands must meet several, often conflicting criteria. From a spectroscopic point of view, it is important to observe that all components must minimise their contributions to the background level of absorption. This is achieved by preventing unnecessary scattering and absorption (*i.e.* attenuation) of the beam by the electrolyte, substrate and cell components. A three electrode arrangement that will not accentuate these effects, but does exhibit a geometry suitable for accurate, dynamic potential control provides for both spectroscopic and electrochemical needs. For practical reasons, the cell should consist of cheap, robust, inert and readily available materials that can easily be machined. In the context of valuable synchrotron beam time it is helpful if assembly, dismantling and cleaning of cell constituents is not complicated and impractical; the assembled cell should also be capable of being precisely positioned and aligned in the beam path. It is desirable for the cell to have a simple design that permits a variety of uses; it should therefore

be possible to adapt and modify the cell for highly specific or demanding applications. The three cells presented in this thesis were designed to meet all of the stated requirements, with minimal loss of performance, though in practice this proved to be a difficult task.

2.1.4 EXAFS Measurements

i) Standard Transmission EXAFS

Absorption spectra of reference samples were usually taken on beamline 7.1 or 9.2 of the CLRC Daresbury Laboratory, operating at an electron energy of $\sim$ 2 GeV and a synchrotron ring current of $\sim$ 125 mA. The three ion chambers were filled with absorbing Ar or an Ar-Kr mixture, backfilled with He to a total pressure of 1 bar. The partial pressures of the gases varied with the absorption edge to be measured and were tabulated for each ion chamber so that 20 % of the incoming radiation was absorbed by the first ion chamber (recording I_0) and 70 % of the initial beam by the second (measuring I_t), leaving the remaining 10 % of the initial beam to be absorbed by the third detector (recording I_c, fig. 1.3).

The EXAFS instrumentation utilised a harmonic-rejecting double crystal Si(111) or Si(220) monochromator. The intensity I_0 was maximum when both monochromator crystals were parallel, being tuned to allow all orders of Bragg reflection to be detected. In most cases, one of the crystals was detuned away from a parallel position, cutting I_0 to half its original value (50 % detune) and therefore rejecting higher harmonic contributions which may distort the spectrum. The beam height and width were fixed by adjusting the entrance slits to 0.5 and 10 mm, respectively. The energy separation of each measurement was set so that the number of data points measured in the pre-edge region was less than in the XANES and EXAFS regions. The detuned monochromator angles were then scanned in a stepwise fashion so that an XAS spectrum of both the sample and the calibrant (the 'monitor')

were recorded simultaneously with a duration of about 15–20 minutes.

ii) Fluorescence Mode EXAFS

Fluorescence spectra were recorded on all electrochemical samples, using spectroelectrochemical cells that were built to facilitate simultaneous operation in transmission or reflection and fluorescence modes. Fluorescence measurements were invaluable because excessively thick films were often required to achieve a good signal (edge step) in the transmission mode, due to the inherent low density of electrochemically-generated metal oxide films. The improved sensitivity of the fluorescence mode allowed spectra of thinner (*i.e.* more electrochemically ideal) or more dilute samples to be measured, though at the expense of a greater noise level due to scattering of the divergent beam. A trade-off between minimising scatter and maximising the signal, without saturating the sensitive detector, was optimised by adjusting the separation between sample and detector. Edge steps in the fluorescence mode were typically $\Delta\text{abs} \ll 0.5$.

Fluorescence detection was compatible with most modes of operation (except EDE, see figs. 1.3 and 1.4) and on all of the beamlines used. The detectors were either scintillation counters or solid state detectors; further details about dual transmission/reflection-fluorescence cells and the detectors used are stated in subsequent experimental sections.

2.1.5 General *in situ* Spectroelectrochemistry

General electrochemical manipulations of samples such as cyclic voltammetry, overcharge and discharge were usually performed *in situ i.e.* in parallel with spectral acquisition, without altering the position of the cell on the optical bench. If the duration of an electrochemical experiment was much longer than the timescale for spectroscopic measurements *e.g.* overcharge or cyclic voltammetry at slow scan rates (≤ 5 mVs^{-1}) combined with any XAS mode, then a series of spectra was sufficient to record any electrochemically-induced

structural evolutions and valency changes without interrupting the electrochemical technique. In the opposite case, *e.g.* cyclic voltammetry at high scan rates (10, 20, 50 100 and 200 mVs^{-1}), when the spectroscopic timescale was similar to or longer than the electrochemical experiment, the potential was held constant at various points of interest (*e.g.* current peaks) while each spectrum or set of spectra was recorded. When the electrochemical response was rapid and could not be interrupted *e.g.* during film discharge, only a fast series of spectra with minimal dead-time would suffice.

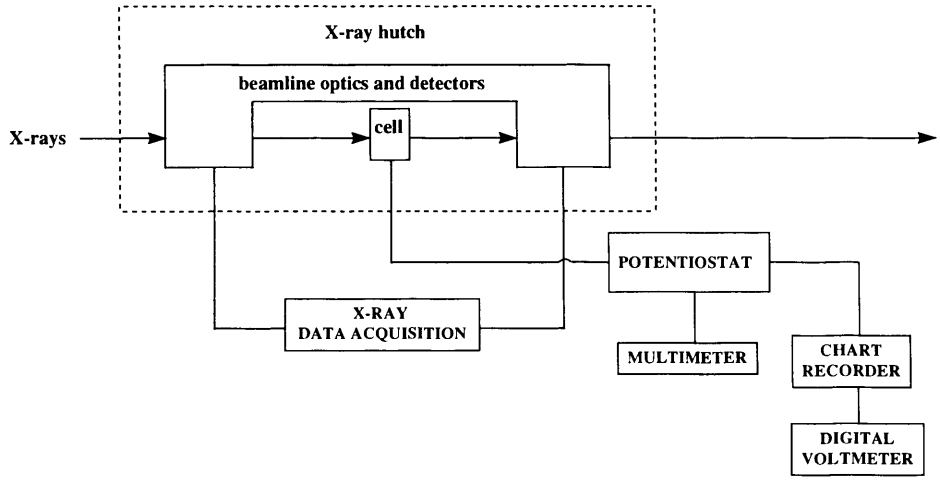

Figure 2.1: Schematic diagram of experimental set-up for *in situ* X-ray absorption spectroelectrochemistry.

The X-ray hutches on all stations were equipped with a junction box, enabling the remote control of all three electrodes via BNC connections to the Oxford Electrodes potentiostat and a Keithley 175A autoranging multimeter (fig. 2.1). This set-up also allowed the resulting current to be measured by an Advance Bryans series 60000 $x-y-t$ chart recorder and a Wavetek 10XL digital voltmeter (DVM, operating as an ammeter), so cyclic voltammograms and current-time profiles were recorded to determine the charge passed.

All experiments were conducted at room temperature (20 ± 2°C). All reference and electrochemical samples were prepared in a fume cupboard in one of the Materials Science Laboratories at Daresbury Laboratory, except the anodised samples that were formed on the station. Milli-Q triply distilled deionised water was used for rinsing and as a solvent when preparing aqueous electrolytes. Each electrolyte solution was degassed for at least 20 minutes using dry, cylinder N_2 (BOC gases) before use. Also, once assembled, the spectroelectrochemical cells were purged with dry N_2 prior to use. All other preparations such as the design, fabrication and preliminary testing of spectroelectrochemical cells, deposition of metal WEs by thermal evaporation and sputtering, cleaning of substrates and the fabrication of reference and counter electrodes took place at Leicester University, using facilities provided by both the Electrochemistry Group at the Department of Chemistry and the Condensed Matter Physics (CMP) Group at the Department of Physics and Astronomy.

2.2 Data Analysis

Once XAS spectra were recorded using any of the described configurations, several computational procedures were undertaken in order to extract quantitative information regarding valency and structure contained within the XANES and EXAFS of each spectrum, respectively. The corresponding electrochemically-derived data were also analysed and the results were used as a quantitative check on the XAS-derived film thickness and valency (eqn. 1.21). Each stage in the data analysis procedure will be described in a similar manner to the Experimental section. For, instance, the procedures detailed here will be of a general nature, applying to all of the systems presented in this thesis. As for the Experimental section, any variations from standard practice (arising from measurements in different configurations) will be explained in the following chapters. Also, analyses relating to system-specific

techniques such as crystal impedance will be dealt with later.

2.2.1 Calibration of Raw XAS Spectra

The first step in data analysis involved calibrating each raw data file so that an XAS spectrum was produced (see fig. 1.1). The data file of each spectrum initially consisted of mono/polychromator positions (in millidegrees), times and detector readings I_0, I_t, I_c and I_f. The x-axis of the XAS spectrum was derived by converting mono/polychromator angles into energy (in eV) using Bragg's equation (eqn. 1.11), which depends upon the type of crystal used *e.g.* Si(111) or Si(220) *etc.* Absorbance or fluorescence, the y-axis, was derived using I_0 and I_t or I_f via equation 1.1 or 1.6, respectively. The raw spectrum was then viewed.

If the edge step of a single spectrum was weak (*i.e.* the absorbance difference between the top and the base of the edge Δabs $\ll 0.5$), the noise obscured the signal. Such a situation was apparent when recording the data from a particularly thin or dilute film (in any configuration) so a series of spectra was recorded from the *static* sample. The set of consecutive spectra was then summed to improve the signal-to-noise ratio, making sure that all spectra in the set were perfectly aligned before summation, thereby eliminating broadening errors arising from summing misaligned spectra.

The calibration procedure was repeated for each corresponding monitor spectrum, using I_c instead of I_t when deriving absorbance. Each single monitor spectrum was then saved for use in the second stage of data analysis. The Daresbury program EXCALIB [52] was used to calibrate all transmission, fluorescence and reflection mode data, and the Daresbury program Proc12 was used to calibrate files recorded in the energy dispersive mode.

2.2.2 Background Subtraction and Normalisation

The ultimate goal of background subtraction was to isolate the EXAFS function $\chi(k)$ (eqn. 1.15) from the rest of the XAS spectrum in preparation for the final step, fitting. Beginning with the absorbance *vs.* energy plot written out from the EXCALIB program, the edge energy E_{edge} was chosen as the greatest peak in the first derivative of the spectrum *i.e.* the inflection point of the edge. This point defined the beginning of the EXAFS. The x-axis was then rescaled with $E_{edge} = 0$ eV. Equation 2.1, a rearrangement of eqn. 1.15, shows that the background absorption μ_0 (initially mentioned in part 1.1.2) must be subtracted from the total linear absorption coefficient in order to determine the EXAFS function

$$\chi(k) = \frac{\mu - \mu_0}{\mu_0} \tag{2.1}$$

μ_0 was extracted by applying polynomial fits to the pre- and post-edge regions, as shown in figure 2.2. The modelled background absorption resembled theoretical absorption spectra (see section 1.1.2 and fig. 1.7) *i.e.* an XAS spectrum without the white line and EXAFS oscillations superimposed upon them. Figure 2.2 shows that the falling pre- and post-edge baseline, evident in both raw experimental and theoretical transmission spectra flattened once the background absorption was subtracted. The same occurred when the rising baselines of fluorescence spectra were background subtracted.

The XAS spectra were then normalised because the edge step varied from one sample to the next, with the density of the sample or even during an experiment; for instance, spectra from the dense, crystalline standards showed much higher absorption than the amorphous films. The y-axes of all background-subtracted spectra were therefore consistently normalised to a similar scale by dividing each absorbance value by the absorbance at a specific feature present in all spectra *i.e.* half way up the first EXAFS oscillation ($y/y_{(point)} = y_{(norm)}$). Normalisation at this point meant that the top of the true absorption edge, (*i.e.* the edge without the white line, section 1.1.1),

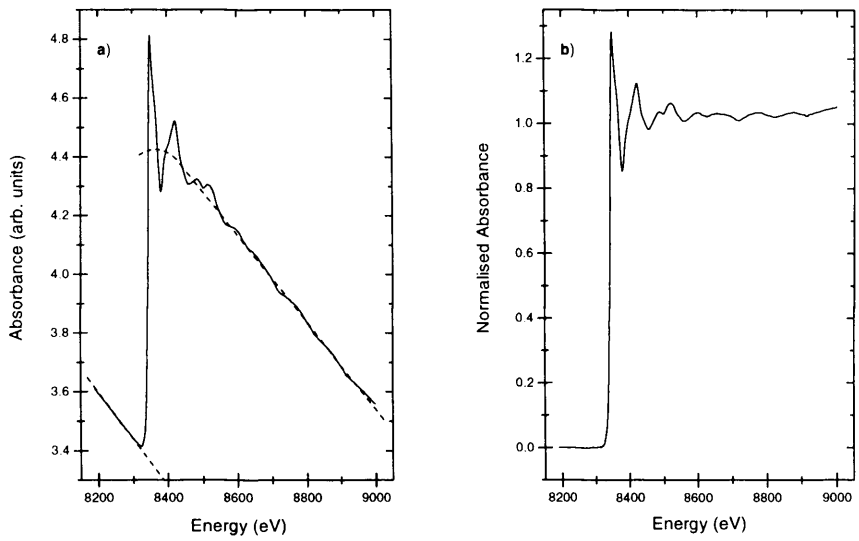

Figure 2.2: Full transmission mode XAS spectrum of $KNiIO_6$ powder a) before background subtraction, with pre-edge and post-edge background marked (dotted lines); and b) after background subtraction and normalisation.

could clearly be identified at $y = 1$, aiding precise evaluation of the edge position at $y = 0.5$ (section 2.2.3). Normalisation therefore enabled direct comparison of spectra from all types of sample.

The background-subtracted fine structure beyond E_{edge} was isolated and plotted as a function of wave vector k (eqn. 1.14). A Fourier transform was then performed on the k-space EXAFS, enabling a rough check on the position and magnitude of the peaks corresponding to each coordination shell. This step determined the success of background subtraction *i.e.* the first metal-oxygen and metal-metal coordination shells (usually between 1.5 and 2.5 Å for metal oxides) should have the greatest amplitudes since backscattering is strongest from these shells. When complete, the background-subtracted EXAFS was exported for use in the fitting process.

The entire background subtraction and normalisation procedure was conducted using the Daresbury program EXBACK [52]. Background subtraction

was not performed on monitor spectra because metal foil structure was already established from the reference sample. It was not desirable to derive metal foil structure from monitor spectra because their quality was not as good as those obtained from the standard sample position, as the third ion chamber only received a fraction of the original beam intensity. Nevertheless, all monitor spectra were normalised because their edge positions were required for calibration purposes, as shown in the next section.

2.2.3 Evaluation of Valency from XANES

Various methods for determining edge positions from spectra (with their original energy-space x-axes) are detailed in section 1.1.1. The obscuring white line, present in all XANES, made measuring the energy corresponding to a normalised absorbance of 0.5 the most reliable method for determining edge positions. In most cases, a data point exactly at 0.500 was not present, so a simple trigonometric interpolation was performed between the two nearest data points in order to establish precisely the energy corresponding to $y = 0.500$. For the purposes of this thesis, the absolute value of the edge position is not as significant as the relative value. For instance, shifting edge positions relative to a pure metal standard or monitor (during oxidation and reduction) were a primary focus; so the choice of method was not as important as complete consistency when normalising spectra and deriving edge positions within each system.

It was always possible for the monochromator crystals to slip up or down by a fraction of a degree from one scan to the next, making successive scans (apparently possessing the same energy scales) to be slightly shifted. As a result, when successive spectra from a stable sample (*e.g.* a metal foil) were overlaid, there was an apparent shift in the position of each spectral feature from one spectrum to another. An edge shift, implying valency change in a stable metal foil was unlikely, so the difference arose from very slightly

shifted energy scales. Apparent edge shifts were eliminated, where possible, by the use of each spectrum's corresponding monitor scan, recorded simultaneously with each measurement in the transmission (standard and quick) and fluorescence modes. Each monitor spectrum was consistently compared with a reference scan from a metal foil standard; the edge position of each was determined, then the energy scales of the monitor and its corresponding sample were adjusted by the same amount (usually $\pm$ 0.5–1.5 eV) so that the edge of the monitor was equal to that of the standard. The true edge position or edge shift ($E_{edge(\text{sample})} - E_{edge(\text{metal})}$) was therefore established. When a third ion chamber could not be used, the sample was replaced by a foil, and a separate monitor spectrum was recorded before and after each series of sample spectra. When comparing edge shifts, differences less than 1.0 eV (*i.e.* $\pm$ 0.5 eV) were considered insignificant because 1 eV was the usual energy separation between data points within a spectrum.

Once the edge positions/shifts of the standards were derived, each value was plotted against the known formal integer valency of the central absorbing metal atoms in each respective material. If there was a clear, unambiguous relationship between standard edge position/shift and formal valency, a straight line or polynomial curve was fit to these points, and the plot was used as a calibration curve to determine the valency of absorbing metal ions in each unknown sample. The edge position/shift of each unknown was then plotted on the graph and the valency was adjusted so that each point aligned with the calibration curve. If a calibration curve could not be established, the valency of electrochemical samples was deemed to be equal to the formal valency of the standard with the closest edge position/shift. The valency of central metal atoms in each unknown sample was thus established. These methods, and all comparisons of standards to unknowns, were only valid if both standards and samples contained the same absorbing metal atoms and backscattering neighbours, and all if all compared spectra were measured at the same absorption edge.

Changes to the appearance of other XANES features such as the white line and pre-edge peaks (see section 1.1.1) were only analysed retrospectively, to qualitatively confirm structures derived during the fitting process. An example is given by the increasing white line intensity evident in normalised metal oxide L-edge XANES during oxidation. This suggests an increase in the density of available empty allowed continuum ϵs or ϵd states necessary for a continuation of the edge to a white line. When considering the filled hybridised states utilised for bonding in the material, such an observation may aid confirmation of a proposed structure. In these analyses, small pre-edge features were not considered significant because their amplitude was similar to the noise level; so only intense pre-edge features would be used for structural deductions.

2.2.4 Evaluation of Structural Parameters from EXAFS

The fitting procedure was performed to determine the values of structural parameters such as interatomic distances (R), coordination numbers (N), root mean square deviation of bond length (Debye-Waller factor or r.m.s. disorder $2\sigma^2$) and the elemental identities of neighbouring atoms. The Daresbury program EXCURV [53] was used to simulate the background-subtracted experimental EXAFS spectra exported from EXBACK. Theoretical spectra (fits) were generated using rapid curved wave theory that used parameters from a model consisting of radial shells of scattering atoms surrounding each central absorber [23].

Firstly, the x-axis of a k-space experimental spectrum was multiplied by a weighting factor of k^n where n was usually 3, to amplify the decaying oscillations at high k. If this step caused the noise to be amplified to an unacceptable level, thus interfering with the fitting process (*i.e.* if the noise was being fitted at the expense of the signal), then the weighting factor was

reduced to k^2, or the spectrum was truncated by 1–2 Å^{-1} at the (noisy) high k end, so that only a signal-dominated spectrum was fitted.

The absorbing atom was treated as a $Z+1$ atom because excited absorbers contain core holes left behind by the ejected photoelectrons, which do not relax before the EXAFS scattering events take place. The elements thought to comprise each backscattering shell were input, then internal atomic scattering data (*e.g.* scattering factors) were used to calculate atomic potentials and phaseshifts for the system (eqns. 1.16 and 1.17). When analysing standards thought to be very similar to the unknown sample (*e.g.* crystalline $Ni(OH)_2$), these calculated phaseshifts were sometimes saved and used when analysing the electrochemical samples (*e.g.* disordered $Ni(OH)_2$). Defining the wrong backscattering elements at this stage would result in erroneous and unphysical values for the final structures.

The first coordination sphere was then modelled. Preset parameters included the amplitude reduction factor (eqn. 1.17) and the core-hole lifetime. An approximate set of structural variables were defined (*e.g.* atom type = oxygen, R_1 = 1.8 Å, N_1 = 6.0 and $2\sigma_1^2 = 1 \times 10^{-3}$ Å^2), then the parameters were refined iteratively using the least-squares method so that each value was altered very slightly during each iteration, in order to effect small changes in the theoretical spectrum. Each iteration varied the extent of overlap between k-space experimental and theoretical spectra, where the difference between them is represented by the fit factor or R-factor, R_{EXAFS}

$$R_{\text{EXAFS}} = \sum_{i}^{N} \frac{1}{\sigma_i} (\mid k^n \chi_i^{exp}(k) - k^n \chi_i^{th}(k) \mid) \times 100 \% \qquad (2.2)$$

where N is the total number of data points and σ_i is the standard deviation between experimental and theoretical data points [53]. The ultimate goal of refinement was to reduce the fit factor and hence mimic the experimental spectrum as closely as possible. An R-factor of $\sim$ 20 % was considered a high quality fit once the final structure had been obtained.

Initially, the four main variables were refined in pairs. The interatomic

distance between the absorbers and the first shell atoms was refined with the Fermi energy to alter the phase of the fit (see phase function eqn. 1.16). Although the Fermi energy E_f was always a fitted parameter, its value will not be reported herein because E_f and E_{edge} are similar ($E_f = E_{edge} \pm 15$ eV) and any change to one is expressed in the other, so E_{edge}, which was measured directly (rather than modelled) is the most reliable and useful of these terms for the purposes of this thesis. The coordination number was then refined with the Debye-Waller factor to correct the amplitude of the peaks (see amplitude function eqn. 1.17). All four parameters were then refined together. A second coordination shell was defined and added to the existing model, then the refinement procedure was repeated for the two-shell system until a minimum fit factor was achieved and refinement ceased. The refinement procedure was repeated for the third shell onward until the furthest shell fit became inconclusive ($\leq$ 5 Å), a situation exemplified by errors larger than the given value or when the number of variables fitted approached the number of data points present.

Each experimental and theoretical spectrum was overlaid and plotted in both k-space and distance or R-space as Fourier transforms of the k-space spectra. Radial distribution functions (RDFs) were also derived during each fit in order to observe the radial positions of all backscattering shells in the coordination environment. The final structure consisted of a multiple-shell fit having a minimised overall fit factor (*i.e.* the best fit), where each jth shell had values for R_j, N_j and $2\sigma_j^2$, all with respective statistical errors of $\pm 2\sigma$ (95 % confidence level); all of these values were noted down. The fitting procedure was initially performed on the standards; fitted structures were then compared with published values for R and N [50] for each substance. If fitted and published structures agreed, the fitting procedure was applied to the unknown samples (*i.e.* the films).

2.2.5 Evaluation of Valency from Interatomic Distance

The well-known relationship between bond length and oxidation state was used to derive the valency of central absorbing transition metal ions in the electrochemical samples, using a similar methodology to that described in section 2.2.3 where a calibration curve was used to derive valency from absorption edge position or shift.

The distance of the first coordination sphere is affected more by the ionic charge of the metal ions than subsequent shells, so only first shell bond lengths were used to construct calibration curves. Also, only shells consisting of atoms directly bonded to absorbers were eligible for use *e.g.* metal-oxygen bonds as opposed to metal-metal coordination. Here, as with edge shift plots, metal ion valency formed the x-axis, where reference compounds were assumed to have integer (formal) oxidation states relative to the pure metal foil. If a clear relationship was evident (as in section 2.2.3), a linear or polynomial fit to bond lengths of the standards defined the calibration curve, onto which the electrode bond lengths were aligned. If the first coordination sphere of a film or standard had a regular structure, all bond lengths in that shell would be equal, so averaging was not necessary. However, if the shell was distorted, several interatomic distances would be present (with their respective coordination numbers), so a weighted mean value was required to extract a single value for that shell, where

$$R_{mean} = \sum_{R} \frac{R_j \, N_j}{N_{tot}} \tag{2.3}$$

It is important to emphasise that the bond length method served only to confirm the oxidation states derived from other routes, because the response of interatomic distance to ionic charge is secondary when compared to absorption edges and electrode charge; so changes in ionic charge are more directly expressed by edge shifts and the measured film charge (coulometry).

The necessary criteria for constructing edge shift/position calibrations, specified in section 2.2.3, apply here, with the added condition that all stan-

dards used should possess the same total first shell coordination number N_{tot}. This condition is necessary because the charge density at each bond varies with the number of bonds present (the coordination number), which in turn affects the interatomic distance. So the slope of the bond length plot depends on the structure of the standards used to construct it. As a result, if very similar compounds are not being used to construct the curve, where some factor other than just the oxidation state of the central ions varies, then the calibration curve becomes skewed. Furthermore, the electrode whose valency is to be derived should also have the same coordination number as the standards, otherwise the interpreted valency would be incorrect. It was not always possible to meet these additional criteria, often because a N-coordinate oxide with the required oxidation state did not exist. Therefore, valences derived from bond lengths only provided a secondary guideline to confirm those extracted more reliably from edge shifts and coulometry, which are not only more direct means for deriving ionic charge, but are structure-insensitive as well. The coulometric evaluation of valency is one of the analyses described in the following section.

2.2.6 Analysis of Spectroelectrochemical Data

The thickness (x) of a given film was estimated using the expressions stated in equation 1.21, which shows several spectroscopic, electrochemical and spectroelectrochemical formulae for obtaining film thickness. One of these expressions was used to calculate film thickness from the raw, unnormalised edge step ($\Delta\mu$ or Δabs) using tabulated absorption cross sections for the absorbing element at energies corresponding to the top and the bottom of the absorption edge ($\Delta\sigma$, the second expression in equation 1.21). This method mainly applied to transmission spectra because unknown functions of energy are present in data collected in the fluorescence, reflection and energy dispersive modes. As a result, the absorption coefficient, as calculated

by EXCALIB using equation 1.1 (or the first expression in equation 1.21) is equal to μx plus the slowly-varying functions of energy. These unknown functions are also present in transmission spectra, but their magnitude and origin are known, *i.e.* they arise from the gas pressure in the ion chambers, air absorption and amplifier settings. As a result, their contribution to transmission spectra is neglected, despite the fact that absolute values for μ are never actually known.

The use of edge steps to derive thickness was validated by performing the calculation on metal foil spectra where both the thickness and density (and hence absorber concentration) of the sample were known. If this was successful, the unknown functions were proven to be insignificant. This test was also performed on metal foil spectra recorded in the energy dispersive mode, to assess the method's viability when analysing corresponding spectra from electrodes. The beam did not traverse the sample in reflection and fluorescence modes, and fluorescence detection was too sensitive to record data from dense metal foils, rendering the test, (and hence the full methodology) inapplicable to thickness evaluation for these modes.

In order to complete the edge step calculation of film thickness for unknown samples, the coverage of electroactive sites on the WE surface (Γ) and the concentration (C) of absorbing electroactive sites in the film was evaluated coulometrically. Current-time correlations, measured directly during deposition (when films were electrochemically deposited), during overcharge (prolonged oxidation or reduction) and the subsequent discharge, or derived from cyclic voltammograms, were integrated to calculate the charge (Q) passed during that electrochemical procedure and the coverage of electroactive, absorbing metal sites (see eqn. 1.18). The expressions in eqn. 1.21 were then used to calculate the amount of electroactive species (N). If these calculations proved to be consistent when derived independently for deposition, oxidation and reduction, the derived value for absorber coverage was used to calculate film thickness from the edge step (last expression in eqn.

1.21).

Coulometric measurements were also used to establish the change in valency of electroactive absorbing metal ions. The coverage of electroactive sites was used to calculate n, the number of electrons transferred per metal site upon overcharge and at various points during discharge. Once calculated, n was compared with valency changes derived from the calibration curves.

The analyses detailed in this section illustrate the means by which electrochemically-derived current and voltage measurements were used to extract quantitative information that was used to support values derived from spectroscopic analyses alone. It was also shown how electrochemically-derived quantities were necessary to complete some calculations, thereby affirming the utility and complementarity of the spectro-electrochemical combination. Combined *in situ* X-ray absorption and electrochemical techniques were exploited for the study of electrochemically-manipulated tungsten oxide, niobium oxide and nickel hydroxide, the system studied in the following chapter.

Chapter 3

The Nickel Hydroxide Electrode

The redox reactions of the nickel hydroxide electrode have attracted much attention for over two decades primarily due to its capacitive and electrochromic properties, and hence its relevance to both battery technology [54] and to the development of optoelectronic devices [30], respectively. Previous assessments of the nickel hydroxide $Ni(OH)_2$ system have explored these applications using various electrode arrangements and preparative methods to monitor the structural [55] and electrochemical [56] changes taking place during redox cycling. For example, spectroelectrochemical investigations regarding the structural responses of graphite-bound $Ni(OH)_2$ battery electrodes were once commonplace due to the interest generated by industry [30, 57]. More recently, much attention has been paid to the performance of electrochemically-prepared, electrochromic $Ni(OH)_2$ film electrodes (the type investigated here) due to their application to display devices and 'smart' windows [30] (section 1.2.4). In fact, nickel hydroxide films have been used in prototype ECDs where $Ni(OH)_2$ was the secondary electrochrome, with WO_3 providing primary colouration [30]. As a result, much is already known about the redox chemistry of nickel hydroxide and its short- and long-range structures (via XAS [2, 55] and XRD [58], respectively), though many ambiguities

remain. Problems are commonly attributable to the disordered nature of electrochemically prepared nickel hydroxides and their associated oxy-hydroxides (their redox couples, hereafter collectively termed nickel (hydr)oxides). X-ray methods are natural candidates for structural determination. However, the lack of long range order in electrodes prepared this way precludes X-ray diffraction as a viable tool for obtaining unambiguous *in situ* structural information, leaving EXAFS as the most effective method yet for directly studying the structure of nickel (hydr)oxide electrodes *in situ*. Confusion may also arise from the fact that derived results seem to vary with preparation method, though this situation is common for most transition metal oxide systems.

So far, it has been shown that the electrochemically-driven oxidation and reduction of nickel (hydr)oxide electrodes is accompanied by subtle structural changes [54]. Numerous EXAFS studies on chemically prepared reference nickel oxides have shown that both Ni-O and Ni-Ni distances are shorter in oxides of higher Ni valency. Capehart and co-workers [59] and Mansour *et al.* [60] demonstrated a linear relationship between Ni-O bond length and the oxidation state of nickel for crystalline nickel oxides of varying known formal oxidation states. This relationship was then shown to apply to electrochemically prepared nickel (hydr)oxide electrodes, and this linear dependency has been used as a calibration curve to determine the oxidation state of Ni ions in nickel (hydr)oxide electrodes [55, 59, 61, 62]. *In situ* EXAFS measurements show that significant contractions of both Ni-O and Ni-Ni distances take place when a freshly deposited electrode is oxidised (charged); these bonds subsequently lengthen when the electrode is reduced (discharged) [54, 57, 63]. In fact, the contraction and elongation of interatomic distances within the first Ni-O and Ni-Ni shells is not uniform, so a certain degree of coordination shell distortion is induced by the redox process. However, the disordered nature of nickel (hydr)oxide electrodes has led to difficulty in conclusively quantifying this effect as a function of electrode charge.

In some instances, the oxidation states determined from bond lengths were corroborated using a calibration curve based on the linear relationship between Ni K-edge position and formal (integer) Ni valency, for which the edge energy rises as Ni valency increases [55, 60, 61, 62, 64] (section 1.1.1). Non-integer values for Ni valency were often obtained by considering the films as consisting of Ni sites at a range of integer oxidation states in various proportions, represented by the mixture of Ni-O bond lengths present in the nickel (hydr)oxide electrode [55, 59, 65]. The weighted mean value of these states was then used to derive an overall non-integer Ni valency. Non-integer Ni valences of 3.67 or 3.5 for charged electrodes and 2.5 for fresh/discharged electrodes have been deduced on this basis [54, 55, 59] or using spectroscopically-, coulometrically- and iodometrically-determined transfer of 1.67 electrons per nickel atom [59, 66, 67].

Over the past twenty years, many thorough electrochemically-focused studies have been carried out to characterise electrochemically prepared $Ni(OH)_2$ and its redox couples. Agreement on all precise details is yet to be reached, but there is a general consensus that nickel hydroxide undergoes the following redox reactions, initially proposed by Bode [68], where the freshly-deposited electrode has the α-form:

$$\begin{array}{ccc} \alpha - Ni^{II}(OH)_2 & \underset{\text{discharge}}{\overset{\text{charge}}{\rightleftharpoons}} & \gamma - Ni^{III}OOH + H^+ + e^- \\ \text{dehydration}\downarrow & & \uparrow\text{overcharge} \\ \beta - Ni^{II}(OH)_2 & \underset{\text{discharge}}{\overset{\text{charge}}{\rightleftharpoons}} & \beta - Ni^{III}OOH + H^+ + e^- \end{array} \qquad (3.1)$$

NiOOH is nickel oxyhydroxide; α, β and γ classify the type of structure present (distinguished by their broad, but differing X-ray diffraction patterns [54, 58]); the α and γ forms are highly hydrated and disordered and the β types have more compact and regular structures. The Roman numerals represent the formal valency of Ni, and dehydration may be carried out by repeated voltammetric cycling or 'ageing' by immersion in a concentrated

aqueous hydroxide electrolyte for several hours.

According to some publications, where the mixed integer Ni valency model is used, the electrochromism displayed by $Ni(OH)_2$ films may be represented by equations 3.2 and 3.3. Again, there is some variation in published results (*e.g.* the value of z), and hence the valency of nickel in nickel (hydr)oxide electrodes is still being debated [66]; but there is agreement about the general outline of the pathway.

In terms of proton movement:

$$\underbrace{[Ni^{III}_{(1-z)}Ni^{II}_{z}]O_2H_2}_{\text{COLOURLESS}} \underset{\text{discharge}}{\overset{\text{charge}}{\rightleftharpoons}} \underbrace{[Ni^{IV}_{(1-z)}Ni^{III}_{z}]O_2H}_{\text{BLACK}} + H^+ + ne^- \tag{3.2}$$

or the movement of aqueous KOH electrolyte:

$$\underbrace{[Ni^{III}_{(1-z)}Ni^{II}_{z}]O_2H_2}_{\text{COLOURLESS}} + K^+ + 2OH^- \underset{\text{discharge}}{\overset{\text{charge}}{\rightleftharpoons}} \underbrace{[Ni^{IV}_{(1-z)}Ni^{III}_{z}]O_2H}_{\text{BLACK}} + KOH + H_2O + ne^- \tag{3.3}$$

Another, less common school of thought, exemplified by Pickering and co-workers [69] in the study of chemically prepared lithium nickel oxides, approaches the question of Ni valency from a solid state perspective as opposed to the molecular model given above, which supposes independent bonds and localised electrons for each atom. The solid state argument utilises a quantum description for a conductor in the solid state, with a properly developed band structure, in which mobile, itinerant electrons are not associated with individual atoms throughout the solid. Here, electrons are progressively exchanged between the Ni-O valence band and that of the metal WE. The resulting effect on valency is that Ni ions do not exist in a variety of formal oxidation states in varying proportions, but are in fact represented by a non-integer value throughout the solid. So the terms in square brackets in equations 3.2 and 3.3 may simply be replaced by Ni, with a non-integer value of n electrons transferred, per site, during the redox process.

Use of a solid state or molecular model has implications when considering the mechanism for charge transport during oxidation (charge) and re-

duction (discharge) and when classifying electrochemically prepared nickel (hydr)oxide as a conductor, semiconductor or an insulator. The distinction between the two standpoints will be discussed to greater depth in the Discussion section of this chapter (section 3.5.1).

Some XAS studies conclude that K^+ becomes reversibly bound to the coloured oxyhydroxide during oxidation, forming a potassium nickelate (see eqn. 1.19), but evidence provided by techniques focusing on the flux of solvent and low-Z counter and co-ions, such as the electrochemical quartz crystal microbalance (EQCM) [33], neutron reflectivity [39] and probe beam deflection [70] suggest that protons, hydroxide ions (OH^-) and water are the only active participants in the redox process and electrochromic action, so K^+ may be replaced by H^+ in equation 3.3.

3.1 Objectives

Despite the wealth of information accumulated on the nickel (hydr)oxide system over the past two decades, several contentious issues remain. These relate to the valency of nickel ions and their influence upon shell distortion, the role of counter and co-ions in the redox process and the structural development taking place at various stages during electrochemical manipulation. Of those issues that may be solved using EXAFS, relationships between electrochemically-controlled charge and Ni valency, and the consequent effects on Ni-O and Ni-Ni environments, are investigated in this work.

The novel approach here is the use of EXAFS in the fast energy dispersive mode [71]. This technique allows interpretation of the structural behaviour of discharging nickel hydroxide films following prolonged charging (overcharge). In particular, the previously unresolved structural evolution taking place *during* discharge is presented for the first time, thereby extending the existing structural picture based on a framework previously obtained for the *static end-points* of the fresh, discharged, overcharged and recharged

electrode. Dynamic changes are monitored *in situ* with energy dispersive EXAFS (EDE); the fluorescence (flEXAFS) and transmission modes (standard and quick EXAFS) are used to characterise the films at specific stages in electrode development. It is hoped that this work will clarify the link between electrode charge, Ni valency, Ni-O and Ni-Ni distance, coordination numbers and structural disorder. Electrochemical measurements, by means of cyclic voltammetry and coulometry are used to characterise the films and to monitor the progress of overcharge and discharge.

This study is geared toward the development of optoelectronic technology, so there is a necessity for film electrodes and conditions to be representative of working electrochromic devices. The first step toward meeting this challenge is the design of a suitable spectroelectrochemical cell, which will be discussed in the following section.

3.2 Experimental

3.2.1 *In situ* Spectroelectrochemical Cell

The cell used in this chapter (fig. 3.1) meets all of the criteria detailed in section 2.1.3, thus providing a means for measuring changes in structural parameters under conditions in which the potential, and hence the current and charge of the electrode vary. The *in situ* cell that was designed to study nickel (hydr)oxide films (fig. 3.1) contains features that allow it to be used in the transmission and fluorescence modes, with the added advantage that both types of spectrum may be acquired simultaneously, without the need for realignment with the respective detector geometries. A further attraction is that good quality spectra can be taken in the energy dispersive mode; this is a novelty when compared to previously described cells. The utility of this cell is therefore extended to fast, time-resolved measurements that are needed when carrying out cyclic voltammetry at high scan rates, and other

fast electrochemical experiments. In this mode, the cell is placed at the focal point of a dispersed, polychromatic beam. As a result, a high standard of alignment precision is a requirement which is met by this cell.

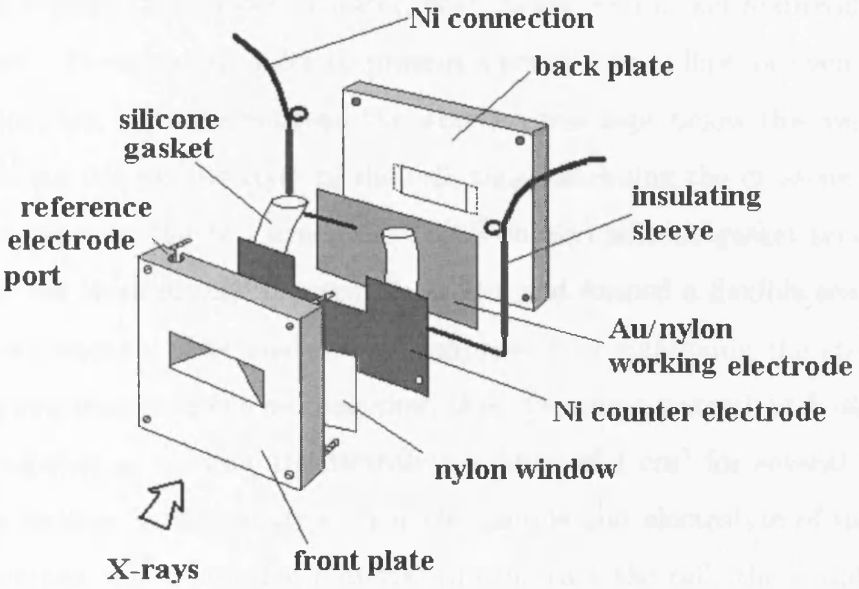

Figure 3.1: Exploded view of *in situ* spectroelectrochemical cell.

Figure 3.1 shows that the *in situ* thin layer X-ray absorption spectro-electrochemical cell comprised three layers, the rigid front and back plates which contained X-ray transparent windows and provided support for the middle layer, a flexible gasket. The thick perspex front plate (5 x 5 x 1 cm^3) had a window opening, cut with its sides slanting inward at 45° to facilitate operation in either transmission, fluorescence or both modes simultaneously. In the dual transmission/fluorescence mode, the beam entered the cell at 45° to the sample; the fluorescent radiation was collected (from the other side of the front window) by a detector placed at 90° to the incoming beam (fig. 1.3). The transmitted beam then left the cell through the rear window cut into the back plate (5 x 5 x 0.5 cm^3) with sides slanting outward at 45°. The back window opening was slightly wider than the front in order to minimise scattering the outgoing, diverging beam. For purely transmission or EDE

experiments, the cell was placed perpendicular to the incoming beam, which passed through the cell toward the in-line transmission or EDE detectors. At the energy range used (8.2–8.8 keV), the calculated extinction distance [7] through various thicknesses of water, gold, nylon, and nickel hydroxide was *ca.* 2 mm. Therefore, in order to prevent a costly loss of flux, or even beam extinction, the distance between the windows was kept below this value by compressing the middle layer of the cell, thus restricting the cross-sectional distance between the two windows. The U-shaped silicone gasket served to separate the working and counter electrodes and formed a flexible seal that prevented leakage. The gasket was compressed by tightening the stainless steel screws that held the cell together, thus creating a watertight U-shaped cavity capable of holding an electrolyte volume of 1 cm^3 for several hours without leakage or degradation. For the sample and electrolyte of interest here, perspex was a suitable material to construct the cell; the simple cell design permits construction from other materials, more tolerant to organic solvents if necessary. The front plate was thicker than the rear to accommodate the reference electrode port, into which the RE was slotted. This port terminated at the top of the front window, and its full length contained a slit that opened into the cell cavity. The reference electrode was specially designed to have a long, thin, but sturdy fritted probe that permitted constant and direct contact with the electrolyte. An Hg/HgO/NaOH (aq) reference electrode (to which all potentials are referred) was chosen for the present study, primarily because of its compatibility with the $Ni(OH)_2$ system, as both film and electrolyte contained hydroxides, though any other suitably shaped reference electrode can be used with this cell.

A $\sim$ 2000 Å thick evaporated layer of gold on transparent nylon (12 cm^2) allowed the back window to function as the working electrode [72]. Its electrochemically active area was 8.5 cm^2 in the assembled cell. The front window was a similarly sized piece of plain nylon film. The windows were fixed to the inside surface of the plates (using epoxy resin) to prevent

electrolyte from gathering at the window recesses. The back plates were cheap and easy to construct, so could be disposed of after use. Alternatively, they could be reused by peeling away and replacing the old working electrode and glue.

The Ni foil counter electrode (0.05 mm thick, 99.99+ %, Goodfellow) was shaped so that it surrounded, but did not protrude into, the illuminated area. L-shaped Ni wires (0.5 mm diameter, 99.0 %, Goodfellow) were used as connections to the Au-coated nylon WE and the Ni foil CE sandwiched between the two end plates. These wires contacted the regions next to the windows, ensuring accurate measurement of potentials across the illuminated area. The close proximity of these electrodes makes thin layer arrangements prone to shorting. For this reason, the working and counter electrodes (and their respective connections) were separated by the insulating gasket, and the wire connectors were sleeved.

An inert T-shaped silicone rubber lid (not shown in fig. 3.1) was designed so that part projected into the gap between the plates once the cell is assembled and filled with degassed electrolyte. This lid enables the delivery of purging gas, (N_2 or Ar) into the cell via syringe needles piercing the lid, and the outflow leaves the cell via a second syringe needle. The lid also works as a seal, providing a barrier to solvent evaporation, thereby maintaining the electrolyte concentration as well as preserving the inert environment of the cell. Finally, a simple detachable perspex mount (also not shown) connected to the long screws in the assembled cell, and allowed it to be aligned horizontally or vertically in an optical bench clamp. This mount could also be bolted to an L-shaped metal bracket which attached directly to the sample stage of an optical bench, as in the EDE arrangement.

3.2.2 Sample Preparation

Descriptions of commonly used equipment and preparative techniques are given in section 2.1. A 5 μm thick nickel foil was used both as a standard and to calibrate the energy scale in the transmission and EDE modes (sections 2.2.3 and 3.2.3 iii, respectively). The reference compounds were reagent grade powders consisting of Ni absorbers and O backscatterers: NiO (99.99 %, Aldrich) and $Ni(OH)_2$ (Aldrich). A Ni(IV) oxycompound could not be obtained commercially, so potassium nickel periodate ($KNiIO_6$) was synthesised by the author using Ray's method [73]. Each nickel hydroxide film was deposited cathodically for 1 hour at -1.0 V *vs.* Hg/HgO from degassed 0.1 M nickel nitrate solution ($Ni(NO_3)_2.6H_2O$ 99 %, Acros).

Each film was deposited onto a back plate/working electrode of the cell immersed in a beaker of fresh nickel nitrate solution. When deposition was complete, the film was removed from the bath and gently rinsed with triply-distilled water. Using a previously established deposition efficiency [74], application of Faraday's law to the deposition charge ($\sim$ 20.7 C) yielded a coulometrically based film thickness of about 5 μm. The cell was then assembled and degassed aqueous 1.0 M KOH ($\geq$ 85 %, Aldrich) electrolyte was slowly pipetted in, then the cell was purged with dry cylinder N_2, sealed and mounted onto the optical bench; the maximum assembly time was 10 minutes.

3.2.3 EXAFS Measurements

i) Standard Transmission EXAFS

The three ion chambers were filled with the appropriate Ar-He mixtures for measuring the Ni K-edge. Absorption spectra of the four reference materials (and their respective monitors) were angle scans in the pre-edge and XANES regions, and k-space scans in the EXAFS region. Spectra were measured at the Ni K-edge (8333 eV) on beamline 7.1 at Daresbury Lab-

oratory. Transmission spectra were recorded in a stepwise fashion with 11 mdeg monochromator steps in the XANES region and 0.05 $Å^{-1}$ steps in the EXAFS region, where the EXAFS ranged from 2 to $\sim$ 13 $Å^{-1}$. Each full absorption spectrum was recorded in 15–20 minutes. Further details regarding this experimental set-up are stated in section 2.1.4.

ii) Quick and Fluorescence EXAFS

QuEXAFS, the fast-scanning option for obtaining high quality transmission spectra, was utilised for recording *in situ* spectra of the freshly-deposited $Ni(OH)_2$ films at open circuit. The standard transmission mode was not used for these samples because several publications claimed that electrode ageing or structural 'ripening' (*i.e.* ordering, see eqn. 3.1) may take effect during the relatively long timescales of transmission experiments [68]. QuEXAFS spectra were subsequently recorded during cyclic voltammetry at various scan rates, where the potential was held at the end-points of each scan *i.e.* at the positive and negative limits of the CVs (+0.56 V and -0.15 V, respectively), while each spectrum was recorded (see section 2.1.5). Fluorescence spectra of similar samples were recorded for comparative reasons and because these films produced low edge steps in the transmission mode, despite being electrochemically thick. The fluorescence mode, being more sensitive than transmission, was capable of recording an improved signal for such low density films.

It was expected that ageing may affect disorder (Debye-Waller factors) and short range structure within the films. QuEXAFS was also used to investigate the effects of chemical ageing on films in basic solutions of varying concentration. The influence of ageing was therefore accounted for, so its effects could not be assigned wrongly to those induced by electrochemical manipulations. Freshly prepared films were immersed in aqueous 1.0 M, 2.0 M and 4.0 M KOH electrolyte for approximately 3 hours. Spectra were recorded approximately every 5 minutes for the first 30 minutes, then

at gradually increasing intervals for the remaining time. No electrochemical modifications were attempted and the electrodes remained disconnected throughout these experiments.

All quEXAFS and flEXAFS spectra (and corresponding monitors) were recorded on station 7.1 at Daresbury. QuEXAFS measurements were made in a quarter of the timescale of the standard transmission mode (about 5 minutes) because the double crystal Si(111) monochromator angles were varied in a continuous sweep as opposed to separate steps. Fluorescence spectra were recorded using a NaI scintillation counter. The width of the beam was reduced to 0.5 cm (half the original width, see section 2.1.4) to prevent the beam from clipping the window edges when the cell was positioned for operation in the dual transmission/fluorescence mode. Consequently, the flux halved and the quality of fluorescence spectra was significantly degraded when compared with those recorded solely in the fluorescence mode. Hence, only pure fluorescence spectra were used for analysis, because the beam width was not shortened since the transmission signal was unimportant for these measurements.

iii) Energy Dispersive EXAFS

Energy dispersive absorption spectra were recorded on beamline 9.3 at Daresbury. This mode utilised a curved Si(111) crystal polychromator and a Reticon RL1024S linear photodiode array (position-sensitive) detector. A 5 μm thick Ni foil was used for separate energy calibration at the Ni K-edge. The summation of 2000 x 25 ms scans comprised each raw spectrum, resulting in an acquisition time of under 2 minutes per spectrum. The spectral range of the white beam was typically 8200 to 8800 eV, producing EXAFS ranging from 2 to 10 Å^{-1}. Once the cell was aligned at the focal point of the white beam (roughly 1 m away from the polychromator), the beam spot was 200 μm wide.

The fast acquisition times offered by EDE allowed XAS spectra to be

taken *during* cyclic voltammetry. The potential was cycled between the aforementioned limits at various scan rates; see section 2.1.5 for more details. At slow scan rates ($\leq$ 5 mVs^{-1}), the spectra were taken without interrupting the cyclic voltammograms, producing spectra that would display averaged structural changes. At higher scan rates (10, 20, 50 and 100 mVs^{-1}), the potential scan was intermittently interrupted at selected points of interest during the cycle, particularly current peaks, while each set of spectra was recorded. About 6 sets of spectra were collected during each complete cyclic voltammogram.

In addition to cyclic voltammetry, a freshly deposited film was anodically overcharged at +0.5 V for 125 minutes in 1.0 M KOH solution. Time-resolved spectra were then taken without interrupting the flow of current, as the nickel hydroxide film discharged at 0 V; dynamic *in situ* measurements were therefore made throughout the 2 hour duration of discharge.

3.3 Data Analysis

The spectra of reference compounds, Ni foil and nickel (hydr)oxide electrodes were calibrated, background subtracted, normalised and fitted using the standard procedures detailed in section 2.2. The fits from the standards were compared with published structures [50] to ensure a correct fitting procedure (sections 2.1.1 and 2.2.4). The energy scales of all spectra were corrected to account for monochromator 'drift'. This was achieved using either the sample's corresponding monitor spectrum (recorded simultaneously) or a monitor spectrum recorded separately, as described in section 2.2.3. The latter procedure was necessary when correcting EDE spectra, and the former was performed on transmission (standard and quick modes) and fluorescence spectra. An additional energy correction was necessary when comparing normalised spectra recorded on different beamlines. Ni foil edge positions recorded on beamlines 7.1 and 9.3 differed by 1.98 eV. This value was sub-

tracted from the energy scales of all EDE spectra. During data fitting, the EXAFS of each EDE spectrum was truncated to $k_{max} = 9.5$ Å^{-1} to remove excessive noise at the high k end; as a result, there was only enough data to reliably fit the first Ni-O and Ni-Ni shells.

All spectra were k^3-weighted and curve fitting was achieved using the EXCURV97 program [53]. The phase shifts calculated for $Ni(OH)_2$ powder were used to analyse the EXAFS of electrochemically prepared samples. Fits to various combinations of regular (unsplit) and distorted (split) Ni-O and Ni-Ni coordination shells were performed for all samples; those producing the greatest and most conclusive overlap of experiment and fit are presented. The reproducibility of fits to data from the films was enhanced by setting coordination numbers to integer values. The final extracted values for each coordination sphere were first Ni-O and Ni-Ni interatomic distances, coordination numbers and Debye-Waller factors. Edge positions and shifts, Ni valency and coulometric charge densities were also calculated. These results are presented in various forms, and their structural and electronic implications are discussed in section 3.5.

3.4 Results

3.4.1 Characterisation of Nickel Hydroxide Films

Cyclic voltammograms obtained from freshly deposited nickel (hydr)oxide films displayed peak potentials and an overall appearance that epitomised (apart from some distortion) the well-documented $\alpha - Ni(OH)_2 \rightleftharpoons \gamma - NiOOH$ interchange [74]. These transitions coincided with the characteristic reversible electrochromic response of the redox couple in aqueous KOH electrolyte *i.e.* colourless when uncharged (fresh) or reduced, to black when charged or overcharged (eqns. 3.2 and 3.3). A typical cyclic voltammogram is shown in figure 3.2. The distortions visible at the

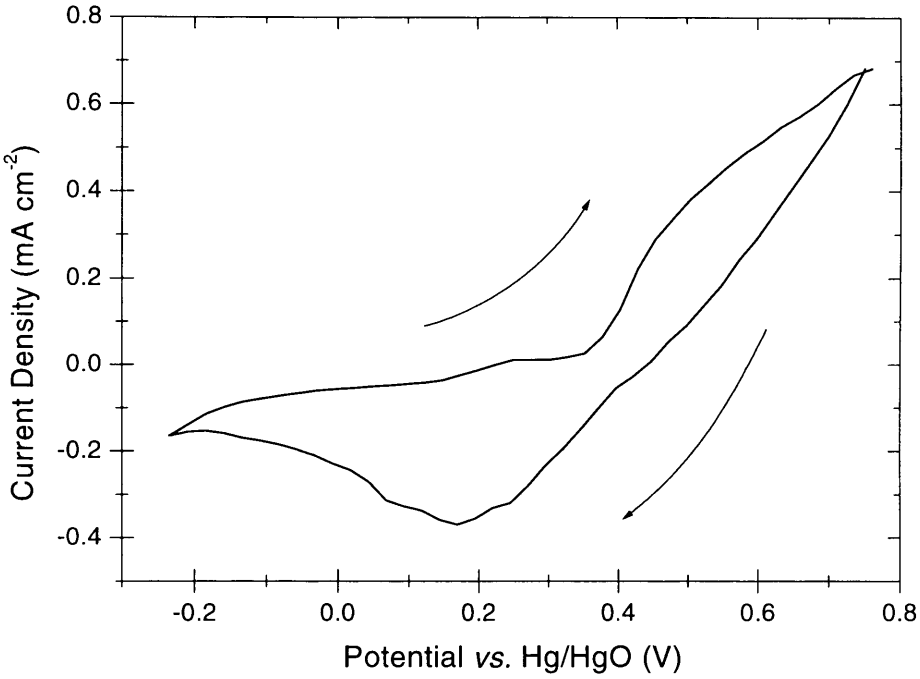

Figure 3.2: Cyclic voltammogram for an electrodeposited nickel hydroxide film (on thin Au/nylon substrate) exposed to 1.0 M KOH. Potential scan rate 20 mVs^{-1}. $\Gamma = 17.9\ \mu\text{mol}\,\text{cm}^{-2}$.

current peaks are probably caused by ohmic drop due to slightly non-ideal electrode placement. The trade-off between electrochemical and X-ray demands meant that thick films were necessary to produce a reasonable edge step, and the counter electrode could not span the entire surface of the working electrode. However, these compromises had little effect on the voltammograms as the distortions are minor and the overall form is clear and identifiable.

Figure 3.3b is a typical raw EDE spectrum of a fresh nickel hydroxide film, displaying an edge step of $\ln\left(\frac{I_0}{I_t}\right) \simeq 0.5$. The absorption edge of a 5 μm thick nickel foil, recorded in the EDE mode was used to determine the efficacy of deriving film thickness from the edge step of EDE spectra (see

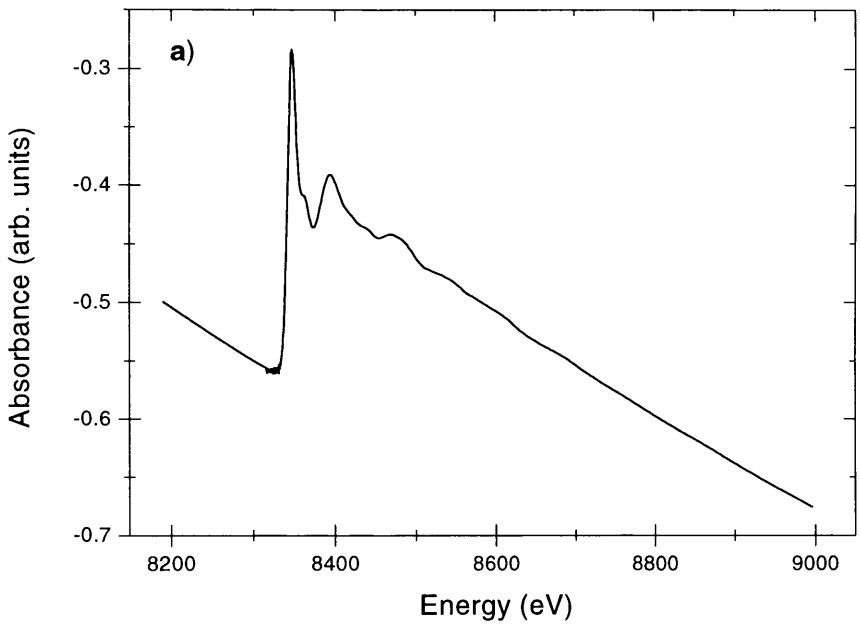

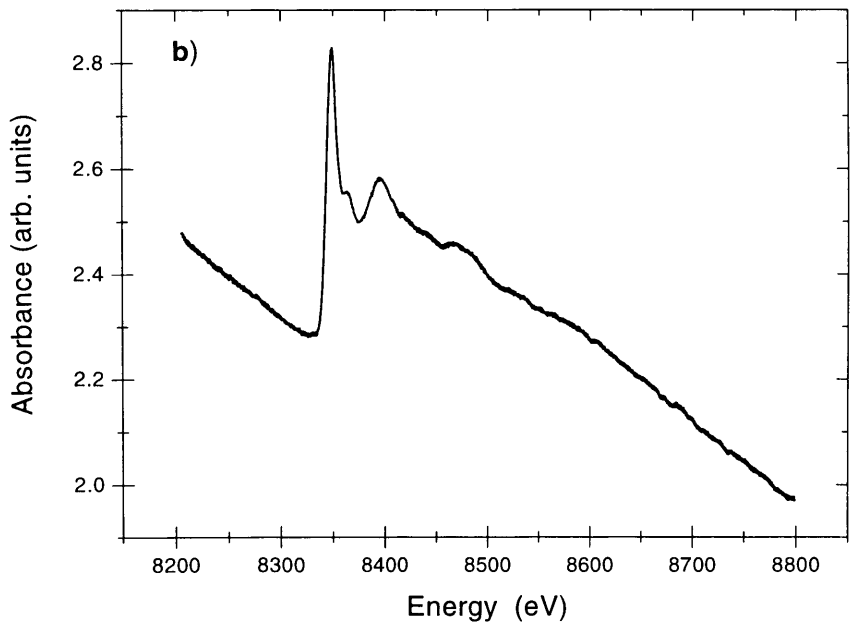

Figure 3.3: Raw a) standard transmission and b) EDE spectra of a freshly deposited nickel hydroxide film.

section 2.2.6). This test proved to be unsuccessful for the reasons given in section 2.2.6, deeming the calculation inapplicable to EDE spectra of the films with unknown thickness. Edge steps of the fresh electrode, recorded in transmission mode were $\ln\left(\frac{I_0}{I_t}\right) \simeq 0.3$ (fig. 3.3a). The thickness of a given film was calculated using the raw edge step of the transmission spectrum (eqn. 1.21) using tabulated values for the difference in the absorption cross-section of Ni ($\Delta\sigma = 2.9 \times 10^4$ cm^2 barn/atom $= 1.75 \times 10^4$ cm^2 mol^{-1} [7]) and both the coulometrically-determined concentration of Ni sites *at deposition* ($C = 35.8$ mmol cm^{-3}) and the surface coverage of Ni sites at deposition ($\Gamma = 17.9$ μmol cm^{-2}), as described in section 2.2.6. These calculations yielded a film thickness of about 5 μm, which is consistent with the value derived at deposition in section 3.2.2. The surface coverage was also used to independently calculate the edge step (eqn. 1.22), producing a value that is equal to the measured edge step in transmission mode ($\Delta\mu = 0.3$). The surface coverage ($\Gamma = 23.8$ μmol cm^{-2}) and concentration ($C = 47.6$ mmol cm^{-3}) of sites *at overcharge* were used to repeat these calculations independently. The calculated edge step ($\Delta\mu = 0.4$), film thickness (~ 5 μm) and number of Ni sites ($N = 0.2$ mmol) are all self-consistent and agree with both experimental data and results derived from deposition data.

3.4.2 Discharge of the Electrode

Figure 3.4 shows the measured discharge current as a function of time after overcharging a freshly deposited film; the dots show when each set of EDE spectra was recorded. It is evident that two sets of spectra were recorded while the discharge current dropped abruptly. The current plateau before 25 mins is due to current limitation through the potentiostat, which prolonged the discharge process. 20.7 C passed during deposition, about 19.5 C of charge was input to overcharge the electrode and 19.5 C passed during discharge, suggesting effectively full conversion of all electroactive sites both

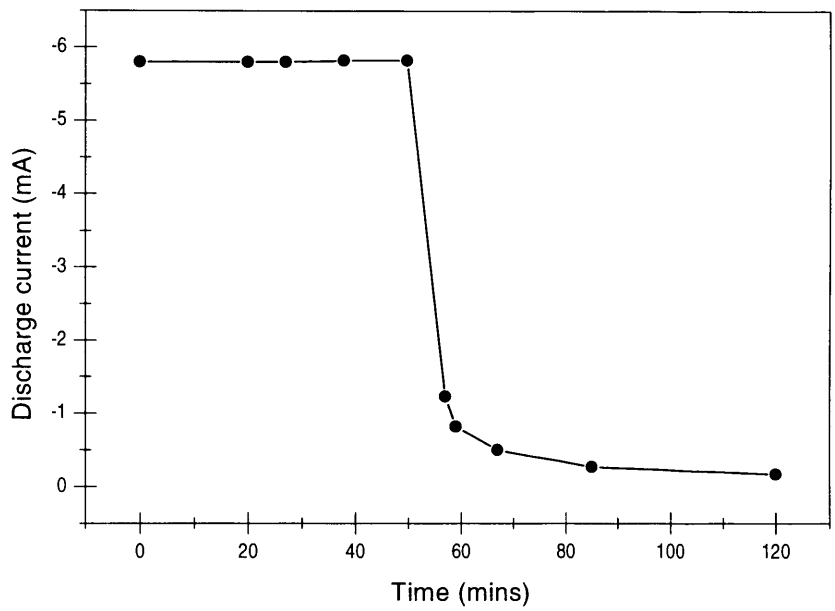

Figure 3.4: Current-time profile of discharging nickel (hydr)oxide film and the points (dots) at which each set of EDE spectra were taken.

at overcharge and upon discharge.

Normalised Ni K-edge XANES of the standards and a nickel (hydr)oxide electrode are shown in figure 3.5. Four stages of electrode development are evident: the fresh, overcharged, discharging and discharged electrode. A substantial positive shift of edge position occurs when the electrode undergoes overcharge. This edge shift subsequently reverses during discharge, resulting in a progressive negative shift of Ni K-edge position as the electrode discharges.

Qualitatively, the expected progressive decrease of edge shift during discharge is evident in figure 3.5. A quantitative interpretation of edge shifts is given in figure 3.6, which is a calibration plot that was used to derive the valency of nickel ions in the electrode. Edge positions were measured at half the height of the edge step, and edge shifts were calculated as the difference

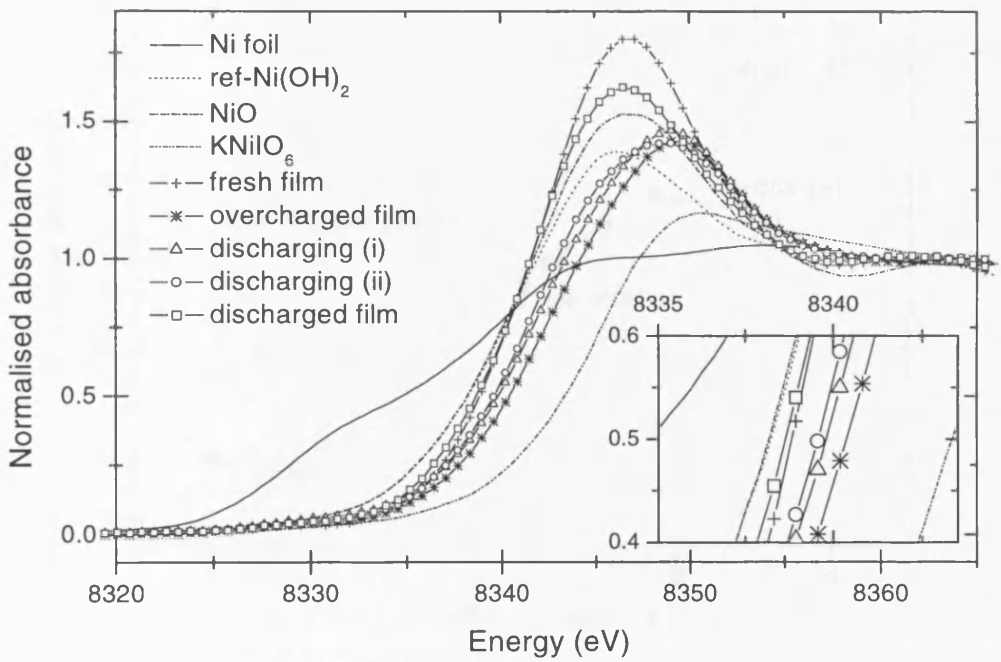

Figure 3.5: Normalised Ni K-edge XANES of reference materials, together with those of a nickel (hydr)oxide film at varying charge states.

between sample and Ni foil edge positions. The calibration curve is defined by a linear fit to the shift of reference Ni oxycompound edge position. The reference compounds have known oxidation states and these are assumed to have integer (formal) values. From the slope of this plot, an average edge shift of 1.8 eV per unit change in Ni valency is calculated, in agreement with previous work [55, 59, 60]. When fixed to the calibration curve, the edge shift of the freshly prepared film corresponds to a Ni valency of 2.2; by the same argument, overcharging increases the oxidation state to 2.9. The edge shift (and hence the valency of Ni) of the discharged film is the same as the fresh electrode, suggesting that nickel reverts to its original valency when the film is fully discharged. All edge shifts and derived valences are listed in tables 3.1 and 3.2.

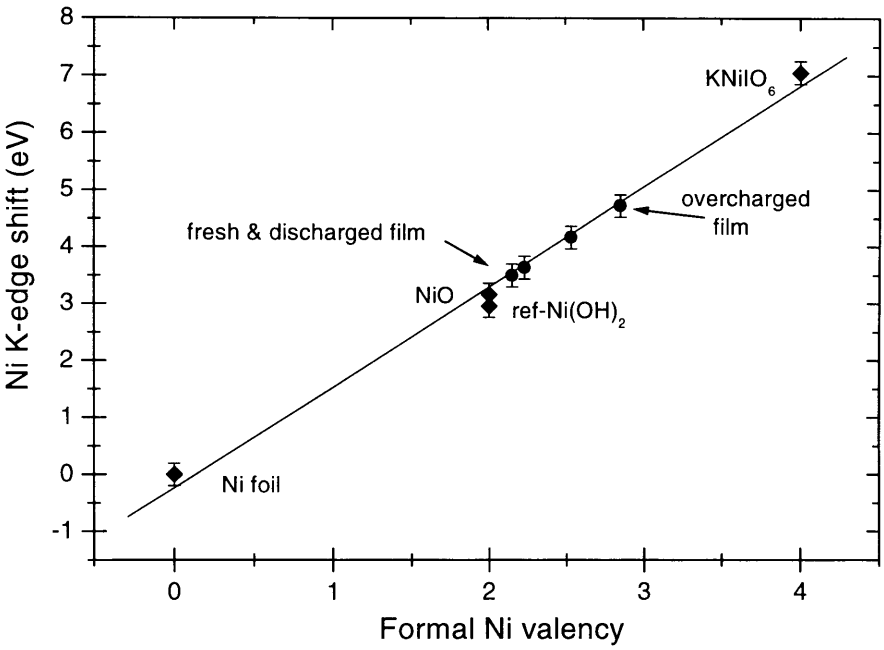

Figure 3.6: Calibration curve defined by a linear fit to Ni K-edge shifts of standards (diamonds) at various integer Ni valences. Edge shifts of film (dots) are aligned with calibration.

Typical fits to the EXAFS data from a standard and an electrode are shown together with their corresponding Fourier transforms (radial structure functions) in figure 3.7. The first Ni-O shell distances, derived from fits to EXAFS of the standards define the calibration curve in figure 3.8. These display the movement of first shell Ni-O atoms as Ni valency changes. As in fig. 3.6, a linear fit to bond lengths of the standards defined the calibration curve, onto which the weighted mean electrode bond lengths were applied (see eqn. 2.3 and section 2.2.5). The fresh electrode exhibits a single 6-coordinate bond length of 2.01 ± 0.01 Å (see table 3.3); when applied to the calibration curve, this bond length corresponds to a Ni valency of 2.5 (table 3.2). When overcharged, the first Ni-O shell becomes a distorted

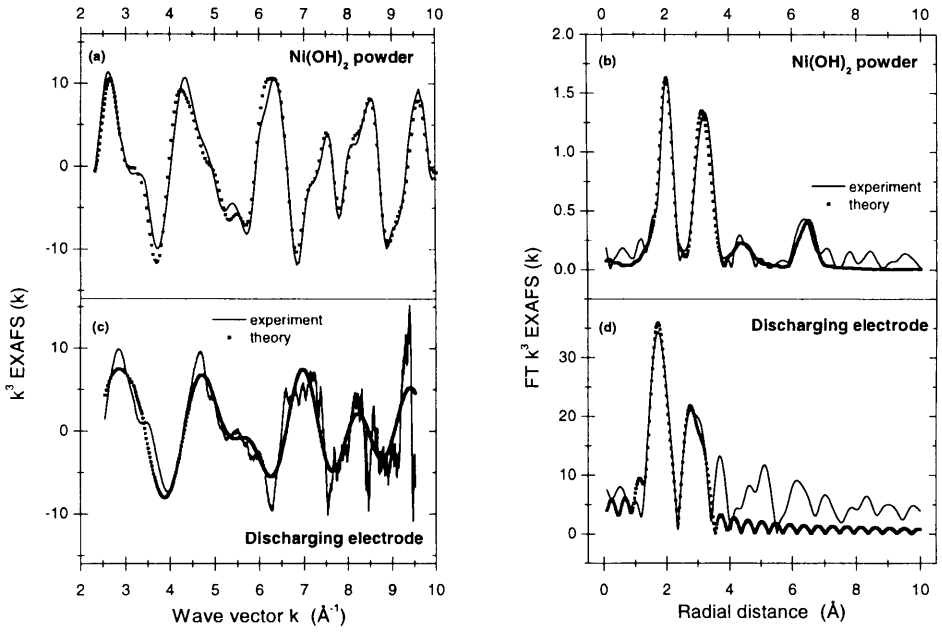

Figure 3.7: k^3 EXAFS with fits (a) & (c) and corresponding fitted Fourier transforms (b) & (d) for $Ni(OH)_2$ powder and the discharging electrode (1.5 C cm^{-2}, $Q = 12.8$ C), respectively.

octahedron, with 2 close O atoms at 1.73 ± 0.01 Å and 4 more distant atoms at 1.93 ± 0.01 Å, having a mean Ni-O distance of 1.86 ± 0.01 Å. This value corresponds to a Ni valency of 4.1. Such a 4-long, 2-short bond arrangement within a shell signifies a Jahn-Teller distortion of Ni-O octahedra [75]. The bond lengths derived from our *in situ* measurements demonstrate that this distortion was not permanent, but reversed progressively (as a function of charge) during the discharge process, eventually returning the Ni-O shell to its original regular octahedral configuration (within error) with 6 oxygens at 2.00 ± 0.01 Å. This implies a reversion to the initial valency, as suggested by the edge shifts. As the central Ni ions are not bonded to their Ni neighbours, their movement is not primarily affected by ionic charge. Therefore, the first Ni-Ni distance was not used to derive Ni valency.

The results derived from the bond lengths in fig. 3.8 reinforce the trends

Standards	Edge Shift (eV)	Ni Valency	Charge Density ($C\,cm^{-2}$)
Ni foil	0	0	–
ref-$Ni(OH)_2$	+2.96	2	–
NiO	+3.16	2	–
$KNiIO_6$	+7.05	4	–

Table 3.1: Information obtained from Ni K-edge XANES of standards.

expressed by the edge shifts in fig 3.6, demonstrating the link between Ni valency and charge density, as shown in fig. 3.9, which shows that the relationship is indeed approximately linear. This pivotal relationship confirms the link between the driving force (electrochemical charge) and film responses, in terms of Ni valency.

The effect of charge on first Ni-O and Ni-Ni distances is displayed in fig. 3.10. The effect of charge upon the first Ni-Ni shell is more complex than that described for the Ni-O shell. The first Ni-Ni shell of the fresh electrode is initially a distorted octahedral sphere with two Ni atoms at a distance of 3.04 ± 0.02 Å and 4 atoms at 3.59 ± 0.01 Å (table 3.4). When the film is overcharged, all of these Ni-Ni distances shorten: the atoms in this shell converge to produce regular octahedra with a single 6-coordinate bond length of 2.82 ± 0.01 Å. Both of these effects reverse during discharge. First, the octahedra distort: the two nearer atoms in the shell move increasingly closer to the central atom while the four others in the shell do not veer significantly from their overcharged position. When the two closer Ni atoms approach the Ni-O shell, a substantial shift in the position of the Ni-Ni shell occurs and a distorted shell, with two longer Ni-Ni distances of 2.99 ± 0.01 Å and four shorter distances at 3.56 ± 0.01 Å, results when the film is discharged. The Ni atoms do not quite return to their original positions, but as the distances differ by only 0.02 Å outside the error bars, it may be assumed

Electrode	Edge Shift (eV)	Ni Valency			Charge Density ($C\,cm^{-2}$)
		Derived from edge shift	Derived from electrode charge*	Derived from mean $R_{(Ni-O)}$	
fresh	+3.50	2.2	2.0	2.5	0
overcharged	+4.72	2.9	3.0	4.1	2.3
discharging (i)	+4.17	2.5	2.8	3.8	1.8
discharging (ii)	+3.64	2.2	2.7	3.3	1.5
discharged	+3.50	2.2	2.0	2.6	0

* Assuming a nominal initial valency of 2.0.

Table 3.2: Information obtained from Ni K-edge XANES, electrochemical measurements and EXAFS fits for nickel (hydr)oxide films.

that an effective reversion of structure occurs. This is the first time that such a complete description of oxygen and nickel movement in a discharging nickel (hydr)oxide film has been reported.

Figure 3.10 shows that distortion of Ni-O and Ni-Ni shells is dependent on electrode charge. Distortion of the first Ni-O shell is maximised at high charge, and the extent of distortion diminishes as discharge proceeds, shown by convergence of the two linear fits. The opposite trend is evident in the first Ni-Ni shell, with movement which seems to respond antagonistically to the Ni-O shell; the least distorted environment is induced when electrode charge is high, and the shell is highly distorted at low charges.

The experimental radial structure functions (FT EXAFS) and calculated radial distribution functions (RDFs, derived using the EXCURV97 fitting

Sample	R (Å)	Mean R (Å)	Ni-O N	$2\sigma^2$ (10^{-4} Å^2)	Fit Index (%)
Standards					
Ni foil	–	–	–	–	–
ref-$Ni(OH)_2$	2.05 ± 0.01	–	6.0 ± 0.4 (6)	130 ± 18	24.3
NiO	2.07 ± 0.01	–	4.5 ± 0.7 (6)	81 ± 32	28.2
$KNiIO_6$	1.87 ± 0.01	–	4.1 ± 0.3 (4)	63 ± 16	22.8
Electrode					
fresh	2.01 ± 0.01	–	6	89 ± 14	8.3
overcharged	1.73 ± 0.01	1.86 ± 0.01	2	121 ± 38	3.6
	1.93 ± 0.01		4	7 ± 13	
discharging (i)	1.84 ± 0.12	1.89 ± 0.05	2	208 ± 413	8.6
	1.91 ± 0.05		4	94 ± 67	
discharging (ii)	1.83 ± 0.02	1.94 ± 0.02	2	60 ± 63	10.4
	1.99 ± 0.03		4	340 ± 179	
discharged	2.00 ± 0.01	–	6	218 ± 21	7.9

Table 3.3: Structural parameters for first Ni-O shell, derived from fits to EXAFS of standards and nickel (hydr)oxide electrode. Coordination numbers shown in brackets are expected (literature-based) values (section 2.2.4). Uncertainties represent 95 % confidence levels.

Sample	R (Å)	Mean R (Å)	Ni-Ni N	$2\sigma^2$ (10^{-4} Å^2)	Fit Index (%)
Standards					
Ni foil	2.49 ± 0.01	–	9.9 ± 0.8 (12)	113 ± 10	25.2
ref-$Ni(OH)_2$	3.11 ± 0.01	–	6.5 ± 1.0 (6)	160 ± 22	24.3
NiO	2.94 ± 0.01	–	10.2 ± 1.1 (6)	113 ± 15	28.2
$KNiIO_6$	3.56 ± 0.01	–	0.7 ± 0.5 (0)	-24 ± 86	22.8
Electrode					
fresh	3.04 ± 0.02	3.41 ± 0.01	2	131 ± 42	8.3
	3.59 ± 0.01		4	142 ± 35	
overcharged	2.82 ± 0.01	–	6	145 ± 7	3.6
discharging (i)	2.67 ± 0.02	2.78 ± 0.01	2	40 ± 73	8.6
	2.84 ± 0.01		4	32 ± 40	
discharging (ii)	2.50 ± 0.09	2.71 ± 0.03	2	485 ± 278	10.4
	2.81 ± 0.01		4	189 ± 30	
discharged	2.99 ± 0.01	3.37 ± 0.01	2	132 ± 33	7.9
	3.56 ± 0.01		4	107 ± 22	

Table 3.4: Structural parameters for first Ni-Ni shell, derived from fits to EXAFS of standards and nickel (hydr)oxide electrode. Coordination numbers shown in brackets are expected (literature-based) values (section 2.2.4). Uncertainties represent 95 % confidence levels.

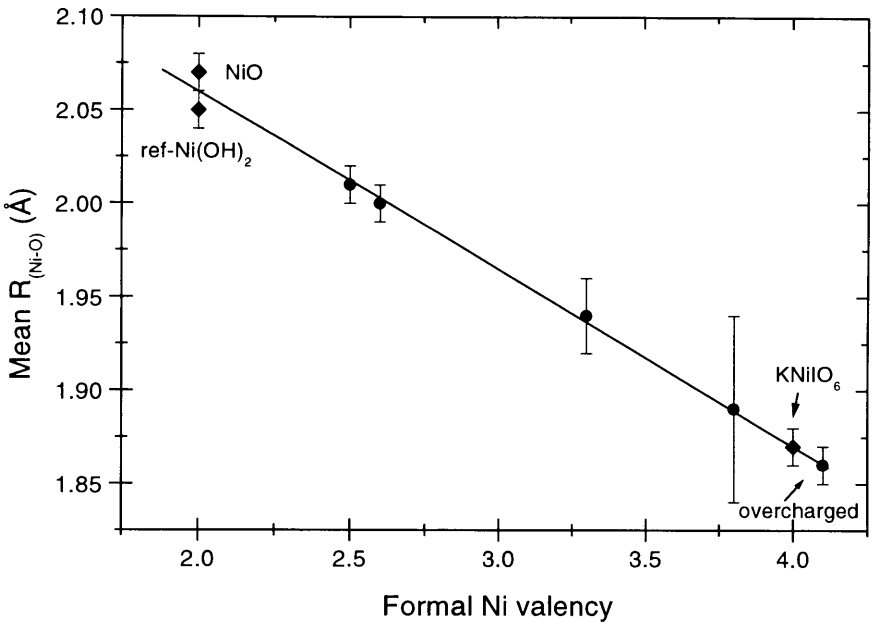

Figure 3.8: Calibration curve defined by linear fit to first Ni-O shell distance of standards (diamonds) at various integer Ni valences. Mean first Ni-O shell distance of discharging film (dots) are aligned with calibration.

program, section 2.2.4 [53]), shown in figures 3.11 and 3.12, respectively, illustrate further the movement of each shell with electrode charge. The way in which the first Ni-Ni distances converge and separate is particularly distinct in both figures. Both Ni-O and Ni-Ni coordination shells are discrete and fairly well defined at the end points of the fresh and overcharged films, but during discharge, the peaks overlap. This made it more difficult to distinguish between the presence of one *vs.* two distances per shell. The lack of data presented between 1.5 and 0 $\mathrm{C\,cm^{-2}}$, in all figures, resulted from the fact that either no significant structural (or other) changes occurred in this region or because the data could not be fitted satisfactorily, yielding no meaningful information.

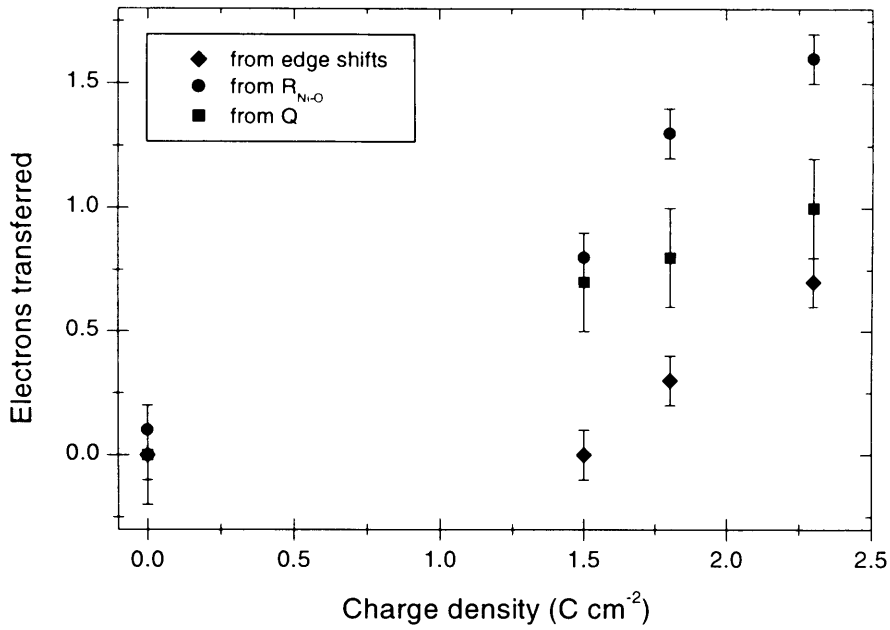

Figure 3.9: Number of electrons transferred at Ni sites, derived from 3 methods, as a function of charge density.

3.4.3 Cyclic Voltammetry and Electrode Ageing

Sets of both potentiostatic quEXAFS spectra recorded under potential control at the positive and negative voltammetric limits, and EDE spectra recorded under potentiodynamic conditions *during* cyclic voltammetry were essentially identical in both the XANES and fine structure regions. No changes in edge position were observed, and fitting these spectra always yielded the same structure as a fresh electrode (fig. 3.13). This situation also became evident when analysing data from films that were immersed in electrolyte for several hours (aged). No structural parameters changed significantly during any of these experiments (section 3.2.3). Therefore, ageing over the timescales of these experiments bore no notable influence upon the structural evolutions taking place during discharge and the effects of ageing are discounted in this study.

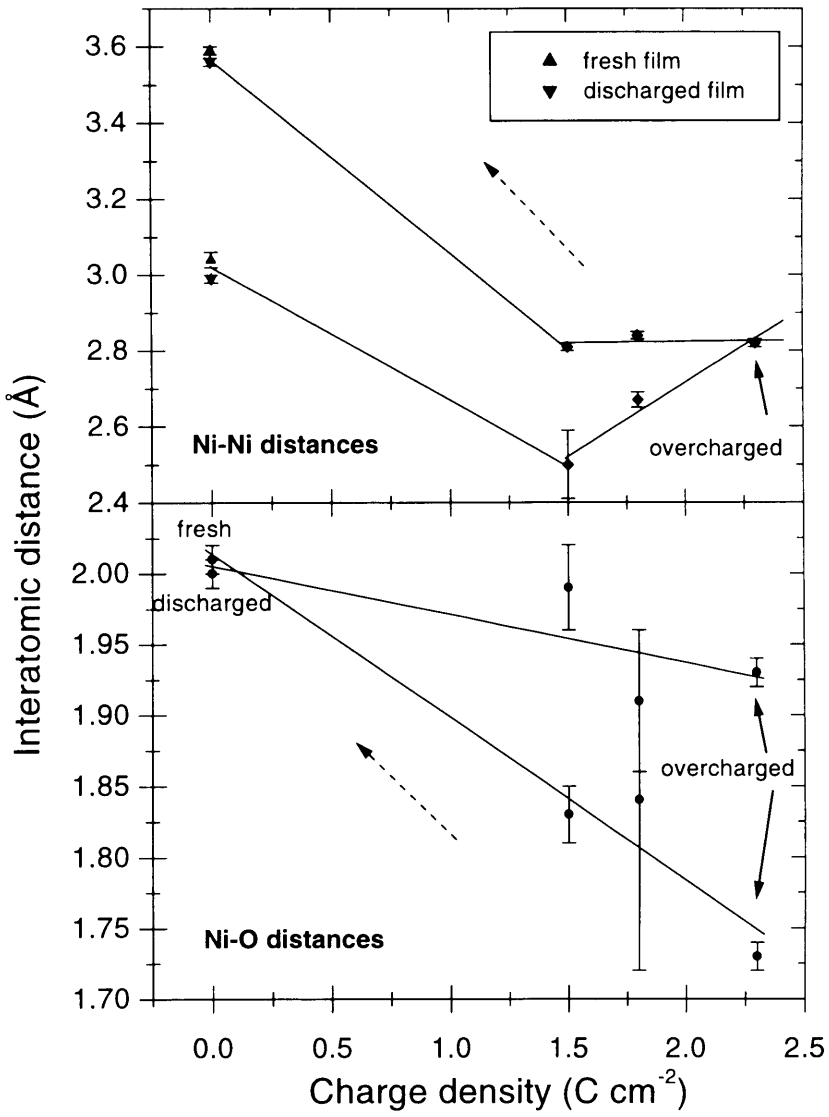

Figure 3.10: Variation of first Ni-O (dots) and Ni-Ni (squares and triangles) shell interatomic distances as a function of charge density. Linear fits emphasise splitting and convergence of distorted shells. Dotted arrows show the direction of discharge.

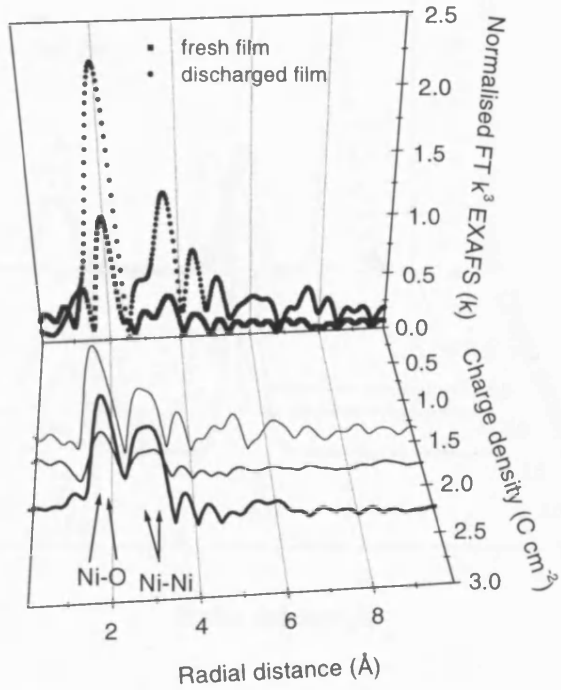

Figure 3.11: Experimental radial structure functions as a function of electrode charge density. Arrows emphasise movement of atoms within first Ni-O and Ni-Ni shells.

3.5 Discussion

3.5.1 Discharge of the Electrode

The evidence presented suggests that the situation regarding Ni valency in nickel (hydr)oxide film electrodes is rather more coherent than previously stated. When derived from both edge shifts and Ni-O bond lengths it is shown that, within experimental uncertainty, Ni valency lies between +2 and +3 in the fresh and discharged electrode, and is between +3 and +4 when the electrode is overcharged. These ranges are supported by the agreement of spectroelectrochemically and electrochemically derived values for film thickness, surface coverage and the number and concentration of Ni sites (for deposition and overcharge) for a one electron transfer at overcharge. The fractional number of electrons transferred (averaged, per Ni site) at various

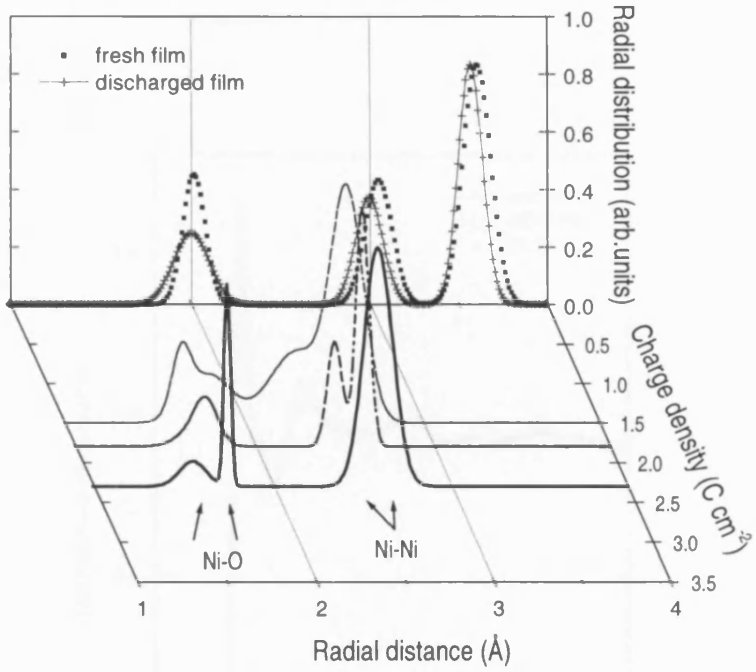

Figure 3.12: Radial distribution functions (calculated using the EXCURV97 program) as a function of electrode charge density. Arrows emphasise movement of atoms within first Ni-O and Ni-Ni shells.

stages during discharge was then calculated (see section 2.2.6, table 3.2 and fig. 3.9). Previous studies have given precise values for Ni valency, but such precision is misleading. This is because, although all the variables in fig. 3.9 are affected by the charge of the Ni ions, the nature of this dependence is not the same in each case (section 2.2.5), so the absolute valency cannot usually be pinpointed so accurately.

Figure 3.9 and table 3.2 imply that the change of derived valency between uncharged and overcharged electrodes, as extracted from bond length data, is 1.6. This is in agreement with other studies, but differs substantially from values of 0.7 and 1.0 derived from edge shifts and coulometric data, respectively. A lesser reliance should be placed on the valences derived from the bond lengths because their responses to ionic charge are secondary (section 2.2.5). Furthermore, the result depends on the structure of standards used to construct the calibration curve. The nature of this problem is

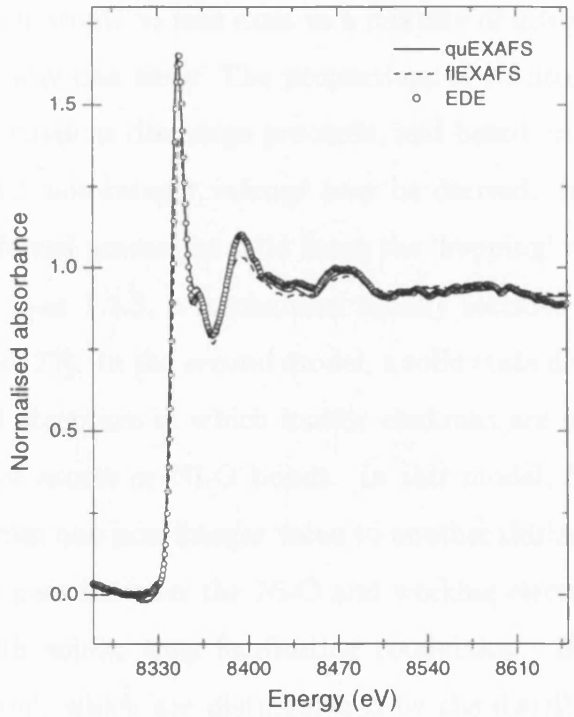

Figure 3.13: Overlaid quEXAFS, flEXAFS and EDE spectra for a fresh nickel (hydr)oxide electrode in the reduced state (Γ = 17.9 μmol cm^{-2}).

illustrated by $KNiIO_6$, which does not consist exclusively of Ni-O and Ni-Ni environments and, not having a Ni coordination number of 6, does not have the short range structure that is directly comparable to both the electrode and the other standards. Thus, valences (and changes therein) derived from bond lengths should only be used as a secondary guideline. On the other hand, edge shifts and coulometry are more direct measures of Ni charge (and changes thereof) and are structure insensitive. Thus they are more reliable sources of Ni valency changes.

In the introduction to this chapter two different approaches to the question of Ni valency and charge transport were introduced. These two models

are considered to explain "non-integer valency" in these results. In the first model, an essentially molecular model with independent bonds and localised electrons for each atom, Ni ions exist in a mixture of integer oxidation states (2, 3 and 4) at any one time. The proportions of Ni atoms present in each of these states varies as discharge proceeds, and based on these proportions, a weighted mean non-integer valency may be derived. In this model, electrons are transferred across the solid using the 'hopping' mechanism initially described in section 1.2.3, a mechanism usually ascribed to solids with low conductivity [26, 27]. In the second model, a solid state description, the solid has a full band structure in which mobile electrons are not associated with particular nickel atoms or Ni-O bonds. In this model, Ni valency changes progressively from one non-integer value to another during discharge as itinerant electrons pass between the Ni-O and working electrode valence bands throughout both solids, thus facilitating conduction. Both of these models are considered, which are distinguished by the distribution of electronic charge between the Ni atoms, but only one model will be supported by the data.

The first model would require evidence of a broad Ni K-edge which overlaps those of the Ni^{2+} and Ni^{4+} standards, implying the presence of several contributing oxidation states. The width of the broad edge would then change with the proportions of valence states as discharge proceeds. Also, from a structural point of view, if several Ni-O bond lengths are measured, Ni^{2+} and Ni^{4+} contributions must only arise from regular octahedra. In other words, no distorted shells should be identified for Ni^{2+} and Ni^{4+} contributions (although a distortion is likely for Ni^{3+} [75]). Each regular bond length would represent one integer oxidation state, and the number of bond lengths present would change with the proportions of oxidation states. This behaviour would be reflected in the Debye-Waller factors (represented by $2\sigma^2$, listed in tables 3.3 and 3.4), where $2\sigma^2$ is the sum of thermal and static (structural) contributions to the total disorder; but as the temperature was constant throughout

the experiment, it may be assumed that any variation in $2\sigma^2$ has a structural origin. A plot of $2\sigma^2$ *vs.* charge density would follow a parabolic form as the structure of numerous distinct Ni-O and Ni-Ni environments changed extensively, resulting in uneven movement and an increase in static disorder during discharge. The presence of a single structure/environment for each of the overcharged and discharged states would result in low $2\sigma^2$ at the end-points of the parabola.

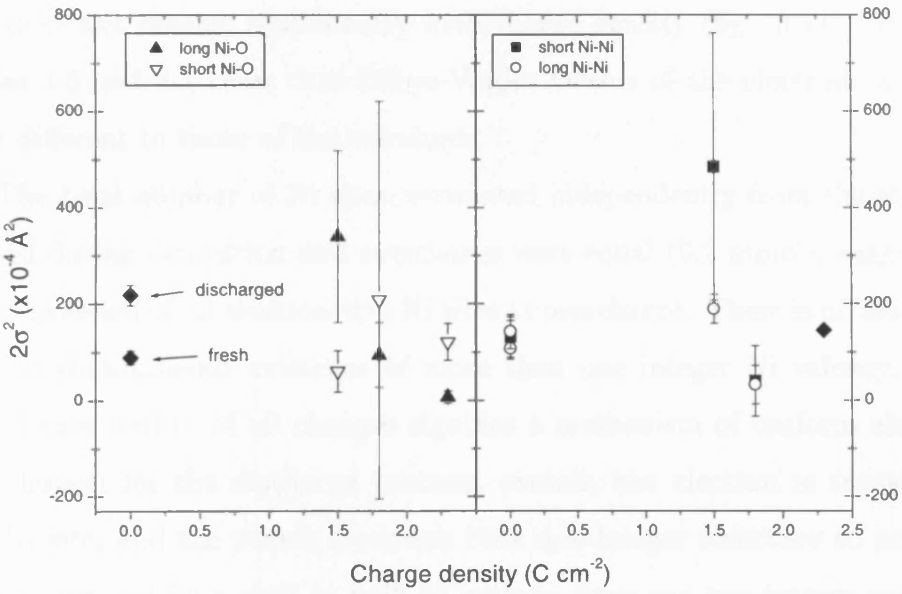

Figure 3.14: $2\sigma^2$, representing static disorder in the first Ni-O and Ni-Ni coordination shells, as a function of charge density during discharge. Diamonds represent undistorted shells.

Validation of the second model would be provided by a discrete (single) Ni K-edge that lay between those of the standards, with a position that changed gradually and smoothly as a function of electrode charge. With respect to structure, the presence of more than one bond length within a coordination shell would indicate bulk distortion and non-integer valency, as opposed to

distinct sites at a range of integer valences. Finally, the Debye-Waller factor would not vary as a function of charge density, as induced structural changes in this model would be more uniform and gradual, and thus would not add significantly to static disorder.

When comparing the characteristics of each model to the experimental data, the second model seems to fit the results in all respects. In fact, the distortion of the first Ni-O shell is consistent with a Jahn-Teller distortion available to low-spin d^7 compounds, the extent to which diminishes during discharge (fig. 3.10). The Ni K-edges have a discrete form (fig. 3.5), and $2\sigma^2$ does not change significantly with charge density (fig. 3.14). In fact, tables 3.3 and 3.4 show that Debye-Waller factors of the electrode are not very different to those of the standards.

The total number of Ni sites, estimated independently from the charges passed during deposition and overcharge were equal (0.2 mmol), suggesting full conversion of all electroactive Ni sites at overcharge. There is no evidence for the simultaneous existence of more than one integer Ni valency. The progressive nature of all changes signifies a mechanism of uniform electron distribution for the discharge process: overall, one electron is transferred per Ni site, and the switch from one bulk non-integer structure to another is accompanied by a shift in bulk Ni valency from one non-integer value to another. The model of a site-by-site, electron-by-electron discharge satisfies the quantum description for a conductor in the solid state. In this model, the Fermi level lies within the partially filled Ni-O valence band and mobile electrons move freely into the band during discharge. Figure 3.9 shows that there is an approximately linear relationship between the derived valency and charge density. Regardless of the functional form of these correlations, the unequal duration of overcharge and discharge indicates hysteresis (*i.e.* the reversal of structural changes was quicker than the time taken to implement them). The kinetic (or other) origins of these effects, are worthy of future study.

It is also evident that the white line intensity decreases when the film is overcharged (fig. 3.5), suggesting that the accessible empty hybridised Ni-O states in the conduction band have less (allowed) p-character with increasing Ni valency. This observation correlates with an increase in the availability of newly empty (forbidden) d-states that accompanies the oxidation of nickel ions. No structural conclusions were drawn from the coincidence of changes in white line intensity with distortion of Ni-O and Ni-Ni octahedra, or from the lack of pre-edge features, since the coordination shells remained octahedra upon overcharge and throughout discharge, and no extensive structural rearrangements required confirmation from these XANES features (see section 2.2.3). A more precise correlation of such distortion with electronic structure can only be achieved using another technique such as XPS. Also, *in situ* infrared (or Raman) spectroscopy would be useful to verify the symmetries of Ni-O and Ni-Ni octahedra (*i.e.* to confirm whether distorted shells have a tetragonal arrangement or another less symmetrical distorted octahedral configuration).

In summary, the previously unresolved structural mechanism for the discharge of electrochemically prepared nickel (hydr)oxide electrodes has been described, and connections between structure, Ni valency and electrode charge have been made. First shell Ni-O atoms separate on overcharge and result in distortion of the shell. Distorted first Ni-Ni shell distances converge and shorten on overcharge. Structural distortion and its reversal do not affect disorder significantly. Ni K-edge energy increases on overcharge. Ni valency increases from 2–3 to 3–4 when overcharged. All of these changes are dependent upon the charge on the electrode. Every one of these trends reverses *during* discharge. A correlation between short-range structure and the charge transfer properties of the Ni ions has also been given, adding credence to the concept of non-integer-valent nickel hydroxide films. X-ray absorption spectroscopy identifies the dominant structures over the sample cross-section; these have been presented. Further unequivocal structural or

electronic inferences cannot be made using the existing XANES and EXAFS data. It is also important to emphasise that these conclusions apply to thick electrochemically deposited films, prepared as described in section 3.2.2. The literature shows that films prepared under different conditions may not exhibit the characteristics described.

Now that it has been shown that nickel (hydr)oxide films essentially behave as solid state conductors, and that all induced structural and electrochemical changes are reversible, the optoelectronic technologist may note that no extra measures, apart from reducing the film thickness, are necessary to enhance the charge/discharge properties of the films. However, film density or morphology may require optimisation to improve the contrast ratio between coloured and bleached states (section 1.2.4) and to address the inequality in the duration of charge and discharge, both of which could remain issues even in thinner films.

3.5.2 Cyclic Voltammetry

The absence of significant detectable structural changes, even when the films charged during quEXAFS acquisition ($\sim$ 5 minutes per spectrum) leads to the important conclusion that a substantial build-up of charge (*i.e.* overcharge) is required to induce even slight structural alterations in films of this thickness. This behaviour is not caused by relatively low electrical conductivity, but by the films being many times thicker than electrochemically ideal, as the double-exchange mechanism of counter/co-ion diffusion and the transport of electrochemically-delivered charge throughout such a thick low-density oxide film will inevitably be slow. Also, once structural changes occur, they can only be maintained by the persistent injection of charge, so reversion (structural and electrochromic) occurs when the electrode discharges; this phenomenon is termed a poor memory effect (section 1.2.4). The observed memory effect is consistent with the fact that certain forms

of Jahn-Teller distortion to metal-ligand bonds are unstable [75], and the fact that discharge occurred so readily supports the evidence for a film of relatively high conductivity.

3.6 Conclusions

Detailed analysis of EXAFS data for nickel (hydr)oxide films does not provide support for the commonly held view of a mixture of distinct integer-valent Ni sites, each contributing to an overall (mean) non-integer valency. Instead, the EXAFS data suggest a more homogeneous model, in which the overall one electron transformation of each electroactive Ni site involves a progressive conversion of Ni valency, and the associated local structure, from one bulk condition to another. This is the quantum description for a conductor in the solid state. The dynamics and distribution of counter and co-ions (present to satisfy electroneutrality of the Ni sites during redox conversion) do not require the charge on individual Ni ions to be represented by integer values. Also, the lack of evidence for spectroscopically identifiable Ni^{2+} and Ni^{4+} sites in the electrode leads to the belief that the bulk valency of nickel sites (generally agreed to change according to a one electron transfer during (dis)charge of the film) may vary from a value between +3 to +4 at overcharge to one between +2 and +3 at discharge.

The instrumental capability for carrying out XAS on electrochemically modified films has been proven using the *in situ* spectroelectrochemical cell. Energy dispersive EXAFS was successfully applied to reveal the structural evolution taking place during electrode discharge, in real time. The results obtained have been used to clarify the connection between electrode charge, Ni valency, interatomic distance, distortion of coordination shells and structural disorder. In essence, from fitting these data it has been shown that Ni valency, and hence the bulk structural form adopted by nickel hydroxide films is dependent upon electrode charge. A mechanism for the full structural

behaviour of nickel (hydr)oxide electrodes will be achieved by extending this work to a real time study of overcharge; this would help to identify the onset of structural change, and therefore investigate the possibility of hysteresis with regard to the structural pathway for this evolution.

The results derived from spectra recorded in different configurations agree, and both spectroscopic and electrochemical results correlate. The understanding provided by this work will be beneficial to optoelectronic technology, whose main challenges include reproducing these structural changes over large working areas and stabilising high-valent nickel in nickel (hydr)oxide electrodes. These results, and any future developments thereof, may also prove useful to battery technology, whose use of nickel hydroxide electrodes is long established.

Chapter 4

The Niobium Oxide Electrode

Since the late 1980s, niobium oxides, and principally Nb_2O_5 have attracted great attention due to the catalytic activity of the hydrated form $Nb_2O_5 \cdot xH_2O$, (commonly termed niobic acid) for diverse liquid and gas phase dehydration, dehydrogenation and selective oxidation reactions. These include the dehydration of ethanol to ethene [76] (or the reverse hydration [77]), the esterification of ethanol with acetic acid [77, 78] and methanol oxidation [79] for application to pollution reduction and hydrocarbon conversion industries. The origins of the wide-ranging catalytic activity have been researched extensively and is attributed mainly to the protonic and Lewis (electron accepting/donating) acid/base properties of the hydrated surface oxide, where the pH varies greatly with surface coverage [80] (*i.e.* surface loading) or pretreatment temperature [77, 79], ranging from highly acidic ($\sim$ pH 1) at low coverage [80] or low pretreatment temperature ($< 100\,^{\circ}C$ [77]) where the oxide is a solid protonic acid, to moderately acidic ($\sim$ pH 5) at higher loadings [80, 81] or higher temperatures (200–300 °C [77, 80]). Many of these publications also assessed $Nb_2O_5 \cdot xH_2O$ activity as a function of temperature, showing that films calcined at temperatures $> 500\,^{\circ}C$ are inactivated due to the eradication of all traces of water and a consequent reduction of surface area.

The relevance of hydrated Nb_2O_5 to catalysis has stimulated a wealth of

structural investigations, most commonly using Raman and infrared spectroscopies [81, 82] and EXAFS, where the primary focus (where possible) has been the active surface region where the adsorption of reagents occurs. Structural assignments were made difficult by the amorphous structure of the active hydrated form [78], exemplified by its broad and weak Raman and IR bands [81], inevitably leading to confusion when seeking a definitive structure. In fact, it is stated that acidic catalytic activity persists as long as the hydrated oxide remains X-ray amorphous [79]. Despite the lack of agreement in the literature, it has been widely reported that mainly tetrahedral environments exist at the uppermost layer of the hydrated oxide surface [76, 78, 80, 82]. These differ markedly from bulk regions where oxygens occupy a predominantly octahedral arrangement, and it has been suggested that a 5-fold structure is present at the intermediate, sub-surface region [82], though even the tetrahedral surface structure has been disputed in favour of an octahedral configuration throughout [81]. Pre-edge XANES of the bulk oxide has been analysed to identify the presence of tetrahedral *vs.* octahedral coordination spheres (section 2.2.3) [76, 80, 83]. It is also generally accepted that each surface NbO_4 or NbO_6 unit contains a terminal Nb=O bond, which distorts these environments, and which is responsible for its strong Lewis acidity. Beyond this scant description, the overall picture becomes decidedly unclear.

In terms of EXAFS, there is little consensus in reported values of bond lengths and coordination numbers. On all accounts, analysis of EXAFS data has proven very difficult, but it is generally agreed that the Nb=O bond length in niobic acid is 1.73–1.91 Å and the Nb-O single bond ranges from 1.90–2.28 Å, depending on whether they constitute monomeric NbO_x species or Nb-O-Nb bridges in dimeric, oligomeric or polymeric structures. Nb-O distances can also vary if they are bridging O-Nb-reagent bonds, forming links to the support or to oxygen-containing reagent molecules [78, 83, 84]. Also, the number of oxygen neighbours is affected by coordination to water

or the adsorption of reagents during activity. To complicate matters further, the distortion of NbO_6 octahedra (*i.e.* the difference between single and double bond distances) increases as surface acidity decreases, *i.e.* with loss of water or increasing surface coverage [81]. Nb-Nb distances range from 2.95–3.68 Å, depending on the extent of the dimeric to polymeric network. Nb-Nb coordination numbers may change if monomeric units link during catalytic activity [76, 84] or after calcination [83], though the number of relatively distant Nb neighbours in this amorphous solid has proven difficult to evaluate with certainty.

To this point, the description has centred about amorphous, supported niobium oxide catalysts with low water content, ($Nb_2O_5 \cdot xH_2O$ or niobic acid) hereafter referred to as niobium oxide. The other major body of work, more relevant to this thesis, investigated niobium oxide for its electrochemical and electrochromic properties for which niobium oxide has functioned as a secondary electrode in electro-optic displays and energy efficient windows which reduce heating, cooling and lighting costs in large buildings (see section 1.2.4) [30]. Electrochromic Nb_2O_5 films have been prepared using a range of methods such as sputtering [29, 85, 86, 87, 88], thermal oxidation [89], chemical vapour deposition [90], anodisation [91] and the sol-gel process [28, 92, 93, 94, 95, 96, 97, 98, 99, 100, 101, 102], the technique used in this chapter. As with nickel (hydr)oxide, the diverse range of preparative conditions leads to numerous morphological variations, which in turn strongly influence the electro-optical properties of the films.

A variety of techniques has been used to assess electrochemical and electrochromic performance in terms of response times, colouration efficiency, diffusion coefficients and cycling durability (section 1.2.4). These include scanning electron microscopy [29, 97, 99, 101], UV-vis spectrophotometry [87, 93, 94, 97, 98, 99, 101, 102], IR spectroscopy [28, 92, 97], often in combination with electrochemical techniques such as cyclic voltammetry and chronoamperometry in operating conditions comparable to those of a working

electrochromic device. These studies have demonstrated far more agreement over the electro-optical properties of niobium oxide than with structural characterisation. This is because, regardless of preparation method or thickness, films pre-treated at temperatures $\leq 300\,^{\circ}\mathrm{C}$ are amorphous [28, 87, 92]. Amorphous niobium oxide films undergo reversible colouration from transparent when fresh or oxidised to dark brown during Li^+ insertion when electroreduced at cathodic potentials in non-aqueous lithiated electrolyte. Although many details of the electrochromic mechanism are still not fully understood, it is thought that equations 4.1 and 4.2 are most representative of the amorphous and crystalline systems [30, 34, 87, 89, 99, 101, 102], where the coloured form is commonly referred to as a 'niobium bronze'.

In terms of lithium exchange:

$$\underbrace{Nb_2O_5}_{\text{BLEACHED}} + xLi^+ + xe^- \underset{\text{ox}}{\overset{\text{red}}{\rightleftharpoons}} \underbrace{Li_xNb_2O_5}_{\text{COLOURED}} \tag{4.1}$$

or proton (de)intercalation:

$$\underbrace{Nb_2O_5}_{\text{BLEACHED}} + xH^+ + xe^- \underset{\text{ox}}{\overset{\text{red}}{\rightleftharpoons}} \underbrace{Nb_2O_{5-x}(OH)_x \quad \text{or} \quad H_xNb_2O_5}_{\text{COLOURED}} \tag{4.2}$$

In most publications, an aprotic, lithium-containing, non-aqueous electrolyte is preferred because the potential at which the onset of colouration occurs in protonic electrolyte (usually dilute H_2SO_4) coincides with the more favourable proton reduction process, resulting in hydrogen evolution ($2H^+ + 2e^- \rightleftharpoons H_2 \uparrow$, +0.24 V *vs.* SCE, see section 1.2.1). The oxidation of hydroxide ions may also act as a parasitic side-reaction during bleaching ($2OH^- \rightleftharpoons \frac{1}{2}O_2 \uparrow + H_2O + 2e^-$, +0.64 V *vs.* SCE). The unfortunate overlap of both Nb^{5+} and H^+ reduction potentials drastically reduces the colouration efficiency of the electrode (section 1.2.4) so that only about a seventh of the charge passed achieves a colour change [103]. Also, hydrogen and oxygen production is undesirable in most electrochemical reactions because bubble evolution causes the film (and the WE, if a metal film WE is used) to

crack and peel, affecting the overall durability of the electrode and eventually leading to electrode failure [101]. Furthermore, gas production is extremely undesirable in sealed electrochromic devices. Therefore, the exclusion of protonic solutes and water as a solvent is preferable. Nevertheless, water is a universal contaminant, since it is difficult to remove all traces at ambient conditions.

The mobility of the cationic counter ion should be high because the electrochemical reaction kinetics are controlled by the simultaneous exchange of ionic pairs (Li^+, e^-) to/from the film at opposite interfaces [91]. Accordingly, diffusion limits the colouration and bleaching times, which, as demonstrated for the $Ni(OH)_2$ electrode (section 3.5.2), are affected by film thickness. Despite the increase in colouration and bleaching times imposed by thick films (where diffusion lengths are greater), a trade-off between low response times and a large number of electrochromic centres must be achieved in ECDs.

Electrochromic activity is also affected by the conductivity of the oxide (section 1.2.3). It has been shown that niobium oxide is an extrinsic p-type semiconductor with a bandgap of 3.2–3.9 eV according to preparation method, where the most disordered films seem to have the widest bandgap [34, 85, 90]. Bandgap widening was reported to follow ion insertion into undoped Nb_2O_5 [34] (*i.e.* after the formation of $Li_xNb_2O_5$) implying that, notwithstanding other factors, structural changes and/or an increase in disorder take place upon formation of the lithiated oxide. Another effect of bandgap widening may be the incomplete reversal of colouration, which is repeatedly observed, exemplified by an integrated transmittance of $\sim 75\%$ for a bleached film [85, 87], which is ~ 10 % less than an as-deposited film in the UV-visible region [88]. Maček and co-authors [28, 92] reported an increase in conductivity, levelling of colouration and bleaching times and improved reversibility in thick sol-gel-derived films by pre-doping the sol precursor with Li^+ acceptor impurities, in the form of $LiCF_3SO_3$. An improvement in the conductivity of doped Nb_2O_5 films has also been reported by Rosario *et al.*

[104] and Hirai *et al.* [105]. This behaviour is consistent with *p*-type semiconduction.

At the beginning of this introduction, it was stated that dehydrated Nb_2O_5 demonstrated poor catalytic activity; in general, the literature shows that crystalline films, calcined at temperatures exceeding 500° C perform best electrochromically [29]. For instance, the optical modulation range (*i.e.* the difference in transmittance between coloured and bleached states) is wider than in unheated films [85, 87]. A more appealing colour change is displayed by crystalline films in the same electrolyte *i.e.* transparent $\leftrightarrow$ dark blue (instead of dark brown for the amorphous form); colouration efficiency is better, and stability and durability are greatly improved by heat-treatment [86, 92]. SEM studies indicate that heat-treated films have a denser, less porous structure than amorphous films, but this does not appear to adversely affect ionic mobility [29], which is affected by thickness [34]. A possible reason for the improved performance of calcined films is the absence of water, which diminishes the niobium oxide redox reaction.

The structure of electrochemically-modified films have been analysed using IR and Raman [105, 106] spectroscopies, and changes to the oxidation state of Nb were often monitored using XPS [34, 90, 99, 102]. X-ray diffraction was frequently used to distinguish amorphous from crystalline forms [29, 28, 87, 88, 92, 93, 94, 97, 98, 99], but EXAFS investigations have not to our knowledge been published to provide direct evaluation of short-range structural parameters of electroactive films. Existing (IR and Raman) structural studies have provided information regarding morphology and bonding within niobium oxide films. For instance, it was stated that the vibrational modes representing Nb-O, Nb-O-Nb and Nb_3O units in the fully-developed oxy-polymer network, present in both calcined films and niobium oxide powders, cannot be identified in unheated and relatively low-temperature films [28]. It was also suggested that a modification, in which the double bond character of Nb^{4+}-O increases, occurs upon colouration, as evidenced by a

blue frequency shift of the Nb-O band. This change reverses upon anodic polarisation [92]. Both IR and Raman studies concluded that the formation of the NbO_6 octahedral network is unaffected by the introduction of metal ion impurities as dopants to improve conductivity [105]. This assertion implies that the foreign cations occupy interstitial positions. The only other EXAFS studies (apart from catalytically-motivated works) have investigated the formation of Nb_2O_5 prior to and following the sol-to-gel transformation. By virtue of its name, the sol-gel process implies extensive rheological changes; these motivated the work described in this chapter.

4.1 The Sol-Gel Process

Sol-gel chemistry is based on inorganic polycondensation reactions and in this case, the method involves the controlled hydrolysis of a high purity niobium alkoxide (niobium ethoxide $Nb(OC_2H_5)_5$, shortened to $Nb(OEt)_5$). The method has the advantages of control of porosity and microstructure, good chemical and mechanical stability and the ability to coat objects of any size or shape with adherent, homogeneous films. An added advantage of the process is convenience; preparation is without the use of specialised instruments such as a vacuum chamber. The goal of sol-gel processing is to control the morphology of materials during the earliest stages of production to yield materials of very high purity and homogeneity with minimised processing temperatures and times.

Over the past two decades, much effort has been given to the development and application of alkoxide sol-gel processes [107, 108]. The rheological properties of sols and gels make these processes well-suited to the synthesis of thin films and fibres by techniques such as spin-drawing and dip-coating. The sol-gel process has already been used extensively by industry for the fabrication of ceramics and coatings for glass *e.g.* anti-reflective layers on spectacles or conductive layers on glass for optoelectronic applications, where

controlled chemical composition, purity and homogeneity are very important [109]. More recently, there has been interest in the sol-gel synthesis of transition metal oxide films for electrochromic devices. The method has already been employed successfully in the synthesis of Nb_2O_5, V_2O_5, TiO_2, WO_3 and $Ni(OH)_2$ films for various optoelectronic applications [30].

$$\begin{aligned}
\text{Uncontrolled hydrolysis:} \quad & 2Nb(OEt)_5 + 5\,H_2O \longrightarrow Nb_2O_5 + 10\,H_2O \\
\text{Controlled hydrolysis:} \quad & Nb(OEt)_5 + H_2O \xrightarrow{\text{EtOH}} Nb(OEt)_4OH + EtOH \\
\text{Condensation:} \quad & Nb(OEt)_4OH + Nb(OEt)_5 \longrightarrow Nb_2O(OEt)_8 + EtOH \\
\text{Polycondensation:} \quad & \text{Various condensation reactions} \xrightarrow[\text{catalyst}]{\text{HCl}} Nb_2O_5 + xEtOH
\end{aligned} \tag{4.3}$$

Transition metal alkoxides are very reactive with water (hydrolysis), and the presence of water in such alkoxide solutions leads to precipitates that are not suitable for the production of thin oxide films and fibres. Sols and gels must therefore be stabilised in order to prevent the bulk precipitation of inhomogeneous oxide. One way to control hydrolysis is to use an alcohol as the main solvent, instead of water. The alcohol decouples hydrolysis and condensation reactions, hence preventing bulk precipitation and promoting the formation of homogeneous sols and gels via alcholysis. Hydrolysis and condensation reactions occur at numerous sites in the solution and when sufficient interconnection of metal-oxygen bonds occurs in a mixture, they exist as a colloidal dispersion of sub-micron particles or a sol. A gel is formed by the interconnection of an extensive three-dimensional metal-oxygen network via the simultaneous hydrolysis, condensation and polycondensation of the sol. An increase in the cross-linking of metal-oxygen bonds initiates the structural evolution of colloidal particles, resulting in the formation of a homogeneous inorganic polymer network through aggregation, which causes gelation [100, 109].

The main chemical steps involved in the sol-gel conversion of niobium oxide are given in the schematic equation 4.3 [99]. EtOH represents ethanol which remains in the pores of the film during hydrolysis, and is expelled from the structure toward the final stages of (poly)condensation (gelation). A gel is a continuous, interconnected, 'solid' skeletal framework with liquid-filled pores (≤ 1 μm across) and polymeric chains (average length ≥ 1 μm). All gels have viscoelastic properties due to the continuity of the solid and liquid phases. The point of gelation is typified by a *sharp* increase in viscosity, from a free-flowing viscous liquid to a solid material, perhaps eventually rigid and elastic, whilst retaining homogeneity and usually an unchanged appearance. The precise evaluation of the point of gelation can therefore be difficult.

EXAFS studies by Vandenborre *et al.* [95, 96] have revealed that oxygen coordination around first shell Nb atoms is almost the same in the sol precursor as in the gel *i.e.* distorted octahedra with four short and two long Nb-O bonds, which provide the links between environments in the network of edge-sharing dimeric octahedra with an Nb-Nb separation of $\sim$ 3.14 Å. The only identifiable difference between sol and gel was the presence of a second Nb neighbour at $\sim$ 3.75 Å after hydrolysis and gelation, which was initiated by the introduction of water. This was said to signify the coordination of one corner-sharing octahedron, in addition to the existing edge-sharing dimeric network (fig. ??). Also, an increase in disorder was reported after gelation; this diminished upon thermal treatment. Once gelation has taken place, no further structural modifications occur. It was also found that gels possess a rather open structure and that dried gels have a polymeric rather than a crystalline lattice form. Another structural study used ^{1}H and ^{13}C NMR and infrared spectroscopy of the ethoxide, sol and gels dried at various temperatures [110]. By assessing the placement of the organic functional groups at each of these stages, the study essentially confirmed the reactions shown in equation 4.3.

The description of niobium oxide gelation given here is incomplete, and

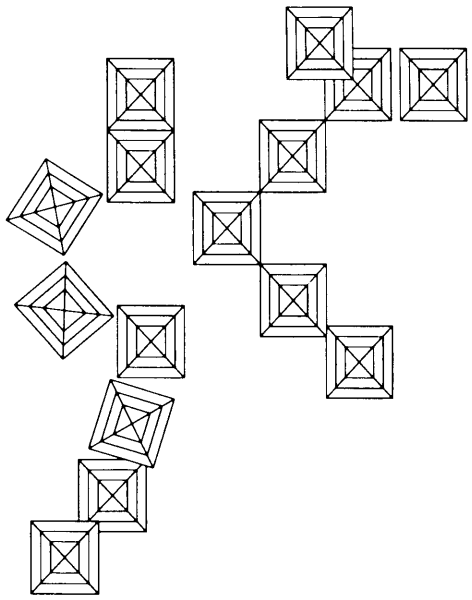

Figure 4.1: Schematic diagram of edge and corner-sharing octahedra in a Nb_2O_5 gel.

the boundary between each stage is blurred due to the lack of dynamic *in situ* investigations. The prime objective of this study is to complete the description by producing precise rheological and structural models for the sol-gel conversion. This was achieved by measuring changes to viscoelasticity and short-range structure.

4.2 Objectives

From a structural point of view, niobium oxide is one of the least studied sol-gel systems. This situation is probably a result of its amorphous form. Despite the anticipated difficulties with assigning structures for the sol-gel transformation of niobium oxide, the inherent rheological development provided a good starting point from which to build a detailed rheological and structural description of the phase transition.

As stated in section 4.1, the entire sol-gel process occurs with little change

in appearance and its duration is affected by a variety of factors, making crystal impedance an ideal diagnostic technique to monitor the progress of gelation, since changes in the position and shape of admittance *vs.* frequency curves (section 1.3.2 and figure 1.24) identify the rheological development taking place. In a quantitative sense, equivalent circuit parameters and shear moduli provide precise information regarding the changing viscoelastic characteristics of the film (section 1.3.2). Crystal impedance has already been used to monitor sol-gel conversions and electropolymerisation reactions of other systems [48, 49]. The use of crystal impedance for the former purpose on niobium oxide films is completely novel.

The theory of gelation (especially with respect to silica) is well documented [109], and it is known that the microstructure of a material becomes set at the point of gelation. Since the physical properties of the material can be manipulated up to the point of gelation, its identification and the conditions affecting its occurrence are vital knowledge to industries seeking to control the structure for specific applications. Previously, the gelation point of sol-gel materials was difficult to predict, monitor and identify [109]. The relatively new crystal impedance technique is a perfectly suited and novel approach to deriving the gelation point of niobium oxide films as rheological changes appear to be the greatest indication of the onset of gelation [49].

In addition to deriving the gelation point from rheology and viscoelastic parameters, a structural characterisation of the material at this point and throughout the full sol-gel transformation are a major goal of this work. *In situ*, time-resolved energy dispersive EXAFS is a prime candidate for making such structural determinations. For instance, the technique can reveal whether a sudden increase in Nb-Nb coordination, an abrupt change in structural disorder or the cessation of structural changes signify the point of gelation. This is yet another new and dynamic application of energy dispersive EXAFS, as previous studies have only derived structures before and after gelation.

The short-range structures of gelled electrochemically-modified niobium oxide films have been neglected in the literature. X-ray diffraction has shown that a lattice expansion occurs upon lithium insertion, which accompanies the reduction of niobium ions [34], and it is generally known that bond lengths respond to changes in oxidation state. As with the nickel hydroxide electrode, changes in structure and valency imposed by electrochemical manipulations such as cyclic voltammetry, overcharge and discharge will be derived using *in situ* X-ray absorption spectroscopy.

In summary, two major techniques are used to monitor the rheological and structural evolutions taking place during the sol-to-gel transformation: The dynamic crystal impedance technique is used to measure rheological changes via qualitative and quantitative routes, by means of admittance curves and equivalent circuits, respectively. X-ray absorption spectroscopy is used to determine structural changes affecting XANES and/or EXAFS regions of spectra *during* sol-gel conversion. In particular, the quEXAFS, flEXAFS and fast energy dispersive modes record this data *in situ*. Once gelation is complete, XAS is performed in conjunction with common electrochemical manipulations to identify electrochemically-induced modifications to structure and valency, which coincide with electrochromic action.

4.3 Experimental

Most of the X-ray and electrochemical techniques used in this chapter are standard, so their use was essentially as described in chapter 2, with the exception of the quEXAFS and energy dispersive modes, which are outlined in section 3.2.3 parts *i* and *ii*, respectively. The crystal impedance technique and associated analyses were only used for the niobium oxide system, so a thorough description of the method will be given in this chapter. The equipment and procedures utilised for the preparation of the films were also unique to this system *e.g.* gelation conditions and the spectroelectrochemi-

cal cell; these will also be detailed in full. Finally, before proceeding, it may be useful to note that this experimental section is structured in an approximately chronological sequence in order to convey the logical progression of experiments.

4.3.1 Preparation of NbO_x Sols

The synthesis described here is based on procedures reported by Ohtani *et al.* [93] and Maček *et al.* [28, 92]. Acid-catalysed, lithium-doped NbO_x sols were prepared using niobium ethoxide ($Nb(OEt)_5$, 99.95 %, Aldrich) as the main precursor. It is well known that $Nb(OEt)_5$ is very reactive, primarily with moisture; it was therefore treated with extreme care and its use was restricted to a sealed, dry, steel glove box flushed with dry cylinder N_2 (BOC Gases). Also, as described in equation 4.3, the amount of water present in the sol itself had to be controlled to prevent bulk precipitation of the oxide. Every piece of equipment was thoroughly cleaned in an ultrasonic bath and dried in an oven before use. Cleanliness was vital for items re-used to make several batches of sol because traces of sol would gel and precipitate when the items were removed from the dry box. These crystals proved very difficult to remove, and if the equipment was not completely clean, the subsequent batch of sol was contaminated by the introduction of a nucleation site from which oxide particles would crystallise, rapidly spoiling the sol. The stock supply of spectroscopic grade ethanol (EtOH, 99.5 %, 0.4 % H_2O, Aldrich) was stored overnight with oven-dried molecular sieves prior to use. Also, the glove box was evacuated using a diaphragm pump before flushing with nitrogen.

In the dry box, 4.67 mL of ethanol was pipetted into a large glass sample tube. 250 μL of niobium ethoxide was added using a Gilson micropipette. The tube was sealed to prevent spillage, then the mixture was swirled and cooled over in insulated flask of liquid nitrogen (to prevent condensation of water on the outside surface before transferral to the dry box). 0.03 g of

lithium triflate ($LiCF_3SO_3$, 99.995 %, Aldrich) was added to the cooled mixture; 40 μL of HCl (12 M, Fluka) was then added in a dropwise manner, swirling the tube after every drop. A small magnetic bead was placed inside the tube, which was stoppered with a tight-fitting rubber Suba seal, sealed with parafilm and removed from the glove box. The mixture was stirred overnight at room temperature using a magnetic stirrer to yield a 4.96 mL batch of clear, homogeneous and slightly yellow sol, containing 0.2 M $Nb(OEt)_5$ and a Li/Nb molar ratio of 0.1 [92].

4.3.2 Preparation of Quartz Crystals

A highly polished 10 MHz quartz crystal (roughness < 1 μm, International Crystal Manufacturing Co Ltd, Oklahoma City, OK, USA) coated with an adhesion layer of (3-mercaptopropyl)trimethoxy silane (98 %, Aldrich) [111], with evaporated gold electrodes (fig. 1.19), was mounted onto an upturned glass cell (fig. 4.2) by applying a small amount of silicone sealant (Farnell, Dow-Corning 3145 RTV MIL-A silastic adhesive) around the rim of the cell's aperture. The crystal was carefully placed on the aperture and tapped gently into place, making sure that neither glue or fingerprints came into contact with the exposed gold electrodes. Care was also taken to ensure that air bubbles were not caught within the seal between the glass and the quartz. The cell was left overnight for the sealant to cure at room temperature. After this, the cell with attached QCM was ready to use for crystal impedance experiments.

4.3.3 Crystal Impedance Measurements

A crystal impedance experiment was performed to determine an approximate timescale for the sol-to-gel conversion, in particular the point of gelation. This information was necessary for planning the subsequent series of EXAFS experiments.

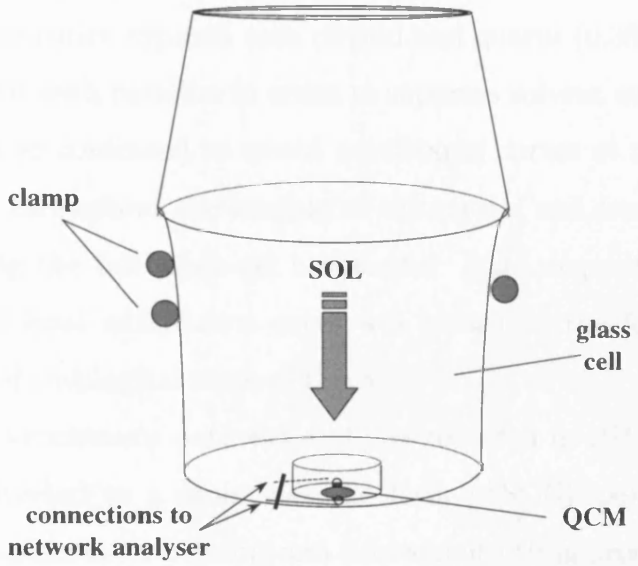

Figure 4.2: Glass cell for conducting crystal impedance experiments.

The cell was clamped into position, as shown in figure 4.2. Crystal impedance measurements were made using a Hewlett Packard HP8751A frequency response analyser (network analyser) in reflectance mode, connected to a HP8512A transmission/reflection unit via 50 Ω coaxial cables. The bare, unloaded crystal (with a piezoelectrically active area of 0.21 cm^2), was oscillated at its first harmonic resonant frequency (fig. 1.20) by the application of a voltage with controlled amplitude. For that particular cut of quartz, the resonant frequency of the bare crystal was always close to 10 MHz. The voltage output (reflected signal) was then recorded and the admittance (and impedance) of the system was calculated from the ratio of the incident and reflected voltages (both magnitude and phase). Thus the admittance *vs.* frequency curve of the bare, unloaded crystal was recorded.

A dry nitrogen-filled balloon, attached to a syringe was then pierced through the suba seal of the sample tube of sol. This enabled the extraction of 0.03 mL of the sol, using a glass syringe, whilst preserving the sealed inert atmosphere within the sample tube. The sol was quickly dropped onto the

inside surface of the QCM (fig. 4.2). The flow was centred so that sol evenly spread over the entire exposed area of gold and quartz (0.38 cm^2). The cell was then sealed with parafilm in order to suppress solvent evaporation. The network analyser continued to record admittance curves at regular intervals of 30 seconds throughout the loading of the crystal and for the following 6 hours, tracking the full sol-to-gel conversion. Data acquisition was halted overnight; the final admittance curve was measured the following day to record the final rheological state of the film.

All of the admittance data was initially recorded in HP basic; the data was then converted to a more versatile form (ASCII) using a conversion program, in readiness for plotting and subsequent fitting procedures (section 4.4). Finally, a preliminary qualitative analysis was undertaken to derive an approximate gelation point from which to plan the duration of EXAFS experiments. The admittance *vs.* frequency curves were plotted as a function of time in order to observe an abrupt change in their shape; this was taken to signify the point of gelation (section 4.1). From this analysis, a conservative approximation of the gelation point was 90 minutes.

4.3.4 Dual *in situ* Spectroelectrochemical / Gelation Cell

A cell was designed primarily to facilitate the simultaneous *in situ* operation of X-ray absorption spectroscopy and electrochemistry in non-aqueous electrolyte. The cell described in section 3.2.1 was not suitable for this purpose because its major components (*i.e.* the front and back plates) were constructed from perspex, which cracks when in contact with many organic solvents. This new cell conforms with all of the design criteria detailed in section 2.1.3. This cell served an added function of allowing most of the sol-gel process to be monitored *in situ* using X-ray absorption spectroscopy.

The main features of this design are similar to those displayed by the

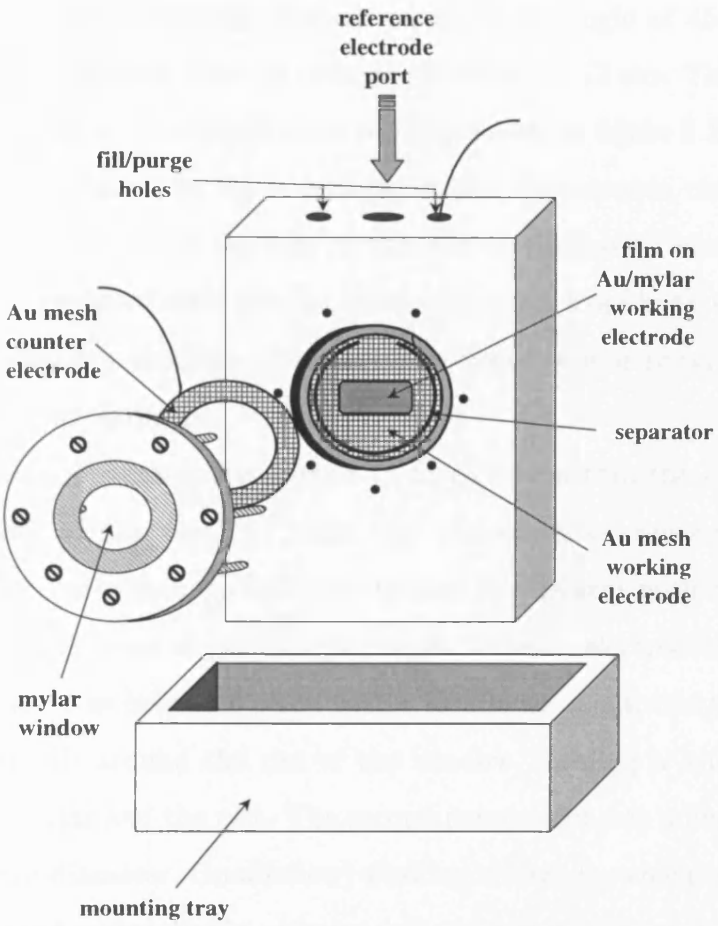

Figure 4.3: Exploded back-to-front view of *in situ* X-ray absorption spectroelectrochemical cell.

nickel hydroxide cell. For instance, its sloping windows facilitate operation in both transmission and fluorescence modes, without the need for realignment. The cell may also be used in the energy dispersive mode for the rapid acquisition of time-resolved spectra. This thin-layer X-ray absorption spectroelectrochemical cell (fig. 4.3) consists of a PTFE block (8 x 5 x 1.6 cm^3) with a central cylindrical cavity (3.5 cm diameter, 0.8 cm depth) that housed loose components such as electrodes, windows and gaskets. A hole passing through the full depth of the cell provided the window openings through

which the beam traversed the cell. From the front view (not visible on figure 4.3), the window opening slanted inward at an angle of 45 °, tapering toward the window hole from an outside diameter of 3.2 cm. This feature is a circular version of the slanted front window shown in figure 3.1, which also enabled dual operation in the transmission and fluorescence modes. Three channels, which led from the top of the cell to the cavity accommodated the elongated probe of the reference electrode, wires from both working and counter electrodes and inlets through which electrolyte or purging N_2 could be introduced via syringes.

The cell components were shaped to fit tightly within the cavity of the assembled cell. From front to back, the first of these components was a mylar window (area 9 cm^2, 0.25 mm thick, Goodfellow) with a $\sim$ 2000 Å thick evaporated layer of gold on its inside surface (electroactive area 6.2 cm^2). This disc was held into place with a thin layer of silicone grease (Dow-Corning, Farnell) around the rim of the window, forming a leak-proof seal between the mylar and the cell. The second component was a fine gold mesh (0.06 mm wire diameter, Goodfellow) working electrode, which connected to the gold-covered mylar disc in order to deliver an even current density across the thick, large area film held between the gold layers. The only break in this mesh was a letterbox-shaped hole, which was necessary as the mesh would have obstructed the passage of the beam through the cell. Gold wire (0.5 mm diameter, Goodfellow), that encircled both outer and 'letterbox' edges of the mesh, provided a good contact to the window/WE and prevented the delicate mesh from fraying with repeated use. This wire led out of the cell via one of the aforementioned channels. The next feature was a silicone o-ring (RS Components) with a small section cut out to avoid blocking the reference electrode channel. This o-ring separated working and reference electrodes and acted as a gasket to create a cavity for containing the electrolyte. A filter paper spacer (not shown in figure 4.3) lay against the o-ring to prevent contact between working and counter electrodes. The counter electrode was

a ring of gold mesh, again edged with gold wire; this wire also extended through one of the drilled channels. A silicone gasket (1 mm thick, cut from sheets, BDH/Merck) protected the counter electrode during compression of the main cell cavity to form a seal. Compression was achieved by gradually pushing in the detachable back window of the cell using a ring of plastic screws. The back window was constructed from PTFE and the window hole (2.2 cm diameter) was wider than that in the front window (as featured in the nickel hydroxide cell) to reduce scatter of the outgoing, divergent beam. Another common feature with the previous cell was a sloping back window opening, which allowed the fluorescent mode beam to exit without clipping the window edges.

The projecting wires were sleeved to ensure effective sealing of the channels through which they passed. The reference electrode port was sealed with a rubber gasket. An electrolyte volume of about 1 mL was contained within the cell cavity, with a thin-layer width of $\sim$ 4 mm, once fully compressed. The assembled cell slotted neatly into a PTFE mounting tray and was held rigidly in place using a pair of long plastic screws (not shown in figure 4.3). The mounting tray was attached to an L-shaped metal bracket, which remained fixed to the sample stage. These allowed the cell to be removed and replaced precisely to its previous position. With practice, the total assembly time was approximately 10 minutes. A duplicate cell was constructed so that experiments could be staggered over long timescales *i.e.* a film could be left to gel in one cell for several hours in preparation for an electrochemical experiment while the other cell was being used for *in situ* XAS.

4.3.5 EXAFS Measurements

i) Standard Transmission EXAFS

Standard transmission experiments generally followed the format outlined in section 2.1.4*i*. Three stable, high purity, powdered niobium oxycom-

pounds, with varying Nb oxidation states, were used as reference samples: NbO (99.9 %, Aldrich), NbO_2 (Aldrich) and Nb_2O_5 (99.99 %, Aldrich). These reference samples were prepared as stated in section 2.1.2. Each of the three ion chambers was filled with the appropriate Ar-Kr-He mixture for measuring the Nb K-edge. Absorption spectra of a 15 μm thick niobium foil and the three reference compounds were recorded on station 9.2 at Daresbury, at the Nb K-edge (18986 eV) utilising a Si(220) double crystal monochromator, recording as a function of angle, with a step size of ~1 mdeg in the pre-edge and XANES regions, and in k-space, with a step size of 0.05 $Å^{-1}$ in the EXAFS region, totalling about 20 minutes per spectrum. The EXAFS of these spectra ranged from about 3 to 15 $Å^{-1}$.

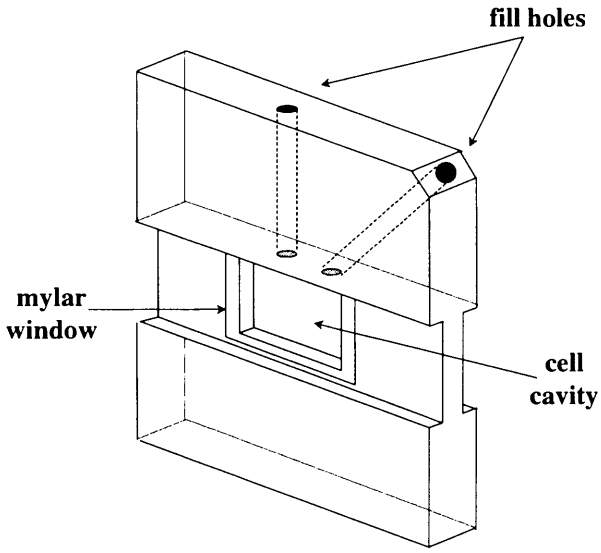

Figure 4.4: Plastic cell for EXAFS measurements of sol.

XAS spectra of the sol were also recorded in the standard transmission mode. The sol was contained in a sealed plastic cell, commonly used to hold liquid samples (fig. 4.4). This cell had mylar windows attached with silicone sealant. The cavity of the cell was 1 mm thick and contained 0.7 mL of sol. The original beam width of 1 cm was reduced by a few millimetres to give adequate clearance to the beam at the edges of the window (10 x

7 mm^2). After an initial series of 5 spectra, the seal on the fill holes was removed and one spectrum was recorded every 15 minutes for the next three hours. It was thought that opening the cell would have introduced enough moisture to initiate gelation. However, the fill holes were small, reducing the exposed area of sol; this may have been advantageous in slowing the rate of hydrolysis to a timescale more compatible with transmission measurements. These measurements were made in order to account for slowly-developing changes occurring during the early stages of the sol-gel process. Also, in order to take full advantage of the low noise level offered by this configuration (resulting from relatively long acquisition times), the gelation of a partially gelled niobium oxide film was monitored over 6.5 hours. A longer version of this experiment was performed in the energy dispersive mode, so a more detailed description of the procedure is given the following part.

ii) Energy Dispersive EXAFS

The samples used for these X-ray absorption measurements were essentially scaled-up versions of those used during crystal impedance experiments; this is because a greater sample area was required by XAS. In order to achieve an equivalent film thickness on a larger scale, the same ratio of electrode area to sol volume used for crystal impedance (CI) experiments was applied here (*i.e.* $A_{(\mathrm{CI})} = 0.38$ cm^2 and $V_{(\mathrm{CI})} = 0.03$ mL, so $x_{(\mathrm{CI})} = 0.08$ cm; $A_{(\mathrm{EXAFS})} = 9$ cm^2 and $V_{(\mathrm{EXAFS})} = 0.7$ mL, so $x_{(\mathrm{EXAFS})} = 0.08$ cm). First, an upturned gold-covered mylar disc WE, placed horizontally onto the sample mount of a Cammax Precima spin coater, was held in place by the suction provided by a diaphragm pump. 0.7 mL of lithiated, acid-catalysed sol was extracted from the sample tube using a 1 mL syringe, as described in section 4.3.3. The sol was then quickly deposited onto the disc. A large beaker was placed over the sample in order to recreate the sealed, humidified environment of the QCM cell (fig. 4.2), and the film was left to gel partially for 15–20 minutes; this is the main difference between the crystal impedance and

EXAFS experiments. Slight solidification of the film was necessary for it to be adherent enough for placement in a vertical position for energy dispersive EXAFS. However, it was shown in part *i* that the initial stages of gelation were indeed monitored in transmission mode. After about 15 minutes, the reasonably solid, even, gel-like, translucent film was placed into the spectro-electrochemical cell, which was assembled without the other electrodes and other components to save time (< 5 minutes). The duration for initial solidification and cell assembly was well within the approximate gelation time of an equivalent film, which was 90 minutes (derived in section 4.3.3). The electrode channels were sealed using parafilm and the cell was fixed to its mounting tray on the sample stage.

Energy dispersive spectra were recorded on station 9.3 at Daresbury Laboratory, using the instrumentation detailed in section 3.2.3*iii*. A 15 μm thick Nb foil was used to calibrate the energy scale between experiments. A summed set of 5(5000 x 2.5 ms) scans comprised each raw spectrum (5000 x 2.5 ms per scan, 5 scans per spectrum), totalling an acquisition time of under 2 minutes per spectrum, including dead-time. A shorter integration time was necessary for these measurements, compared to the nickel hydroxide scans, because the photon energy was greater; any longer than 2.5 ms saturated the detector. The energy range of the white beam was typically about 18800 to 20000 eV, resulting in EXAFS that ranged from about 3 to 13 Å^{-1}. One spectrum was recorded approximately every 2 minutes for the first 2 hours, then at increasing intervals for the next 8 hours. This sequence of measurements provided time-resolved coverage of the sol-to-gel transformation and any subsequent changes associated with ageing of the gelled film. This relatively fast technique was especially suited to recording the abrupt changes associated with the point of gelation. The complete sol-to-gel conversion was therefore monitored by recording good quality XAS spectra in both energy dispersive and standard transmission modes.

After over 8 hours, the film was assumed to have gelled; that film was then used for electrochemical experiments. All of the electrodes and other

components were arranged in the cell and the cavity was filled with a degassed solution of 0.1 M lithium perchlorate ($LiClO_4$, > 99%, Fluka) in anhydrous propylene carbonate (99.7 %, Aldrich). All potentials stated in this chapter are given with respect to a saturated calomel electrode (SCE). The film was overcharged at the negative limit of its CV *i.e.* at -1.2 V for 1 hour, during which the current increased slowly toward zero. The film was then discharged at the positive CV limit of +0.5 V. EDE spectra were taken throughout both overcharge and the subsequent discharge in order to record similar changes to Nb environments and valency to those displayed by the nickel hydroxide electrode.

iii) Quick and Fluorescence EXAFS

No colour change was observed during the one hour overcharge undertaken for energy dispersive measurements, so overcharge was repeated over a longer timescale and spectra were recorded using the quick-scanning transmission mode (quEXAFS). The acquisition time for quEXAFS was longer than EDE, at 5 minutes per spectrum. As with standard transmission measurements, quEXAFS spectra were also recorded on beamline 9.2 at Daresbury. Previously gelled films (over 3 hours old) were overcharged at various negative potentials *i.e.* -1.5, -1.2 and -0.5 V *vs.* SCE for several hours, inducing colour changes (observed by eye). The films were then discharged at either +0.5 or 0 V. QuEXAFS spectra were recorded continually in order to monitor the structural evolution accompanying the reduction of niobium ions that was signalled by the colour change. Prior experience of combined *in situ* EXAFS and cyclic voltammetry of nickel hydroxide films (section 3.5.2) diminished expectations of structural changes within a voltammetric cycle. As a result, experiments such as those described in section 3.2.3ii, where the potential was held (for spectral acquisition) at several points around a CV, were not attempted for this system. Instead, spectra were recorded while films were repeatedly cycled between either lower limits of -1.5, -1.2 and -0.5

V and upper limits of +0.5 and 0 V at various scan rates for several hours, in order to investigate the structural implications of the poor cycling durability often reported for amorphous films without heat treatment.

The fluorescence mode, being more sensitive than transmission, was used to record *in situ* spectra of similar electrochemically-modified samples for comparative reasons. Also, fluorescence measurements were necessary when monitoring thin electrochemically-modified films (deposited from 0.35 mL of sol). Thin films were used in order to increase the likelihood of reducing all Nb ions present. All fluorescence spectra were recorded in the dual transmission/fluorescence mode (with the additional monitor spectrum).

An experiment, in which a film was overcharged for over 12 hours, was also performed, inducing a deep colour change. *Ex situ* fluorescence spectra of this and other highly coloured films were measured to maximise the signal from the film and minimise background absorption by the dense, viscous electrolyte. The electrolyte-damp films (still attached to their Au/mylar WEs) were removed from the cell and sandwiched between mylar discs; the edges were sealed with sellotape to preserve the damp environment, and each film was positioned in a sample clamp so that the beam impinged on the darkest region of the film. It was thought that the identification of slight structural changes in amorphous samples was likely to be difficult, so the beam was directed at the region most obviously affected by electrochemical reduction. The fifteen minute long fluorescence spectra were also recorded on station 9.2, making use of a Canberra multi-element solid state detector. Each series of fluorescence spectra was punctuated by the measurement of short 2 minute transmission spectra recording the XANES region only, specifically for the precise identification of edge shifts, which could be confirmed by the Nb foil calibrant and the third ion chamber. Therefore, these samples were always placed in the dual transmission/fluorescence position.

4.4 Data Analysis

4.4.1 Analysis of XAS Spectra

Spectra of the reference compounds, Nb foil and niobium oxide films were calibrated, background subtracted and normalised using the standard procedures detailed in section 2.2. Energy dispersive spectra were calibrated using the Daresbury program Proc15. When possible, successive spectra from an otherwise static sample were summed to improve the signal-to-noise ratio. As usual, the absorption edges of all spectra (apart from Nb foil) were normalised to half way up the first post-edge oscillation (*i.e.* to the top of the edge, excluding the white line). As the metal foil has no appreciable white line, these were normalised to the apex of the absorption edge. Edge positions of both samples and monitors (recorded simultaneously with most sample spectra) were then determined from the energy corresponding precisely to a normalised absorbance of 0.5 (section 2.2.3). Edge shifts (sample edge minus corresponding monitor edge) were then calculated to account for errors caused by slippage of the monochromator stepper motors. This correction was achieved by subtracting the edge position of the corresponding monitor spectrum from that of the sample, as detailed in section 2.2.3. The use of each spectrum's corresponding monitor was vital to the accurate determination of edge shifts because successive monitors were always in slightly different positions (usually $\pm$ 0.1 eV).

All of the data for this system was collected over four 2 or 3 day sessions, spread over five months; an additional energy correction was therefore necessary to enable the comparison of normalised spectra recorded on different beamlines or sessions (see section 2.2.3). The energy difference between the position of a monitor and the principal reference Nb foil (measured in the standard transmission mode as a reference sample), was added/subtracted from the energy scale of the monitor's corresponding sample spectrum, so that the sample edge corresponded to aligned foil edges. This adjustment

ensured that figures such as 4.12 and 4.13 portrayed true edge positions and shifts, regardless of the station, beam position or experimental configuration.

Daresbury's EXCURV98 program was then used to fit the spectra. During data fitting, the EXAFS from films was truncated at $k_{max} = 13$ Å^{-1} because the EXAFS oscillations produced by most samples (even some standards) ceased relatively soon after the XANES. As a result, the far EXAFS region ($\geq$ 400 eV past the edge) of film spectra (especially thin films) were dominated by noise when k^3 weighting was applied. Instead, only k^2 weighting was appropriate for these spectra. Such a lack of fine structure is usually displayed by materials that are amorphous beyond the closest coordination shells. Consequently, only the first two Nb-O and Nb-Nb distances (up to 2 split shells, <4 Å) could be reliably fit. Extracted coordination numbers having errors greater than the fitted value were considered insignificant, so the fit was repeated without inclusion of that shell. Fits to many combinations of distorted and regular shells, with varying coordination numbers were attempted for each spectrum. Only the best fits, with the lowest fit index, and more importantly the most physically sound structures are presented in section 4.5. Also, once certain shells were deemed significant, the coordination numbers from *ex situ* dual quEXAFS/flEXAFS spectra of thin films were set to integer values to aid reproducibility of fitting because the signal-to-noise ratio of single spectra was relatively low (as with the nickel hydroxide system, section 3.3).

4.4.2 Analysis of Admittance Data

A simple qualitative analysis of the admittance *vs.* frequency curves (section 1.3.3), measured during the niobium oxide sol-gel process, was outlined in section 4.3.3, and will be expanded in the Results section. As stated in section 1.3.2, quantitative analysis of the admittance data enables the evaluation of both equivalent circuit and physical parameters, which provide information

about the rheological state of the film.

Referring to the equivalent circuit model shown in section 1.3.4, the first of the unknown circuit elements (relating to the film) are its resistance R_x and inductance L_x. These were evaluated computationally using the iterative program Newqcm [45], which separated and modelled real and imaginary contributions to the complex electrical load impedance of the crystal with an attached layer Z_E (eqn. 1.28). This procedure modelled the circuit elements pertaining to the film *i.e.* R_x and L_x (equations 1.34, 1.35 and 1.37), so the contributions made by the bare, unloaded crystal *i.e.* R_0, L_0 and C_0, recorded during the initial stages of data acquisition, were subtracted from Z_E. These values were also used to calculate the electrical load impedance of the bare crystal Z_{E0}, which relates to the measured admittance via Z_E in equations 1.28 and 1.31. The data from each consecutive admittance curve was modelled in this way, so the energy loss and mass change characteristics (via R_x and L_x, respectively) throughout the full sol-gel transformation were plotted as a function of time, thereby mapping the changing rheological behaviour of the film.

As with all fitting programs, the difference between experimental and reconstructed data was minimised. For the purpose of extracting these equivalent circuit parameters, the rheological nature of the film *i.e.* the value of $_x$ (*i.e.* the type of film, see pages 43–44) was irrelevant, only the distinction between the layer and the quartz was important. The classification of the film type was the purpose of the next stage in data analysis.

The layer type was determined using another iterative program, written by H. Bandey called Ascii14 or Miracle [45]. This program modelled values for the physical parameters appropriate to the type of layer(s). These physical quantities constitute the surface mechanical impedance of the layer, Z_x, which contributes to the measured admittance via equations 1.30, 1.28 and 1.31. For example, figure 1.21 shows that the relevant parameter for a single finite ideal mass layer is its areal density m_1, the product of its thickness x_1

and density ρ_1 (equation 1.33). When the model considered consists of an ideal mass layer plus a semi-infinite Newtonian fluid (fig. 1.22), the thickness of the liquid layer is unimportant, but the areal density of the 'solid' layer, together with the density and viscosity of the fluid (ρ_2 and η_2, respectively) are fitted (eqn. 1.36). For the model consisting of an ideal mass layer plus a finite viscoelastic film, again the areal mass of the ideal mass layer and the density, thickness and shear moduli (both storage, G' and loss, G'') of the viscoelastic overlayer are extractable quantities (equations 1.38 to 1.41). It follows that the thickness of any 'semi-infinite' layer is not measurable.

Several permutations to the kind of model applied were permitted, *i.e.* finite and semi-infinite versions of up to three types of layer, in series, within one model. A particular model was chosen and the phase and amplitude of the admittance data was reconstructed according to the appropriate terms for that model. If the model chosen was incorrect, no convergence of experiment and theory was achieved. Only fits displaying the lowest fitting error after 5000 iterations are presented in the Results section.

4.5 Results

4.5.1 Characterisation of Niobium Oxide Films

The shape and peak position of *in situ* cyclic voltammograms (fig. 4.5), recorded during XAS experiments were highly characteristic of the well-documented $Nb^{5+} \rightleftharpoons Nb^{4+}$ redox conversion of amorphous Nb_2O_5 in $LiClO_4$/propylene carbonate electrolyte. Distortion of *in situ* CVs, as a result of non-ideal film thickness and electrode placement was slight; this demonstrates the success of the electrode configuration in this cell design. Only a pale reversible colour change was observed during a voltammetric cycle, but prolonged cathodic charging (overcharge) for over 90 minutes ($Q \geq$ 3.0 C) resulted in colouration where the film appeared dark brown, almost

black. This colouration did not reverse upon discharge (at an anodic potential), but persisted for over 12 hours, even when the film was removed from the electrolyte. Features characterising the CVs became less distinct and the overall charge within each CV fell slightly with each successive cycle, implying poor short-term cycling durability, frequently reported for amorphous films [93].

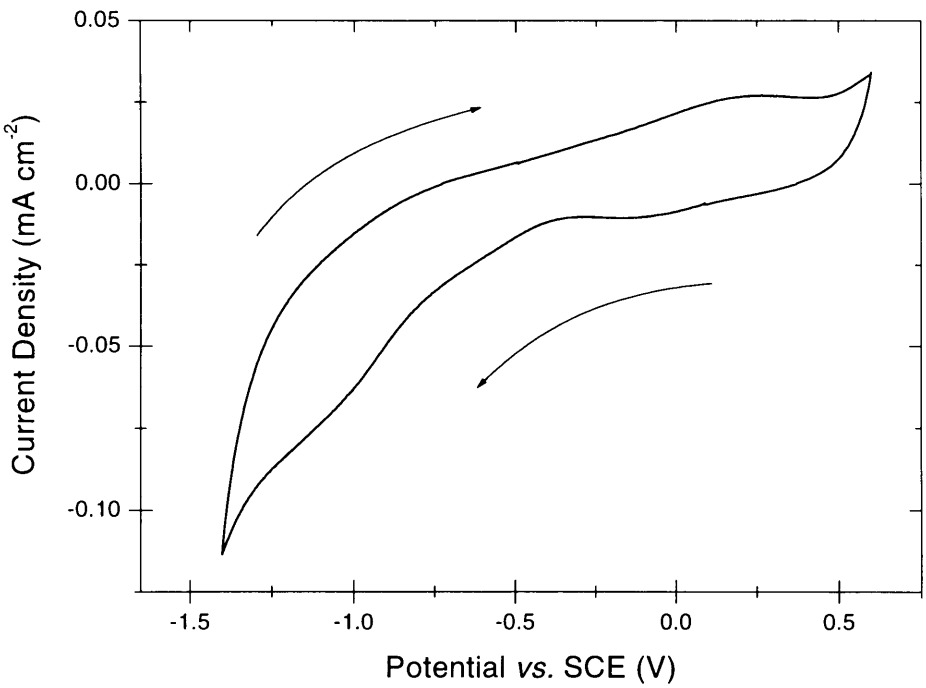

Figure 4.5: Typical cyclic voltammogram of a gelled niobium oxide film (on Au/mylar substrate) exposed to 0.1 M $LiClO_4$ in propylene carbonate. Potential scan rate 20 mV s^{-1}.

Figure 4.5 shows that typical cyclic voltammograms display a characteristically asymmetric form, in which the magnitude and position of the cathodic peak are not matched by the anodic feature. This asymmetry resulted from the unfortunate reduction of traces of water, as mentioned on page 115. Moisture could not be eliminated from the films as its introduction was essential to initiate gelation. Consequently, any residual water would have been

reduced alongside niobium ions. Following gelation, it was not possible to eliminate moisture from the films by heat treatment because the mylar substrate could not withstand the high temperatures necessary for calcination. Also, such electrochemically thick films (necessary to produce a good edge step) would have cracked and fragmented at high temperatures. In any case, electrochemical and X-ray investigations resulted from the viscoelastic study, which took place at room temperature, so a viable comparison of samples could not be made if some were heat treated.

The calculated Nb edge step for a 15 μm thick Nb foil ($\Delta\mu = 1.0$, equation 1.21), where $\Delta\sigma = 6.8 \times 10^3$ cm^2 mol^{-1} [7] and $C = 0.1$ mol cm^{-3}, resulted in an edge step that was consistent with the observed edge steps of Nb foil monitors measured in transmission modes (standard and quick, $\Delta\mu \simeq 1.3$). For the reasons stated in section 2.2.6, this calculation was unsuccessful when applied to foils measured in the energy dispersive mode, so no further edge step calculations were attempted using EDE spectra. With respect to gelled niobium oxide films, with transmission edge steps of $\ln\left(\frac{I_0}{I_t}\right) = 0.2$ (figure 4.6a), film thickness could not be calculated using the cathodic charge passed during a voltammetric cycle (equation 1.21) because only a fraction of the available sites were reduced during a cycle, either due to the thickness of the film (as with nickel hydroxide) or to parasitic side reactions. The calculation was attempted using the cathodic charge passed during the 90 minute overcharge of a film at -1.5 V ($Q = 3.0$ C, $\Gamma = 5.0$ μmol cm^{-3}), which resulted in a deep colour change (implying the redox conversion of at least a significant proportion of available Nb sites). This calculation also was unsuccessful *i.e.* calculated and measured edge steps were not consistent, probably because all of the charge passed is not attributable to the reduction of Nb ions; therefore, no further characterisation of the films using electrochemically-derived terms such as Q or Γ will be made.

Instead, the thickness of a gelled niobium oxide film was estimated by assuming its density of niobium sites is half way between that of the sol and the

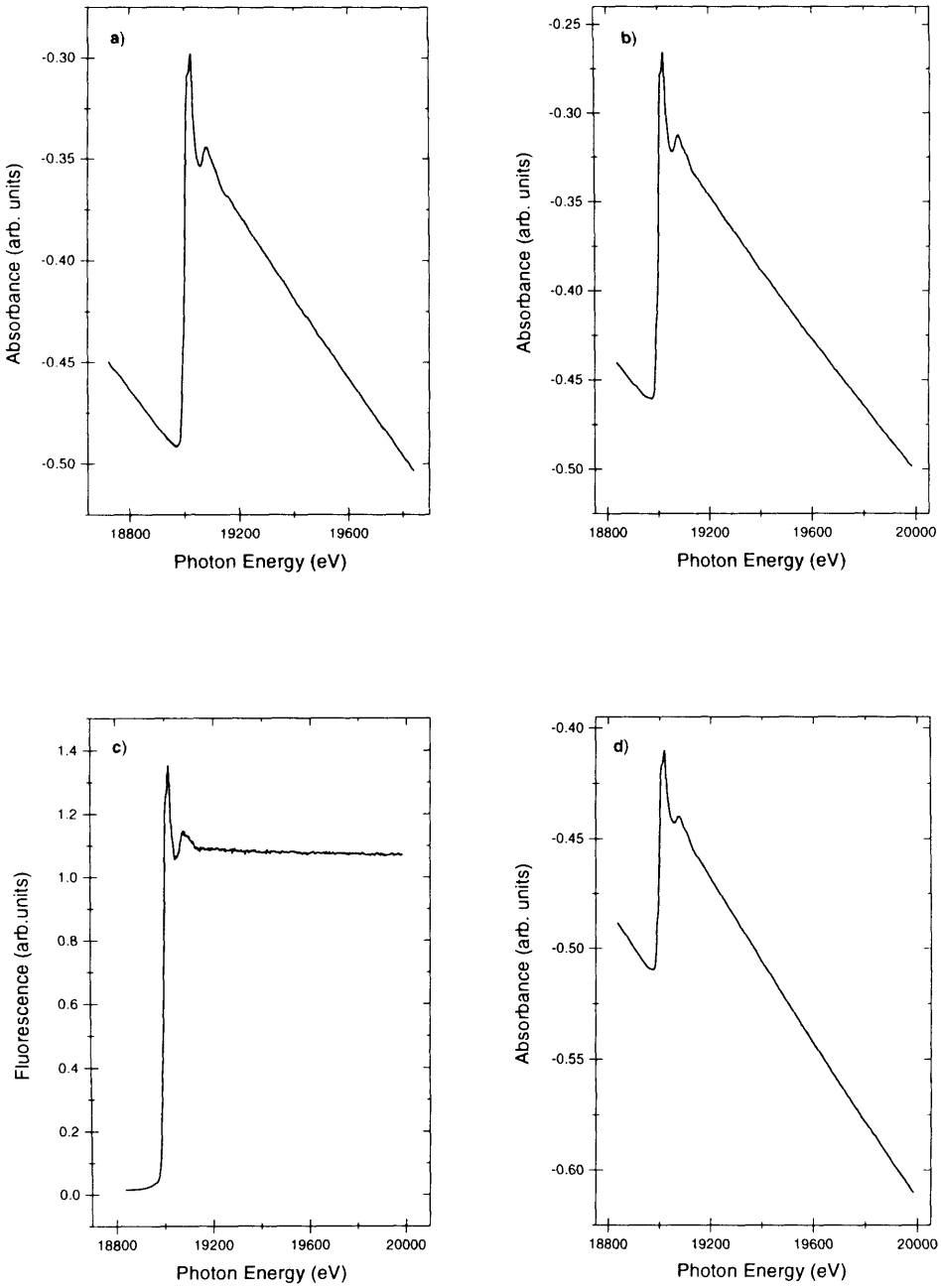

Figure 4.6: Raw a) Standard transmission, b) quEXAFS, c) flEXAFS (dual quEXAFS/flEXAFS mode) and d) corresponding quEXAFS (dual mode) spectra of typical (a, b) and thin (c, d) gelled niobium oxide films.

crystalline solid. Using equation 1.21, the measured edge step ($\Delta\mu = 0.3$) and the known sample thickness of the sol in the solution cell (1 mm) were used to calculate the concentration of Nb sites in the sol ($C = 4.4 \times 10^{-4}$ mol cm^{-3}). Using the relative atomic mass of Nb, a Nb density of 0.04 g cm^{-3} was calculated. The density of Nb_2O_5 powder is 4.5 g cm^{-3}, with a Nb density of 3.2 g cm^{-3}, so a partial density of 1.6 g cm^{-3} was derived for the gel. Using equation 1.21, where $C = 0.02$ mol cm^{-3} and the measured edge step was $\Delta\mu = 0.2$, a film thickness of $x = 14.7$ μm was calculated. This thickness must be equivalent to x_x for the crystal impedance experiment because the same area-to-volume ratio of sol was applied to both experiments, but the thickness quoted on page 132 is about 50 times greater than this estimate. The discrepancy arises from the fact that the thickness calculated using the edge step accounts solely for the amount of niobium present in the film, whereas the values given on page 132 were calculated using the total volume of sol applied to the QCM/mylar disc. This factor accounts for the discrepancy between thickness values. These calculations compensate for the lack of reliable data from electrochemical measurements.

4.5.2 Monitoring the Sol-Gel Conversion of Niobium Oxide Films using Crystal Impedance

As explained in section 4.3, the conversion of a layer of sol to a gel and perhaps a rigid solid was monitored using both crystal impedance, focussing on rheological changes, and EXAFS, identifying short-range structural changes. The former technique was the initial stimulus for subsequent structural investigations, so these results are presented first.

Figure 4.7 shows the admittance curves as a function of time for the complete liquid-to-'solid' conversion. Even though a curve was recorded every 30 seconds, the curves in figure 4.7 are plotted at 5 minute intervals for clarity. A change to both the position and amplitude of the peaks are evident as

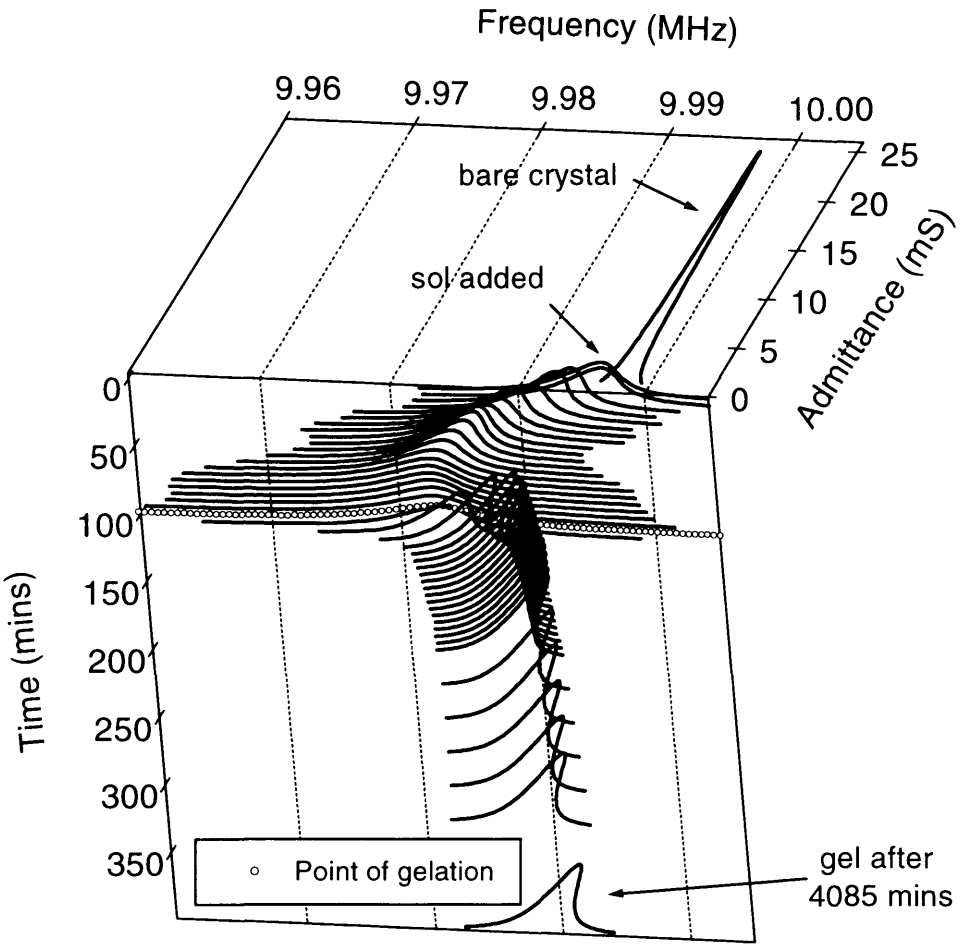

Figure 4.7: Admittance *vs.* frequency curves as a function of time for the sol-to-gel transformation. Circles indicate the point of gelation.

gelation proceeds.

The unloaded crystal displays the sharp admittance curve that is characteristic of a rigid solid. Once the crystal was loaded with sol, the resonant frequency decreased slightly (but significantly) in response to the mass and viscosity of the liquid, implying either a liquid that is not fully dissipative (*i.e.* a Maxwell as opposed to a Newtonian fluid), or perhaps a small quantity of the sol was entrapped within rough features at the surface of the crystal, creating a pseudo ideal mass layer, the rest of the liquid (if a Newtonian fluid) being effectively 'invisible' to the microbalance. The frequency then

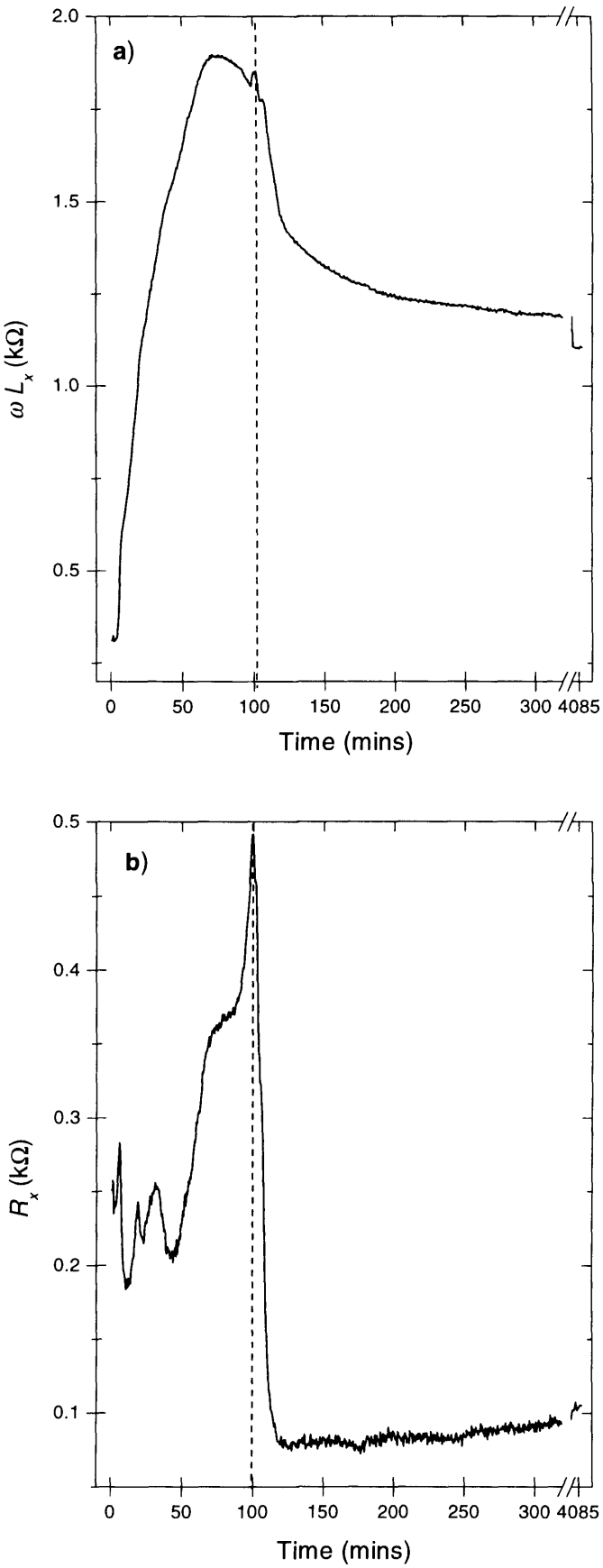

Figure 4.8: a) Inductive reactance and b) film resistance as a function of time for the sol-to-gel transformation. Dashed lines indicate the point of gelation.

continued to decrease and the curves to broaden with time. The negative frequency shift reflects the increasing mass exerted on the resonator as a result of increasing film viscosity. The concurrent loss of amplitude and increase in peak width are characteristics of a viscoelastic material, in which the penetration depth of the shear oscillations is greater than in the liquid, resulting in more extensive dissipation of the waves. These trends reverse at about 100 minutes, as indicated in figure 4.7, where the magnitude of the admittance begins to rise steadily and the frequency shifts in a positive direction. The instant corresponding to this reversal indicates the point of gelation, where the film transforms from a liquid-like material to one with elastic properties. Beyond the point of gelation, the decrease in mass is probably due to the expulsion of solvent from the pores as the film hardened (equation 4.3). After 4085 minutes, the amplitude of the final admittance curve was roughly a quarter of the original value (*i.e.* the reference peak of the bare crystal), suggesting the film did not become a rigid solid, but rather a viscoelastic solid; this must be confirmed by modelling the layer type.

The results derived from the admittance curves are corroborated by the modelled inductive and resistive circuit elements plotted in figures 4.8a and b, respectively. In figure 4.8a, the inductive component of Z_{EL} is plotted as inductive reactance ωL_x (in kΩ, as opposed to L_x in μH) for comparison with the units of the resistive component R_x. This plot resembles the inverse of the frequency shift as a function of time (fig. 4.9). This is not surprising since inductance as well as frequency are affected by the kinetic energy associated with the synchronous movement (*i.e.* coupling) between film and quartz, thus representing changes in the inertial mass of the film as gelation proceeds. The inertial mass of the film rises rapidly with increasing liquid viscosity and reaches an abrupt peak at 101 minutes, signifying the point of gelation. Beyond this point, the mass drops steadily as the film dries, before levelling out.

A very similar gelation point is also indicated by film resistance in figure

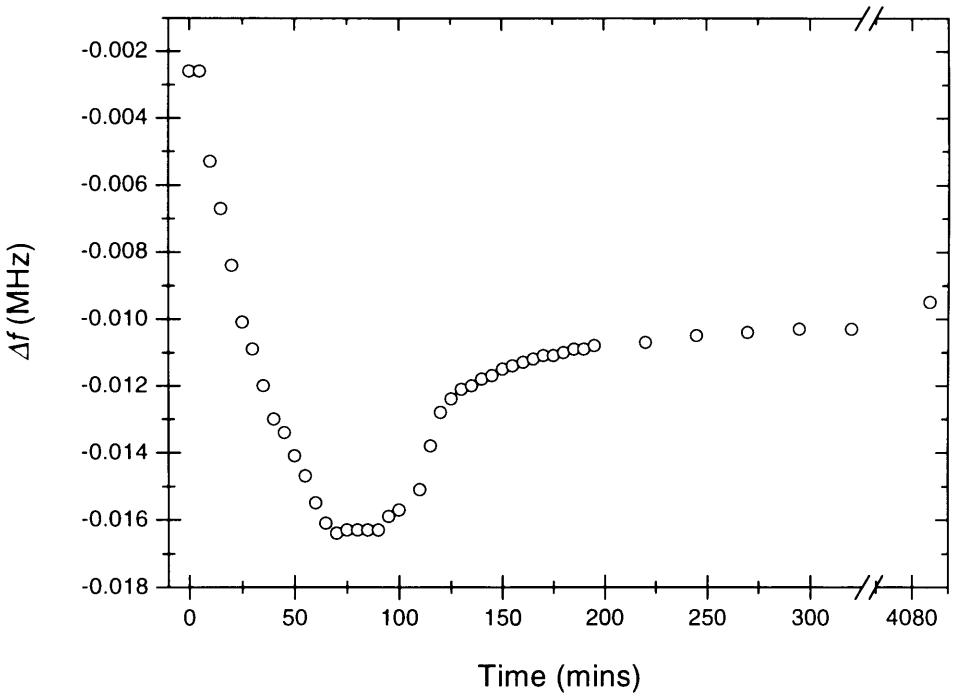

Figure 4.9: Resonant frequency shift as a function of time after loading crystal, where the resonant frequency corresponds to maximum admittance of each admittance curve displayed in fig. 4.7 ($\Delta f = f_{\Delta m} - f_0$, eqn. 1.23).

4.8b, which demonstrates energy loss as a function of time. For the first 50 minutes, the energy dissipation of the film fluctuates about the initial region, followed by a steep increase, which slows for about 20 minutes before again rising sharply at about 90 minutes and peaking at the gelation point (99.5 mins). This sharp increase in resistance coincides with the increase in inertial mass and the concurrent decrease in both resonant frequency and admittance, reinforcing the viscoelastic behaviour interpreted from the previous plots *i.e.* that more extensive shear wave deformation takes place in this region, as the crystal 'experiences' more of the film due to the increase in coupling with rising film viscosity. A sudden, steep drop in resistance subsequently occurs after the gelation point, as the film solidifies and becomes more elastic (*i.e.*

increasing energy storage as opposed to loss), remaining constant at its lowest value for the remaining time. The precise point of gelation is not immediately obvious simply by observing the admittance curves and frequency shifts; the extraction of equivalent circuit parameters was therefore essential to the accurate evaluation of this transition point.

Time (mins)	Measured Δf (MHz)	Sauerbrey Derived Δf (MHz)[a]	Δf Derived from eqns. 1.43 & 1.44 (MHz)	Δf Derived from eqn. 1.45 (MHz)
5	-0.0026	-0.52	-0.0027	-0.0017
50	-0.0141	-0.52	-0.0142	–
100	-0.0157	-0.52	-0.0158	–
125	-0.0124	-0.52	-0.0124	–
160	-0.0113	-0.52	-0.0114	–
320	-0.0103	-0.52	-0.0104	–
4085	-0.0095	-0.52	-0.0097	–

[a] Using estimated Δm_x

Table 4.1: Measured and calculated values for frequency shift Δf at significant times during gelation.

Table 4.1 shows measured frequency shifts and the value calculated by applying the Sauerbrey equation (eqn. 1.23) to the difference between the estimated areal mass of sol and gel, assuming that niobium contributes most to the areal density, where $\rho_2 = 0.04\ \mathrm{g\,cm^{-3}}$, $\rho_3 = 1.6\ \mathrm{g\,cm^{-3}}$, $x_x = 14.7\ \mu\mathrm{m}$, $\Delta m_x = 2.29 \times 10^{-3}\ \mathrm{g\,cm^{-2}}$ and $f_0 = 9.9976$ MHz. As expected, the Sauerbrey-derived value for Δf is much greater than the measured values because much of the kinetic energy of the shear oscillations is lost to the thick, non-rigid film; so only the mass exerted by the film caught within the short penetration depth of the waves actually produces a frequency shift. Table 4.1 also shows the frequency shifts calculated by applying equations

1.44 and 1.45 to fitted values of L_x and $\rho_2 \eta_2$, where $L_0 = 9.09$ mH. It is evident that the similarity between all measured frequency shifts and those calculated using equations 1.43 and 1.44 (which apply to all types of layer and all except for pure Newtonian fluids, respectively) is far greater than those derived using eqn. 1.45, which applies to Newtonian fluids only, even at $t = 5$ mins when the sol was applied to the crystal. These results therefore show that the film is never a rigid, Sauerbrey-type, ideal solid or a pure Newtonian fluid, so Δf from the sol is either produced by a pseudo ideal mass layer plus Newtonian fluid or a Maxwell fluid.

Time (mins)	Stage	Model	Extracted Parameters			
			G_3' (10^4 dyne cm^{-2})	G_3'' (10^4 dyne cm^{-2})	ρ_3 (g cm^{-3})	$\rho_2 \eta_2$ (10^{-3} g^2 cm^{-4} s^{-1})
5	sol added	IML + SINF	–	–	–	7.29
50	pre-gel pt.	IML + SIVL	16.3	28.6	0.80	–
100	gel pt.	IML + SIVL	32.3	20.4	0.82	–
125	post-gel pt.	IML + SIVL	1.34	2.42	1.14	–
160	post-gel pt.	IML + SIVL	2.10	2.11	0.90	–
320	post-gel pt.	IML + SIVL	0.53	6.83	0.93	–
4085	end	IML + SIVL	0.61	9.18	0.83	–

Table 4.2: Models applying to niobium oxide film at significant stages during gelation. Model description IML = ideal mass layer, SINF = semi-infinite Newtonian fluid and SIVL = semi-infinite viscoelastic layer.

Confirmation that the film never behaved as an ideal rigid solid was achieved by fitting the layer type. Figure 4.10 shows the fitted amplitude and phase of subtracted admittance curves (minus the contribution of the crystal). Good correlations between experiment and theory are evident from the overlapped curves, especially at the amplitude maxima and the inflection

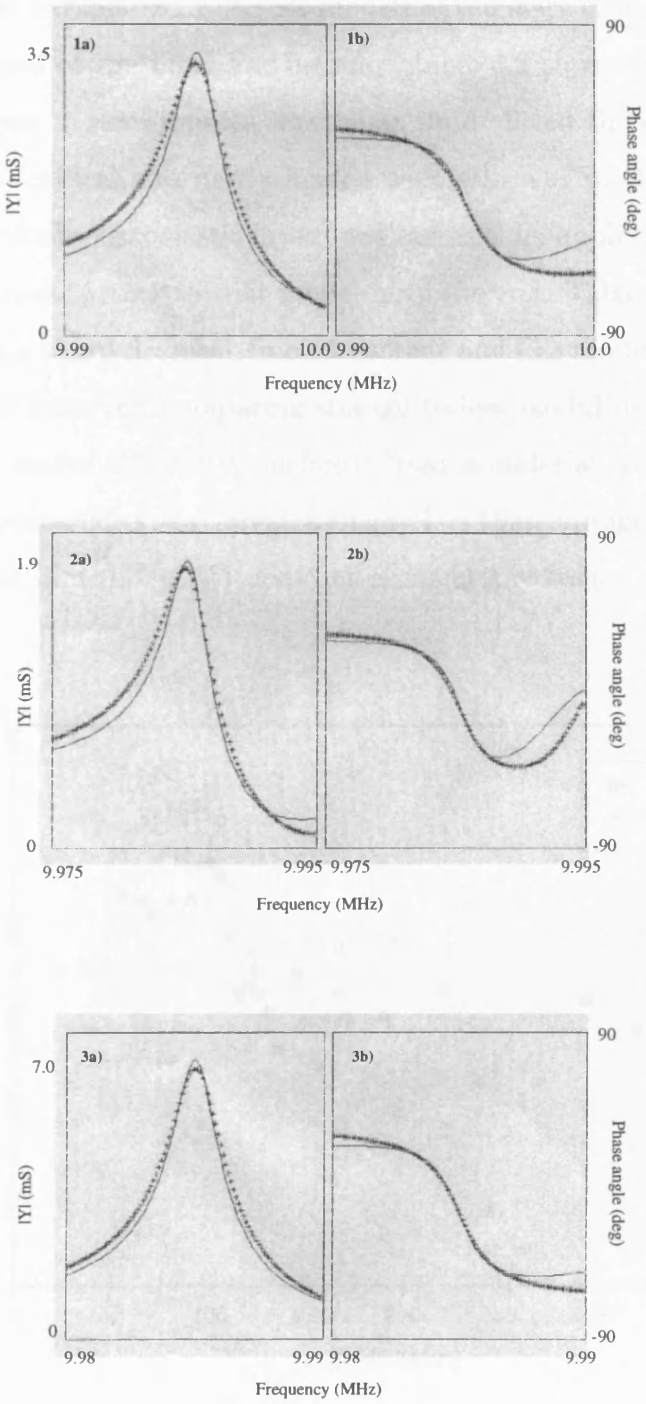

Figure 4.10: Best fits (lines) to experimental data (crosses) for admittance curves of 1) sol at $t = 5$ mins, 2) gelation point at $t = 100$ mins and 3) gel at $t = 4085$ mins. Both a) magnitude and b) phase data are shown.

point of the phase angle. When fitting the admittance data to extract values for physical parameters, different models of the layer type applied to the rheological states of the film. For instance, table 4.2 shows that the model "ideal mass layer + semi-infinite Newtonian fluid" fitted the data at 5 minutes, when the crystal was newly loaded with sol. The model "ideal mass layer + semi-infinite viscoelastic layer" was successfully applied to the gelling film at 50 minutes, fitting to that model until the end. Table 4.2 and figure 4.11 show that a sharp decrease to both storage and loss moduli occur at the gelation point. However, comparing storage to loss moduli indicates that a turning-point, where the film transforms from a material with dominating liquid-like characteristics, *i.e.* greater energy loss than storage ($G'' > G'$), to a mainly elastic film ($G'' < G'$) does not occur at any stage.

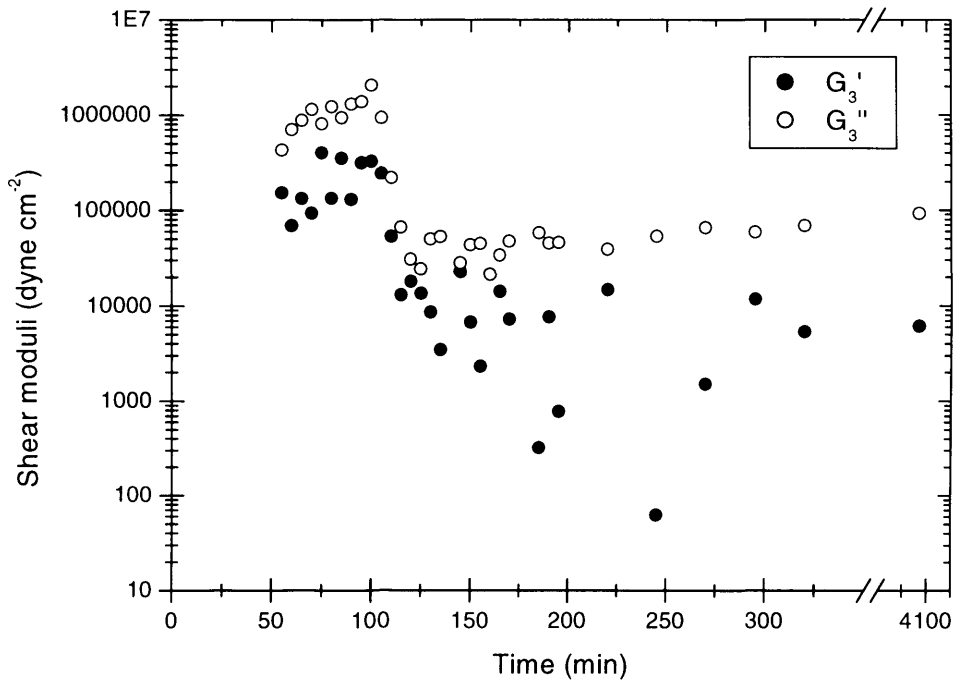

Figure 4.11: Film storage (filled circles) and loss (open circles) moduli, derived from the model "ideal mass layer + semi-infinite viscoelastic layer".

4.5.3 Monitoring the Sol-Gel Conversion of Niobium Oxide Films using X-ray Absorption Spectroscopy

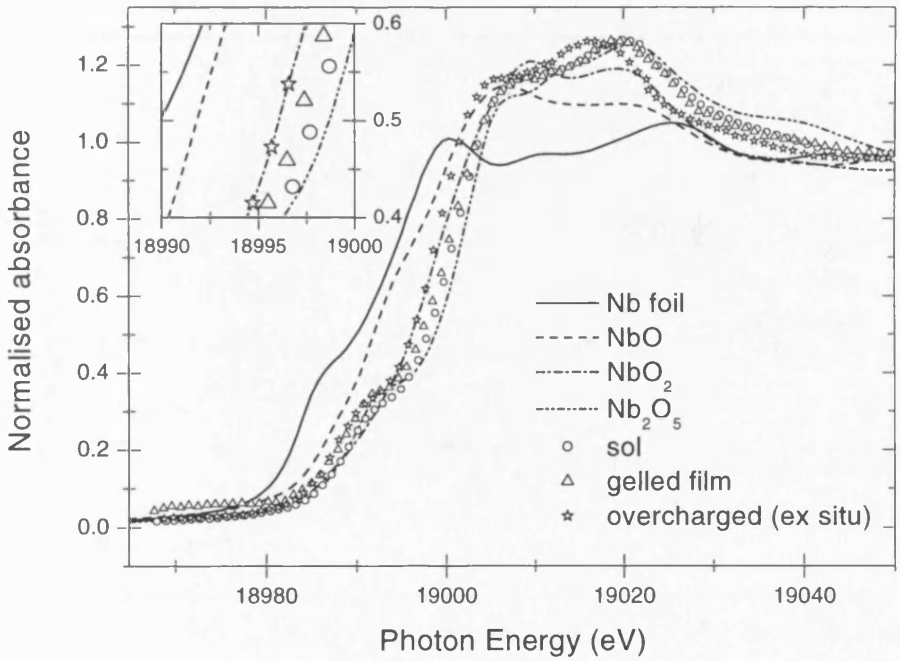

Figure 4.12: Normalised transmission mode Nb K-edge XANES of reference materials, together with those of sol and gelled films.

In terms of X-ray absorption spectroscopy, in particular XANES, data for the standards (figures 4.12 and 4.13) show that the Nb K-edge progressively shifts in a positive direction in response to an increase in valency. In fact, an average edge shift of 1.43 eV per unit change in valency is evident. However, this value does not suggest the form of the relationship between edge position and oxidation state. It can be seen that the data points fit to a curve (second order polynomial), the steepest gradient (*i.e.* the greatest energy separation) being between Nb^{4+} and Nb^{5+}, the current range of interest, where the edge positions differ by 1.8 eV. Also, most of the Nb edges have a curved shape, bending to either a negative or positive direction around the mid-point (*i.e.* NbO or Nb_2O_5, respectively). As the edge posi-

tion is measured at the mid-point (*i.e.* $y = 0.5$), this curving accounts for the non-linearity of the calibration curve (*i.e.* the separation between the edges is not equal).

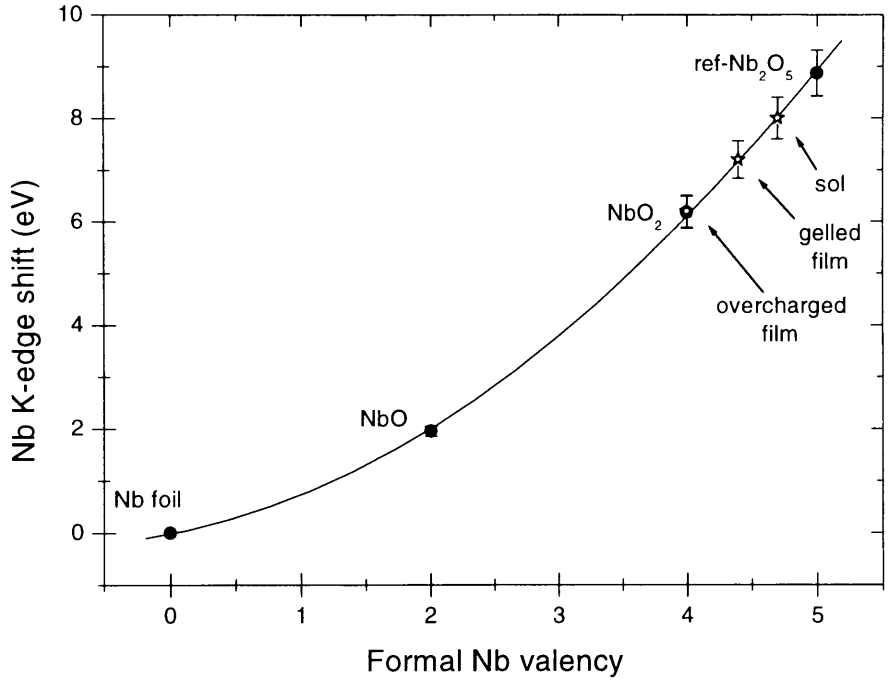

Figure 4.13: Calibration curve defined by 2nd order polynomial fit to Nb K-edge shifts of standards (dots) at various integer valences. Edge shifts of sol and films (stars) are aligned with the calibration curve. Only transmission mode data is presented. Error bars represent 95 % confidence levels.

The valency of niobium in both sol and gel was determined using a calibration curve (fig. 4.13), analogous to that used for the nickel hydroxide system (fig. 3.6), where the standards, which were assumed to possess a known formal integer valency for niobium, were used to define the calibration curve. The edge shifts of the sol and films were then aligned with the curve in order to determine the oxidation state of niobium within these samples. The precise, corrected edge shifts of both sol and gel are listed in table

4.3. When comparing edge shifts, differences less than usual maximum energy separation between data points within a spectrum. A significant edge shift was identified between sol and gel; these edge shifts correspond to Nb valences of 4.7 and 4.4, respectively. However, these spectra were derived from separate samples, *i.e.* one spectrum was measured from a liquid-phase sample contained within the appropriate cell, the other being a pre-gelled thin film (half usual thickness) in the spectroelectrochemical cell. These edge shifts were derived from experiments not originally intended to monitor gelation. The edge shift of the sol is indeed confirmed because preceding and subsequent spectra measured from the same static sample gave identical edge shifts, but there were no preceding spectra to the gelled film, and subsequent spectra gave no significant edge shift, so it cannot categorically be stated that a decrease in edge position accompanies gelation, especially since the experiments specifically designed to monitor gelation (*e.g.* EDE measurements) failed to reveal any changes whatsoever.

Figure 4.12 shows that both sol and gel edges have similar shapes, closely resembling that of ref-Nb_2O_5. These edges are broad, straddling Nb^{4+} and Nb^{5+} positions, suggesting that Nb ions exist in a combination of oxidation states, the edge position representing the average valency, which is dependent on the proportion of each state in the sample. Therefore, this oxide is very different to nickel hydroxide (section 3.5.1). No changes to either the appearance of pre-edge features or to the height of the edge step or white line were evident throughout gelation, so the point of gelation could not be identified from XANES.

Analysis of the EXAFS derived during energy dispersive experiments and standard EXAFS, where a liquid-phase sample and a partially gelled film ($\sim$ 20 mins old) gelled over several hours (sections 4.3.5i & ii, respectively) revealed no significant changes to short-range structure to accompany the previously described rheological development. In fact, the structure of the sol, derived from transmission mode measurements (section 4.3.5i) was in-

Sample	Edge Shift (eV)	Formal Nb Valency	Derived Nb Valency	
			From edge shift	From mean $R_{(Nb-O)}$
Standards				
Nb foil	0	0	–	–
NbO	+1.95	2	–	–
NbO_2	+6.18	4	–	–
ref-Nb_2O_5	+8.87	5	–	–
Sol & Films				
sol	+8.0	–	4.7	4.9
gelled film	+7.2	–	4.4	4.9
overcharged film (ex situ)	+6.2	–	4.0	4.8

Table 4.3: Information obtained from Nb K-edge XANES and EXAFS fits for standards, sol and films.

distinguishable from that of the gel, even in terms of Debye-Waller factors, which were expected to demonstrate the most significant modification from liquid to gel. It follows that no significant changes to any spectral features or fitted parameters occurred during the early stages of gelation, when the cell containing sol (fig. 4.4) was opened to initiate gelation. However, the filling holes may have been too small to allow the introduction of sufficient moisture to initiate gelation. Alternatively, a drier atmosphere in the laboratories in Daresbury (compared to those in Leicester) may have reduced the intake of moisture. Figures 4.14b and 4.15b show that the quality of these standard transmission mode spectra and fits was high, so it is unlikely that slight variations would have been disguised by noise. Finally, no alterations

to any structural parameters signalled the point of gelation.

insert fig here

4.5.4 Electrochemical Modification of Gelled Niobium Oxide Films

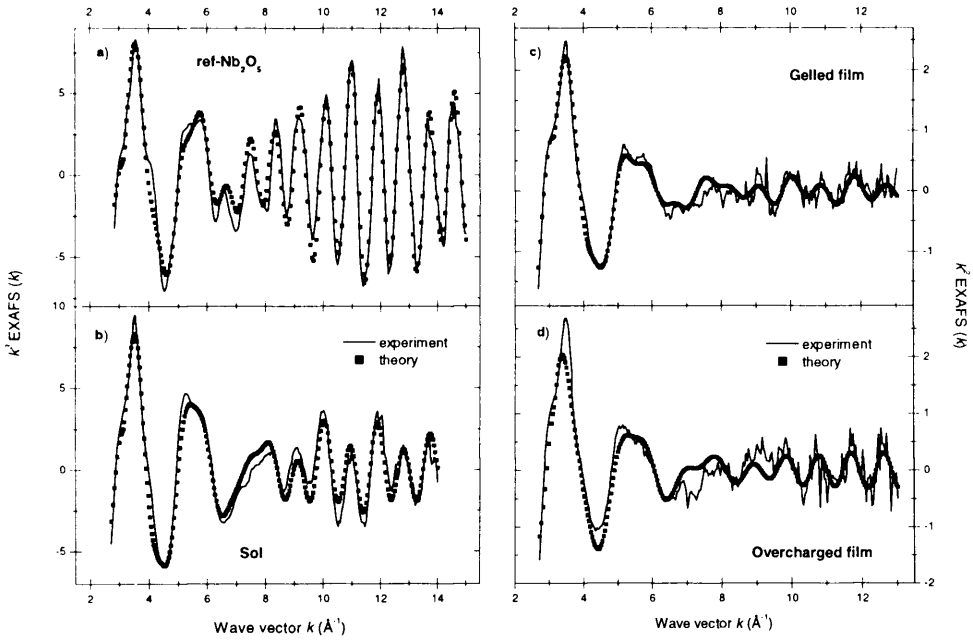

Figure 4.14: k^3 and k^2 weighted EXAFS with fits for (a) Nb_2O_5 powder, (b) the sol, (c) thin gelled film and (d) thin overcharged film (*ex situ*).

Repeatedly cycling gelled films between various limits, at various scan rates (up to 200 times) failed to produce any significant change to either edge position, white line height or pre-edge features, implying that cyclic voltammetry did not affect a sufficient proportion of the available niobium ions to alter the XANES. This situation was repeated when typical, thick films were overcharged for up to 13 hours (fig. 4.16). In most cases, even directing the beam onto the darkest regions of reduced films (*in situ* and *ex*

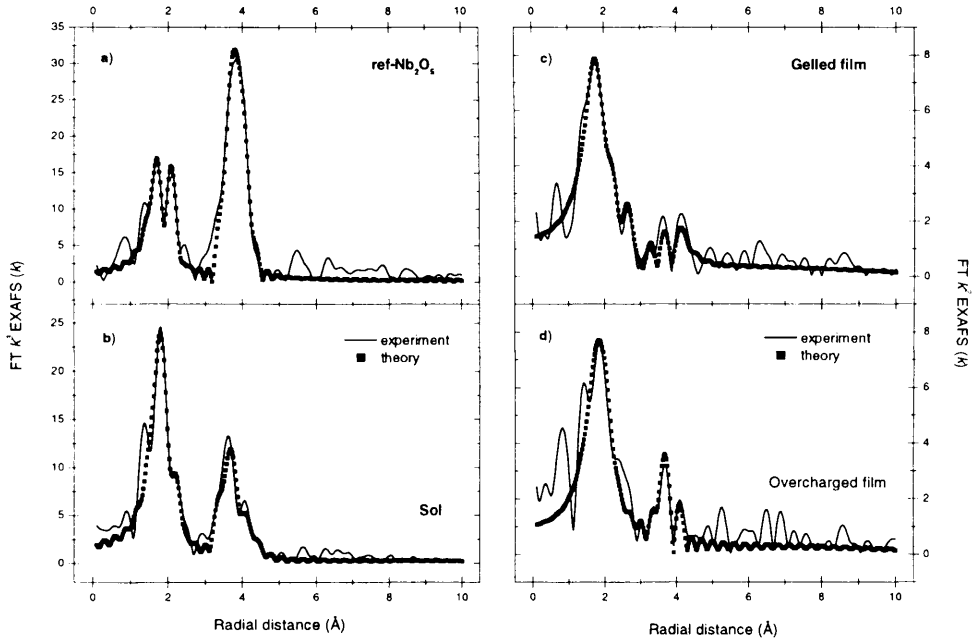

Figure 4.15: k^3 and k^2 weighted radial structure functions with fits for (a) Nb_2O_5 powder, (b) the sol, (c) thin gelled film and (d) thin overcharged film (*ex situ*).

situ) failed to record an edge shift greater than 7.2 ± 0.5 eV (the significant range). This outcome was considered likely since typical films were electrochemically thick and competition from parasitic reactions was strong. To increase the likelihood that a significant proportion of the film was converted (*i.e.* to increase the surface to bulk ratio), a film of half the usual thickness (half the usual volume of sol, giving half the usual film thickness and about half the typical edge step) was cycled, overcharged and discharged. As stated in section 4.3.5iii, fluorescence measurements of these thin films were preferable since the transmission signal halved.

Ex situ dual transmission and fluorescence spectra of a thin film overcharged at -0.5 V for 5 hours produced a single significant edge shift (figs. 4.12, 4.13 and table 4.3); this was revealed by directing the beam onto a particularly dark region of the film for the duration of one set of spectra, be-

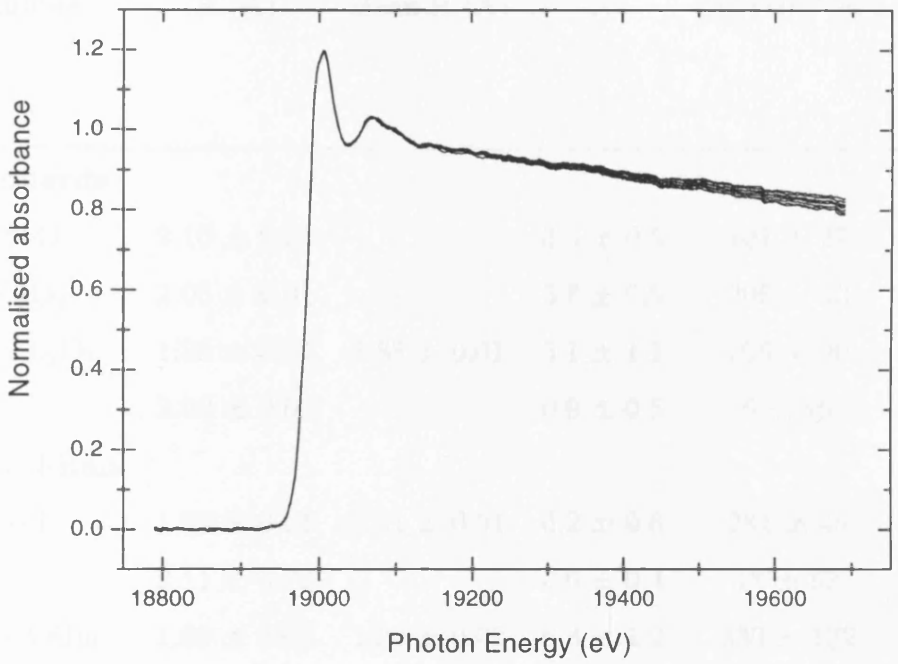

Figure 4.16: Normalised EDE spectra of a niobium oxide film cathodically overcharging at -1.7 V *vs.* SCE.

fore focussing on other dark regions for successive measurements. This edge shift was evident in both the transmission and fluorescence spectra, recorded simultaneously. More precisely, edge shifts of 6.0 and 6.2 eV were derived from fluorescence and transmission mode spectra, respectively. The 0.2 eV difference is within the systematic error arising from choosing the normalisation range of both spectra by hand. It can be seen from figure 4.12 that the overcharged edge is broad; at the mid-point, where the edge position was measured, the edge overlaps the Nb^{4+} position of NbO_2, and at the tip the edge overlaps that of NbO in the Nb^{2+} position, providing further evidence for the existence of Nb ions in several oxidation states at any one time.

Despite the lack of change to edge position in these films, deep dark brown colour changes were induced both by overcharging lithium-doped films (of both thicknesses) and repeated cyclic voltammetry, though colouration was

Sample	R (Å)	Mean R (Å)	Nb-O N	$2\sigma^2$ (10^{-4} Å^2)	Fit Index (%)
Standards					
NbO	2.10 ± 0.01	–	3.5 ± 0.5	101 ± 27	29.5
NbO_2	2.05 ± 0.01	–	5.8 ± 0.6	206 ± 30	29.7
ref-Nb_2O_5	1.85 ± 0.02	1.88 ± 0.01	5.1 ± 1.1	296 ± 90	23.6
	2.02 ± 0.01		0.9 ± 0.6	6 ± 49	
Sol & Films					
sol	1.89 ± 0.01	1.91 ± 0.01	6.2 ± 0.6	284 ± 46	30.9
	2.11 ± 0.02		0.6 ± 0.4	18 ± 68	
gelled film	1.89 ± 0.02	1.92 ± 0.02	6.3 ± 1.2	330 ± 192	29.3
	2.12 ± 0.03		1.0 ± 0.9	62 ± 119	
overcharged film (ex situ)	1.93 ± 0.01	–	6.0	345 ± 34	48.6

Table 4.4: Structural parameters for first Nb-O shell, derived from fits to EXAFS of standards, sol and gelled films. Uncertainties represent 95 % confidence levels.

not even. Although colouration was even across the illuminated area, the darkest part was always in the area above the 'letterbox' shaped slit, designed to accommodate the beam. This area was always enclosed beneath the Au mesh WE, so was only exposed when the film was removed from the cell for *ex situ* measurements. The current density in this area must have been higher than the rest of the film because most of the gold wires welded together to encircle both inside and outside perimeters of the Au mesh working electrode (fig. 4.3) met in this region. The scarcity of significant results in electrochemically modified films, especially since the only edge shift was

Sample	R (Å)	Mean R (Å)	Nb-Nb N	Nb-Nb $2\sigma^2$ (10^{-4} Å^2)	Fit Index (%)
Standards					
Nb foil	2.85 ± 0.003	–	8.0 ± 0.8	140 ± 10	26.4
NbO	2.98 ± 0.004	–	4.0 ± 0.6	86 ± 12	29.5
NbO_2	2.70 ± 0.01	3.09 ± 0.01	1.3 ± 0.6	93 ± 48	29.7
	3.33 ± 0.01		2.1 ± 1.3	167 ± 67	
ref-Nb_2O_5	3.63 ± 0.01	3.82 ± 0.01	1.6 ± 0.7	36 ± 27	23.6
	3.87 ± 0.01		6.7 ± 1.9	135 ± 28	
Sol & Films					
sol	3.62 ± 0.01	3.79 ± 0.01	2.1 ± 1.0	88 ± 37	30.9
	3.84 ± 0.01		7.3 ± 3.4	313 ± 112	
gelled film	2.58 ± 0.03	3.71 ± 0.02	1.1 ± 0.8	263 ± 135	29.3
	3.86 ± 0.02		8.1 ± 3.5	299 ± 147	
overcharged film (ex situ)	3.67 ± 0.01	–	1.1	1 ± 22	48.6

Table 4.5: Structural parameters for first Nb-Nb shell, derived from fits to EXAFS of standards, sol and gelled films. Uncertainties represent 95 % confidence levels.

from an *ex situ* measurement from one dark region (visually indistinguishable from other dark regions), may therefore be attributed (in part) to the great inhomogeneity caused by uneven current density across the working electrode.

Discharging overcharged films always resulted in a rapid drop in current, effectively reaching zero in a matter of seconds, with no observed reversal of colouration. The colouration persisted for over 12 hours after disconnecting

the electrodes and removing the film from the cell and electrolyte. Also, no significant changes to XANES or short-range structure were measured after the current stabilised.

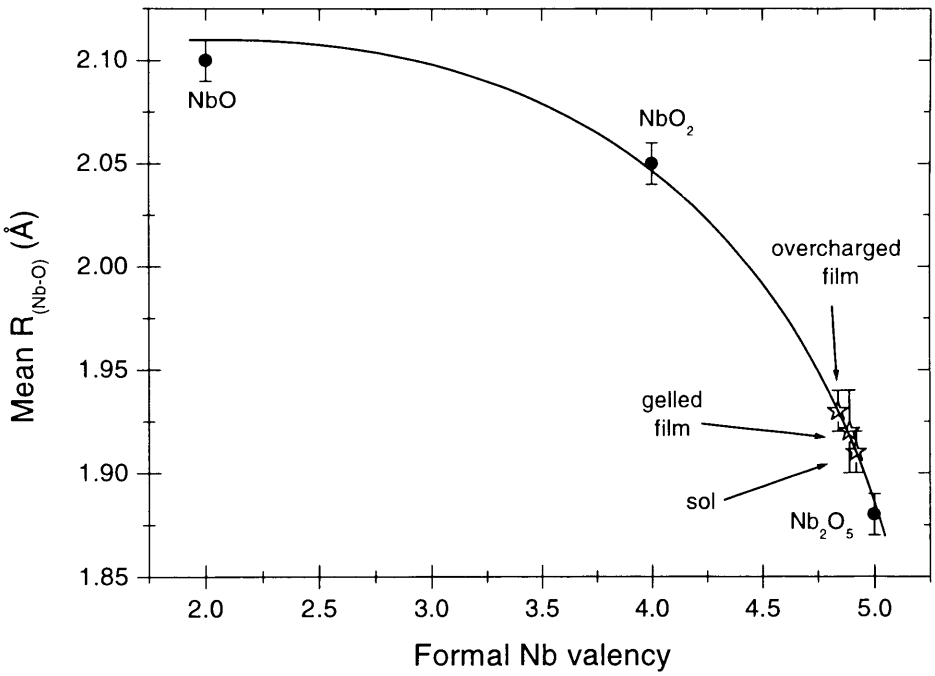

Figure 4.17: Calibration curve defined by curve fitted to mean first Nb-O distances of standards (dots) at various integer valences. Mean first Nb-O distances of sol and films (stars) are aligned with the calibration curve.

In terms of EXAFS, the expected decrease of mean first Nb-O distance with increasing formal valency is displayed by the standards in figure 4.17, where the dependence has a curved form similar to the edge shift relationship in figure 4.13. When superimposed on the appropriate calibration curve, the mean first Nb-O distances suggest that both sol and gel possess the same Nb valency (table 4.3), contrary to the valences implied by the edge shifts. A very similar, though slightly lower valency was derived for the overcharged film. The Nb-O and Nb-Nb shell structures listed in tables 4.4

and 4.5, respectively. Literature values for the coordination numbers for reference compounds are not given in the tables because there was such a wide variation in the published structures that a definitive structure could not be found. The fits in figures 4.14 and 4.15 show that both sol and gel are most closely represented by the structure of Nb_2O_5; distortion of both Nb-O and Nb-Nb shells, coordination numbers and Debye-waller factors are all characteristic of this compound. On the other hand, the overcharged film appears to have a structure mid-way between Nb_2O_5 and NbO_2, where only regular octahedral first Nb-O and Nb-Nb shells proved significant. This is a novel and highly significant result, proving that the measured edge shift was not spurious. Originally, the octahedrally-arranged first coordination sphere of the Nb_2O_5 film consists of 1 long and 5 short Nb-O bonds. Electrochemical reduction caused the distortion to cease, resulting in a regular octahedral shell with a Nb-O separation similar to the weighted mean Nb-O distance of gel-Nb_2O_5. A regular first Nb-O shell was also derived for NbO_2. Very different behaviour was displayed by the first Nb-Nb shell of the overcharged film. A highly distorted octahedral Nb-Nb shell was evident in the uncharged film, with 1 short and 5 long interatomic distances. Only a single Nb atom could be discerned in the overcharged film; its position approached the weighted mean distance of the uncharged distorted shell of the gel. This shell is unlike the first Nb-Nb shell of NbO_2, although it could not be determined with certainty whether this atom formed part of a split Nb-Nb shell containing 4 atoms (as derived for both NbO and NbO_2) because the other atoms were too distant to be identified conclusively from a single spectrum.

4.6 Discussion

4.6.1 Sol-Gel Conversion of Niobium Oxide Films

A considerable rheological evolution has been identified for the sol-gel conversion of niobium oxide using the crystal impedance technique. The conversion will be described as a multi-stage process, beginning with the addition of sol to the crystal at $t = 5$ mins and ending with a gel at $t = 4085$ mins. At this stage, it is useful to remember the terminology used in section 1.3, where the subscript 1 refers to a rigid solid (ideal mass layer), 2 represents a Newtonian fluid and 3 refers to a viscoelastic layer.

It has been shown that the sol is a Newtonian fluid. The relatively well-defined initial admittance curve and the slight negative frequency shift with the addition of sol are attributable to the pseudo ideal mass layer caused by fluid caught within the textured surface of the crystal. As mainly the thin pseudo ideal mass layer is recognised, its mass is the main contributor to ωL_1 and Δf, both of which therefore are low. It behaves as a rigid layer, causing the energy loss term R_1 also to be relatively low. The remainder of the film is almost 'invisible' to the resonator because the penetration depth of the shear waves is very short ($\sim$ 200 nm) in a Newtonian fluid. Despite the short penetration depth, the small portion of the film that is 'visible' to the crystal has a low density-viscosity product, which is characteristic of a Newtonian fluid.

By $t = 50$ mins, half-way to the gelation point, the bulk film is now described as a semi-infinite viscoelastic layer. The contribution from the film has risen considerably as a result of its increasing viscosity and/or density. ωL_3 rises and the resonant frequency becomes more negative in response to the increase of inertial mass. As the shear waves travel further into the film, they experience more extensive dissipation, resulting in a lower and broader admittance curve. Energy dissipation is more extensive because the film is still essentially a liquid (albeit a viscous liquid), as shown by both the

complex shear moduli of the film (where $G_3'' \approx 2G_3'$) and R_3, which begins to rise steeply.

By the point of gelation ($t = 100$ mins), the previous trends have reached a maximum, so the greatest possible contribution from the thick, liquid-like viscoelastic film is recognised by the resonator. As a result, the admittance curve is at its broadest, the resonant frequency is at its most negative and R_3 peaks. From this point, the film no longer behaves as an evenly dispersed colloid. Sufficient interconnection between oxide particles has resulted in an oxide framework with a separate phase of solvent contained within the interstices. Separation of the two phases is evident from the increasing magnitude of G_3' and G_3''. The continuing development of the oxide network (*i.e.* the densification of the solid oxide) subsequently forces the solvent from the pores to the surface, forming a separate layer, beyond the penetration depth of the shear waves. This may have caused the sharp increase in inertial mass that marks the point of gelation. The point of gelation therefore, in this case, effectively signals the end of homogeneity and marks the onset of solvent expulsion.

Solvent and oxide phases continue to separate beyond the point of gelation ($t = 125$–160 mins). G_3' drops after the point of gelation because the entrapped liquid within the pores gave an effect similar to a pseudo ideal mass layer, making the film behave more rigidly. Its subsequent expulsion from the pores caused the storage modulus to fall considerably. The inertial mass of the film drops as solvent moves away from the crystal/film interface and eventually evaporates, as indicated by the positive frequency shift. Further evidence is given by the decrease in film density. The admittance curves sharpen and R_3 drops to its lowest level as the influence of the dissipative liquid in this region diminishes as expulsion proceeds, making the contribution from the oxide phase layer greater.

Toward the end of the sol-gel process, ωL_3 stabilised and Y, Δf and R_3 remained essentially constant. G_3' and G_3'' separate, with a substantial

increase in loss modulus as solvent is expelled, leaving a porous viscoelastic film, as shown by the decreasing density. For the purpose of this investigation, it may be concluded that the Sauerbrey equation was wholly unsuitable for deriving changes to the areal mass sol-gel-derived niobium oxide films, since no ideal solid behaviour was displayed by the film at any time, therefore changes to areal density did not translate fully to frequency shifts. Anyway, even if the film solidified completely, a Sauerbrey-type state could not be attained because film thickness was far greater than ideal (*i.e.* > 0.5 % x_0, page 41).

The good agreement between measured and calculated frequency shifts using eqns. 1.43 and 1.44 in table 4.1 shows that the inductive equivalent circuit parameters used to calculate Δf were very accurate. Δf derived from equations 1.43 and 1.44 was closer to the measured frequency shift of the sol than the value derived using eqn. 1.45 (which applies to Newtonian fluids only) because the latter equation does not account for inertial mass. Therefore, the contribution of the pseudo ideal mass layer is neglected, making the sol appear not to be a Newtonian fluid. The lack of significant changes to EXAFS-derived short-range structure shows that gelation occurs on a (mid-to-long range) intermolecular (which is beyond the scope of the EXAFS technique) rather than a (short-range) intramolecular level. As the structure of sol and gel appear identical, short-range Nb_2O_5 structure was established in the early stages of sol formation, probably soon after the sol was synthesised. However, it is surprising that no significant change to static disorder distinguished the sol from the gel, yet alone signalled the point of gelation. The original 5-short, 1-long Nb-O shell distortion implies the existence of dimeric NbO_x species in both sol and gel. No significant increase in Nb-Nb coordination took place as the film became denser. Such a change was difficult to identify with certainty since the coordination at the short Nb-Nb distance was so small.

The interpreted rheological development is supported by all the measured

and extracted information, being consistent with the main features of the known sol-gel conversion of amorphous silica [109] (section 4.1). Even though the use of sol-gel-derived niobium oxide films is well-documented, this is the first time that a full, dynamic, *in situ* rheological investigation of the initial sol-gel conversion has been reported. This novel approach to deriving a precise model of the niobium oxide sol-gel process has therefore proven successful and can be extended to establish the effects of additives to either retard or advance the onset of the gelation point or alter the texture of this or any other sol-gel-derived material.

4.6.2 Electrochemically Modified Niobium Oxide Films

Virtually all of the structural changes induced by cyclic voltammetry and overcharge (that were signalled by a colour change) evaded measurement for many reasons. Primarily, all electrochemical measurements and calculations were hampered by the unavoidable and unfortunate overlap of Nb^{5+} and H^+ reduction potentials indicated by occasional bubble evolution. Therefore, in most cases, a significant proportion of the Nb ions present were never reduced. Also, the current density across the film was not even or high enough. The nonaqueous electrolyte may have contributed to the high cell resistance, though increasing the $LiClO_4$ concentration did not appear to improve the situation.

Another reason for the lack of electrochemically-induced changes may be attributed to low film conductivity. Several studies have stated that amorphous Nb_2O_5 has a relatively low conductivity. Notwithstanding parasitic reactions, the inability to reduce Nb^{5+} ions, where the edge shift per unit of valency is similar to $Ni(OH)_2$, implies that the Fermi level lies within the band gap, making the molecular (rather than the solid-state) description of the oxide likely. In this model, the oxide consists of separate chemical bonds, each with localised electrons of low mobility. The immobility of the elec-

trons (due to the band gap) makes conduction across the film difficult; Nb ions therefore exist in a range of oxidation states across the film. This mixture of oxidation states varies in proportion, giving an overall weighted mean non-integer oxidation state. This model is supported by the broad, partially overlapping absorption edges of ref-Nb_2O_5, ref-NbO_2 and all edges produced by the films. Also, the immobility of electrons in reduced films is suggested by the stability of reduced ions, evident in the persistence of colouration, even after oxidation at a positive potential or removing the film from the electrolyte for several hours. The very low discharge current, that was almost zero, provides further evidence for the difficulty with the transport of charge. The fact that observed colour changes remained inhomogeneously dispersed across the film, and a definite structural change was only derived from a single location on one overcharged film provides further evidence for this low conductivity. However, this description is not conclusive since a significant change to static disorder was not identified between uncharged, overcharged and discharging films. An increase in $2\sigma^2$ would have suggested the uneven transferral of charge across the film, as electrons pass between non-uniform sites during discharge.

When considering the poor conductivity of the films, Nb_2O_5 should not be classed as in insulator. In fact, the material behaves as an extrinsic p-type semiconductor. This was demonstrated by the effect of the Li^+ donor impurities introduced during sol synthesis. Undoped films gave very poor electrochemical performance, displaying no more than a feint colour change, whereas all of the deep colour changes reported (and the change in structure after overcharge) were achieved by reducing Li-doped films. Cyclic voltammograms from undoped films were shifted by $\sim$ -0.2 V relative to CVs from doped films. The less negative occurrence of cathodic peak in doped films implies that Nb^{5+} is slightly easier to reduce in these films. Unfortunately, the reduction potential is more in line with hydrogen evolution, but doped electrode performance still surpassed the undoped films. Therefore, only Li

doped sols and gels are considered in this chapter. The short-term cycling durability of these films was poor, but no structural evidence for this was suggested by the EXAFS.

Despite the difficulties caused by low film conductivity, there was success with achieving an even (although low) current density across the illuminated area of the film. Prior to EXAFS experiments, many modifications to cell design were undertaken in order to improve current density across the film *e.g.* the additional gold mesh working electrode and increased counter electrode area. Although these improvements had limited success (and prevented total failure), the problems associated with reducing electrochemically thick, large area films with low conductivity, in preference to a competing parasitic reaction, were difficult to surmount.

The EXAFS-derived structures are confirmed by the edge shifts. The decrease in Nb valency induced by cathodic overcharge was accompanied by a oxygen shell structure mid-way between Nb_2O_5 and NbO_2. It is possible that the change of symmetry, where the first Nb-O shell transforms from a distorted to a regular octahedron may have affected the shape of the edge, though this is by no means definite. Table 4.3 shows that the range of valences derived from bond lengths is smaller than those derived from edge shifts. As stated for the nickel hydroxide system, more confidence should be placed with the results derived from edge shifts since edge position is solely affected by the ionic charge of the Nb ions, whereas the influence of ionic charge upon interatomic distance is affected by the number of bonds (*i.e.* the coordination number). Table 4.4 shows that first shell coordination numbers varied between standards, so the bond length calibration curve should be considered an approximate representation of the relationship. As no further confirmation of valency could be made using electrode charge, it can only be stated with certainty that the valency of Nb in uncharged and overcharged films is between +5 and +4, and the valency of the cathodically overcharged film is closer to +4 than uncharged films (*n.b.* anodic overcharge used in the

previous chapter).

4.7 Conclusions

A detailed rheological mechanism for the sol-gel transformation of niobium oxide films was provided by crystal impedance analyses. A multi-stage evolution was identified from the *in situ*, time-resolved measurements over several hours. The crystal impedance technique therefore proved to be perfectly suited to revealing such developments. Conversely, *in situ*, time-resolved energy dispersive EXAFS was not suitable for measuring either subtle structural changes or even for structurally characterising the abrupt point of gelation. A longer-range structural technique such as X-ray diffraction may be more suitable for identifying these changes, but the method may have limited use since these films have been reported to produce the characteristically broad diffraction patterns of an amorphous material.

EXAFS was only slightly more successful for recording structural changes in electrochemically-modified niobium oxide electrodes. In this case, the choice of technique was not the main problem. *Ex situ* dual quEXAFS/flEXAFS measurements from a highly coloured region of a thin, cathodically overcharged film revealed a considerable change to first Nb-O and Nb-Nb shell structure; primarily, upon overcharge, the first Nb-O shell transforms from a highly distorted dimeric-type structure (the bridging Nb-O bond being longer than the rest) to one consisting of a more uniform, regular octahedral structure. The existence of a spectroscopically-identifiable range of distinct Nb oxidation states was only suggested qualitatively by the XANES. Quantitative analysis of the EXAFS only identified one type of regular Nb-O shell, suggesting the presence of a single non-integer oxidation state at overcharge. A summed set of several spectra, recorded from the overcharged region of the film would have conclusively determined whether Nb ions exist in a gradient of distinct oxidation states in the reduced film. It would

also be possible to determine whether the first Nb-Nb shell is distorted in the overcharged electrode. A series of EDE spectra, measured during successful overcharge or discharge, would have determined whether a significant increase in static disorder accompanies reduction/oxidation. In terms of optoelectronic technology, the effect of dopants upon the reproducibility and uniformity of structural, and hence colour changes is a worthwhile extension of this work.

Chapter 5

The Tungsten Oxide Electrode

Tungsten trioxide is one of the most important electrochromic materials. It and its corresponding redox couples possess both absorptive and reflective properties and a range of attractive colours with good stability and electrochemical reversibility [30, 34, 112]. These important properties have made tungsten trioxide one of the most extensively studied electrochromic systems, with numerous investigations into the optical and electrochemical (and hence electrochromic) performance being published; therefore much is already known about the system. The principal authority on this system is C. G. Granqvist, whose definitive works encompass all of the topics covered in this introduction [34, 112, 113, 114].

It is known that electrochemically reducing WO_3 results in the formation of a tungsten 'bronze', in which a fractional amount of electrolyte cations are bound to the oxide during the following redox reaction [115]:

$$\underbrace{WO_3}_{\text{PALE YELLOW}} + nM^+ + ne^- \underset{\text{ox}}{\overset{\text{red}}{\rightleftharpoons}} \underbrace{M_nWO_3}_{\text{DEEP BLUE}} \tag{5.1}$$

where M is usually H^+ or Li^+. Colouration is independent of the cation used, but insertion is irreversible for larger cations such as Na^+ or K^+ [116]. The value of n affects the optical properties of the oxide, so the colour of the oxide is a function of n, where n is proportional to the injected charge (eqn. 1.21). In general, the relationship is given in the following scheme [30]:

$n =$	0.1	0.2 – 0.4	0.6	0.7	0.8 – 1.0
	grey	blue	purple	red	golden brown

This scheme applies to the stoichiometric oxides (*i.e.* those having 3 oxygens per tungsten). Oxygen deficiency in the oxide, where a sub-stoichiometric form with $WO_{(3-y)}$ exists, shifts the dependence of colour on n.

The morphology, physical and optical properties of WO_3 and its reduction products vary with the mode of preparation. X-ray diffraction has shown that microcrystalline WO_3 is prepared by reactive sputtering (in the presence of oxygen) [117, 118, 119] while the amorphous form may be prepared by thermal evaporation [120], the sol-gel method [34], electrodeposition from a solution formed from tungsten powder and H_2O_2 [34, 121] or anodisation [34, 122, 123], the method used in this study. It is thought that amorphous films show faster electrochromic response times (section 1.2.4) as their porosity and water content are higher than crystalline films [115, 124]. The water content was measured using IR absorption spectroscopy [125] or SERS [123]. This dependence on morphology was demonstrated in studies that compared the electrochromic performance (especially in terms of response times and optical density) in films prepared by different methods. Also, studies where the initially amorphous film was gradually heated to a crystalline form reported a lengthening of response times and a decrease in absorbance with increasing crystallinity [115, 126], but this loss of performance may be due to reduced water content. Depending on the preparation method, the band gap of WO_3 and its reduction products range from 2.5 to 4.0 eV [120, 127], where the band gap decreases with increasing crystallinity [125].

The injected electrons in the relatively electron-rich reduced form are responsible for metallic (and hence reflective) properties displayed by the oxide when n is above a critical composition of $n_c = 0.3$ [30, 114]. Conductivity measurements have shown that this value marks the boundary between non-metal and metallic properties [119]. If $n > n_c$, the conductivity is char-

acteristic of a metal, and *vice versa* for $n < 0.3$. It is accepted that the oxide exists in a mixed-valent form when a non-metal. Tungsten is present in two oxidation states in the mixed-valent form, $M_nW^{VI}_{(1-n)}W^{V}_{n}O_3$, where the Roman numerals represent the oxidation state of W; this makes sense since the valence electrons are more likely to be localised to individual integer-valent sites in a non-metal. The origin of the blue colouration in the 'metallic' oxide where $n \approx 0.2$ is not fully understood, though the strongest evidence supports the idea that electron transfer between 5+ and 6+ sites causes the colouration [115].

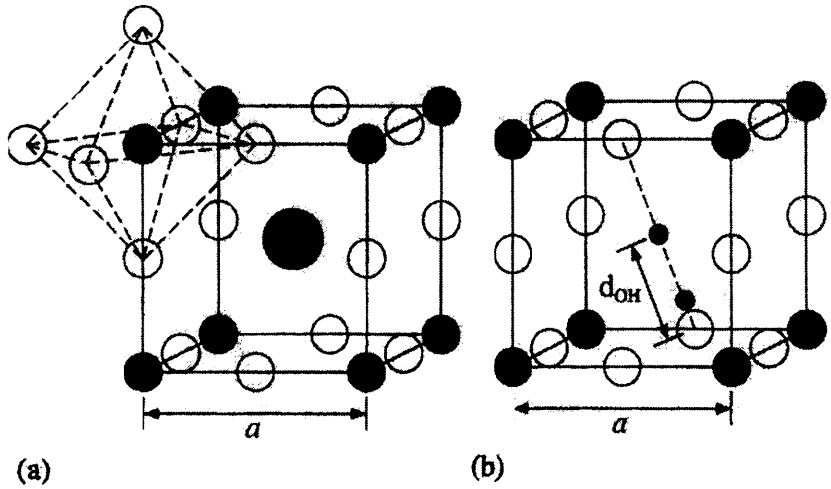

Figure 5.1: Unit cells for cubic (Li,Na)WO_3 (a) and HWO_3 (b). W atoms are large black dots, oxygen atoms are open circles, Li or Na is the grey dot, and H atoms are small black dots. Reproduced from ref. [112].

Structural aspects of electrochromic performance are less well investigated. The tungsten trioxide lattice is known to consist of a distorted octahedral structure with injected cations occupying the central position in the unit cell [112, 127] (fig. 5.1). A SERS study of anodically-grown oxides has

derived approximate W-O bond lengths ranging from 1.83–2.34 Å for the long distances in the distorted octahedron and *ca.* 1.69 Å for the short [123]. An EXAFS and XRD study of the crystalline oxide has shown that a lattice expansion of 6 % takes place upon reduction to accommodate the inserted cations [128]. This publication derived a 2-component model of the coloured film, consisting of W^{5+} and W^{6+} contributions with a total 1st shell coordination number of 6.0. From this model, the W-O bond lengths corresponding to both oxidation states were extracted. The first shell from the W^{6+} ions of the coloured film had 4 W-O distances ranging from 1.74 to 2.05 Å, with a weighted mean bond length of 1.88 Å; the 4 first shell W^{5+} ion bond lengths ranged from 1.82 to 2.19 Å, with a mean value of 1.99 Å. Colouration was also accompanied by an increase of Debye-Waller factors. Another study by the same authors examined the L_1 and L_2-edge spectra of a series of sub-stoichiometric oxides of WO_3, *i.e.* $WO_{(3-y)}$ (fabrication method not stated), where y varied by several fractional amounts between 0.10 and 0.30, in order to interpret the effect of multiple scattering shells on XANES and EXAFS [129].

Infrared and Raman spectroscopies by Daniel *et al.* characterised colouration and bleaching in terms of injection and ejection of water, respectively, and the formation and destruction of a terminal W=O bond at the surface [119, 127]. A long-range XRD and Raman study by Nanba *et al.* [130] disputed the previously mentioned remarks regarding the effects of crystallinity upon electrochromic performance. They stated that amorphous WO_3 films exist as networks of edge and corner-sharing octahedra forming 3, 4, and 6-membered rings of octahedra (see fig. 4.1); electrochromic performance (in terms of cation diffusion coefficients) increased with the number of 6-membered rings facing the electrode-electrolyte interface, *i.e.* with increasing crystallinity.

5.1 Objectives

Several short-range structural determinations for 'coloured' and 'bleached' states are documented, but from reading the introduction, it is clear that the coloured state encompasses a range of colours and compositions. The main aim of this investigation is to characterise the evolution of structure, composition and physical characteristics as an oxide layer grows on a tungsten surface. This study will not use the cathodic reduction route followed in most publications, but the approach will be from the other direction, *i.e.* anodic formation. The surface sensitive reflection mode EXAFS technique will be used to monitor changes in surface structure as a function of time or thickness. This is a novel application of the reflEXAFS technique. It is hoped that the low probing depth of the beam, tuned by using a very small grazing angle, will sample the growing oxide film, but not the thin tungsten electrode below as it is progressively converted to oxide. It is also hoped to determine film thickness from varying the probing depth of the beam, then interpreting the structure as it changes from oxide to metal.

It is understood that an *in situ* investigation in this configuration is ambitious, but it is an ultimate goal worth trying to achieve. An in-depth structural study of anodically-grown, electrochromic tungsten oxide films would be of benefit, of course, to the optoelectronic device industry. The work may also be useful to those wishing to understand corrosion, because these oxide films are known to form a (passive) protective barrier against corrosion.

5.2 Experimental

5.2.1 Sputter-Deposition of Thin Tungsten Films

Highly reflective tungsten oxide films were grown by anodically oxidising thin, dense, uniform tungsten films. The tungsten films were prepared by sputter-deposition using the radio frequency (RF) sputtering technique. RF

sputtering involved the bombardment of a tungsten sputtering target (12 cm diameter, exposed area 78.5 cm^2, 6 mm thick, 99.95 %, Goodfellow) with high energy ionised argon to displace W atoms from the target surface. The displaced atoms subsequently deposited onto the substrates.

The substrates were either polished float glass slides (75 x 25 x 0.7 mm^3) pre-coated on one side with a thin, transparent conductive layer of sputtered indium-doped tin oxide (ITO, surface resistance 4–8 $\Omega\,cm^{-2}$, ITO thickness $\sim$ 2000 Å, Delta Technologies Ltd., MN, USA) or plain float glass slides (76 x 26 x 0.8 mm^3, Chance Propper Ltd., UK). The slides were ultrasonically cleaned for 20–30 minutes in a glass slide stand filled with diluted Teepol cleaning fluid, then with acetone, and finally isopropyl alcohol. The slides were then dried in a stream of hot air. A batch of 4 slides (ITO coating facing outward) was secured to an aluminium foil-covered Cu mounting plate using a steel mounting frame, which also served to shield a small portion of each slide from deposition. The securely mounted substrates were then fixed into the sputtering chamber.

Deposition was achieved using a Nordiko NM-200 sputtering module connected to Nordiko N4-700 and N6-1400 pumping systems (rotary and diffusion pumps). A projection, onto which the substrate plate was fixed, was surrounded by a liquid nitrogen-filled cooling coil that enabled the chamber to be pumped down (overnight) to a base pressure of 5 x 10^{-7} mbar. Argon (99.998 %, BOC) was then introduced to the chamber at a rate of 46 $cm^3\,min^{-1}$, giving a constant chamber pressure of 12 mbar, maintained using a Vacuum General 78-7 flow control unit. A plasma of Ar ions was formed between the target and substrates by applying a radio frequency power of 300 W (3.82 $W\,cm^{-2}$) to the target. The power was supplied by a 13.56 MHz generator. The resultant DC target bias of 1.25 kV propelled the Ar^+ ions toward the oppositely charged target. The difference in mobility between the electrons (at the target) and Ar^+ caused a build-up of negative charge at the target surface, further accelerating the Ar ions. Earthing prevented the

other components within the chamber from also being bombarded.

A shutter, which shielded the substrates from deposition, was kept in place while the target was cleaned by the plasma during a pre-sputter lasting 90 minutes. The shutter was then removed, allowing the W atoms to deposit. Films were deposited for 45, 90 and 120 minutes. When deposition was complete, the plasma was extinguished by reducing the RF power to zero and stopping the flow of argon. The chamber remained under vacuum until the next day in order to remove hazardous vapours before the chamber was opened. Once removed from the chamber, the samples were stacked between soft paper strips to prevent scratching. Films sputtered for 90 mins or longer appeared uniform and were adherent; those deposited for < 90 minutes contained pinholes.

5.2.2 Measurement of Film Thickness

The thickness of the tungsten films was measured using a Rank-Taylor Hobson surface profilometer (or talystep), utilising a motor-driven stylus which passed from a bare (previously masked) region of the substrate to the film. The motion of the sensitive stylus was amplified and a profile of the edge of each film was recorded. The accuracy of these readings was ± 0.05 μm. Five measurements were taken from every film, each at a different position along the film edge. These measurements were averaged to give an overall film thickness for (the edge of) each film. Films deposited for 45 minutes gave a mean thickness of 0.31 μm, films deposited for 90 minutes were about 0.71 μm thick, and 1.0 μm was the thickness of 120 minute films, giving an average deposition rate of about 8 nm min^{-1}.

5.2.3 Spectroelectrochemical Cell

Reflection mode XAS and X-ray reflectivity pose a substantial challenge to spectroelectrochemical cell design. Since grazing angles less than the critical

angle of tungsten are small ($\theta_c \simeq 0.4°$ at 10 keV), the film, underlying working electrode (ITO in this case) and substrate must be very flat to prevent scattering from rough features. Techniques such as sputtering are necessary to deposit uniform surface layers, and extremely flat substrates such as float glass are essential. The peak-to-peak roughness of the polished float glass slides used was < 3.8 nm mm^{-1} (Delta Technologies Ltd.). A large working electrode area is also a necessity for grazing incidence reflection because the beam 'footprint' is long at such low angles. A surface layer of electrolyte is required for *in situ* spectroelectrochemical applications, but the long beam trajectory through the absorbing electrolyte limits *in situ* use to hard X-rays ($\geq$ 10 keV). Potentiostatic and potentiodynamic procedures such as overcharge, discharge, cyclic voltammetry and some deposition techniques (section 5.2.4) are problematic in this configuration because the large electrode area encourages uneven current density, and maintaining a dynamic diffusive exchange of ions across the whole illuminated area is difficult to achieve. The novel cell described here was designed for *in situ* use and contains features intended to counter all of the aforementioned difficulties.

The cell (fig. 5.2) consisted of a watertight epoxy resin-sealed perspex box (outside dimensions 100 x 48 x 37 mm^3, inside dimensions 90 x 38 x 25 mm^3). Samples were fixed to the PTFE sample stage (13 mm high, 80 x 30 mm^2 from the top) using short strips of double-sided tape. Two pegs fixed to the bottom of the stage allowed samples to be removed and replaced precisely to the original position within the cell. A mylar window located in the lid of the cell enabled the (simultaneous) measurement of fluorescence spectra. Mylar windows at each end of the cell transmitted the incident and specularly reflected beam. The angle of incidence was low for these experiments, so the windows aligned with the top of the sample stage. All mylar windows were glued to the inside surface of the cell to prevent condensation from collecting at the window recesses in the humidified environment of the sealed cell. A plastic tap at the bottom of the cell enabled the drainage of electrolyte

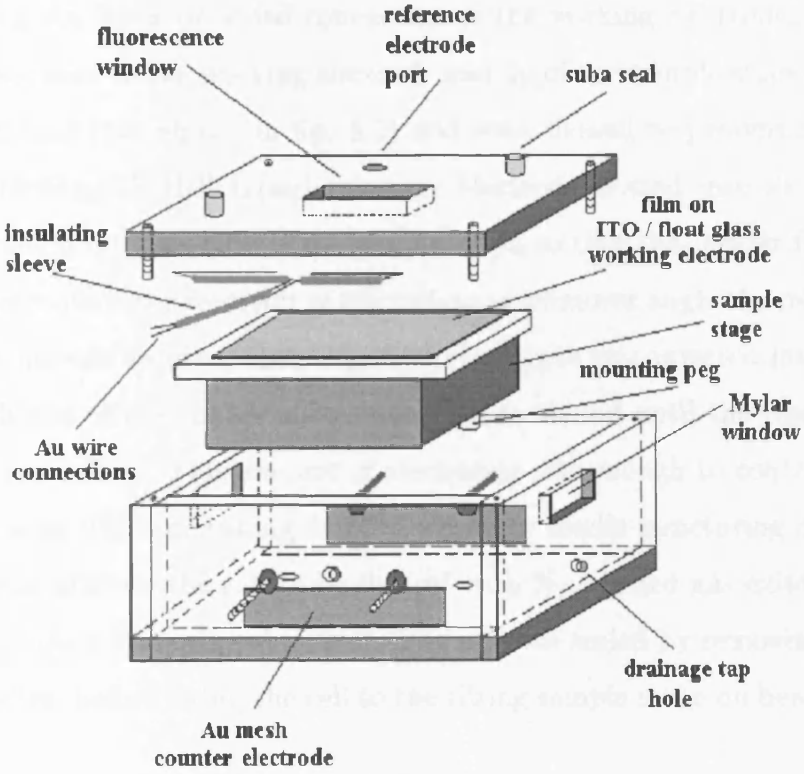

Figure 5.2: Exploded view of reflection mode spectroelectrochemical cell.

without dislodging the cell from its position.

For *in situ* electrochemical use, two filter paper 'wicks' (not shown in fig. 5.2) were gently clipped to both lengths of the sample stage using slitted silicone tubing. These 'wicks' facilitated contact between the film upon the sample stage and the reservoir of electrolyte below, without interrupting the beam path. Ionic species would therefore be able to exchange between film and electrolyte, but at a rate that precludes potentiodynamic experiments such as cyclic voltammetry. Au mesh counter electrodes, positioned along both lengths of the cell were designed to provide constant contact with the electrolyte from both sides of the sample stage. These electrodes were held in place using steel screws, which projected outside the cell. Wires attached

to the ends of the screws provided electrical connection to the counter electrodes. Long Au wires provided connection to the working electrode; these wires were secured to the working electrode and lip of the sample stage using PTFE G-clamps (not shown in fig. 5.2) and were sleeved to prevent shorting. The $Hg|Hg_2SO_4|H_2SO_4$ (aq) reference electrode slotted into its port, situated in the lid, to one side of the sample stage, so that the slender fritted probe would contact the reservoir of electrolyte at whatever angle the cell was tilted. The lid was secured, then degassed electrolyte was injected into the cell through one of the rubber suba seals fixed to the lid until the reservoir was about 1 cm deep. This amount of electrolyte was enough to contact all three electrodes. Silicone tubing fixed to a syringe needle puncturing one of the suba seals allowed the cell to be flushed with N_2; ejected gas exited via a syringe needle in the other suba seal. The cell was sealed by removing the syringe needles, before fixing the cell to the tilting sample stage on beamline 9.3.

5.2.4 Preparation of Tungsten Oxide Films

A sputtered tungsten film (electroactive area 12.5 cm^2) was placed vertically into a beaker of degassed aqueous 0.1 M H_2SO_4 solution. The masked end of ITO-coated slides projected from the surface of the solution; a small portion of the W film was exposed for non-conductive slides. The projecting end of the slide was gripped between two nickel strips using a crocodile clip. The strips prevented the crocodile clip from piercing the ITO (or W) coating or breaking the delicate slide; they also served to spread a more uniform current density across the width of the film. A gold mesh counter electrode (the one used as a working electrode in the previous chapter) and a Hg/Hg_2SO_4 reference electrode (section 1.2.1), to which all potentials refer, completed the three-electrode cell.

A Kepko potentiostat was used to apply an initial cathodic potential of

-0.1 V for 15–20 minutes to remove any oxide film that may have formed on the tungsten surface. A linearly increasing anodic potential was then applied to the tungsten film at a constant rate of either 0.2 or 0.5 mV s^{-1} (details given in table 5.1). These scan rates proved to be suited to even layer formation; the high current densities imposed at higher scan rates caused the tungsten to pit and peel from bubbles generated at the ITO surface, arising from the acid attacking the ITO. The voltage was increased to a value between 4 and 30 V and stopped when the desired film colouration was achieved. This wide voltage range was necessary since the tungsten atoms required oxidation from a valency of zero to around 4–6. The film was then rinsed with deionised water, fixed to the sample stage and mounted into the spectroelectrochemical cell on the optical bench.

Most films appeared dense and shiny, and colours ranged from brown (at lower potentials) to deep blue and pale yellow (at higher voltages). Oxide films deposited on ITO-coated glass exhibited uniform colouration across the illuminated area; only a slight difference in colour was observed at the edges of some slides. W films without an ITO layer (where tungsten itself acted as the WE) produced films displaying a range of colours with a gradation that implies a significant voltage drop along the length of the film. Such films were therefore unsuitable for further analysis. The uniform oxide films created are listed in table 5.1 where charge density was derived from the anodic formation charge and the electroactive area.

5.2.5 EXAFS and X-ray Reflectivity

All reflectivity and EXAFS measurements were performed *ex situ*, in most cases soon after the preparation of each film. *In situ* measurements, with the film immersed in electrolyte proved unsuccessful, primarily because an electrolyte layer could not adhere evenly to the shiny surfaces of the tungsten films when mounted into the spectroelectrochemical cell. This effect was

W thickness (μm)*	Max. voltage (V)	Scan rate ($mV\,s^{-1}$)	Charge Density ($C\,cm^{-2}$)
0.78	5	2	0.2
0.78	5	2, 5	0.9
0.78	10	5	1.6
0.40	20	5	3.2

* Average film thickness for batch

Table 5.1: Conditions for anodic growth of tungsten oxide films on ITO-coated float glass substrates.

accentuated when the cell was tilted.

i) Standard Transmission EXAFS

Tungsten foil, WO_2 (Aldrich) and WO_3 (99+ %, Aldrich) were used as reference materials. The powdered oxides were prepared as stated in the General Experimental chapter. Transmission mode spectra of the standards were taken at the W L_3-edge (10207 eV) on beamline 9.2 at Daresbury, following the procedure given in sections 2.1.4i and 4.3.5i. The spectra ranged from 9950 to 10750 eV and the EXAFS ranged from about 2 to 11.5 $Å^{-1}$.

ii) Reflectivity Profiles

Reflectivity profiles were recorded on beamline 9.3 at Daresbury, using the configuration shown in figure 1.4, with ion chambers filled with the appropriate mixtures of gases for measuring the W L_3-edge. Correct alignment of the sample was essential in order to maximise the reflected signal from the film.

The incident and reflected beams were collimated with horizontal slits positioned to the front and rear of the cell. These slits were constructed

from tungsten blocks separated by 50 μm thick Cu strips. Both front and rear slits could be tilted forward or backward and moved vertically (raised or lowered). The stepper motor-controlled stage, onto which the cell was fixed, could also be moved vertically and tilted forward or backward. First, the sample was moved down so that it completely cleared the beam, making $I_o \approx I_t$. I_o was maximised by altering the vertical position of the front slit, then by tilting the slit until it lay completely flat, so that I_o was at its highest. I_t was then maximised by repeating the procedure for the rear slit. The sample was then moved up into the beam, so that I_t was halved. Then the sample was tilted to optimise the remaining beam; here, the angle of optimum flux corresponded to $\theta_0 = 0°$. Now that the sample was completely flat, fine-adjustment of the vertical position of the sample ensured that half the original optimised intensity was cut.

Alignment was now complete and an angle scan could be measured. The rear slit was moved upward in 0.05 mm steps until the remaining intensity was reduced by 90 %, so that only the specularly reflected signal was recorded. The upper half of the rear slit was removed, then the sample angle was scanned in 50 mdeg steps from $\theta_0 < 0°$ (*i.e.* where the sample was blocking part of the beam) to $\theta_0 > \theta_c$ ($\sim 0.6°$). Alignment was repeated when the sample was changed and after significant beam movements (*i.e.* when the beam was restored after shut-down). Most angle scans were measured at 10.1 keV, just below the energy of the W L_3-edge, where the probing depth of the beam is short and the critical angle is well-defined (see figs. 1.5, 1.6, 1.8 and 1.9).

The reflectivity profile of a plain tungsten film was measured before the profile of each oxide film was recorded, so that the critical angle of the tungsten film could be used as the equivalent of a monitor absorption edge in the transmission geometry; once 'monitor' angle scans were aligned, the shift between critical angles of oxide and metal could therefore be established.

iii) Reflection and Fluorescence Mode EXAFS

A Canberra multi-channel solid state detector positioned above the cell enabled fluorescence spectra to be recorded simultaneously with reflEXAFS measurements. A series of dual reflEXAFS/flEXAFS measurements was made once the corresponding angle scan of a sample had finished. The incident angle was usually set at $\theta_0 < \theta_c$ (0.16 °) so that the probing depth would be very low and reflectivity would be high (see figs. 1.5, 1.6, 1.8 and 1.9). The procedure for recording reflEXAFS spectra is essentially the same as for the standard transmission mode, detailed in sections 2.1.4i, 3.2.3i and 4.3.5i. ReflEXAFS and fluorescence spectra at the W L_3-edge usually spanned 9780 to 10750 eV and the EXAFS ranged from about 2.5 to 12 $Å^{-1}$. Single monitor spectra were recorded before and after each set of reflEXAFS/flEXAFS measurements from the oxide sample was taken because, as stated in the previous section, I_o was much lower for reflection mode experiments than conventional transmission measurements. The reflected signal was therefore too weak to subsequently traverse a metal foil monitor. When probing the depth of an oxide layer, the incident angle was increased from about 200 to 1200 mdeg while each set of reflEXAFS measurements was taken, (spectra were sometimes measured at 2 or 3 angles in this range). The resulting series of spectra sampled progressively downward from the surface region.

5.2.6 Characterisation of Films Using UV/visible Spectrophotometry

A less subjective characterisation of the oxide films, in terms of the wavelength corresponding to maximum UV/vis absorbance was attempted after EXAFS and X-ray reflectivity measurements were completed. A Perkin Elmer 330 spectrophotometer, operating between 2500 and 200 nm, with a beam size of about 1.5 x 1.0 cm^2 was used to measure UV/vis transmittance (I_t/I_o) as a function of photon wavelength. The transmittance of the ITO-

coated float glass was 83 % (at 800 nm). Transmittance measurements from the oxide films (and tungsten) were unsuccessful because all films gave almost zero transmittance throughout the full spectral range, presumably due to the underlying metallic phase. Instead, reflectance mode measurements were made. I_0 was measured by calibrating using a highly polished metal mirror, and reflectivity $R = I_R/I_0$ was measured as a function of energy for each sample.

5.3 Data Analysis

5.3.1 Analysis of Reflectivity Profiles

Even though the reflectivity profiles were measured at an energy where the probing depth was short ($E < E_{edge}$), a contribution from the underlying metal was always present in the reflectivity profiles of the films. The critical angles of tungsten and the oxide samples were similar, and the critical angle of the metal was higher than the oxides, so the critical angle of the metal was usually obscured by the sample signal. Successive reflectivity profiles from the same metal film were in different positions, giving different critical angles for the metal, probably due to slight variations to the position of the beam from one scan to the next (although the shapes of the curves were identical). This meant that the use of a 'monitor' angle scan to determine the critical angle of a subsequently measured oxide sample would lead to erroneous results. However, the presence of a tungsten signal in every oxide scan proved fortunate because its signal could be used as an internal monitor spectrum. The first derivative of each reflectivity curve was taken. The oxide films always showed two negative peaks in the first derivative. These corresponded to the inflection points of oxide and metal curves. The peak at higher angle was taken to be the critical angle of the metal. The tungsten peaks in the first derivatives were aligned. Each corresponding profile

was then adjusted by the same amount so that the tungsten peak in each profile aligned. These corrections allowed the relative positions of the oxide curves to become evident. Since all of the curves were arbitrarily aligned to the tungsten peak in one of the spectra, it is unlikely that this represented the true critical angle of tungsten. The aligned tungsten peaks were then corrected to the tabulated value for tungsten at that energy [7]. The critical angle of sputtered tungsten is probably lower than the tabulated value for a tungsten mirror, because sputtered films are likely to have a lower density, but the slight variation to the position of each scan means that the true critical angle of the sputtered films is not known. Once the reflectivity profiles were aligned in the correct position, the relative position of the critical angle of each oxide layer could be determined from the corresponding first derivative of its profile. Changes to oxide layer density and thickness were interpreted qualitatively from the relative position of the oxide critical angle and the variation of tungsten reflectivity, respectively.

Plotting log R *vs.* angle revealed no appreciable interference fringes in the region of low reflectivity above the critical angle. Oxide film thickness therefore could not be derived from the reflectivity profiles.

5.3.2 Analysis of EXAFS Spectra

All spectra recorded in standard transmission, reflEXAFS and flEXAFS modes were calibrated and summed (where necessary) using EXCALIB, normalised and background subtracted using EXBACK and fitted using EXCURV98. Edge steps were consistently normalised to a post-edge feature common to all spectra. Edge positions were measured as the energy corresponding to a normalised edge height of 0.5. Edge shifts were calculated as the difference between oxide and corresponding monitor flEXAFS edge positions. ReflEXAFS edges were not used to determine edge positions because they sometimes displayed a distorted pre-edge, implying some rough

samples. Pre-edge subtraction was therefore inconsistent and erroneous edge shifts were more likely to be derived from these spectra. Simultaneous monitor spectra were not measured because the reflected intensity was too low to subsequently traverse a foil calibrant. A reflEXAFS monitor spectrum was therefore recorded prior to each set of oxide spectra. This methodology is valid since successive monitor edges were in virtually identical positions. As in previous chapters, the energy scales of spectra recorded on different beamlines and different sessions were corrected by moving the flEXAFS-derived edge of each tungsten monitor (station 9.3) to the position of the principal reference metal foil measured in standard transmission mode (station 9.2). Then the energy scales of all corresponding oxide spectra were adjusted by that amount in order to overlay the XANES recorded on different stations and during different sessions on the same energy scale. The sputtered W film used for dual reflEXAFS/fluorescence measurements had a slightly higher white line than the metal foil standard, indicating that the surface of the metal film had oxidised, but they were assumed to possess the same edge position for energy scale correction. This assumption is reasonable since the shape of the W film edge matched that of the metal foil in the lower XANES region, where edge positions were measured.

Standard transmission EXAFS of the standards were analysed using the general procedures followed in previous chapters. Tabulated crystallographic structures for W foil and the oxide powders were used to provide an outline of the expected structure [50]. Great difficulty with fitting the amplitudes of both ref-WO_2 and ref-WO_3 spectra required setting the coordination numbers of the first W-O shell to their literature values. This action resulted in a great improvement to the fits. Several successive spectra from each standard were summed to improve the signal-to-noise ratio. Successive reflEXAFS (and flEXAFS) spectra were also summed. Numerous distorted and regular fits to W-O and W-W shells were attempted; multiple scattering fits were also tried where it was considered likely *i.e.* where 3 shells were equally separated. Both

reflEXAFS and flEXAFS spectra were fitted. Only fits producing the lowest fit index and most physically reasonable structures are presented, *i.e.* the corresponding (2σ) error for each coordination number could not exceed the magnitude of the fitted value, and Debye-Waller factors had to be positive.

5.4 Results

5.4.1 Characterisation of Tungsten Oxide Films

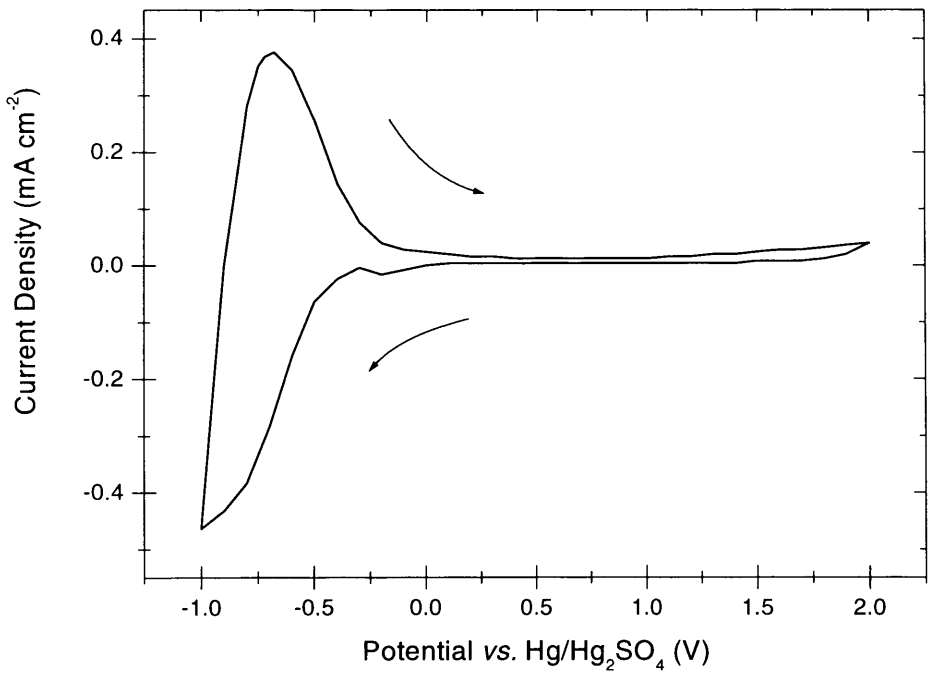

Figure 5.3: Typical cyclic voltammogram for an anodic tungsten oxide film (on ITO/float glass substrate) exposed to aqueous 0.1 M H_2SO_4 solution. Potential scan rate 50 mVs^{-1} and Γ = 0.03 μ mol cm^{-2} of W.

The cyclic voltammograms recorded (fig. 5.3) were highly characteristic of the well-known $WO_3 \rightleftharpoons H_nWO_3$ redox conversion for anodic tungsten oxide films in aqueous electrolyte [34]. It was not always possible to observe a

definite colour change during cyclic voltammetry, but when films that were originally blue were oxidised, they displayed a yellow tinge when removed from the electrolyte. Conversely, scanning the potential to the cathodic limit reversed the yellow colouration, resulting in a deep blue film. These attractive colour changes are typical electrochromism for the system. Figure 5.3 shows that typical cyclic voltammograms were not distorted; this is because the ITO underlayer delivered a uniform current density across the film, indicated by the even colouration both after anodisation (formation) and after voltammetric cycling. Another reason for the lack of distortion was the fact that CVs were recorded from the deposition bath, not the spectroelectrochemical cell, which has a non-ideal electrode geometry. Potentiodynamic procedures such as anodisation and cyclic voltammetry could not be achieved *in situ* for the reason stated in section 5.2.5 *i.e.* that electrolyte could not be maintained across the surface of the film mounted on the cell's sample stage. The cathodic and anodic charges were equal at 0.04 C. The charge passed during a voltammetric cycle was much smaller than the formation charge of any of the films, so only a small fraction of the total number of tungsten oxide sites were oxidised or reduced during a voltammogram, as indicated by the yellow tinge induced by cyclic voltammetry. Voltammograms recorded from brown films were highly asymmetric (in terms of total charge and peak shape) and not reproducible, *i.e.* successive CVs did not overlay at all; these voltammograms probably corresponded to dissolution of the oxide and reversion of the oxide film to the metallic state when reduced. All of the films visibly retained their original colours for over a year after removal from the electrolyte, suggesting that the oxides formed were stable and the 'memory' effect was lasting (section 1.2.4).

When characterising the films in terms of UV/vis reflectance (fig. 5.4), a slight change that signifies an optical absorption edge (and hence an optical band gap) and a colour (via λ_{max}) was identified in the brown oxide film (charge density during formation = 0.2 $\mathrm{C\,cm^{-2}}$) and the tungsten film. The

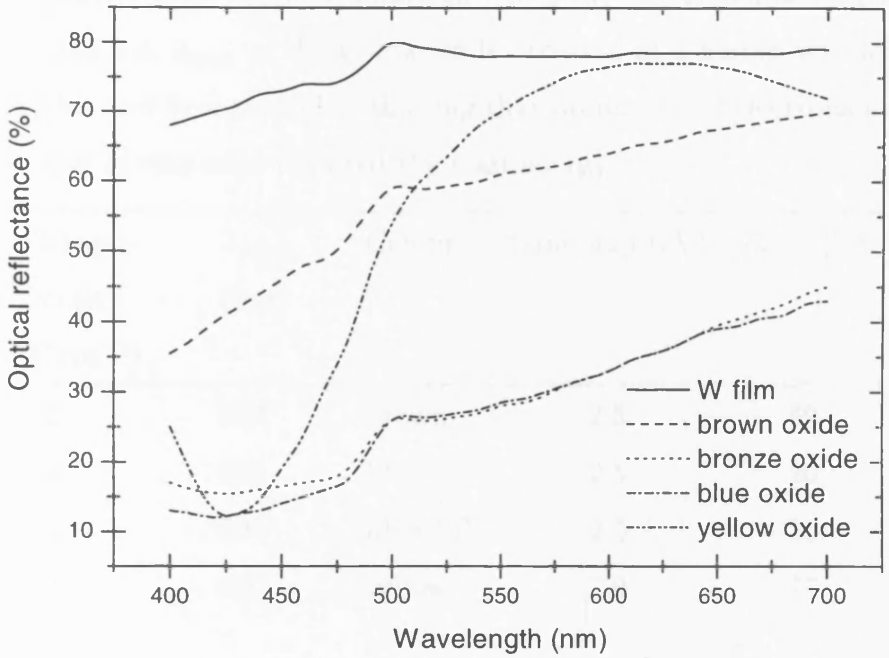

Figure 5.4: Optical reflectance of a sputtered tungsten film and four oxides.

brown oxide generally behaved as a metallic sample, having a high reflectivity and a shallow absorption edge. The cruder description of observed colour will be used when referring to this film. The other films gave an absorption edge, though in most cases the edge was weak, implying either a significant contribution from the metal or metallic behaviour. The wavelength corresponding to maximum reflectivity (λ_{max}) was used to characterise the colour of the films. Tabulated values for λ_{max} with their corresponding colours [131] defined the colour of each film; these are listed in table 5.2. To avoid confusion with the deep blue oxide, the first blue film (formed at 0.9 C cm^{-2}) will be referred to hereafter as the bronze film, as its colour was originally perceived to be a deep bronze, rather than a blue. The film formed at 3.2 C cm^{-2} was the only film to give a strong absorption edge, suggesting that this sample was less metallic than the rest. The energy corresponding to the reflectance maximum also indicates the optical band gap of the film. This

optical transition signifies the promotion of electrons across the band gap, from the valence band to the conduction band; the experimental values are given in table 5.2. λ_{max} of the yellow oxide occurred at a higher wavelength than the blue and bronze oxides, showing that promotion of electrons across the band gap of this solid required the least energy.

Charge Density ($C\,cm^{-2}$)	λ_{max} (nm)	Colour	Band gap (eV)	R_{max} (%)
0.2	502	brown	2.5	59
0.9	505	blue (i)	2.5	26
1.6	505	blue (ii)	2.5	26
3.2	620	yellow	2.0	77

Table 5.2: Optical properties of tungsten oxide films on ITO-coated float glass substrates.

All of the films were highly absorbing in the visible region, giving virtually zero transmittance. This may be due, in part, to the presence of an unconverted metal underlayer beneath each oxide. The optical reflectivity of the metal film, at 50 %, was similar to both brown and yellow films, and the darkest coloured films gave the lowest maximum reflectivity, less than half of the metal value (see table 5.2). The reflectivity minimum of all films was about 15 %. Optical interference effects were recorded before the absorption edge of some of the oxides, but too few fringes were present to establish a regular period. The presence of the fringes implies that the thickness of some of the oxide layers were similar to the wavelengths used (0.2–2.5 μm).

Figure 5.5 shows that the critical angle for X-ray reflection of the oxide was always lower than the metal, correctly implying a lower oxide density than the sputtered metal. The critical angles of oxide and metal were similar; about 0.3–0.4° for the oxides, compared to 0.4° for the metal, implying that

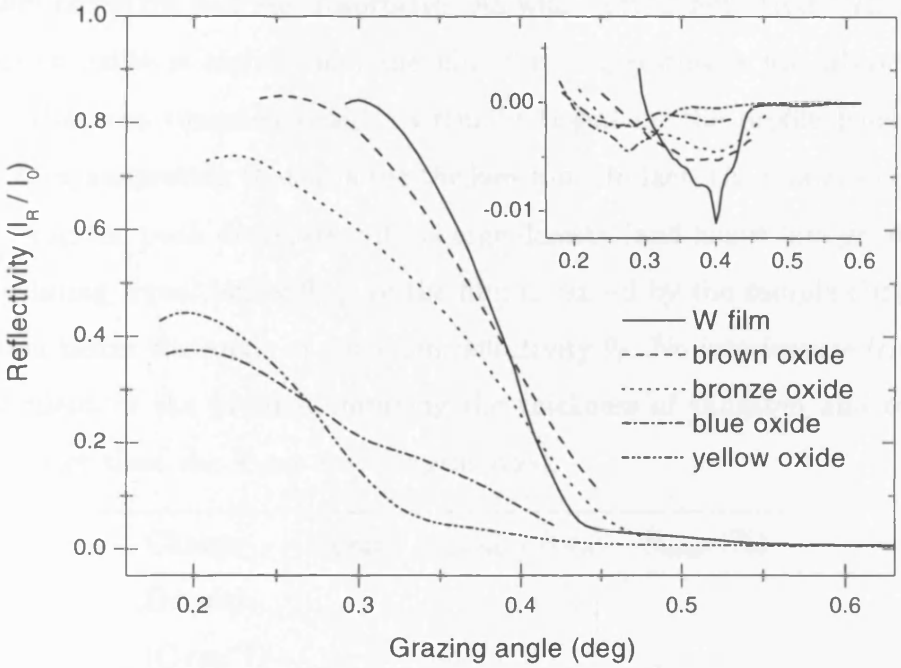

Figure 5.5: X-ray reflectivity profiles of a sputtered tungsten film and four oxides. Scans measured at 10.1 keV. The inset shows the first derivative of the curves.

tungsten and oxide films had similar densities. The maximum reflectivity of metal 'monitor' scans was always at least 80 %. In most cases, the maximum X-ray reflectivity of the metal was obscured by the film signal, where a low metal reflectivity usually coincides with a thick film. R_{max} follows a similar trend to the optical reflectivity (table 5.2), for instance the brown oxide and the metal have similar maxima. Both figure 5.5 and table 5.3 show that the brown oxide has the highest, and bronze the lowest critical angle, implying that the bronze film has the highest density of all the films. Contrary to optical reflectivity, bronze and blue oxides do not display similar maxima, so the bronze film is more reflective in this region. By the same argument, blue films display more absorptive behaviour. This difference also suggests that their colours and valence shell structure are similar, but they differ in terms

of physical properties such as density, since denser, shinier, metallic materials are more reflective and less absorptive. As with optical reflectivity, R_{max} of the yellow oxide is higher than the blue film, suggesting a less absorbing layer. Also, the tungsten peak is virtually absent on the profile from the yellow film, suggesting that it is the thickest film. In fact, the relative height of the tungsten peak decreases with charge density (and hence film growth). The declining signal below θ_{max} of the film is caused by the sample clipping the beam below the angle of optimum reflectivity θ_0. No interference fringes were evident in the profiles, implying the thickness of tungsten and oxide were greater than the X-ray wavelengths used.

Charge Density ($C\,cm^{-2}$)	Colour	$\theta_{c(film)}$ (deg)	R_{max} (%)
0.2	brown	0.36	85
0.9	bronze	0.26	75
1.6	blue	0.28	37
3.2	yellow	0.28	44

Table 5.3: Properties for X-ray reflection, derived from reflectivity profiles of the oxide films. Critical angles were derived the inflection points of the angle scans.

Film thickness could not be calculated using the absorption edge step because the it is likely that the edge step would include a contribution from the metal. In any case, it would not be a viable method since the beam path through the film is longer than if transmitted through the thickness of the sample. The thickness of the tungsten, measured using the talystep (section 5.2.2), was not useful for deriving oxide film thickness (except as an approximate upper limit) because all of the evidence suggests that the tungsten was not fully converted to oxide in any of the films. Thickness

could not be calculated using the electrochemically-derived charge because it could not be guaranteed that the concentration of the film was constant as charge density increased. Therefore, three variables required evaluating: the number of electrons transferred, n, the concentration (or density) of the film and film thickness.

5.4.2 Conversion of Tungsten Metal to Tungsten Oxides

From a first glance at figure 5.6, the XANES of the oxides appear to follow no particular pattern. Upon closer inspection, it can be seen that the blue oxide gives the furthest edge shift at the normalisation point of $y = 0.5$. This trend is not continued above this point, and the edge of the bronze oxide is in the most positive position by around $y = 1.0$, though it crosses with the yellow oxide edge in the white line region. These oxide edges appear broad, the yellow oxide displaying the broadest edge, spanning all of the other samples, including W foil, implying that tungsten atoms exist in a range of oxidation states within the yellow film (at least).

It is not surprising that all of the edges overlap at some point because all of the derived edge shifts were small. The average edge shift per formal unit of valency, calculated from the edge shift of the standards, is only 0.32 eV. A second order polynomial fit to the edges of the standards (figure 5.7) shows that a curved relationship exists between edge shift and formal valency. The gradient of the curve decreases with valency, and WO_2 and WO_3 edges differ by only 0.26 eV. At this level, the difference between WO_2 and WO_3 edges is not significant since the energy difference between the data points was 1 eV; therefore, only edge shifts greater than ± 0.5 eV were significant. Consequently, all of the measured edge positions must be considered approximate *i.e.* yellow oxide and tungsten edges are not significantly different; this also applies to the brown oxide and WO_2, and to both oxide standards as well.

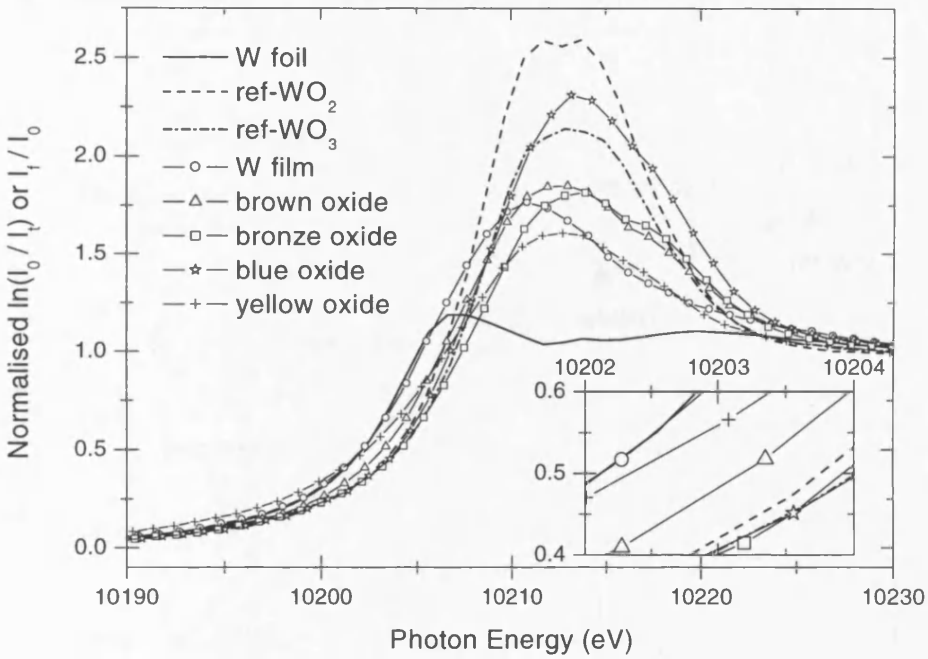

Figure 5.6: Normalised W L_3-edge XANES of reference materials (standard transmission mode), sputtered tungsten and oxide films (dual reflEXAFS/flEXAFS mode, fluorescence XANES shown here). Corresponding reflEXAFS scans measured at 0.16 °.

An additional source of error is the fact that simultaneous internal monitor spectra were not measured. Nevertheless, the error associated with determining edge shifts was minimised, so pre-edge subtraction and normalisation was performed as consistently as possible.

Bronze and blue edges are not significantly different and could be characteristic of WO_2, WO_3 or H_nWO_3. Analysis of the EXAFS data can establish whether a significant difference exists between them. From the calibration curve, overall W non-integer valences ranging from 0.65 for the yellow oxide to 5.7 for the blue oxide were derived (table 5.4). These valences were used to derive an approximate value of n for each of the films, assuming a maximum valency of 6.0 (*i.e.* 6 – derived valency = n). Table 5.4 shows that the blue

film contains the critical amount of incorporated cations, which marks the boundary between metallic and non-metallic properties ($n = 0.3 = n_c$).

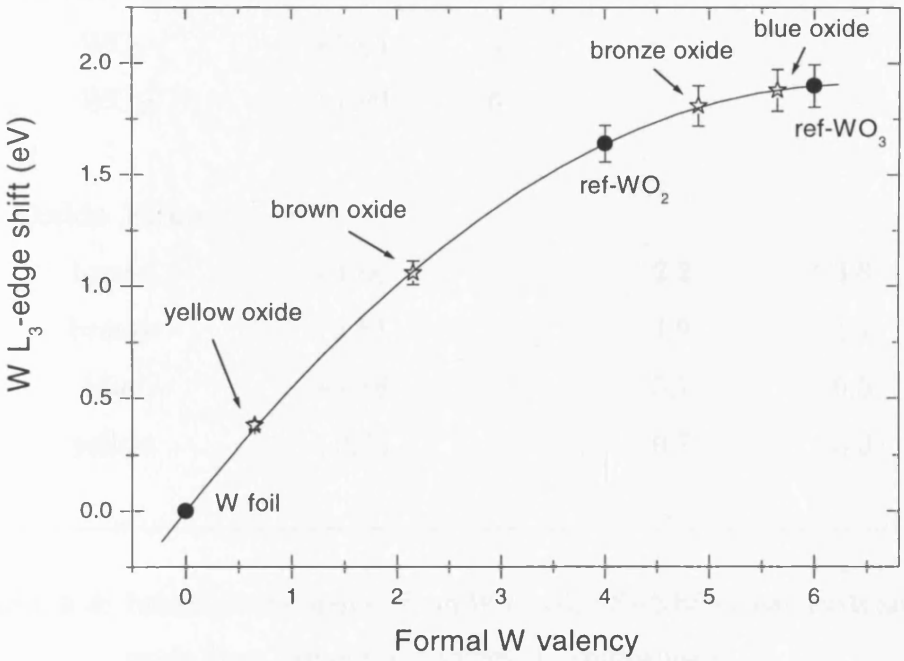

Figure 5.7: Calibration curve defined by a 2nd order polynomial fit to the transmission mode W L_3-edge shifts of the standards (dots) at various integer W valences. Fluorescence mode edge shifts of the films (stars) are superimposed on the calibration curve. Error bars represent 95 % confidence levels.

It can be seen that the absorption edges of the sputtered W monitor film and W foil follow the same shape for most of the foil edge (beyond $y = 0.5$), showing that the contribution of the surface oxide layer was small. The largest white line height was produced by the blue oxide, its amplitude approaches that of WO_2. Conversely, the yellow oxide spectrum has the lowest white line, lower than that of the W film. Bronze and brown film spectra have similar white line heights to the W film. The wide variation in white line height suggests a change in the structure of the oxide as a function

Sample	Edge Shift (eV)	Formal W Valency	Derived W Valency	n
Standards				
W film & foil	0	0	–	–
WO_2	+1.64	4	–	–
WO_3	+1.90	6	–	–
Oxide Films				
brown	+1.06	–	2.2	3.8
bronze	+1.81	–	4.9	1.1
blue	+1.88	–	5.7	0.3
yellow	+0.38	–	0.7	5.3

Table 5.4: Information obtained from W L_3-edge XANES of standards and oxide films. All of these values are approximate.

of formation charge. These implied structural changes were pinpointed by analysing the EXAFS.

Figure 5.8 displays typical reflEXAFS and flEXAFS spectra that were recorded simultaneously. Slight curving of pre-edge and EXAFS regions of most reflEXAFS spectra was evident, implying that the films had rough surfaces. The roughest films, which gave the most distorted spectra are not presented in this chapter. These films were grown at high potential scan rates; the rapidly increasing current density caused the films to pit, and generally their XANES and EXAFS were dominated by the tungsten exposed at the surface.

The fact that the probing depth constantly varied during an energy scan (fig. 1.5) may have caused these spectra to be slightly warped compared to the corresponding flEXAFS spectra, *i.e.* the beam wasn't always passing

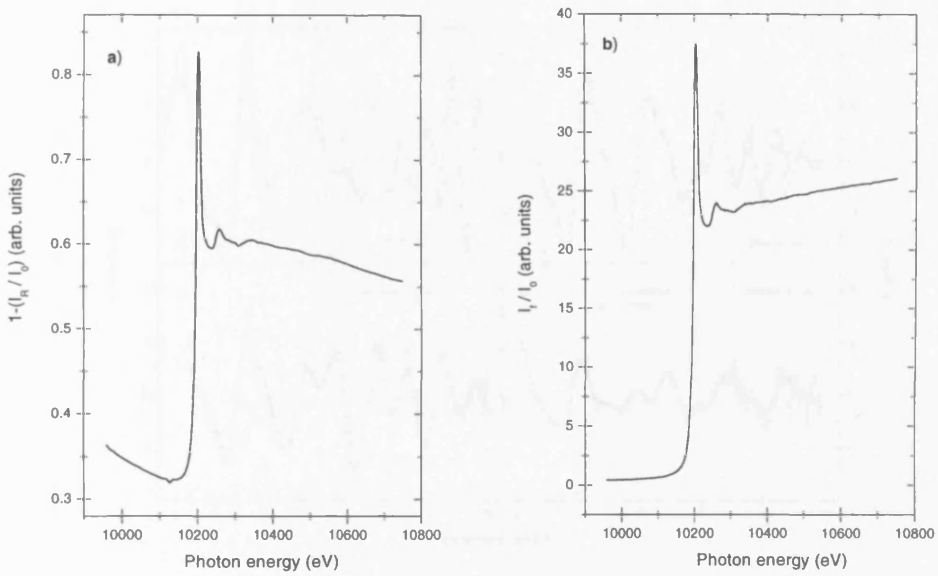

Figure 5.8: Simultaneously recorded reflEXAFS (a) and flEXAFS (b) spectra from the bronze oxide. Refer to text for preparation details.

through the same amount of material. However, when summed, all of the spectra were of a good quality, though fluorescence spectra usually gave the best fitting results (lowest errors). Typical fits are displayed in figures 5.9 and 5.10. In all cases, fits derived from corresponding reflEXAFS and flEXAFS spectra agreed. Small tungsten peaks in the position of the shells in the metal were present in every spectrum, but were too small to be significant. These arose either from small amounts of unconverted tungsten within the oxide layer or from a separate tungsten layer beneath the oxide. However, the insignificance of W metal shells shows that the amount of metal was small compared to the amount of oxide for the sampling depths used; this was also evident from the reflectivity profiles.

The valency of tungsten could not be derived from a calibration curve based on first W-O distances because only two points would have defined the curve, making the method invalid for this system. Fitted values for first W-O and W-W distances of the standards and films are listed in table

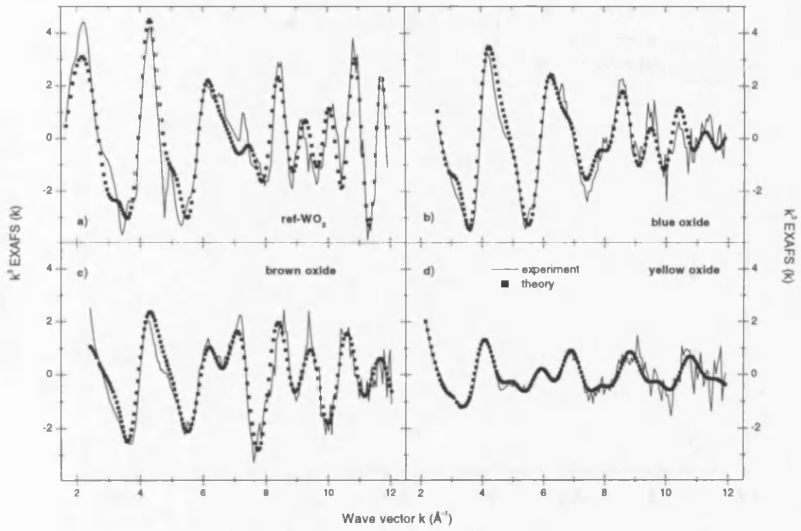

Figure 5.9: k^3 weighted EXAFS with fits for (a) WO_2 powder and (b–d) oxide films grown at 0.2, 1.6 and 2.3 $C\,cm^{-2}$, respectively.

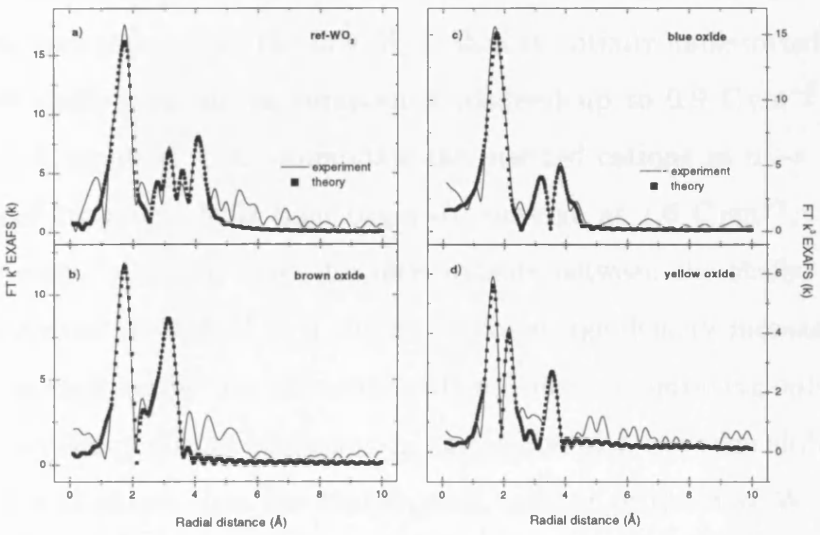

Figure 5.10: k^3 weighted radial structure functions with fits for (a) WO_2 powder and (b–d) oxide films grown at 0.2, 1.6 and 2.3 $C\,cm^{-2}$, respectively.

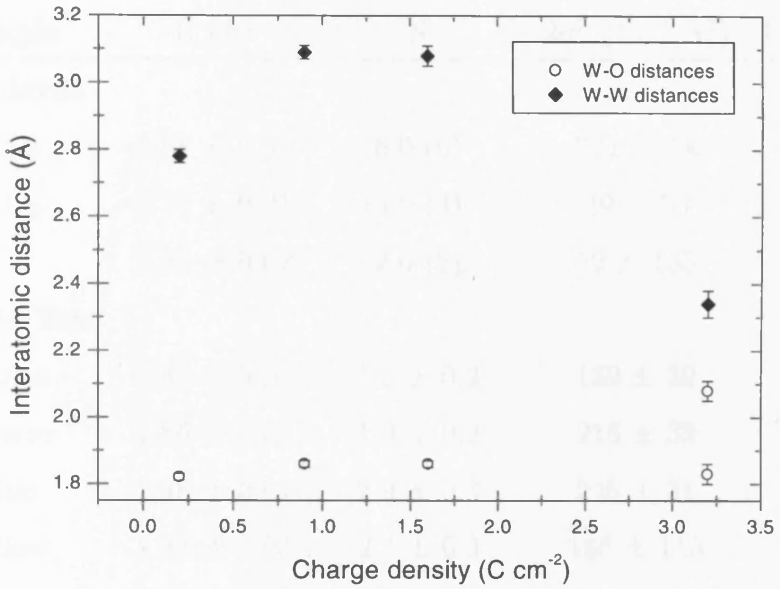

Figure 5.11: Variation of first W-O (circles) and W-W (diamonds) shell interatomic distances as a function of charge density during formation.

5.5; those of the films are plotted as a function of charge density in figure 5.11. This plot shows that the first W-O shell is initially undistorted. W-O and W-W shells separate as tungsten is oxidised up to 0.9 C cm^{-2}. This movement is required to accommodate the inserted cations as $n \rightarrow 1$. The oxygen and tungsten shells then begin to converge at 1.6 C cm^{-2}. As the shells converge, a second W-O distance appears between the shells, ending with a distorted W-O shell at 3.2 C cm^{-2}. As charge density increases, the first oxygen shell hardly moves from its original position, implying only slight changes to valency during oxidation, in agreement with the edge shifts.

Figure 5.12 shows that the coordination number of the first W-O shell increases as a function of charge density, confirming that the oxide phase does indeed develop with anodic charge. The amount of oxygen in the first W-O shell of the oxides is small compared to the literature values stated in table 5.5. However, these coordination numbers are consistent with the

		W-O		
Sample	R (Å)	N	$2\sigma^2$ (10^{-4} Å^2)	Fit Index (%)
Standards				
WO_2	1.88 ± 0.01	6.0 (6)	321 ± 54	37.2
WO_3	1.71 ± 0.01	4.0 (4)	39 ± 50	57.5
	1.86 ± 0.02	2.0 (2)	52 ± 135	
Oxide Films				
brown	1.82 ± 0.01	1.3 ± 0.2	139 ± 32	35.7
bronze	1.86 ± 0.01	1.9 ± 0.2	216 ± 38	40.6
blue	1.86 ± 0.01	2.9 ± 0.3	245 ± 31	31.3
yellow	1.83 ± 0.03	2.4 ± 0.3	168 ± 113	39.7
	2.08 ± 0.03	1.0 ± 0.3	108 ± 156	

		W-W		
Sample	R (Å)	N	$2\sigma^2$ (10^{-4} Å^2)	Fit Index (%)
Standards				
W foil	2.71 ± 0.01	4.2 ± 1.4 (8)	63 ± 39	40.8
W film	2.75 ± 0.01	4.2 ± 0.9 (8)	103 ± 22	38.1
WO_2	2.70 ± 0.01	0.4 ± 0.4 (2)	35 ± 94	37.2
WO_3	2.23 ± 0.03	10.9 ± 1.8 (6)	487 ± 10	57.5
Oxide Films				
brown	2.78 ± 0.02	3.3 ± 1.5	259 ± 95	35.7
bronze	3.09 ± 0.02	0.5 ± 0.5	76 ± 86	40.6
blue	3.08 ± 0.03	1.0 ± 1.0	152 ± 131	31.3
yellow	2.34 ± 0.04	3.4 ± 2.6	610 ± 181	39.7

Table 5.5: Structural parameters for first W-O and W-W shells, derived from fits to EXAFS of standards and oxide films. Coordination numbers shown in brackets are expected (literature) values (section 2.2.4). Uncertainties represent 95 % confidence levels.

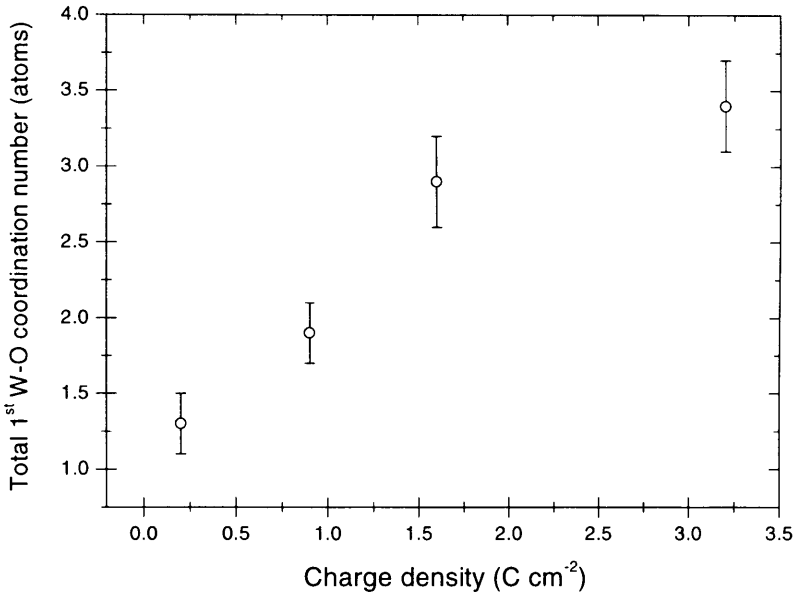

Figure 5.12: Number of first W-O shell neighbours as a function of charge density for the oxide films.

values derived from fits to the standards before they were set (section 5.3.2), so if a spectral effect has caused this consistent lowering, the coordination numbers will be correspondingly offset from their literature values. The short W-O distance of ref-WO_3 is reasonable since the ionic radius of W^{6+} is only 0.6 Å.

The position of both W-O and W-W shells appear to be between WO_2 and WO_3. As charge density increases, the structure of the oxides changes, initially moving away from WO_2 and WO_3 structures, then approaching WO_3 at the end. The movement of the shells is also evident in figure 5.13. The structures of bronze and blue oxides are almost identical in the first 2 coordination spheres. The yellow film has a structure that is very similar to WO_3, though it appears that this oxide has not quite reached the full WO_3 structure.

The movement of all the fitted coordination shells is shown by the radial

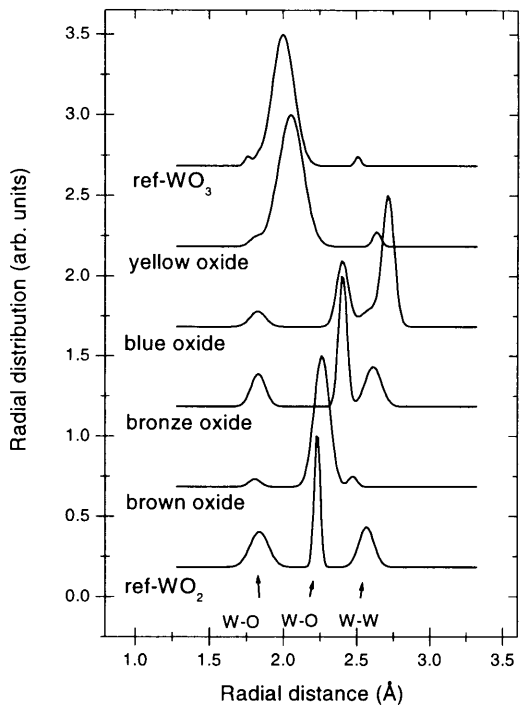

Figure 5.13: Calculated radial distribution functions for first and second W-O and W-W shells of the oxide films as a function of charge density. Curves are offset by an arbitrary amount for clarity.

distribution functions (fig. 5.13) derived from each fit shown in figs. 5.9 and 5.10. These were calculated using the EXCURV98 program [53], when a final fit was achieved for each film. These clearly display the shifting position and amplitude of each coordination shell; they also convey the separation and subsequent convergence of W-O and W-W shells, and the emergence of a second W-O distance.

5.5 Discussion

The results derived from cyclic voltammetry, UV/vis spectrophotometry, X-ray reflectivity and reflection-absorption spectroscopy all suggest the same general trends. Firstly, they confirm that the metal is converted to a lower density material, as shown by the lower oxide critical angle. The oxides displayed increasing UV/vis range absorbance with anodic charge, as shown by their optical absorption edges and their colouration. This evidence proves the formation of another phase with a finite band gap. The colours and approximate valency of W in bronze and blue films, and hence the value of n, correspond with the scheme on page 171, where films containing more than $n = 0.3$ are metallic. This split between metallic and non-metallic characteristics for films with oxidation states ranging from W^{5+}–W^{6+} is displayed by the data presented in this chapter. The appearance, optical reflectance, X-ray reflectance, XANES and EXAFS of the bronze film all indicate a film that is metallic in nature. For instance, the relatively high X-ray reflectivity of the film and its metallic-bronze appearance are indicative of such a material. The very slight UV/vis edge step also suggests a material having either a narrow band gap or a Fermi level close to or within a band containing a many accessible conduction band states (*i.e.* a good electronic conductor). The optical band gap is indeed small, but its magnitude relative to the other oxides is not as important as the positioning of the Fermi level. The bronze colouration accounts for the relatively low UV/vis reflectivity. Regardless of its position, the X-ray absorption edge is relatively discrete, not crossing with any of the other edges, apart form the yellow oxide, suggesting a single, non integer oxidation state for W ions, rather than a spread of integer oxidation states with varying proportions. In terms of structure, the separation between first W-O and W-W shell atoms is furthest in this oxide. This suggests more reduced W ions, with a structure that is between that of WO_3 and WO_2, and where the degree of ion insertion (causing the two shells to

separate) has reached a maximum, therefore agreeing with the derived valency of 4.9 (*i.e.* $n \approx 1$). The only evidence that appears to contravene the stated evidence for metallic behaviour is its relatively low density, indicated by the lowest θ_c of all the films.

When considering the more oxidised blue film, having less incorporated cations and a value of $n = 0.3$, the question arises as to whether film characteristics are representative of the metallic or non-metallic side of n_c, or whether it possesses a mixture of these properties. The UV/vis range reflectance is the same as the bronze film, though its X-ray reflectivity is a lot lower than the bronze oxide, indicating higher absorbance, which is characteristic of a non-metal. The critical angle suggests mass density is relatively low, which also indicates a non-metal. The fairly discrete edge of the blue film signifies a more uniform valency than the yellow film, which is characteristic of a conductor. In this oxide, the well-separated first W-O and W-W shells begin to converge, coinciding with the continual rise in Debye-Waller factors (fig. 5.14). This rise results from the structural rearrangement that was required to accommodate the inserted cations and/or the distorted oxygen shell in WO_3.

Despite the edge shift, the yellow film, having a higher anodic charge density is even more oxidised than the blue film. This film displays typical non-metallic characteristics, from its large UV/vis absorption step to its very broad L_3-edge. The shape of the yellow oxide edge in particular was so broad that it crossed all of the other edges at some point. Such a broad edge (regardless of its position) suggests the presence of a gradient of integer W oxidation states within the film, the broadness of the edge changing with the composition of the film. The yellow oxide gives the clearest illustration of this effect, but the other oxides possess edges that cross to a far lesser extent, though this may be a consequence of the close proximity of all the edges. The presence of unconverted tungsten in the yellow film probably had only a small effect on broadening the edges because the presence of metal in

its EXAFS and reflectivity profile was very small.

It is stated in chapter 2 that the mixed-integer valence model would require evidence for a series of regular coordination shells, each type of coordination sphere having a bond length characteristic of one integer W state rather than distorted shell with a mean bond length associated with a non-integer valency. For the yellow film, the slight difference between the first two W-O distances, and their small coordination numbers indicates the presence of a distorted shell (as for crystalline WO_3). Another factor necessary to confirm the model for non-uniform integer valency is a gradual increase in static disorder as charge density increases. The disorder would be caused by the reorganisation of individual tungsten sites as each is oxidised, forming the previously mentioned gradient of tungsten oxidation states. Figure 5.14 shows that there is a significant rise in Debye-Waller factor between 0.2 and 0.9 $\mathrm{C\,cm^{-2}}$, and the error bars show that disorder is still high in the yellow oxide, even though a more compact WO_3-type structure is achieved; this implies that an alternative mechanism (other than shell separation) accounts for high static disorder. In this oxide, with its very broad absorption edge, it may be concluded that a mixed-valence state is responsible for the high first shell Debye-Waller factors are in the yellow oxide. Since this model is more appropriate for describing more insulating, less conductive solids, where low mobility valence electrons that are localised at specific sites within the solid. It may then be concluded that the Fermi level of the yellow oxide lies within the small band gap.

Finally, the structure of the films was initially between WO_2 and WO_3, implying a valency of about 5+ and the final state of the film was close to WO_3 at 6+. The first W-O coordination numbers show that the oxides may be sub-stoichiometric with respect to oxygen. When cycled, these films exhibited the characteristic electrochromism of the tungsten trioxide system, so the structural changes described are characteristic to H_nWO_3, where the value of n corresponds to the non-integer (for metallic films) and mixed-

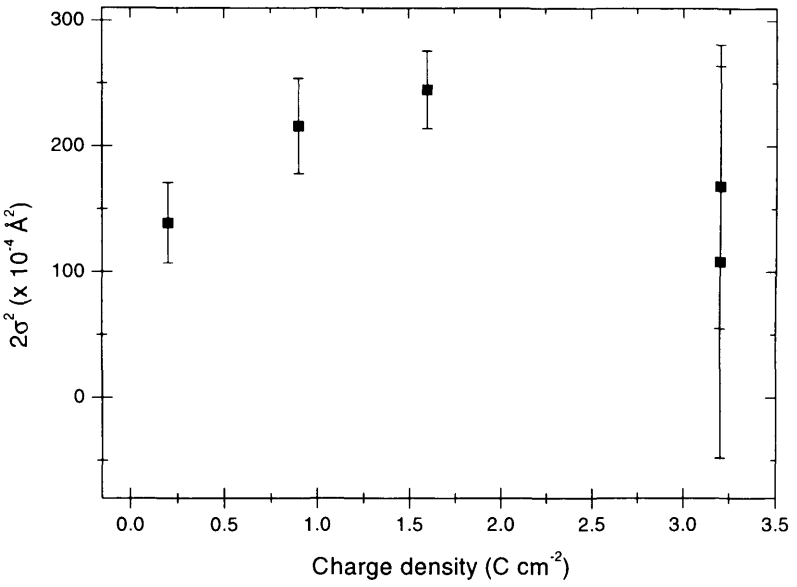

Figure 5.14: Debye-Waller factor $2\sigma^2$, representing static disorder for the first W-O shell as a function of charge density.

integer valency of tungsten.

5.6 Conclusions

The derived values for n account for the difference between the data derived from blue and bronze films. On the whole, brown oxide has similar optical and X-ray characteristics to metal. It may be concluded that in the case of the bronze film, the non-integer value for W valency does not represent a mixture of W sites at a range of oxidation states, though this model may be used to represent the yellow, non-metallic oxide. On the other hand, conclusive evidence for either case does not exist for the blue film. This is not surprising since the value for n in this films is 0.3.

Even though a great deal is already known about the tungsten trioxide system, and despite the fact that measurements were *ex situ*, a short-range

structural study of anodic oxide growth as a function of charge density has not been reported until now. The particularly novel aspect of this study is the use of reflection mode EXAFS to explore the newly formed surface oxide phase. These achievements satisfy many of the original aims of this study. The main reason for the failure to reliably operate the cell *in situ* may not have occurred if the films were more porous; unfortunately, this is the property that would have significantly reduced their X-ray reflectivity.

This study has provided a preliminary insight into the growth of anodic oxide films. A four-stage expansion and subsequent contraction of the distance between first W-O and W-W shells has been identified. These shell movements coincide with cation insertion/expulsion and the emergence of the a long W-O distance with increasing charge density. There is plenty of scope for future study, the most important being the development of a fully functioning, potentiodynamic, *in situ* spectroelectrochemical cell. An *in situ* investigation would be able to derive structural information regarding the earlier stages of film growth, where n is between 0.3 and 1.

Chapter 6

Conclusions and Future Directions

The instrumental capability for X-ray absorption spectroscopy on electrochemically modified films has been proven using the specifically-designed spectroelectrochemical cells described in this thesis. EXAFS spectra recorded in transmission (standard and quick), fluorescence, reflection and energy dispersive modes revealed the structural evolutions taking place during or after lengthy electrochemical manipulations (leading to a build-up of charge) such as overcharge (WO_3 and Nb_2O_5 systems) discharge ($Ni(OH)_2$ system).

The results obtained have been used to clarify the connection between electrode charge, metal ion valency, interatomic distance, distortion of coordination shells and structural disorder. In essence, it has been shown how the valency of metal ions, and hence the bulk structural form adopted by the films is affected by electrode charge. Interpretation of the electronic properties of these films through a combination of qualitative and quantitative analyses is a particularly novel aspect of this work. It was shown, by use of solid-state and molecular descriptions, that nickel hydroxide, niobium pentoxide and tungsten trioxide behave as a conductor, semiconductor and insulator, respectively, and WO_3 underwent a metal-insulator transition when oxidised. It was also shown that the oxidised forms of each of the oxides consisted of

a distorted first metal-oxygen shell, and a regular shell was evident in the reduced forms. Also, the first metal-metal shell did not always move antagonistically to metal-oxygen environments. These results therefore satisfy most of the original aims stated on page 1.

Mechanisms for the full structural behaviour of each of the electrodes could be achieved by extending this work to real-time studies of both overcharge and discharge; this would help to investigate the possibility of hysteresis with regard to the structural pathway for these evolutions. It was not possible to observe structural changes during voltammetric cycling of thick films because EXAFS, being a technique that averages across the illuminated area, accounts for the dominant structure(s), whereas cycling may only induce a change in a small proportion of a sample. Also, dynamic, *in situ* investigations were not always possible due to the trade-off between spectroscopic and electrochemical requirements. This factor, combined with poor film conductivity proved a significant hindrance to progress. However, further refinement of experimental design may achieve success; this would be highly desirable for dynamic *in situ* reflEXAFS.

The results derived from spectra recorded in different configurations agree, and both spectroscopic and electrochemical results correlate. The understanding provided by this work should be beneficial to optoelectronic technology, whose main challenges include reproducing these structural changes over large working areas and stabilising unstable valence states.

Bibliography

[1] M. D. Foster, "X-ray Scattering Methods for the Study of Polymer Interfaces," *Crit. Rev. Anal. Chem.*, vol. 24, no. 3, pp. 179–239, 1993.

[2] C. A. Melendres, A. Tadjeddine, *Synchrotron Techniques in Interfacial Electrochemistry.* London: Kulwer, 1992.

[3] A. Davenport, J. G. Gordon II, *X-ray Methods in Corrosion and Interfacial Electrochemistry.* Pennington, New Jersey: The Electrochemical Society Inc., 1992.

[4] M. F. Toney, J. McBreen, "In Situ Synchrotron X-ray Techniques for Determining Atomic Structure at Electrode/Electrolyte Interfaces," *Electrochem. Soc. Interface*, vol. Spring, pp. 22–31, 1993.

[5] R. J. Gale, *Spectroelectrochemistry: Theory and Practice*, pp. 9–40. London: Plenum, 1988.

[6] L. R. Sharpe, W. R. Heineman, R. C. Elder, "EXAFS Spectroelectrochemistry," *Chem. Rev.*, vol. 90, pp. 705–722, 1990.

[7] M. J. Berger, J. H. Hubbell, "Database of Calculated Photon Cross Sections (XCOM), NIST,." http://physics.nist.gov/PhysRefData/Xcom/html/xcom1.html.

[8] B. K. Teo, *EXAFS: Basic Principles and Data Analysis.* Berlin: Springer-Verlag, 1985.

[9] A. G. Michette, C. J. Buckley, *X-ray Science and Technology.* Bristol: IOP, 1993.

[10] Y. Kitajima, "Soft X-ray Absorption Spectroscopy with Variable Surface Sensitivity Using Fluorescence Yield Detection," *J. Phys. IV France*, vol. 7, no. C2, pp. 705–706, 1997.

[11] N. R. S. Farley, S. J. Gurman, A. R. Hillman, "Simple Cell for In Situ X-ray Absorption Spectroelectrochemistry," *Electrochem. Comm.*, vol. 1, pp. 449–452, 1999.

[12] M. R. Antonio, L. Soderholm, I. Song, "Design of Spectroelectrochemical Cell for In Situ X-ray Absorption Fine Structure Measurements of Bulk Solution Species," *J. App. Electrochem.*, vol. 27, pp. 784–792, 1997.

[13] C. A. Melendres, A. N. Mansour, "X-ray Absorption Spectroelectrochemical Cell for *in situ* Studies of Thin Films ," *Electrochimica Acta*, vol. 43, no. 5-6, pp. 631–634, 1998.

[14] S. Kim, I. T. Bae, M. Sandifer, P. N. Ross, R. Carr, J. Woicik, M. R. Antonio, D. A. Scherson, "In Situ XANES of an iron Porphyrin Irreversible Adsorbed on an Electrode Surface," *J. Am. Chem. Soc.*, vol. 113, pp. 9063–9066, 1991.

[15] S. Kim, D. A. Tryk, M. R. Antonio, R. Carr, D. Scherson, "In Situ X-ray Absorption Fine Structure Studies of Foreign Metal Ions in Nickel Hydrous Oxide Electrode Electrodes in Alkaline Electrolytes," *J. Phys. Chem.*, vol. 98, pp. 10269–10276, 1994.

[16] E. M. Gullikson, "Database of X-ray Interactions with Matter, Berkley Lab.."
http://cindy.lbl.gov/optical_constants/.

[17] S. J. Gurman, R. Fox, "Surface EXAFS Measurements from Specular Reflectivity of X-rays," *Phil. Mag. B*, vol. 54, no. 2, pp. L45–L49, 1986.

[18] J. McBreen, W. E. O'Grady, K. I. Pandya, "EXAFS: A New Tool for the Study of Battery and Fuel Cell Materials," *J. Power Sources*, vol. 22, pp. 323–340, 1988.

[19] B. K. Agarwal, *X-ray Spectroscopy - An Introduction.* Berlin: Springer-Verlag, 1979.

[20] S. J. Gurman, "Interpretation of EXAFS Data," *J. Synchrotron Rad.*, vol. 2, pp. 56–63, 1995.

[21] S. S. Hasnain, *Synchrotron Radiation and Biophysics.* Chichester: Ellis Horwood, 1990.

[22] M. Roy, S. J. Gurman, G. van Dorssen, "The Amplitude Reduction Factor in EXAFS," *J. Phys. IV France*, vol. 7, no. C2, pp. 151–152, 1997.

[23] S. J. Gurman, N. Binsted, I. Ross, "A Rapid, Exact Curved-Wave Theory for EXAFS Calculations," *J. Phys C*, vol. 17, pp. 143–152, 1984.

[24] D. J. G. Ives, G. J. Janz, *Reference Electrodes: Theory and Practice.* New York: Academic Press, 1961.

[25] A. C. Fisher, *Electrode Dynamics.* Oxford: Oxford University Press, 1996.

[26] N. F. Mott, *Conduction in Non-Crystalline Materials.* Oxford: Clarendon Press, 1987.

[27] A. R. West, *Solid State Chemistry and its Applications.* Chichester: Wiley, 1984.

[28] M. Maček, B. Orel, U. O. Krašovec, "The Effect of Lithiation on the Electrochromism of Sol-Gel Derived Niobium Oxide Films," *J. Electrochem. Soc.*, vol. 144, no. 9, pp. 3002–3010, 1997.

[29] N. Kumagai, Y. Tateshita, Y. Takatsuka, M. Baba, T. Ikeda, K. Tanno, "Intercalation of Lithium in RF-Sputtered Niobium Oxide Film as Electrode Material for Lithium-Ion Batteries," *J. Power Sources*, vol. 54, pp. 175–179, 1995.

[30] P. M. S. Monk, R. J. Mortimer, D. R. Rosseinsky, *Electrochromism: Fundamentals and Applications.* Cambridge: VCH, 1995.

[31] M. J. Henderson, A. R. Hillman, E. Vieil, C. Lopez, "Combined Electrochemical Quartz Crystal Microbalance (EQCM) and Probe Beam Deflection (PBD): Validation of the Technique by a Study of Silver Ion Mass Transport," *J. Electroanal. Chem.*, vol. 458, no. 1–2, pp. 241–248, 1998.

[32] H. French, M. J. Henderson, A. R. Hillman, E. Vieil, "Ion and Solvent Transfer Discrimination at a Nickel Hydroxide Film Exposed to LiOH by Combined Electrochemical Quartz Crystal Microbalance (EQCM) and Probe Beam Deflection (PBD) Techniques," *J. Electroanal. Chem.*, vol. 500, no. 1–2, pp. 192–207, 2001.

[33] M. Gonsalves, A. R. Hillman, "Effect of Time Scale on Redox-Driven Ion and Solvent Transfers at Nickel Hydroxide Films in Aqueous Lithium Hydroxide Solutions," *J. Electroanal. Chem.*, vol. 454, no. 1–2, pp. 183–202, 1998.

[34] C. G. Granqvist, *Handbook of Inorganic Electrochromic Materials.* Amsterdam: Elsevier, 1995.

[35] I. Jureviciute, S. Bruckenstein, A. R. Hillman, A. Jackson, "Kinetics of Redox Switching of Electroactive Polymer Using the Electrochemical Quartz Crystal Microbalance, Part I: Identifying the Rate Limiting Step in the Presence of Coupled Electron/Ion and Solvent Transfer," *Phys. Chem. Chem. Phys.*, vol. 2, no. 18, pp. 4193–4198, 2000.

[36] L. Bailey, M. J. Henderson, A. R. Hillman, N. Gadegaard, A. Glidle, "In Situ Neutron Reflectivity Studies of Poly-o-Toluidine Films," *Physica B*, vol. 276, pp. 373–374, 2000.

[37] W. C. Dautremont-Smith, "Transition Metal Oxide Electrochromic Materials and Displays: A Review, Part I: Oxides with Cathodic Colouration," *Displays*, vol. Jan., pp. 3–22, 1982.

[38] A. E. Russell, S. Maniguet, R. J. Matthew, J. Yao, M. A. Roberts, D. Tompsett, "In Situ X-ray Absorption Spectroscopy and X-ray Diffraction of Fuel Cell Electrocatalysts," *J. Power Sources*, vol. 96, no. 1, pp. 226–232, 2001.

[39] P. M. Saville, M. Gonsalves, A. R. Hillman, R. Cubitt, "Dynamic Neutron Reflectivity Measurements During Redox Switching of Nickel Hydroxide Films," *J. Phys. Chem. B*, vol. 101, no. 1, pp. 1–4, 1997.

[40] M. R. Deakin, D. A. Buttry, "Electrochemical Applications of the Quartz Crystal Microbalance," *Anal. Chem.*, vol. 60, no. 20, p. A1147, 1989.

[41] R. Schumacher, "The Quartz Crystal Microbalance - A Novel Approach to the In Situ Investigation of Interfacial Phenomena at the Solid Liquid Junction," *Agnew Chem. Int. Edit.*, vol. 29, no. 4, pp. 329–343, 1990.

[42] S. Bruckenstein, A. R. Hillman, A. T. Hubbard (ed.), *Handbook of Surface Imaging and Visualisation.* USA: CRC Press, 1995.

[43] R. Houwink, H. K. Decker (eds.), *Elasticity, Plasticity and the Structure of Matter.* Cambridge: Cambridge University Press, 1971.

[44] H. L. Bandey, A. R. Hillman, M. J. Brown, S. J. Martin, "Viscoelastic Characterisation of Electroactive Polymer Films at the Electrode/Solution Interface," *Faraday Discuss.*, vol. 107, no. 7, pp. 1–17, 1997.

[45] H. L. Bandey, *Viscoelastic Characteristics of Electroactive Polymer Films.* PhD thesis, University of Leicester, Department of Chemistry, 1998.

[46] "*Faraday Discussion*," 107 (7), 1997. Several references therein.

[47] D. S. Ballantine, *Acoustic Wave Sensors - Theory, Design and Physio-Chemical Applications.* USA: Academic Press, 1997.

[48] M. Skompska, A. R. Hillman, "Electrochemical Quartz Crystal Microbalance Studies of the Electropolymerization, Electroactivity and Complexing Properties of Poly(1,8-diaminonapthalene) Films," *J. Chem. Soc. Faraday Transactions*, vol. 92, no. 20, pp. 4101–4108, 1996.

[49] M. A. Cowen, S. L. Gilbert, M. Gonsalves, A. R. Hillman, S. Bruckenstein, "Crystal Impedance: A New Technique for Monitoring the Sol-Gel Process," *J. Chem. Soc. Faraday Transactions*, vol. 92, no. 6, pp. 1079–1082, 1996.

[50] "Inorganic Crystal Structure Database (ICSD), Daresbury Laboratory."

[51] M. E. Herron, S. E. Doyle, K. J. Roberts, J. Robinson, F. C. Walsh, "Instrumentation and Cell Design for In Situ Studies of Electrode Surfaces Using

X-ray Synchrotron Radiation," *Rev. Sci. Instrum.*, vol. 63, no. 1, pp. 950–955, 1992.

[52] A. J. Dent, F. W. Mosselmans, "An Introduction to EXAFS Data Analysis," 1995. CLRC Daresbury Laboratory, Warrington.

[53] N. Binsted, "EXCURV97/98 Manual, Daresbury Laboratory."

[54] R. E. White, J. O'M Bockris, B. O. Conway, *Modern Aspects of Electrochemistry*, vol. 21, pp. 29–63. New York: Plenum, 1990.

[55] W. E. O'Grady, K. I. Pandya, K. E. Swider, D. A. Corrigan, "In Situ X-ray Absorption Near-Edge Structure Evidence for Quadrivalent Nickel in Nickel Battery Electrodes," *J. Electrochem. Soc.*, vol. 143, no. 5, pp. 1613–1616, 1996.

[56] Y. Ushio, A. Ishikawa, T. Niwa, "Degradation of the Electrochromic Nickel Oxide Film Upon Redox Cycling," *Thin Solid Films*, vol. 280, pp. 233–237, 1996.

[57] K. I. Pandya, R. W. Hoffman, J. McBreen, W. E. O'Grady, "In Situ X-ray Absorption Spectroscopic Studies of Nickel Oxide Electrodes," *J. Electrochem. Soc.*, vol. 137, no. 2, pp. 383–388, 1990.

[58] N. Sac-Epée, M. R. Palacìn, A. Delahaye-Vidal, Y. Chabre, J-M. Tarâscon, "Evidence for Direct $\gamma-\mathrm{NiOOH} \leftrightarrow \beta-\mathrm{Ni(OH)_2}$ Transitions During Electrochemical Cycling of the Nickel Hydroxide Electrode," *J. Elcetrochem. Soc.*, vol. 145, no. 5, pp. 1434–1441, 1998.

[59] T. W. Capehart, D. A. Corrigan, R. S. Connell, K. I. Pandya, R. W. Hoffman, "In Situ Extended X-ray Absorption Fine Structure Spectroscopy of Thin-Film Nickel Hydroxide Electrodes ," *Appl. Phys. Lett.*, vol. 58, no. 8, pp. 865–867, 1991.

[60] A. N. Mansour, C. A. Melendres, "X-ray Absorption Spectra and the Local Structure of Nickel in some Oxycompounds and Fluorides," *J. Phys. IV France*, vol. 7, no. C2, pp. 1171–1172, 1997.

[61] N. R. S. Farley, S. J. Gurman, A. R. Hillman, "In Situ EXAFS Study of Nickel Hydroxide Electrodes During Discharge," *J. Synch. Rad.*, vol. 6, no. 3, pp. 198–200, 1999.

[62] N. R. S. Farley, S. J. Gurman, A. R. Hillman, "Dynamic EXAFS Study of Discharging Nickel Hydroxide Electrode with Non-Integer Valency," *Electrochimica Acta*, vol. 46, pp. 3119–3127, 2001.

[63] Y. Hu, I. T. Bae, Y. Mo, M. R. Antonio, D. A. Scherson, "In Situ X-ray Absorption Fine Structure and Optical Reflectance Studies of Electrodeposited Nickel Hydrous Oxide Films in Alkaline Electrolytes," *Can. J. Chem.*, vol. 75, pp. 1721–1729, 1997.

[64] A. N. Mansour, J. Mc Breen, C. A. Melendres, "An In Situ X-ray Absorption Spectroscopic Study of Charged $Li_{(1-z)}Ni_{(1+z)}O_2$ Cathode Material," *J. Electrochem. Soc.*, vol. 146, no. 8, pp. 2799–2809, 1999.

[65] X. Qian, H. Sambe, D. E. Ramaker, K. I. Pandya, W. E. O'Grady, "Quantitative Interpretation of K-edge NEXAFS Data for Various Nickel Hydroxides and the Charged Nickel Electrode," *J. Phys. Chem. B*, vol. 101, pp. 9441–9446, 1997.

[66] Electrochemical Society 194th Meeting, Boston, "vol. 98-2," 1998. several abstracts therein.

[67] D. A. Corrigan, S. L. Knight, "Electrochemical and Spectroscopic Evidence on the Participation of Quadrivalent Nickel in the Nickel Hydroxide Redox Reaction," *J. Electrochem. Soc.*, vol. 136, no. 3, pp. 613–619, 1989.

[68] P. Oliva, J. Leonardi, J. F. Laurent, "Review of the Structure and the Electrochemistry of Nickel Hydroxides and Oxyhydroxides," *J. Power Sources*, vol. 8, pp. 229–255, 1982.

[69] I. J. Pickering, G. N. George, J. T. Lewandowski, A. J. Jacobson, "Nickel K-edge X-ray Absorption Fine Structure of Lithium Nickel Oxides," *J. Am. Chem. Soc.*, vol. 115, pp. 1437–4144, 1993.

[70] H. French, "Internal Report." Electrochemistry Group, Chem. Dept., Univ. of Leicester, 1999.

[71] R. J. Matthew, A. E. Russell, "XAS of Carbon Supported Platinum Fuel Cell Electrocatalysts: Advances Toward Real Time Investigations," *Topics in Catalysis*, vol. 10, no. 3–4, pp. 231–239, 2000.

[72] M. E. Kordesch, R. W. Hoffman, "Strongly Adhesive Gold Electrodes on Melinex," *Thin Solid Films*, vol. 107, pp. 365–371, 1983.

[73] P. Ray, *Inorganic Synthesis*, vol. V. New York: McGraw Hill, 1957.

[74] C. C. Streinz, A. P. Hartman, S. Motupally, J. W. Weidner, "The Effect of Current and Nickel Nitrate Concentration on the Deposition of Nickel Hydroxide Films," *J. Electrochem. Soc.*, vol. 142, no. 4, pp. 1084–1089, 1995.

[75] D. F. Shriver, P. W. Atkins, C. H. Langford, *Inorganic Chemistry (2nd ed.)*. Oxford: Oxford University Press,, 1994.

[76] N. Ichikuni, Y. Iwasawa, "Observation of the Structural Change in the Nb Sites During Ethanol Dehydration on a SiO_2-Attached Nb Dimer Catalyst by EXAFS," *J. Phys. Chem.*, vol. 98, pp. 11576–11581, 1994.

[77] A. Florentino, P. Cartraud, P. Magnoux, M. Guisnet, "Textural, Acidic and Catalytic Properties of Niobium Phosphate and of Niobium Oxide: Influence of the Pretreatment Temperature," *Appl. Catal. A*, vol. 89, pp. 143–153, 1992.

[78] T. Ushikubo, Y. Koike, K. Wada, l. Xei, D. Wang, X. Guo, "Study of the Structure of Niobium Oxide by X-ray Absorption Fine Structure and Surface Science Techniques," *Catalysis Today*, vol. 28, pp. 59–69, 1996.

[79] S. M. Maurer, D. Ng, E. I. Ko, "Structural and Acidic Properties of Aerogels of Niobia, Niobia/Silica and Niobia/Titania," *Catalysis Today*, vol. 16, pp. 319–331, 1993.

[80] H. Yoshida, T. Tanaka, T. Yoshida, T. Funabiki, S. Yoshida, "Control of the Structure of Niobium Oxide Species on Silica by the Equilibrium Absorption Method," *Catalysis Today*, vol. 28, pp. 79–89, 1996.

[81] J-M. Jehng, I. E. Wachs, "Molecular Structures of Supported Niobium Oxide Catalysts Under In Situ Conditions," *J. Phys. Chem.*, vol. 95, pp. 7373–7379, 1991.

[82] I. E. Wachs, J-M. Jehng, G. Deo, H. Hu, N. Arora, "Redox Properties of Niobium Oxide Catalysts," *Catalysis Today*, vol. 28, pp. 199–205, 1996.

[83] T. Tanaka, T. Yoshida, H. Yoshida, H. Aritani, T. Funabiki, S. Yoshida, J-M. Jehng, I. E. Wachs, "XAFS Study of Niobium Oxide on Alumina," *Catalysis Today*, vol. 28, pp. 71–78, 1996.

[84] N. Ichikuni, Y. Iwasawa, "Structures and Catalysis of New Nb Dimers on SiO_2," *Catalysis Today*, vol. 16, pp. 427–434, 1993.

[85] K. Yoshimura, T. Miki, S. Iwama, S. Tanemura, "Characterisation of Niobium Oxide Electrochromic Thin Films Prepared by Reactive DC Magnetron Sputtering," *Thin Solid Films*, vol. 181–182, pp. 235–238, 1996.

[86] K. Yoshimura, T. Miki, S. Tanemura, "Electrochromic Properties of Niobium Oxide Thin Films Prepared by DC Magnetron Sputtering," *J. Electrochem. Soc.*, vol. 144, no. 9, pp. 2982–2985, 1997.

[87] K. Yoshimura, T. Miki, S. Iwama, S. Tanemura, "Niobium Oxide Electrochromic Thin Films Prepared by Reactive DC Magnetron Sputtering," *Jpn. J. Appl. Phys.*, vol. 34 (2), no. 10A, pp. L1293–L1296, 1995.

[88] T. Maruyama, S. Arai, "Electrochromic Properties of Niobium Oxide Thin Films Prepared by Radio-Frequency Magnetron Sputtering Method," *Appl. Phys. Lett.*, vol. 63, no. 7, pp. 869–870, 1993.

[89] M. A. B. Gomes, L-O. de S. Bulhões, S. C. de Castro, A. J. Damião, "The Electrochromic Process at Nb_2O_5 Electrodes Prepared by Thermal Oxidation of Niobium," *J. Electrochem. Soc.*, vol. 137, no. 10, pp. 3067–3070, 1990.

[90] T. Maruyama, T. Kanagawa, "Electrochromic Properties of Niobium Oxide Thin Films Prepared by Chemical Vapour Deposition," *J. Electrochem. Soc.*, vol. 141, no. 10, pp. 2868–2871, 1994.

[91] S. L. de A. Maranhão, R. M. Torresi, "Electrochemical and Chromogenics Kinetics of Lithium Intercalation in Anodic Niobium Oxide Films," *Electrochimica Acta*, vol. 43, no. 3–4, pp. 257–264, 1998.

[92] M. Maček, B. Orel, "Electrochromism of Sol-Gel Derived Niobium Oxide Films," *Solar Energy Materials and Solar Cells*, vol. 54, pp. 121–130, 1998.

[93] B. Ohtani, K. Iwai, S. Nishimoto, T. Inui, "Electrochromism of Niobium Oxide thin Films Prepared by the Sol-gel Process," *J. Electrochem. Soc.*, vol. 141, no. 9, pp. 2439–2442, 1994.

[94] M. Schmitt, S. Heusing, M. A. Aegerter, A. Pawlicka, C. Avellaneda, "Electrochromic Properties of Nb_2O_5 Sol-Gel Coatings," *Solar Energy Materials and Solar Cells*, vol. 54, pp. 9–17, 1998.

[95] M. T. Vandenborre, B. Poumellec, C. Alquier, J. Livage, "EXAFS Study of the Hydrolysis of Niobium Pentaethoxide," *J. Non-Crystalline Solids*, vol. 108, pp. 333–337, 1989.

[96] M. T. Vandenborre, B. Poumellec, J. Livage, "Etude EXAFS de la Formation d'Oxyde Nb_2O_5 par Hydrolyse-Condensation de Chloroethoxyde de Niobium," *J. Solid State Chemistry*, vol. 83, pp. 105–114, 1989.

[97] A. Pawlicka, M. Atik, M. A. Aegerter, "Synthesis of Multicolor Nb_2O_5 Coatings for Electrochromic Devices," *Thin Solid Films*, vol. 301, pp. 236–241, 1997.

[98] A. Pawlicka, M. Atik, M. A. Aegerter, "Synthesis of Nb_2O_5 Thin Films for Electrochromic Devices," *J. Materials Science Letters*, vol. 14, pp. 1568–1570, 1995.

[99] N. Özer, D-G. Chen, C. M. Lampert, "Preparation and Properties of Spin-Coated Nb_2O_5 Films by the Sol-Gel Process for Electrochromic Applications," *Thin Solid Films*, vol. 277, pp. 162–168, 1996.

[100] C. Alquier, M. T. Vandenborre, M. Henry, "Synthesis of Niobium Pentoxide Gels," *J. Non-Crystalline Solids*, vol. 79, pp. 383–395, 1986.

[101] G. R. Lee, J. A. Crayston, "Electrochromic Nb_2O_5 and Nb_2O_5/Silicone Composite Thin Films Prepared by Sol-Gel Processing," *J. Mater. Chem.*, vol. 1, no. 3, pp. 381–386, 1991.

[102] N. Özer, M. D. Rubin, C. M. Lampert, "Optical and Electrochemical Characteristics of Niobium Oxide Films Prepared by Sol-Gel Process and Magnetron Sputtering: A Comparison," *Solar Energy Materials and Solar Cells*, vol. 40, pp. 285–296, 1996.

[103] W. C. Dautremont-Smith, "Transition Metal Oxide Electrochromic Materials and Displays: a Review, Part1: Oxides with Cathodic Colouration," *Displays*, vol. January, pp. 3–22, 1982.

[104] A. V. Rosario, E. C. Pereira, "Lithium Insertion in TiO_2 Electrochromic Thin Films," *Electrochimica Acta*, vol. 46, pp. 1905–1910, 2001.

[105] Y. Hirai, T. Fukuda, H. Kuwahara, Y. Kobayashi, K. Kubota, "Synthesis of Fine Particles of Niobium Oxide Compounds from Metal Alkoxides," *Solid State Communications*, vol. 61, no. 4, pp. 267–269, 1987.

[106] B. X. Huang, K. Wang, J. S. Church, Y-S. Li, "Characterisation of Oxides on Niobium by Raman and Infrared Sprctroscopy," *Electrochimica Acta*, vol. 44, pp. 2571–2577, 1999.

[107] J. D. F. Ramsay, ed. D. J. Wedlock, *Controlled Particle, Droplet and Bubble Formation*, pp. 1–36. Oxford: Butterworth-Heinemann, 1994.

[108] H. Dislich, "Sol-Gel: Science, Processes and Products," *J. Non-Crystalline Solids*, vol. 80, pp. 115–121, 1986.

[109] L. L. Hench, J. K. West, "The Sol-Gel Process," *Chemical Review*, vol. 90, pp. 33–72, 1990.

[110] P. Griesmar, G. Papin, C. Sanchez, J. Livage, "Sol-Gel Route to Niobium Pentoxide," *Chem. Mater.*, vol. 3, pp. 335–339, 1991.

[111] M. I. Newton, G. McHale, P. D. Hopper, M. R. Willis, S. D. Burt, "Electrical Properties of Thin Gold Films on (3-mercaptopropyl)trimethoxy silane (MPS) Treated Glass Substrates," *Vacuum*, vol. 46, no. 3, pp. 315–318, 1995.

[112] C. G. Granqvist, "Electrochromic Tungsten Oxide Films: Review of Progress 1993–1998," *Solar Energy Materials and Solar Cells*, vol. 60, pp. 201–262, 2000.

[113] C. G. Granqvist, "Progress in Electrochromics: Tungsten Oxide Revisited," *Electrochimica Acta*, vol. 44, pp. 3005–3015, 1999.

[114] C. G. Granqvist, "Electrochromic Oxides: A Bandstructure Approach," *Solar Energy Materials and Solar Cells*, vol. 32, pp. 369–3822, 1994.

[115] B. W. Faughnan, R. S. Crandall, ed. J. I. Pankove, *Display Devices: Topics in Applied Physics*, vol. 40, p. 181. Berlin: Springer Verlag, 1980.

[116] D. Dini, F. Decker, E. Masetti, "A Comparison of the Electrochromic Properties of WO_3 Films Intercalated with H^+, Li^+ and Na^+," *J. App. Electrochem.*, vol. 26, pp. 647–653, 1996.

[117] R. A. Batchelor, M. S. Burdis, J. R. Siddle, "Electrochromism in Sputtered WO_3 Thin Films," *J. Electrochem. Soc.*, vol. 143, no. 3, pp. 1050–1055, 1996.

[118] K. Kaneda, S. Suzuki, "Physical Properties of Tungsten Oxide Films Deposited by a Reactive Sputtering Method," *J. App. Phys*, vol. 30, no. 8, pp. 1841–1846, 1991.

[119] M. F. Daniel, B. Desbat, J. C. Lassegues, R. Garie, "Infrared and Raman Spectroscopies of RF Sputtered Tungsten Oxide Films," *J. Solid State Chem.*, vol. 73, pp. 127–139, 1998.

[120] A. Temmink, O. Anderson, K. Bange, H. Hantsche, X. Yu, "4f Level Shifts of Tungsten and Colouration State of a-WO_3," *Vacuum*, vol. 41, no. 4–6, pp. 1144–146, 1990.

[121] S. I. Córboda de Torresi, A. Gorenstein, R. M. Torresi, M. V. Vázquez, "Electrochromism of WO_3 in Acid Solutions: An Electrochemical, Optical

and Electrogravimetric Study ," *J. Electroanal. Chem.*, vol. 318, pp. 131–144, 1991.

[122] D-J. Kim, S-I. Pyun, "Stress Generation and Annihilation During Hydrogen Injection into and Extraction from Anodic WO_3 Films," *Electrochimica Acta*, vol. 44, pp. 1723–1732, 1999.

[123] R. S. Lilliard, G. S. Kanner, D. P. Butt, "The Nature of Oxide Films on Tungsten in Acidic and Alkaline Solutions," *J. Electrochem. Soc.*, vol. 145, no. 8, pp. 2718–2725, 1998.

[124] D-J. Kim, S-I. Pyun, "Hydrogen Transport Through Anodic WO_3 Films," *Electrochimica Acta*, vol. 43, no. 16–17, pp. 2341–2347, 1998.

[125] M. Kitao, S. Yamada, S. Yoshida, H. Akram, K. Urabe, "Preparation Conditions of Sputtered Electrochromic WO_3 Films and their Infrared Absorption Spectra," *Solar Energy Materials and Solar Cells*, vol. 25, pp. 241–255, 1992.

[126] C. Bohnke, O. Bohnke, "Heat Treatment of Amorphous Electrochromic WO_3 Thin Films Deposited onto Indium-Tin Oxide Substrates," *J. App. Electrochem.*, vol. 18, pp. 715–723, 1988.

[127] P. Delichere, P. Falras, A. Hugot-Le-Goff, "Electrochromism in Anodic WO_3 Films II: Optical and Electrochromic Properties of Coloured Distorted Hexagonal Films," *Thin Solid Films*, vol. 161, pp. 47–58, 1988.

[128] A. Kuzmin, J. Purans, "X-ray Absorption Spectroscopy Study of Local Structural Changes in a-WO_3 under Colouration," *J. Phys. Condens. Matter*, vol. 5, pp. 2333–2340, 1993.

[129] A. Kuzmin, J. Purans, "The Influence of the Focusing Effect on the X-ray Absorption Fine Structure Above All the Tungsten L Edges in Non-Stoichiometric Tungsten Oxides," *J. Phys. Condens. Matter*, vol. 5, pp. 9423–9430, 1993.

[130] T. Nanba, T. Takahishi, J. Takada, A. Osaka, Y. Miura, I. Yasui, A. Kishimoto, T. Kudo, "Characterization of Amorphous Tungsten Trioxide Thin

Films Prepared by RF Magnetron Sputtering Method," *J. Non-Crystalline Solids*, vol. 178, pp. 233–237, 1994.

[131] P. W. Atkins, *Physical Chemistry (5th ed)*. Oxford: Oxford University Press, 1994.